Tandem, triple and quadruple junction polymer solar cells

Tandem, Triple, and Quadruple Junction Polymer Solar Cells

PROEFSCHRIFT

ter verkrijging van de graad van doctor aan de Technische Universiteit Eindhoven,
op gezag van de rector magnificus prof.dr.ir. F.P.T. Baaijens,
voor een commissie aangewezen door het College voor Promoties, in het openbaar
te verdedigen op maandag 10 december 2018 om 13:30 uur

door

Dario Di Carlo Rasi

geboren te Frascati, Italië

Dit proefschrift is goedgekeurd door de promotoren en de samenstelling van de promotiecommissie is als volgt:

voorzitter:	prof.dr.ir. E.J.M. Hensen
1e promotor:	prof.dr.ir. R.A.J. Janssen
copromotor:	dr.ir. M.M. Wienk
leden:	prof.dr. K. Vandewal (Universiteit Hasselt)
	prof.dr. J. Martorell (ICFO)
	prof.dr.ir. W.M.M. Kessels
	prof.dr. L.J.A. Koster (RUG)
	dr. S.C.J. Meskers

Het onderzoek of ontwerp dat in dit proefschrift wordt beschreven is uitgevoerd in overeenstemming met de TU/e Gedragscode Wetenschapsbeoefening.

Printed by: Gildeprint

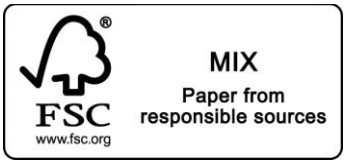

A catalogue record is available from the Eindhoven University of Technology Library

ISBN: 978-90-386-4642-8.

The research described in thesis has been financially supported by the European Community's Seventh Framework Programme in the ITN project OSNIRO (No. 607585), the European Research Council (Advanced, Grant (No. 339031), and the Ministry of Education, Culture and Science (Gravity Program No. 024.001.035).

Table of Contents

Chapter 1: Introduction **1**

1.1 Solar cells 2
1.2 Organic solar cells 3
1.3 Characterization of solar cells 5
1.4 Multi-junction organic solar cells 7
1.4.1 Working principles 7
1.4.2 Early developments 8
1.4.3 Characterization of multi-junction organic solar cells 11
1.4.4 Determination of the wavelength-dependent *n* and *k* optical constants 12
1.5 Aim and outline of the thesis 13
1.6 References 15

Chapter 2: Recent Developments on Solution-Processed Multi-Junction Organic Solar Cells **19**

2.1 Introduction 20
2.2 Tandem solar cells 21
2.2.1 ICL materials 21
2.2.2 Processing multi-junction stacks 25
2.2.3 Light management 28
2.2.4 Active layer materials 31
2.2.5 Upscaling 42
2.3 Three- and four-fold junction solar cells 49
2.4 Accurate characterization 52
2.5 Unusual device architectures 56
2.6 Use of multi-junction polymer solar cells for photoelectrochemical water splitting 57
2.7 Conclusions 59
2.8 References 61

Chapter 3: A Universal Route to Fabricate n-i-p Multi-Junction Polymer Solar Cells via Solution Processing **67**

3.1 Introduction 68
3.2 Results and Discussion 69
3.2.1 Materials and device architectures 69
3.2.2 PEDOT:PSS as HTL 73
3.2.3 PEIE and ZnO nanoparticles as ETL 76
3.2.4 Tandem solar cells 77
3.2.5 ICL for triple-junction solar cells: need for second order orthogonality 79
3.2.6 Triple-junction solar cells 81
3.2.7 Synopsis 85
3.3 Conclusions 85
3.4 Experimental Section 86
3.5 References 91

Chapter 4: Accurate Characterization of Triple-Junction Polymer Solar Cells **95**

4.1 Introduction 96
4.2 Results and Discussion 97
4.2.1 The design of the triple-junction cell 97
4.2.2 Measuring the performance under simulated AM1.5G light 99
4.2.3 EQE of the triple junction using bias light 100
4.2.4 Corrections to the EQE measurement 102
4.2.5 Reconstructing the $J-V$-curve 105
4.3 Conclusions 108
4.4 Experimental Section 109
4.5 References 113

Chapter 5: Quadruple-Junction Polymer Solar Cells with Four Complementary Absorber Layers **115**

5.1 Introduction 116
5.2 Results and discussion 117
5.2.1 Layers stack and optimization 117
5.2.2 Performance of the quadruple-junction solar cell 121
5.3 Conclusions 126
5.4 Experimental Section 126
5.5 References 130

Chapter 6: Solution-Processed Tin Oxide-PEDOT:PSS Interconnecting Layers for Efficient Inverted and Conventional Tandem Polymer Solar Cells **131**

6.1 Introduction 132
6.2 Results and Discussion 133
6.2.1 Single-junction Cells with SnO_2 Charge Transport Layers 133
6.2.2 Tandem Solar Cells with SnO_2 and PEDOT:PSS Interconnecting Layer 134
6.2.3 Advantage of SnO_2 over ZnO 141
6.3 Conclusions 142
6.4 Experimental Section 143
6.5 References 148

Summary **149**

Biography **153**

List of Publications and Contributions **155**

Acknowledgements **159**

Appendix **163**

Chapter 1

Introduction*

Abstract

This Chapter starts with a brief history of solar cells and describes the current status of existing photovoltaic technologies. Further, the basic principles of organic solar cells are outlined, referring to the first seminal studies on these devices. Important device metrics for solar cells are introduced and the characterization methods to determine these are described. With these notions laid down, the topic of the thesis, multi-junction organic solar cells, is introduced with explaining the working mechanism, the principal advantages and providing a short historical description of early developments on these devices. Next, the aim and outline of the thesis is presented.

* Part of this chapter has been included in an article, submitted for publication as: D. Di Carlo Rasi, R. A. J. Janssen. Advances in Solution-Processed Multi-Junction Organic Solar Cells.

1.1 Solar cells

The world's population increases steadily, counting around 7.7 billion people nowadays and is expected to further grow to 9.8 billion around 2050.[1] This growth implies a high future demand for energy. Global energy is currently mainly provided by tapping from traditional sources based on fossil fuels. Intrinsic to the consumption of fossil fuels is the production of carbon dioxide. Consequently, carbon dioxide concentrations in the earth atmosphere are now over 400 ppm and progressively raise the global temperature, known as the greenhouse effect. To mitigate the threat of climate change it is of great urgency to exploit alternative energy sources. Solar energy reaching the surface of the earth can comply with the current and future energy demand,[2] while preserving the quality of the environment. The conversion of solar light into electricity was first observed by Bequerel in the 19th century,[3] but the development of crystalline silicon p-n junction solar cells in 1954 by Chapin et al. at Bell Labs can be considered as the inception of the current photovoltaic (PV) technology.[4,5] Initially, the power conversion efficiency was only 6% but research developments made it possible to increase it to the current record for solar cells based on silicon of 26%.[6] Looking at this value in perspective: the theoretical limit for silicon as a semiconductor was estimated to be 29.1% and, hence, the experimental value is closing in on this limit. Technological development and mass production of crystalline silicon solar cells enabled to reach a global photovoltaic capacity of 402 GW (end 2017).[7] Nevertheless, until some years ago the tradeoff between efficiency and manufacturing cost was not appealing.[8] Reason for this is the high purity of materials that is required. A second generation of solar cells was therefore developed, based on thin film absorber materials. Different from crystalline silicon, materials used for second generation PV have a direct band gap, resulting in effective light absorption at thicknesses < 5 µm. This in turns allows for less material consumption and permits to have lightweight devices. Successful examples from this class of materials are amorphous silicon (a-Si), gallium arsenide (GaAs), cadmium telluride (CdTe), copper indium gallium selenide (CIGS) and the relatively new lead halide perovskites. Efficiencies of in order, 14.0%, 28.8%, 22.1%, 22.6% and 22.1% have now been reached by these thin-film technologies.[9] While these materials present an advantage in terms of absorption coefficient over crystalline silicon, other aspects such as high cost, use of scarce or toxic elements, and early-stage technology development currently limit their ubiquitous use. Third generation PV devices aim at providing very high efficiency at low cost.[10] In this spectrum of PV technologies, organic photovoltaic (OPV) is now positioned as a second-generation technology that may provide efficiencies similar to other thin-film technologies, but allows easy processing from solution, use of non-toxic organic semiconductors, flexibility of panels, and the possibility to adjust color and transparency. As such OPV offers opportunities e.g. in building integrated panels that cannot be met by other PV technologies at present.

1.2 Organic solar cells

Organic solar cells are based on organic semiconductor materials. Since the discovery in 1977 of electrical conductivity in doped polyacetylene by Shirakawa, MacDiarmid and Heeger,[11,12] which was later awarded with the Nobel Prize in 2000, thousands of organic semiconducting materials for opto-electronic application have been developed. These are either small molecules or polymers. The common structural denominator of organic semiconductors is the conjugation of alternating single and double bonds which confers them with semiconducting properties and causes optically allowed transitions in the visible range of the spectrum. Interestingly, their chemical structure allows them to be deposited not only by thermal evaporation, but also using inkjet or roll-to-roll printing techniques.[13,14] Organic light-emitting diodes, field-effect transistors, solar cells and photodetectors are some of the devices that have been developed and commercialized. The use of thin film functional organic materials enables manufacturing solar cells on flexible, bendable and stretchable substrates.[15-17] Furthermore, organic photovoltaic cells can be made transparent in the visible spectrum,[18,19] or their molecular structure can be engineered to confer specific properties such as adjustable colors,[20] which could open new market shares in the future.

Seminal works on OPV cells date back to the late 1950s.[21] The light absorbed by the organic material generates an electron-hole pair. The latter is particularly bound due to the low dielectric constant of organic materials and it is referred to as an exciton. In order to split the exciton and collect the separated charges, it is necessary to interface two organic materials with suitable electronic properties. Their frontier energy orbitals, the highest occupied molecular orbital (HOMO) and the lowest unoccupied molecular orbital (LUMO), are involved in the photovoltaic process (**Figure 1**a). In one of the two absorbers an electron is excited from the HOMO to the LUMO by a photon, provided the photon has an energy larger than the gap between these two. In order to overcome the exciton binding energy, the second material interfaced to the first has to have deeper-lying HOMO and LUMO levels. From energetic considerations, when the exciton reaches the donor-acceptor interface (i) an electron is transferred from the donor to the acceptor leaving the hole on the donor (ii), provided the difference between the HOMOs and between the LUMOs exceeds the exciton binding energy. The charges can dissociate from the interface and percolate through their respective domains to be collected at the electrodes (iii). A device based on this concept was first reported in 1986 by Tang and consisted of a bilayer of donor and acceptor materials.[22] In a bilayer device a large fraction of the excitons generated by absorption of a photon recombines before reaching the donor/acceptor interface, due to the limited exciton diffusion length in organic materials (5−10 nm).[23] An elegant and simple solution to increase exciton splitting was introduced in 1995 by Halls et al.[24] and Yu et al.[25] Their idea was to intimately mix donor and acceptor materials in the same layer, creating a so-called “bulk heterojunction” (Figure 1b). The crucial advantage of a bulk heterojunction is that excitons can reach the

donor-acceptor interface within a short distance, independent of where they were generated. After splitting at this interface, the free charges can percolate to the corresponding electrodes through domains of the single materials. Domain sizes on the order of magnitude of the exciton diffusion length guarantee a good balance between exciton dissociation and continuity of percolation paths. More than two decades later, power conversion efficiencies for OPV have reached 14% for solution-processed bulk-heterojunction devices.[26-28] This achievement resulted from optimization of structural, morphological, optical and electronic properties of photoactive materials. In addition, device engineering played an important role, with particular merit to the development of selective charge transport layers for electrons (ETL) and holes (HTL). Either organic or inorganic materials are employed for this purpose and they can be deposited using vacuum techniques such as thermal evaporation or via solution processing. Each charge transport layer is placed in between the corresponding electrode and the photoactive layer (Figure 1) and its work function needs to match the relevant HOMO (or LUMO) energy to allow holes (or electrons) to reach the electrode. The difference in work functions of the two transport layers creates a built-in field, assisting collection of photo-generated charges. The arrangement of ETL and HTL determines the polarity of the device. Being the first to be adopted, the p-i-n structure, in which the deposition of layers is HTL, photoactive layer, ETL is normally indicated as “conventional”, while the n-i-p configuration is referred to as “inverted”. To enable light to enter the device, one of the two electrodes needs to have high transparency in the visible range. Indium tin oxide (ITO) is typically used. The other electrode is usually a metal that reflects light into the absorber.

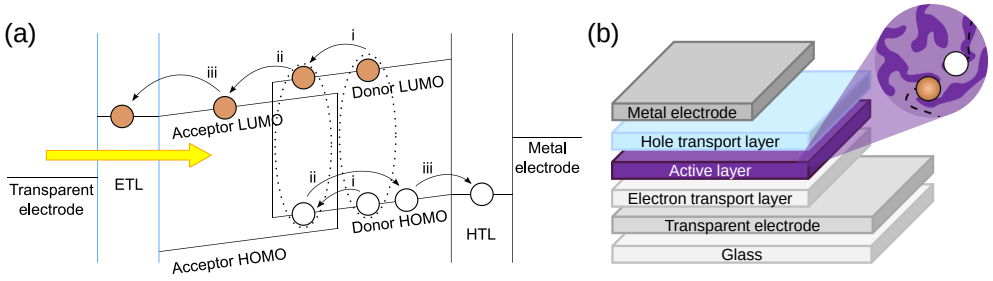

Figure 1. Arrangement of energy levels and conversion process from exciton to free charges in organic solar cells (a). Generic device stack of a bulk-heterojunction solar cell (b).

1.3 Characterization of solar cells

The standard characterization of solar cells consists in the measurement of their current density as a function of an applied voltage in sunlight. This returns the *J*−*V* characteristic and it is performed while illuminating the cell under a reference solar spectrum, keeping the cell at 25 °C. The reference spectrum is the one of the solar light at the sea level and at a latitude such that the mass of air in the atmosphere through which the light travels is 1.5 times the one at zenith. This is formally referred to as the AM1.5G spectrum and its intensity is defined as 100 mW cm^{-2}.[29] **Figure 2** shows the tabulated AM1.5G spectrum and an example of a *J*−*V* characteristic showing the relevant photovoltaic parameters.

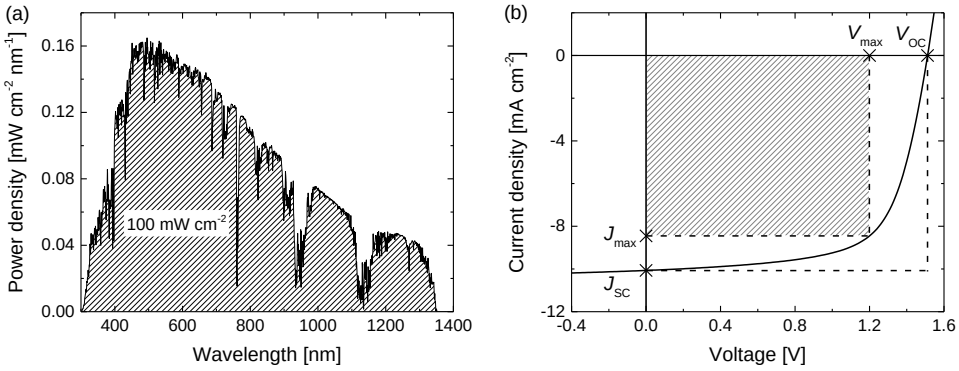

Figure 2. Reference AM1.5G solar spectrum (a), and an example of *J*−*V* characteristic of a solar cell (b).

The relevant information for solar cells that can be derived from the *J*−*V* characteristic lies in the fourth quadrant. The maximum power density the device generates, P_{max}, corresponds to the point on the *J*−*V* curve where the product of *J* and *V* maximizes. The voltage and current density at this maximum power point are referred to as V_{max} and J_{max}, respectively. Other relevant metrics are the open-circuit voltage V_{OC} and the short-circuit current density J_{SC}. For organic solar cells the V_{OC} is related to the difference between the HOMO energy of the donor material and the LUMO energy of the acceptor material. The J_{SC} is related to the optical band gap of the photoactive layer and the quantum efficiency by which charges are created and collected. Another relevant parameter is the fill factor (FF). The FF reflects recombination mechanisms occurring in the device, which affect the efficiency of charge collection. Referring to Figure 2b, the FF corresponds to the ratio between the area of the rectangle at maximum power condition and the area of the rectangle

determined by V_{OC} and J_{SC}. In other words, FF = $P_{max}/(V_{OC} \cdot J_{SC})$. The power conversion efficiency (PCE) is calculated as P_{max}/P_{in}, where P_{in} is the power density of the incident light. Hence, the PCE can be expressed as: $\mathrm{PCE} = V_{OC} \cdot J_{SC} \cdot \mathrm{FF} / P_{in}$. Because the intensity of the AM1.5G solar spectrum is 100 mW cm^{-2}, P_{max} (expressed in mW cm^{-2}) corresponds numerically to the PCE (expressed in %). Optimizing the PCE of a solar cell involves the simultaneous increase of J_{SC}, V_{OC} and FF.

Another useful characteristic of a solar cell is the external quantum efficiency (EQE) spectrum. The EQE spectrum is measured at each wavelength by comparing the number of photons $N_{ph}(\lambda)$ incident on the device to the number of electrons $N_e(\lambda)$ that can be extracted under these conditions, usually at short-circuit. The EQE at wavelength λ is defined as the ratio $\mathrm{EQE}(\lambda) = N_e(\lambda)/N_{ph}(\lambda)$. Since a solar simulator cannot reproduce the AM1.5G spectrum exactly, it is challenging to determine the PCE of a solar cell. Especially, the J_{SC} is very susceptible to small deviations from the AM1.5G spectrum. The correct J_{SC} can be determined from measuring the EQE spectrum at short-circuit conditions followed by numerical of the product of the EQE with the tabulated AM1.5G solar power density spectrum (P_{sun}). This returns the desired current density (J_{SC}^{EQE}):

$$J_{SC}^{EQE} = \int \mathrm{EQE}(\lambda) \cdot P_{sun}(\lambda) \frac{e\,\lambda}{h\,c} \mathrm{d}\lambda \,.$$

Other quantities appearing in the equation are the elementary charge (e), the Planck constant (h) and the speed of light (c).

In some cases, the internal quantum efficiency (IQE) spectrum of the photoactive layer is of interest. The IQE(λ) is the ratio between the number of charges collected ($N_e(\lambda)$) and the number of photons absorbed by the photoactive layer ($N'_{ph}(\lambda)$) at each wavelength λ. A practical way to estimate the IQE derives from a simple manipulation of this definition:

$$\mathrm{IQE}(\lambda) = \frac{N_e(\lambda)}{N'_{ph}(\lambda)} = \frac{\mathrm{EQE}(\lambda)}{f_A(\lambda)},$$

where $f_A(\lambda)$ is the fraction of absorbed photons by the photoactive layer ($f_A = N'_{ph}(\lambda)/N_{ph}(\lambda)$). f_A is a quantity that can be estimated via optical modeling simulations. Interference effects play an important role in determining the fraction of photons absorbed by the photoactive layer in an OPV stack of semitransparent thin films because the total thickness is on the same order of magnitude as the wavelength of visible light. As reported in the experimental section of some chapters of this thesis, it is sometimes useful to use the spectrally integrated average IQE. This quantity can be determined from $\mathrm{IQE} = J_{SC}^{EQE}/J_{SC}^{max}$, where J_{SC}^{max} is obtained from integration of f_A with the AM1.5G reference spectrum. When using the spectrally integrated IQE one effectively assumes that the IQE is independent of the wavelength over the wavelength range where the photoactive layer absorbs light.

1.4 Multi-junction organic solar cells

1.4.1 Working principles

So far, solar cells relying on a single absorber layer have been discussed. For this architecture, the maximum attainable efficiency in the detailed balance limit was calculated first in 1961 by Shockley and Queisser.[30] Under the AM1.5G reference solar spectrum, a 33.8% efficiency is the highest theoretical value, corresponding to an absorber with a band gap of 1.34 eV.[31] Single-junction solar cells are mainly limited in performance by two factors, represented in **Figure 3**a.

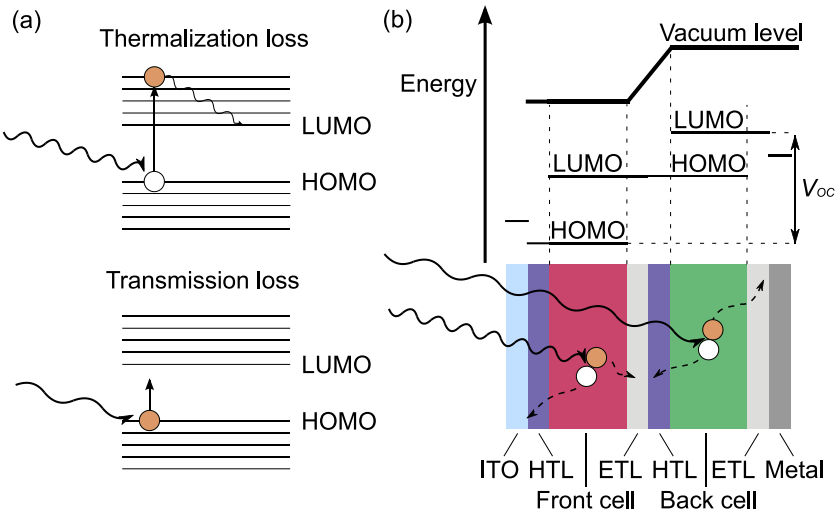

Figure 3. Thermalization and transmission loss (a). Arrangement of functional layers and energy levels in an organic tandem solar cell (b). The ETL/HTL stack between the subcells forms the interconnecting layer.

Photons with energy higher than the band gap are not fully exploited. In fact, the excited electron relaxes to the LUMO level, releasing energy in the form of heat (thermalization loss). On the other hand, photons with energy lower than the band gap are not absorbed but transmitted by the absorber layer. To reach higher efficiencies, more than one absorber layer can be used. The first layer should feature a wide band gap material that is capable of absorbing the high energy photons but providing less thermalization. The second layer should have a low band gap absorber that can absorb photons that cannot be absorbed by the first layer. When carefully designed, a tandem cell affords less thermalization loss and less transmission loss than the corresponding single-junction cells. Following the Shockley and

Queisser detailed balance limit a double-junction (tandem) cell can reach a maximum efficiency of 42% and a triple-junction cell 49%.[32]

To make a tandem cell the two complementary absorber layers must be connected both optically and electrically in the same device. A series connection can be accomplished using an interconnecting layer (ICL), made of a stack of similar interlayer materials used in single-junction cells. Figure 3b provides a schematic representation of an organic tandem solar cell. The role of the ICL is to provide an internal contact for recombination of charges from the active layers, as suggested by the arrows. This internal recombination is necessary to sustain the photocurrent in the tandem cell. A simple schematic representation of the energy levels in an OPV tandem is given in Figure 3b. As for single-junction cells, the HTL and the ETL Fermi level needs to match the relevant HOMO and LUMO levels. These materials also need to have sufficient Ohmic character to guarantee fast recombination of charges and avoid voltage loss in the ICL. The voltage of the tandem is the sum of the voltages of the subcells, since these are connected in series. Therefore the V_{OC} is ideally the sum of the V_{OC}s of the subcells. Also for tandem cells, the arrangement of HTLs and ETLs determines the polarity of the device. Because the subcells are connected in series, the photocurrent of a tandem solar cell is limited by the subcell generating less current. Thus to overcome the intrinsic limits of single-junction cells, it is of paramount importance that the subcells of a series-connected tandem cell absorb in complementary regions of the solar spectrum and generate equal photocurrent.

1.4.2 Early developments

In the first demonstrations of tandem organic solar cells, the materials were thermally evaporated. Initially only metal clusters were used to interconnect the subcells,[33-35] later complemented by p- and n-doped organic transport layers.[36,37] In a second stage, active layers based on solution-processed materials were introduced, with the aim of further moving the manufacturing towards all-solution-processing.[38,39] The latter consisted of an electron-donating polymer and an electron-accepting fullerene derivative. In these first publications, only one active layer was processed from solution and the other one by thermal evaporation. This choice derived from the intricate requirements of processing all the layers from solution on top of each other. Further advances in the research field allowed to interconnect in the same device two solution-processed active layers, first by connecting two single-junction solar cells deposited on individual substrates,[40] and then by integrating the two subcells monolithically on the same substrate.[41] In 2007 the first all-solution-processed tandem polymer solar cells were reported by Gilot et al.[42] and Heeger et al.[43] In both cases the ICL featured a layer of poly(3,4-ethylenedioxythiophene):polystyrene sulfonate (PEDOT:PSS) as HTL, stacked on top of a metal oxide layer as ETL. In one case,[42] the stack consisted of zinc oxide nanoparticles on top of which a pH-neutral formulation of PEDOT:PSS was casted. In the other case,[43] a film of titanium oxide obtained via a sol-gel route was followed by

deposition of PEDOT:PSS. The tandem in this second work yielded a PCE of 6.5%. PEDOT:PSS was later adopted in the vast majority of the tandem solar cells reported (see also Chapter 2). Starting from there, several advances have been accomplished, which contributed to increase the efficiency. These improvements concerned for instance the use of photoactive blends that could afford a high V_{OC}, relative to their optical band gap E_g.[44] This is usually expressed as the minimum photon energy-loss (E_{loss}), defined as $E_{loss} = E_g - eV_{OC}$. It must be noted though that the real energy loss per converted photon under operating condition is higher than E_{loss}, and it corresponds to $E - eV_{max}$, E being the photon's energy. As stressed in the previous paragraph, it is important to have active layers with complementary absorption spectra. The development of low band gap absorbers with increased performance paved the way towards tandems with efficiencies of 8.6% in 2012[45], and 10.6% in 2013[46], at hand of Yang and coworkers. On the manufacturing perspective, as alternative to the initially developed conventional structure, inverted tandem solar cells made their advent.[47] The ICL was also object of developments, gaining properties like enhanced resistance against common solvents like chlorobenzene, used for the processing of the back cell.[48] Self-assembled layers were introduced to engineer the work function at the ICL, and match the active layer's relevant frontier energy levels. One of these was the partially ethoxylated polyethylenimine (PEIE), used to lower the work function of PEDOT:PSS and match the back cell's acceptor LUMO.[49] In 2013, Heeger and coworkers found that a similar function could be carried out by a conjugated polyelectrolyte.[50] As will be discussed in Chapter 2, this innovation permitted polymer:fullerene based tandem solar cells to set their record efficiency above 11% in 2015.

Multi-junction cells based on more than two absorber layers have been demonstrated as well. Initial studies demonstrated the feasibility of realizing such intricate device structures, both by thermal evaporation[34] as well as via solution-processing[42,51] and with up to 10[52] and 6 active layers[53], respectively. Triple-junction devices in particular moved progressively forward with the efficiency, reaching an outstanding 13.2% for evaporated cells.[54] For solution-processed triples, a PCE of 5.3% was reported in 2013 by Esiner et al.[55] and 9.6% by Li et al. the same year.[56] Both these triples featured a wide band gap absorber in the front cell and the same small band gap absorber as both middle and back subcells. The choice of using twice the same absorber, although not ideal, was practically successful in virtue of the high current generated by the low band gap cell, with respect to the wide band gap front cell. A remarkable efficiency of 11.6% was reported in 2014 by Yang and coworkers for a triple-junction cell where active layers with complementary band gaps were adopted.[57] **Figure 4** shows the device stack and optical properties of the three active layers of this device. The complementarity of the absorption spectra and optimization of interference effects afforded a high J_{SC} of 7.6 mA cm^{-2}. In addition, a V_{OC} of 2.28 V and FF of 0.66 contributed to the high efficiency.

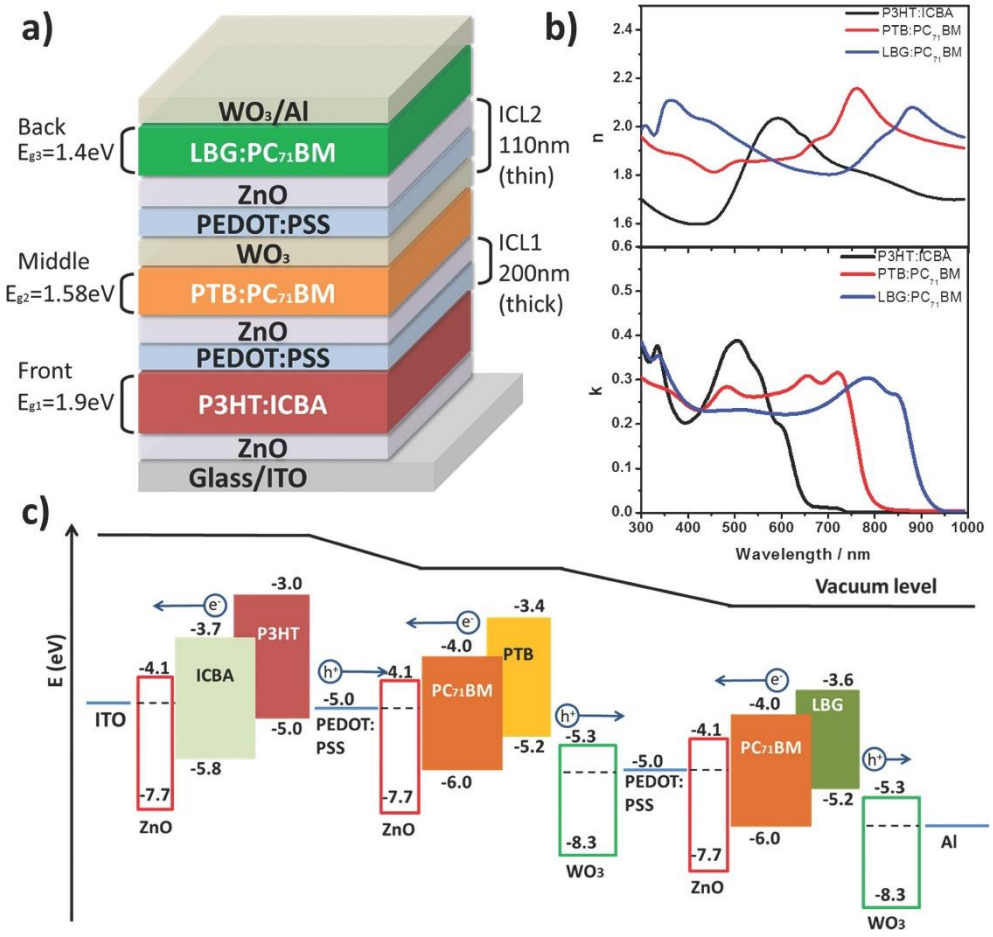

Figure 4. Triple-junction polymer solar cell realized by Chen et al. Device configuration (a), optical constants of the absorber materials (b), and arrangement of the energy levels (c). Reproduced with permission from Ref. 57. Copyright 2014 WILEY-VCH Verlag GmbH & Co. KGaA, Weinheim.

1.4.3 Characterization of multi-junction organic solar cells

The measurement of the $J-V$ characteristic of a multi-junction solar cell is performed similarly to the single-junction counterpart. The EQE measurement instead, requires some extra steps, due to the fact that in the vast majority of the devices the ICL is not accessible or it does not provide a good contact. As already addressed in Section 1.4.1, the current of the tandem is limited by the subcell generating less photocurrent. The absorption spectra of the subcells are such that at each wavelength one of the two absorbs less. By measuring the EQE

of the tandem in the same way as for the single-junction cells, i.e. using a monochromatic probe light of variable wavelength, the subcell absorbing less light limits the overall current. Therefore, the EQE of the tandem under this condition follows the lower envelope of the EQE of the individual subcells (black squares in **Figure 5**a).[58] In order to isolate the EQE of a specific subcell over the whole range of measurement, the other subcell needs to be saturated by a flood light, also referred to as bias light. The spectrum of this bias light should be selected according to the absorption spectrum of the subcells. By using a lock-in detection technique, the differential current response to the superposition of a frequency-controlled chopped probe light returns the desired EQE spectrum of the non-biased subcell (Figure 5a).

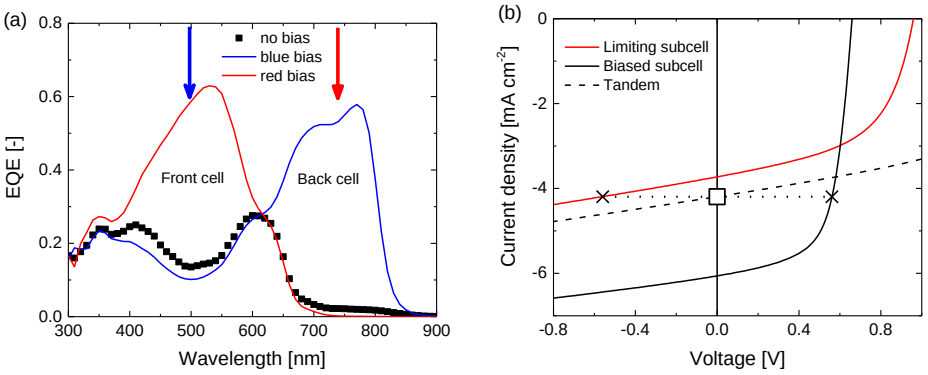

Figure 5. EQE spectrum of a tandem (a) without light bias (black symbols) and with the addition of red or blue bias lights (arrows). *J*−*V* characteristic curve of the subcells and the tandem when a red bias light shines on the device (b).

In 2010 Gilot et al. reported that for organic solar cells, the optically-biased subcell generates an electric field with non-negligible effects on the characterization.[59] In particular, while the tandem is kept at short-circuit condition, the flooded subcell is in a forward voltage bias condition and the current-limiting subcell is in a reverse voltage bias condition (Figure 5b). For most (if not all) organic solar cells this leads to overestimation of the current with respect to the short-circuit condition, due to the field dependence of the current in reverse bias. To comply with solving this problem and obtaining a correct measurement, a voltage bias correction should be applied at the terminals of the tandem during the EQE measurement with light bias. Accurate determination of this voltage correction is intricate, but according to reference [59] the latter can be approximated as the V_{OC} of the optically-biased subcell.

Similar considerations can be extended to the case of solar cells with more than two junctions, as will be addressed in Chapter 4 and Chapter 5.

1.4.4 Determination of the wavelength-dependent *n* and *k* optical constants

As mentioned in Section 1.3, interference effects have an influence on the absorption behavior of the active layers in a multiple-stack device. Optical modeling simulations allow to estimate the fraction of absorbed photons in each layer of a specific sequence, taking into account reflection and transmission at the interface between adjacent layers. As will become clear when reading Chapters 3-6, this tool is particularly useful to find the optimal thickness of the subcells in a multi-junction cell that gives high and balanced absorption of light. It further allows to estimate the EQE spectrum of these subcells and to determine the IQE (discussed in Section 1.3). The wavelength-dependent refractive index $n(\lambda)$ and extinction coefficient $k(\lambda)$ are used as input for such simulations and it is therefore very useful to estimate them for all the layers in the stack of interest. The following procedure focuses on the determination of these constants for the active layers. For other materials used in interlayers and electrodes the n and k are readily available from literature, since they are frequently used.

To determine $n(\lambda)$ and $k(\lambda)$, polymer:acceptor blend layers were spin-coated on quartz substrates and the reflectance and transmittance of the films was measured perpendicular to the surface. The reflectance spectra ($R(\lambda)$) of the layers were used to correct the transmittance spectra ($T(\lambda)$), resulting in the corrected transmission $T' = T/(1-R)$ of the layers. Subsequently, the thickness d of the layers was measured with a profilometer and used to evaluate the extinction coefficient k as: $k(\lambda) = -\lambda \ln(T'(\lambda))/(4\pi d)$. The calculation of the refractive index $n(E)$ as function of the energy E was implemented in a Python script, following the Kramers-Kronig relation: $n(E) - 1 = (2/\pi)\, P\int E'\, k(E')/(E'^2 - E^2)\, \mathrm{d}E'$.

Compared to ellipsometry, widely used to determine the optical constants, this approach does not involve a tedious and time-consuming fitting of the experimental data with a model. On the other hand, ellipsometry allows to determine the n and k components parallel to the plane of the layer, which can be relevant in case of anisotropy and when the angle between the direction of light and the inward surface normal is non-zero. For the studies involved in this thesis, where devices are illuminated at zero angle, analyzing the reflectance and transmittance suffices. Moulé and Meerholz already addressed the problem of determining $n(\lambda)$ and $k(\lambda)$ using UV/vis measurements, although in a slightly different way, and they pointed out the criticalities for which ellipsometry provided less accurate estimations than their method.[60]

To account for interference effects in the absorber layer on quartz, the optical constants were determined for three different layer thicknesses and subsequently averaged to obtain the $k(\lambda)$ and $n(\lambda)$ spectra. Although the averaging does not provide a rigorous solution to the

problem, it provided satisfactory results in terms of modeling the optical absorption of complex layer stacks, as demonstrated previously, see Refs. [56] and [61].

1.5 Aim and outline of the thesis

The goal of this thesis is to advance in the design, manufacturing, modeling and characterization of multi-junction polymer solar cells.

Recent trends in the field covering the time lapse between 2015 and 2018 are reported in Chapter 2. The development of new functional materials for the interconnecting layers and the photoactive layers represents a significant part of the reported results. Also studies that focus on manipulating the optical electric field in the device to enhance light absorption are reviewed next to an overview on the characterization practices. As processing of the multi-layers stacks is challenging new processing methods and industry-oriented applications are described.

The first problem which was tackled was the development of a processing technique of the ICL to fabricate inverted tandem and triple-junction solar cells with good versatility, i.e. compatible with numerous chemically different active layer materials as subcells without the need to constantly adopt choice of layers or choice of processing conditions to the specific characteristics of the photoactive layer. The solution to this is provided in Chapter 3. Suitable formulations of PEDOT:PSS and ZnO nanoparticles as charge transport materials in solvent mixtures have been developed that allow for sufficient wetting and spreading during deposition drying and at the same time fulfill the requirement of orthogonality, implying that during deposition of the second layer, the first layer is not re-dissolved. In this way six different tandem cells and three triple-junction solar cells involving a variety of active layers could be made with the same ICL without adjusting the deposition conditions.

Triple-junction organic solar cells represent an intriguing kind of device for the high efficiency they can achieve. In order to perform a correct characterization, the peculiarity of OPV materials should be taken into account, to not overestimate the efficiency. Chapter 4 presents a detailed characterization protocol to fulfill this task, and shows the corresponding results on a state-of-the-art triple-junction device with a PCE of 10.0%. The method used is based on opto-electrical modeling simulations and measurements on representative single-junction cells and provides an excellent match between experimental and modeled $J-V$ and EQE data.

To further extend the spectral response of triple-junction cells, another absorber material was stacked on top of the back cell, with an ultralow band gap of ca. 1.1 eV. The result, presented in Chapter 5, represents the first example ever reported of solution-

processed quadruple-junction organic solar cell with four complementary absorber layers. Opto-electrical modeling was involved to optimize the performance. The processing of the ICL developed in Chapter 3 was used to interconnect all the subcells, and the characterization protocol reported in Chapter 4 was extended to characterize the EQE of the four individual subcells. The PCE of this cell equals 7.6%, only slightly less than the modeled value of 8.2%.

The versatile deposition technique reported in Chapter 3 allows to fabricate exclusively inverted configuration devices. In a conventional device PEDOT:PSS would be processed on top of a zinc oxide layer. Unfortunately the acidic dispersion from which PEDOT:PSS is processed is not compatible with zinc oxide. In Chapter 6, commercial tin oxide colloidal dispersions were combined with PEDOT:PSS to form new ICLs for tandems. Both conventional and inverted tandem solar cells were manufactured with these materials, by changing the sequence in which these were processed. Both tandem cell configurations afforded PCEs of more than 10%.

1.6 References

[1] United Nations. Department of Economic and Social Affairs, Population Division. *World Population Prospects: The 2017 Revision, Key Findings and Advance Tables*. Working Paper No. ESA/P/WP/248. **2017**.

[2] J. Goldemberg, World energy assessment; United Nations Development Programme: New York, NY, **2000**.

[3] A. E. Becquerel, *Comptes Rendus* **1839**, *9*, 561.

[4] "April 25, 1954: Bell Labs Demonstrates the First Practical Silicon Solar Cell". APS News. American Physical Society. 18 (4). April **2009**.

[5] D. M. Chapin, C. S. Fuller and G. L. Pearson, *J. Appl. Phys.* **1954**, *25*, 676.

[6] K. Yoshikawa, H. Kawasaki, W. Yoshida, T. Irie, K. Konishi, K. Nakano, T. Uto, D. Adachi, M. Kanematsu, H. Uzu, K. Yamamoto, *Nat. Energy* **2017**, *2*, 17032.

[7] International Technology Roadmap for Photovoltaic Results 2017, Ninth edition, March **2018**.

[8] N. S. Lewis, *Science* **2007**, *315*, 798.

[9] National Renewable Energy Laboratory, Photovoltaic Efficiency chart, available at: https://www.nrel.gov/pv/; accessed on 5 September **2018**.

[10] M. A. Green, Third Generation Photovoltaics, Springer, **2003**, ISBN: 3-540-40137-7.

[11] C. K. Chiang, C. R. Fincher, Y. W. Park, A. J. Heeger, H. Shirakawa, E. J. Louis, S. C. Gau, A. G. MacDiarmid, *Phys. Rev. Lett.* **1977**, *39*, 1098.

[12] H. Shirakawa, E. J. Louis, A. G. MacDiarmid, C. K. Chiang, A. J. Heeger, *J. Am. Chem. Soc., Chem. Commun.* **1977**, *16*, 578.

[13] R. Søndergaard, M, Hösel, D. Angmo, T. T. Larsen-Olsen, F. Krebs, *Mater. Today* **2012**, *15*, 36.

[14] A. Reale, L. La Notte, L. Salamandra, G. Polino, G. Susanna, T. M. Brown, F. Brunetti, A. Di Carlo, *Energy Technol.* **2015**, *3*, 385.

[15] M. Kaltenbrunner, M. S. White, E. D. Glowacki, T. Sekitani, T. Someya, N. S. Sariciftci, S. Bauer, *Nat. Commun.* **2012**, *3*, 1772.

[16] R. Ma, J. Feng, D. Yin, H.-B. Sun, *Org. Electron.* **2017**, *43*, 77.

[17] Y. W. Li, G. Y. Xu, C. H. Cui, Y. F. Li, *Adv. Energy Mater.* **2018**, *8*, 1701791.

[18] K.-S. Chen, J.-F. Salinas, H.-L. Yip, L. Huo, J. Hou, A. K.-Y. Jen, *Energy Environ. Sci.* **2012**, *5*, 9551.

[19] C.-C. Chen, L. Dou, J. Gao, W. H. Chang, G. Li, Y. Yang, *Energy Environ. Sci.* **2013**, *6*, 2714.

[20] J. Min, C. Bronnbauer, Z.-G. Zhang, C. Cui, Y. N. Luponosov, I. Ata, P. Schweizer, T. Przybilla, F. Guo, T. Ameri, K. Forberich, E. Spiecker, P. Bäuerle, S. A. Ponomarenko, Y. Li, C. J. Brabec, *Adv. Funct. Mater.* **2016**, *26*, 4543.

[21] D. Kearns, M. Calvin, *J. Chem. Phys.* **1958**, *29*, 950.

[22] C. W. Tang, *Appl. Phys. Lett.* **1986**, *48*, 183.
[23] O. V. Mikhnenko, P. W. M. Blom, T.-Q. Nguyen, *Energy Environ. Sci.* **2015**, *8*, 1867.
[24] J. J. M. Halls, C. A. Walsh, N. C. Greenham, E. A. Marseglia, R. H. Friend, S. C. Moratti, A. B. Holmes, *Nature* **1995**, *376*, 498.
[25] G. Yu, J. Gao, J. C. Hummelen, F. Wudl, A. J. Heeger, *Science* **1995**, *270*, 1789.
[26] S. Zhang, Y. Qin, J. Zhu, J. Hou, *Adv. Mater.* **2018**, *30*, 1800868.
[27] Z. Zheng, Q. Hu, S. Zhang, D. Zhang, J. Wang, S. Xie, R. Wang, Y. Qin, W. Li, L. Hong, N. Liang, F. Liu, Y. Zhang, Z. Wei, Z. Tang, T. P. Russell, J. Hou, H. Zhou, *Adv. Mater.* **2018**, *30*, 1801801.
[28] S. Li, L. Ye, W. Zhao, H. Yan, B. Yang, D. Liu, W. Li, H. Ade, J. Hou, *J. Am. Chem. Soc.* **2018**, *140*, 7159.
[29] American Society for Testing and Materials (ASTM), Standard G173-03, available at: http://rredc.nrel.gov/solar/spectra/am1.5/.
[30] W. Shockley, H. J. Queisser, *J. Appl. Phys.* **1961**, *32*, 510.
[31] S. Rühle, *Sol. Energy* **2016**, *130*, 139.
[32] A. De Vos, *J. Phys. D: Appl. Phys.* **1980**, *13*, 839.
[33] M. Hiramoto, M. Suezaki, M. Yokoyama, *Chem. Lett.* **1990**, *19*, 327.
[34] A. Yakimov, S. R. Forrest, *Appl. Phys. Lett.* **2002**, *80*, 1667.
[35] K. Triyana, T. Yasuda, K. Fujita, T. Tsutsui, *Jpn. J. Appl. Phys.* **2004**, *43*, 2352.
[36] J. Drechsel, B. Männig, F. Kozlowski, D. Gebeyehu, A. Werner, M. Koch, K. Leo, M. Pfeiffer, *Thin Solid Films* **2004**, *451–452*, 515.
[37] B. Maennig, J. Drechsel, D. Gebeyehu, P. Simon, F. Kozlowski, A. Werner, F. Li, S. Grundmann, S. Sonntag, M. Koch, K. Leo, M. Pfeiffer, H. Hoppe, D. Meissner, N. S. Sariciftci, I. Riedel, V. Dyakonov, J. Parisi, *Appl. Phys. A* **2004**, *79*, 1.
[38] G. Dennler, H.-J. Prall, R. Koeppe, M. Egginger, R. Autengruber, N. S. Sariciftci, *Appl. Phys. Lett.* **2006**, *89*, 073502.
[39] A. Colsmann, J. Junge, C. Kayser, U. Lemmer, *Appl. Phys. Lett.* **2006**, *89*, 203506.
[40] V. Shrotriya, E. H.-E. Wu, G. Li, Y. Yao, Y. Yang, *Appl. Phys. Lett.* **2006**, *88*, 064104.
[41] K. Kawano, N. Ito, T. Nishimori, J. Sakai, *Appl. Phys. Lett.* **2006**, *88*, 073514.
[42] J. Gilot, M. M. Wienk, R. A. J. Janssen, *Appl. Phys. Lett.* **2007**, *90*, 143512.
[43] J. Y. Kim, K. Lee, N. E. Coates, D. Moses, T.-Q. Nguyen, M. Dante, A. J. Heeger, *Science* **2007**, *317*, 222.
[44] J. Gilot, M. M. Wienk, R. A. J. Janssen, *Adv. Mater.* **2010**, *22*, E67.
[45] L. Dou, J. You, J. Yang, C.-C. Chen, Y. He, S. Murase, T. Moriarty, K. Emery, G. Li, Y. Yang, *Nat. Photonics* **2012**, *6*, 180.
[46] J. You, L. Dou, K. Yoshimura, T. Kato, K. Ohya, T. Moriarty, K. Emery, C.-C. Chen, J. Gao, G. Li, Y. Yang, *Nat. Commun.* **2013**, *4*, 1446.

[47] C.-H. Chou, W. L. Kwan, Z. Hong, L.-M. Chen, Y. Yang, *Adv. Mater.* **2011**, *23*, 1282.

[48] J. Yang, R. Zhu, Z. Hong, Y. He, A. Kumar, Y. Li, Y. Yang, *Adv. Mater.* **2011**, *23*, 3465.

[49] Y. Zhou, C. Fuentes-Hernandez, J. W. Shim, T. M. Khan, B. Kippelen, *Energy Environ. Sci.* **2012**, *5*, 9827.

[50] J. Jo, J.-R. Pouliot, D. Wynands, S. D. Collins, J. Y. Kim, T. L. Nguyen, H. Y. Woo, Y. Sun, M. Leclerc, A. J. Heeger, *Adv. Mater.* **2013**, *25*, 4783.

[51] D. W. Zhao, X. W. Sun, C. Y. Jiang, A. K. K. Kyaw, G. Q. Lo, D. L. Kwong, *IEEE Electron Device Lett.* **2009**, *30*, 490.

[52] Y. Zou, Z. Deng, W. J. Potscavage, M. Hirade, Y. Zheng, C. Adachi, *Appl. Phys. Lett.* **2012**, *100*, 243302.

[53] J. Gilot, Polymer Tandem Solar Cells, Ph.D. thesis, Eindhoven University of Technology, **2010**, ISBN: 978-90-386-2279-8.

[54] Heliatek, available at: http://heliatek.com.

[55] S. Esiner, H. Van Eersel, M. M. Wienk, R. A. J. Janssen, *Adv. Mater.* **2013**, *25*, 2932.

[56] W. Li, A. Furlan, K. H. Hendriks, M. M. Wienk, R. A. J. Janssen, *J. Am. Chem. Soc.* **2013**, *135*, 5529.

[57] C.-C. Chen, W.-H. Chang, K. Yoshimura, K. Ohya, J. You, J. Gao, Z. Hong, Y. Yang, *Adv. Mater.* **2014**, *26*, 5670.

[58] R. Timmreck, T. Meyer, J. Gilot, H. Seifert, T. Mueller, A. Furlan, M. M. Wienk, D. Wynands, J. Hohl-Ebinger, W. Warta, R. A. J. Janssen, M. Riede, K. Leo, *Nat. Photonics* **2015**, *9*, 478.

[59] J. Gilot, M. M. Wienk, R. A. J. Janssen, *Adv. Funct. Mater.* **2010**, *20*, 3904.

[60] A. J. Moulé, K. Meerholz, *Appl. Phys. Lett.* **2007**, *91*, 061901.

[61] C. Duan, A. Furlan, J. J. van Franeker, R. E. M. Willems, M. M. Wienk, R. A. J. Janssen, *Adv. Mater.* **2015**, *27*, 4461.

Chapter 2

Recent Developments on Solution-Processed Multi-Junction Organic Solar Cells*

Abstract

This chapter offers an overview of the recent (2015 to mid-2018) developments in the field of solution-processed multi-junction organic solar cells. In this time lapse different strategies have been investigated to improve the performance of these devices. An important one involves the development of new materials and processing methods for the photoactive layers and the interconnecting layers. In addition, specific layers or combinations thereof have been conveniently adopted to increase light absorption and improve the photocurrent by utilizing optical interference effects that play a key role in these multi-junction semitransparent thin layer stacks. Together with the increase in power conversion efficiency, accurate characterization procedures are required to keep a critical view on the results and new insights in this matter are discussed. Application of multi-junction cells for photoelectrochemical water splitting and upscaling towards a commercial technology are briefly addressed.

* This chapter has been submitted for publication as part of: D. Di Carlo Rasi, R. A. J. Janssen. Advances in Solution-Processed Multi-Junction Organic Solar Cells.

2.1 Introduction

In this chapter recent developments in the field of solution-processed organic tandem solar cells are discussed.† The topic was last reviewed in 2015 and since then significant progress has been made.[1-8] The materials forming the interconnecting layer (ICL) are key to the optimal performance of tandem cells. The ICL serves to connect the subcells, both optically and electrically, preferably without losses. Optical transparency, uniformity, mechanical robustness, solvent orthogonality during processing, matching with the relevant HOMO and LUMO levels and Ohmic character are important requisites that the ICL has to fulfill. Besides the specific materials choice, the processing of the ICL from a liquid medium plays a decisive role in the success of manufacturing the multi-layer stacks. Co-solvents, additives, blends, and deposition techniques in general are commonly explored factors to tweak the characteristics of the ICL. Because the absorber and ICL films are semitransparent thin layers, interference effects play an important role in the distribution of the optical electric field in the subcells and in turn in the absorption of light and the generated photocurrent. Different approaches like the insertion of a thin reflecting materials inside the ICL can alter the distribution of the optical field, to achieve a better balance in current generation. As discussed in Chapter 1, tandem solar cells require photoactive materials with different band gaps. In the context of solution-processed organic photovoltaic (OPV), the absorbers consists of semitransparent thin films which can have a substantial overlap of their absorption spectra. Hence, in addition to having different band gaps, photoactive layers should preferably also have complementary absorption spectra, such that high energy photons that pass the first layer are not absorbed in the second layer and are reflected at the back electrode. The optimal thickness of single-junction cells is known to be limited by bimolecular recombination. Developing photoactive absorber blends with thickness-insensitive performance can alleviate the disadvantages of spectral overlap between the two subcells and increase the photocurrent. Moreover, a high external quantum efficiency (EQE) is a prerequisite to absorb the incident photons and increase the short-circuit current density (J_{SC}). To afford a high open-circuit voltage (V_{OC}) tandem, both the subcells should possess a low minimum photon energy loss (E_{loss}), defined as the difference between their optical band gap (E_g) and eV_{OC}. Recombination mechanisms should also be kept under control mainly via the creation of a suitable blend morphology. A significant part of this chapter addresses recent developments of tandem solar cells where new combinations of photoactive materials are presented. Although not yet mature for the market, solution-processed tandem OPV technology was studied also related to industry-oriented aspects such as the processing under ambient atmosphere, the increase

† The results presented in this chapter are largely based on a search on Web of Science, using the keywords: "TI=((tandem OR triple* OR (multi*junction*) OR (multi-junction*)) AND (organic OR polymer OR (small molecul*) OR (non-fullerene) OR (*fullerene*) OR (*fullerene-)) AND ((solar cell*) OR photovoltaic* OR (photovoltaic cell*))) AND PY=(2015-2018)", limited to the period from January 2015 to August 2018. Articles about hybrid tandem solar cells, articles where no actual device was fabricated and out-of-topic entries were excluded.

in device area by interconnecting more tandem cells to make a module, and the processing from solution of the electrodes. The combination of more than two absorbers in solution-processed multi-junction solar cells is still object of research, aiming at a further increase in efficiency with respect to tandems. Overall, the reliability of the OPV field hinges on accurate characterization protocols, taking into account the peculiarities of organic photovoltaic materials. A detailed protocol for this was published at the beginning of the time period covered here, and a brief analysis of how researchers now use the protocol is presented. Some newly-developed exotic device stacks that do not fall in the category of tandems are included. Besides the clear interest in increasing the power conversion efficiency (PCE) over that of single-junction devices, specific applications can be identified where the properties of OPV tandem cells turn advantageous. Photoelectrochemical water splitting is one of them, because OPV tandem cells can provide the necessary voltage at the operating point. This voltage should exceed the standard potential of 1.23 V for the water splitting reaction plus the overpotentials at the electrodes. Conclusive general considerations complete the chapter. An overview of the relevant features of the tandem cells published in the covered period is collected in **Table 1**.

2.2 Tandem solar cells

2.2.1 ICL materials

The ICL generally consists of combinations of polymeric and metal oxide materials. Poly(3,4-ethylenedioxythiophene):polystyrene sulfonate (PEDOT:PSS) as hole transporting layer (HTL) and zinc oxide nanoparticles as electron transporting layer (ETL) remain a widely adopted combination of materials. From Table 1, it emerges that also evaporated molybdenum oxide (HTL), followed by a thin (discontinuous) layer of silver and poly[(9,9-bis(3′-(*N*,*N*-dimethylamino)propyl)-2,7-fluorene)-alt-2,7-(9,9-dioctylfluorene)] (PFN) as ETL are frequently used. Nevertheless, several new materials have been introduced in recent years. Especially, conjugated polyelectrolytes (CPE) and structurally related pH-neutral self-doped conductive polymers (SCPs) are a largely explored alternative both for the p- as well as for the n-type charge transporting layers. Decorating a conjugated polymer with anionic or cationic side groups can create dipole moments that change the work function of the substrate on which they are coated. The CPEs are often wide band gap semiconducting materials that serve to change the work function. CPEs and SCPs are typically used as thin layers (< 25 nm) to reduce parasitic light absorption. Generally, CPEs are processed from alcoholic solvents because these are compatible with most of the tandem stacks. **Figure 1** provides the chemical structure of the materials discussed hereafter.

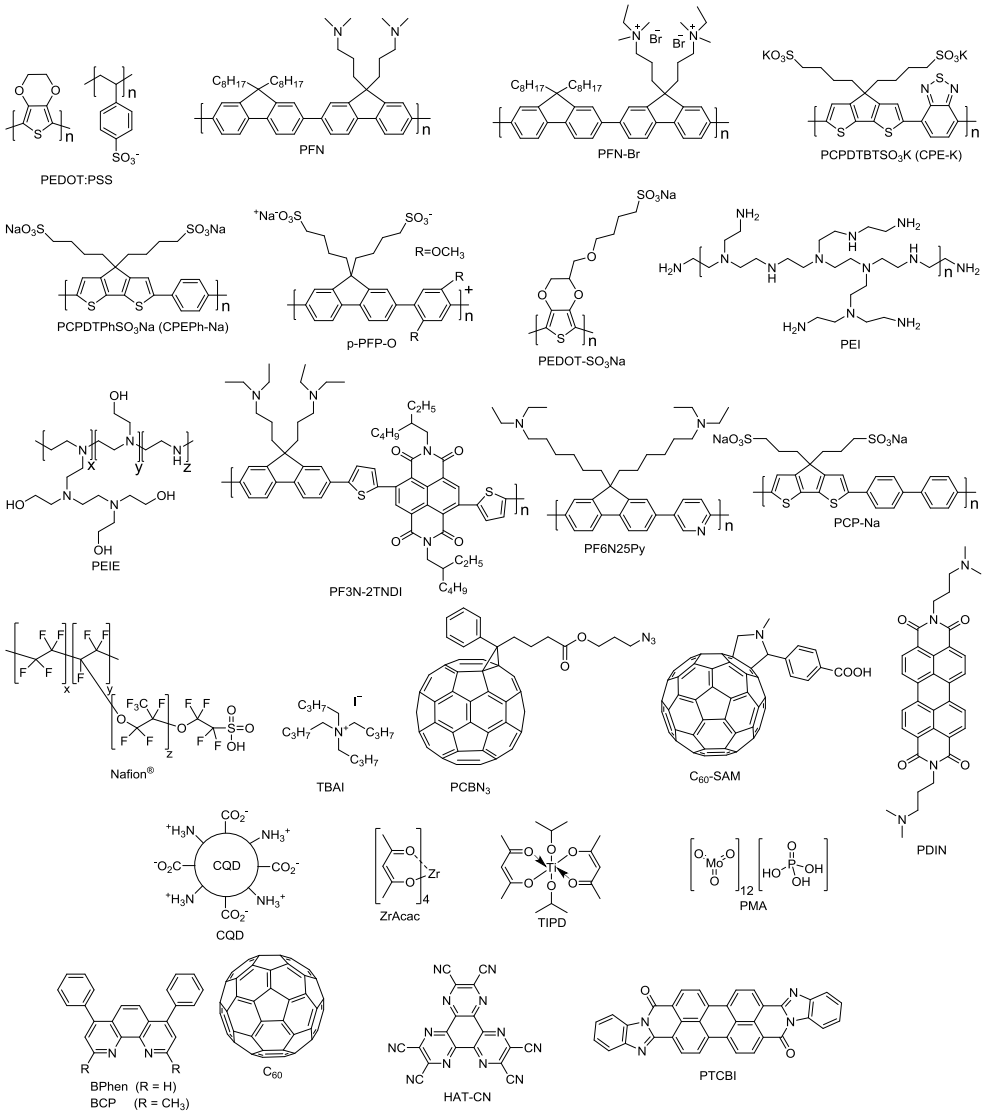

Figure 1. Materials adopted in the ICL of tandem solar cells covered by this chapter. The references for publications using these materials are provided in Table 1.

In 2015, Zhou et al. presented two new CPEs: PCPDTBTSO$_3$K (CPE-K) and PCPDTPhSO$_3$Na (CPEPh-Na).[9] Owing to the ionic side groups, a thin layer (10−15 nm) of these p-type materials could effectively increase the work function of the substrate to 5.2 eV. Tandem devices using a zinc oxide nanoparticles layer coated with CPEPh-Na as ICL showed PCE up to 11.3%. Structurally similar is the p-type CPE PCP-Na, adopted by Cui et al. in

2017.[10] An ICL of zinc oxide nanoparticles and PCP-Na allowed the realization of over 13% PCE in tandems with state-of-the-art photoactive materials. An interesting CPE in this series is p-PFP-O, used in a tandem device by Lee et al. in 2016.[11] p-PFP-O derives from the oxidative doping of its n-type counterpart (PFP-O), by treating the latter with ammonium persulfate. As consequence of the oxidation, the orientation of the dipole moment is reversed, with respect to PFP-O. The authors successfully demonstrated the good performance (PCE ca. 10%) of this CPE in a tandem cell with a zinc oxide/PEDOT-SO_3Na/p-PFP-O ICL, where PEDOT-SO_3Na is a pH-neutral form of PEDOT. pH-neutral PEDOT has a low work function and to avoid loss in V_{OC}, the p-PFP-O was used. In 2016 Zhang et al. presented PF3N-2TNDI as a useful CPE for the n-type side of an ICL in combination with PEDOT:PSS on the p-side and a ultra-thin silver layer in between.[12] The role of silver is to provide a recombination center for charges from the subcells, thanks to its high conductivity. PF3N-2TNDI could reduce the work function of silver down to 4.1 eV. The CPE proposed by Zhang et al. outperformed the well-known PFN, not only in terms of PCE but also as reduced dependence of the performance on its thickness (PCE still 9.7% at 20 nm). The same group demonstrated in 2018 that by mixing PF3N-2TNDI with polyethyleneimine (PEI), the work function could be further lowered without significantly affecting charge transport. [13,14] With the optimal mixed ETL, a high performing tandem could be fabricated without the need of the silver layer in between ETL and PEDOT:PSS. The tandem with this mixed ETL could afford a PCE of 11%, even at 70 nm thickness of the ETL (the optimal PCE was 12.6% at 20 nm of thickness).[13] A good performance for tandems adopting PFN was reported independently by Zuo et al.[15] and Martinez-Otero et al.[16], both in 2015. The ICL used consisted of evaporated molybdenum oxide with an ultra-thin layer of silver and PFN on top. PCEs approaching 11%[15] and an extraordinarily high FF of 0.76[16] were achieved. Even with a total thickness below 20 nm,[16] the ICL provided the necessary protection of the front cell from processing of the back cell on top, and good optical transparency. Continuing with the n-type CPEs, Lu et al. demonstrated a novel ICL consisting of an all-solution-processed metal oxide/dipole layer/metal oxide stack.[17] PF6N25Py was used to make a layer on top of another layer of molybdenum bronze. The work function of the latter was effectively lowered, improving the energy level alignment with a subsequent film of titanium dioxide nanoparticles.[17] By fabricating homo tandems with this ICL, a correct addition of the V_{OC} of the subcells was obtained, together with comparable FF to the single-junction reference cell and improved overall efficiency.

Metal oxides are a very popular class of interlayer materials for electronics in general and for OPV as well. Metal oxides commonly adopted in OPV are deposited either from pre-formed nanoparticles suspensions, from a metal-organic precursor in solution which converts to some extent to a metal oxide, or via thermal evaporation in high vacuum. Concerning their use in solution-processed tandem solar cells, it is worth to mention that examples of all-oxide ICLs are rare in general and always involve the presence of thin metal clusters to improve

their conductivity.[18,19] Only in 2018 Becker et al. reported the first all-oxide ICL for polymer tandem solar cells.[20] A possible reason for the scarcity of such examples might be because very few materials (like PEDOT:PSS) can guarantee the protection of the front cell active layer against the processing from solution of the back cell active layer.[21] The exceptional example of Becker et al. consisted of an inverted (n-i-p) configuration tandem in which thermally evaporated molybdenum oxide (HTL) and tin oxide (ETL) deposited via atomic layer deposition were stacked together to form the ICL. Together with the singular protection against solvents, the authors indicated that a large intrinsic interface dipole at the interface HTL/ETL makes the conduction bands of molybdenum oxide and tin oxide to align. In addition, the tandem featuring this ICL did not suffer from the well-known problem of necessity of UV light soaking. In fact, it is known that exposing common conductive metal sub-oxides, such as zinc oxide and titanium dioxide, to UV light illumination can increase their conductivity by a photodoping mechanism.[22] In Chapter 6, the use of solution-processable tin oxide nanoparticles suspensions for OPV tandems is presented for the first time.[23] In combination with PEDOT:PSS as HTL, both conventional (p-i-n) and inverted architecture tandems were realized using only these two materials, with performance in good agreement with the expectations. For conventional tandems tin oxide offers the possibility to avoid the use of pH-neutral PEDOT:PSS, which can cause a loss in V_{OC} due its reduced work function. In fact, tin oxide proved to be resistant against the acidity of the commercial formulation of PEDOT:PSS (Al 4083), while zinc oxide is washed away. In 2015 Mitul et al. implemented solution-processed aluminum-doped zinc oxide (AZO) in a PEDOT:PSS/AZO/PEIE ICL, where PEIE is the partially ethoxylated polyethyleneimine.[24] Thermal annealing at 150 °C was required to form AZO from its precursor. To demonstrate the proper working of this ICL, the authors built a homo tandem using P3HT:PCBM, which can sustain this temperature. In 2017 Du et al. reported molybdenum oxide nanoparticles as a solution to overcome interfacial losses occurring in some tandem solar cells where PEDOT:PSS is used as HTL.[25] They attributed poor hole transporting properties of the interface between PEDOT:PSS and an active layer with polymers containing nitrogen atoms to the protonation of the latter. By mixing PEDOT:PSS and MoO_3 nanoparticles, the problem was reported to be solved and tandem solar cells using a PEDOT:PSS:MoO_3/ZnO/PEI ICL showed improved performance compared to the control tandem devices with only PEDOT:PSS or MoO_3. Concerning composite materials with PEDOT:PSS, Torabi et al. reported in 2015 a mixture of modified PEDOT:PSS and silver nanoparticles as HTL in the ICL, in combination with sol-gel titanium dioxide as ETL.[26] The silver nanoparticles were synthesized directly in the dispersion of the modified PEDOT:PSS by reduction of the silver nitrate precursor with sodium borohydride, without the need of a stabilizer. A homo tandem was realized to check the performance. The V_{OC} was 1.1 V and the FF 0.60, against the 0.59 V and FF of 0.55 of the reference cell.

Recently, few examples of tandem solar cells have emerged in which metal-organic compounds have been adopted in the ICL. Lu et al. in 2016[27] and Chang et al. in 2017[28] adopted zirconium acetylacetonate (Zr-acac) to lower the work function of PEDOT:PSS in the ICLs: PEDOT:PSS/Zr-acac/PF6N25Py and MoO_3/PEDOT:PSS/Zr-acac, respectively. Zr-acac has the advantage that it can be easily processed from solution and does not require a thermal annealing treatment. Another example of metal chelate in tandems was published in 2018 by Shi et al.[29] In their work, Shi et al. used titanium (diisopropoxide)bis(2,4-pentanedionate (TIPD) on top of evaporated MoO_3/Ag as ICL, applying a post-treatment of 150 °C to get the optimal performance of the tandem. A single example of an inorganic transition metal compound for tandem applications is represented by the phosphomolybdic acid hydrate (PMA), presented by Lu et al. in 2017 in both conventional and inverted structure tandems.[30] In their work, a modified pH-neutral PEDOT:PSS layer served as recombination center for the charges extracted by the PMA HTL and the zinc oxide nanoparticles ETL. The ICL was then PMA/PEDOT:PSS/ZnO in inverted tandems and *vice versa* for the conventional ones. As will be discussed in more detail in Chapter 6, the work function of pH-neutral PEDOT:PSS does not match the deep-lying HOMO energy level of some photoactive polymers, generally provoking a loss in V_{OC}.[31] By using PMA in between pH-neutral PEDOT:PSS and the active layer of P3HT:PC_{60}BM the authors showed a recovery in the V_{OC} with respect to the control device without PMA (0.62 V vs 0.48 V, respectively).

Concerning the use allotropic forms of carbon in the ICL, three examples have been reported in the last period. In 2015 Chang et al. used a cross-linkable azidofullerene derivative ((C-)$PCBN_3$), doped with tetrabutylammonium iodide (TBAI) as ETL, on top of PEDOT:PSS.[32] A temperature of 140 °C was used for the curing of the ETL, which allowed the manufacturing of tandems on a flexible polyethylene naphthalate substrate with good performance (PCE of 8.7% vs 9.3% on glass). The ETL showed also a weak thickness dependence of the performance, with an optimum at 10 nm. A mixture of PEDOT:PSS and graphene oxide has been reported to work in an ICL, together with lithium-doped zinc oxide (LZO) as ETL, in a publication published in 2015 by da Silva et al.[33] Another form of carbon for the ICL are carbon quantum dots (CQDs), mixed with PEI described by Kang et al. in 2018.[34] CQDs were synthesized by a microwave reaction starting from citric acid and β-alanine, resulting in particles with size of ca. 3 nm. A thin layer of the CQDs/PEIE composite on top of PEDOT:PSS was reported to provide an efficient tunneling junction for the recombination of charges in the ICL, affording a best efficiency of 12.1%.

2.2.2 Processing multi-junction stacks

For the commercial success of future tandem OPV technology is important to simplify the manufacturing processes as much as possible. In this section recent advances focusing on processing of tandem OPV cells are reported.

Lee et al.[11,35,36] adapted a concept first introduced by Wei et al.[37] for single-junction OPV devices to tandem solar cells. The idea is to process both the photoactive components and interlayer material from the same solution. By taking advantage of different surface energy of these components, a favorable spontaneous segregation of the interlayer materials at the desired interfaces can take place during the deposition (**Figure 2**). In their tandem devices, Lee et al. mixed either PEI[35,36] or p-PFP-O[11] with the active layer blend materials. For the latter, they choose a widely reported combination: PTB7-Th as electron donor and $PC_{70}BM$ as electron acceptor. Inverted[35,36] and conventional[11] tandems were demonstrated using this technique to process both the front and the back subcells, where the ICL was either PEDOT:PSS/PEI[35,36] or zinc oxide/PEDOT-SO_3Na/p-PFP-O.[11] Time-of-flight secondary-ion mass spectrometry measurements confirmed the localization of PEI at two positions (bottom and top subcells) along the vertical direction of the stack, rather than being uniformly distributed.

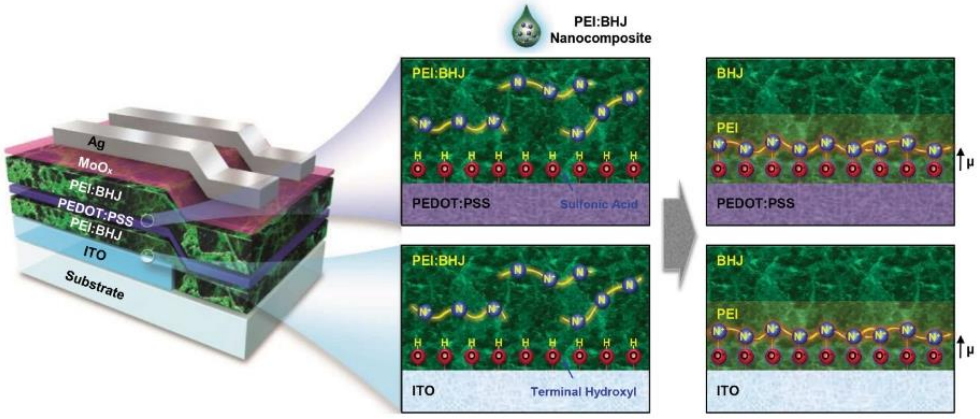

Figure 2. Tandem polymer solar cell processed from bulk heterojunction:PEI nanocomposite solution. Reproduced with permission from Ref. 35. Copyright 2014 WILEY-VCH Verlag GmbH & Co. KGaA, Weinheim.

Recent reports focused on the improved processing of the traditional combination PEDOT:PSS/zinc oxide as ICL for inverted tandem solar cells. In 2017 Chen et al. reported the processing of diethyl zinc precursor on top of a "wet" (not annealed) layer of PEDOT:PSS as ICL.[38] According to the authors, the residual moisture in the PEDOT:PSS film promoted the conversion of the precursor to zinc oxide. The as-formed layer of zinc oxide only needed a mild thermal annealing at 80 °C, which was compatible with the front cell active layer. As a result a record 2.16 V of V_{OC}, combined with a 10.2% efficiency were achieved in a tandem

device, demonstrating the good functioning of the ICL. Given the hydrophobic nature of commonly adopted active layer materials, the deposition of a layer of PEDOT:PSS from an aqueous dispersion requires the use of surfactants to lower the surface energy. Surfactants are in general insulating and the amount of them necessary to improve the casting can eventually be substantial and deteriorate the desired properties of PEDOT:PSS. Moreover, modifying PEDOT:PSS might affect unfavorably the distribution of the insulating PSS part, creating an energy barrier. In 2016 Prosa et al. proposed a simple approach to recover the good functioning of a PEDOT:PSS film deposited from a suspension including a surfactant (Zonyl FS-300).[39] By simply rinsing the film with isopropanol, part of the surfactant and the excess of PSS at the surface of the layer could be removed. Tandems with isopropanol-rinsed PEDOT:PSS, followed by zinc oxide nanoparticles as ICL demonstrated optimal performance, contrary to the pristine device with non-rinsed PEDOT:PSS. In fact, the latter featured an s-shape in the *J–V* characteristics, likely denoting the presence of an interfacial barrier. The results discussed in the Chapter 3 of this thesis[40] demonstrate how both the requirements of a low annealing temperature of the ICL and a low surface energy of the PEDOT:PSS dispersion can be satisfied at the same time. It was found that by processing in inert atmosphere the commercial formulation of PEDOT:PSS (Al4083) from a mixture of water/1-propanol (1:2 v/v) provides a good coverage for a wide selection of different active layer materials, without the need of a surfactant. A synthetic procedure of zinc oxide nanoparticles was also reported, and isoamyl alcohol was adopted as liquid for the dispersion. The processing of zinc oxide from such suspension did not negatively affect the PEDOT:PSS layer. Without any thermal annealing treatment, the proposed processing technique afforded six tandems and three triple-junction solar cells featuring eight active layer materials of different chemical nature. Using the same technique, the first example of a solution-processed quadruple-junction polymer solar cell with four complementary absorber layers was reported, discussed in detail in Chapter 5.[41]

Orthogonality of the solutions is a stringent requirement for fabricating complex device stacks such as tandems directly from solution. A possible way to get around this constraint is to stamp transfer the top subcell, avoiding the use of solvents. In 2017 Ka et al. demonstrated an example of device fabricated in this fashion. In their work they deposited a front cell consisting of the small molecular donor TAPC blended with C_{70}.[42] Next in the stack they deposited, also by thermal evaporation, a PTCBI:C_{70} buffer electron transport layer, preceding a PTCBI/Ag/HAT-CN interconnecting layer. For the back cell they adopted PCPDTBT:$PC_{70}BM$, which has a low band gap of 1.38 eV. The latter was deposited by spin-coating onto a poly(dimethylsiloxane) stamp, dried in high vacuum from solvents, coated onto the evaporated front subcell/ICL stack and detached from the stamp after annealing at 100 °C under applied pressure, to form a conformal contact at the interface. The resulting tandem was characterized by a correct addition of the V_{OC} of the subcells: this was 0.89 and 0.59 V for the front and the back subcells respectively, while for the tandem 1.46 V of V_{OC}

was measured. Maybe due to the limited FF of both the single-junction cells, the tandem featured a FF of only 0.51, limiting the efficiency to 6.26%. Later, in 2018 Ka et al. also demonstrated a polymer tandem solar cell where both the front and the back subcells were deposited by stamp transfer and the interlayers were obtained by thermal evaporation.[43] P3HT:$PC_{60}BM$ was adopted in the front cell and PCPDTBT:$PC_{70}BM$ as back cell. The tandem showed full addition of the V_{OC} (1.20 V) and a FF of 0.60. In 2018, Che et al. revisited the same concept of combining a thermally evaporated front cell together with a solution-processed back cell.[44] Differently from the work discussed before, the back subcell was directly deposited by spin-coating on top of the evaporated front subcell. The former was a DTDCPB:C_{70} co-evaporated cell, coated with ETL BPhen:C_{60}/Ag, also by thermal evaporation. Following, PEDOT:PSS was cast to complete the ICL, and the back cell of PTB7-Th:BT-CIC was deposited by spin-coating. The front cell donor material has a wide band gap of 1.68 eV, while donor and acceptors in the back cell have band gaps of 1.58 and 1.38 eV, respectively. An outstanding high PCE of 15 % was obtained by this tandem cell, arising from an EQE between 70% and 80%, corresponding to a measured J_{SC} of 12.7 mA cm^{-2}. By applying an antireflection coating on the glass facade the J_{SC} increased even further, up to 13.3 mA cm^{-2}. In addition, the V_{OC} of 1.59 V followed the sum of the constituent subcells (0.90 and 0.69 V for the front and back cells, respectively), together with a high FF of 0.71. Another remarkable aspect of this work is the high yield accompanying the high efficiency: 97% and 95% for solar cells with active area of 2 and 9 mm^2, from a total of 130 devices.

2.2.3 Light management

Organic multi-junction solar cells feature stacks of several semitransparent thin films. For such kind of devices, optical interference effects play an important role, reason for which a number of papers have focused their attention on how to take advantage of these effects, in order to improve the balance of absorption of light from the two subcells. In 2015 Zuo et al. explored the influence of the thickness of the Ag layer in a MoO_3/Ag/PFN ICL on the balance of current from the subcells.[15] In particular, an optical micro-cavity is formed between the thin silver layer in the ICL (8−14 nm) and the opaque silver contact on the back cell (**Figure 3**).

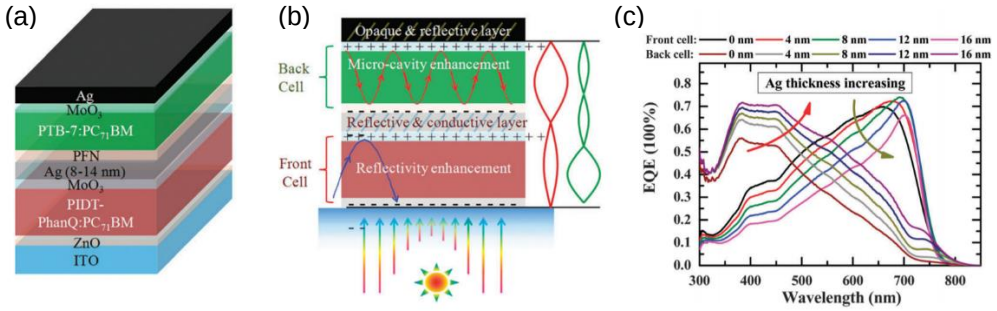

Figure 3. Micro-cavity tandem polymer solar cell. Device scheme (a), cartoon illustrating the micro-cavity enhancement in the back cell (b), and modeled EQE spectra of the subcells as function of the thickness of the Ag layer in the ICL. Reproduced with permission of RSC, from Ref. 15 conveyed through Copyright Clearance Center, Inc.

By acting on the thickness of the thin silver layer, the balance of absorption between front and back subcells could be tuned to achieve current matching. Moreover, the authors were able to measure the individual subcells directly by accessing externally the intermediate silver contact. A similar phenomenon was observed in tandem cells with parallel-connection by Lee et al. in 2015[45] and Zuo et al. in 2017.[46] In the first case MoO_3/Ag/MoO_3 was the ICL, while in the second case it was PEDOT:PSS/Ag/Au/MoO_3. In a parallel-connection tandem the requirement of current matching drops, since the total current is the summation of the current of the subcells. Besides the increase in current, the voltage is pinned to the lowest voltage between the two subcells. Due to the limited charge mobility in most of the organic semiconductors, the optimal thickness of a single-junction device is usually determined by the tradeoff between increasing charge generation by more light absorption in thicker layers and the concomitant decrease because of bimolecular charge recombination. To increase light absorption while preserving the fill factor (influenced by charge recombination), the same active layer absorber can be deposited twice in a homo tandem. The one reported by Zuo et al. in particular, represented at the time the most efficient example for organic tandem solar cell with parallel connection (PCE of 11.1%). PTB7-Th:4TIC was used as active layer. Again to improve the absorption of active layers suffering from thickness-dependent performance, in 2015 Mantilla-Perez et al. fabricated a four-terminal homo-tandem solar cell.[47] A glass substrate coated with indium-doped tin oxide (ITO) on both sides was used to build single-junction cells on each side (**Figure 4**a).

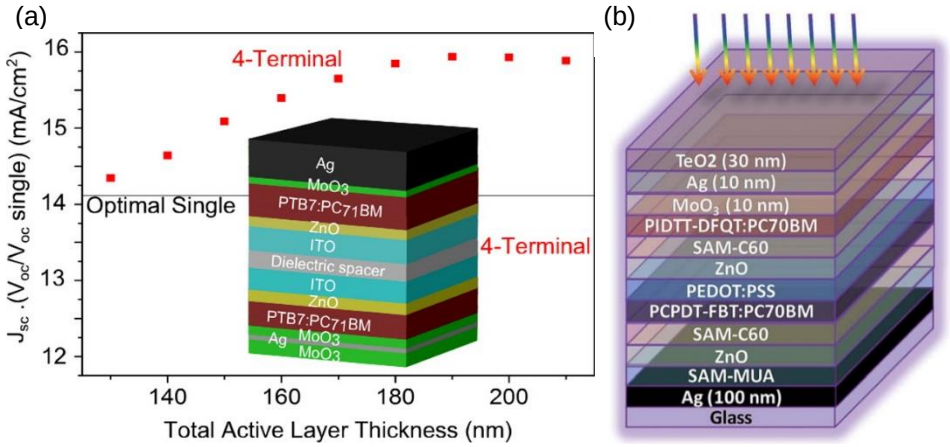

Figure 4. Four-terminal tandem (a) and top-illuminated tandem with DMD electrode (b). Reprinted with permission from Ref. 47 (Copyright (2015) American Chemical Society) and with permission of RSC from Ref. 48 (conveyed through Copyright Clearance Center, Inc).

As transparent electrode, a dielectric-metal-dielectric (DMD) electrode was deposited by thermal evaporation on top of one of the active layers, consisting of MoO_3/Ag/MoO_3. The top electrode on the other subcell was an opaque metal. Another advantage of this special architecture is that the two subcells can be operated independently, which solves the requirement of current or voltage matching. As stressed by the authors, a limiting factor in their particular device was the DMD electrode, due to its poor transparency. Related to this point, Zuo et al. reported in 2016 a series-connected tandem solar cell featuring a MoO_3/Ag/TeO_2 DMD transparent top electrode.[48] The device was built starting from an opaque silver layer on glass as bottom electrode, and finished with the DMD stack on top (Figure 4b). Interestingly, the DMD tandem had a performance close to the ITO-based counterpart, thanks to the TeO_2 capping layer, which reduced the reflection at the thin silver layer, the first one encountered by light. Another way to enhance the absorption of the active layers was reported in 2018 by Mayer et al.[49] Here a templated periodical structure was applied externally on the glass side of an ITO-based tandem solar cell. The structure reported was made with a UV-curable polymer on a glass substrate and a master template fabricated with laser interference lithography. A relative increase by 9% in the PCE was recorded following the application of this diffractive structure.

Optical interference in tandem solar cells is usually optimized considering illumination in the direction perpendicular to the surface of the device. Nevertheless, in practical scenarios the solar cell is not constantly oriented in such direction but there is rather a certain angle of incidence. In 2016 Mertens et al.[50] tried to understand a peculiar behavior of organic tandem

solar cells, already reported by Riede et al.[51] for evaporated tandem cells in 2011. In detail, when their device was at a certain angle of orientation Θ with respect to the direction of incidence of light, the short-circuit current density corrected by the effective area of illumination ($J^*_{SC}=J_{SC}/\cos(\Theta)$) was relatively insensitive to this angle, up to 65°.[50] In their work, the authors showed that both the measured and modeled EQE spectra of the individual subcells change according to Θ. Nevertheless, both of the corresponding spectrally integrated J^*_{SC}s stay relatively constant. The angle-insensitivity of the performance of organic tandem solar cells is particularly interesting for their application in realistic operating conditions.

In order for tandem organic solar cells to succeed in their commercialization, appealing characteristics like the possibility to easily tune their color are very important. In 2017 Luo et al. reported flexible all-solution-processed polymer tandem solar cells with different colors.[52] Thanks to the highly conductive PEDOT:PSS top electrode, the reflectivity of the device was engineered by simply changing the thickness of it. PCE values from 7.23 to 8.34% were achieved, corresponding to different colors.

2.2.4 Active layer materials

In order to exploit the full potential of tandem solar cells, the active layer materials need to be engineered to absorb light in complementary regions of the solar spectrum. A number of materials, either newly developed or previously reported in single-junction devices, have been adopted in tandem solar cells for this purpose. For a complete list of photoactive materials, either small molecules or polymers, and their optical gap, the reader should refer to Table 1. **Figures 5-10** show their chemical structure.

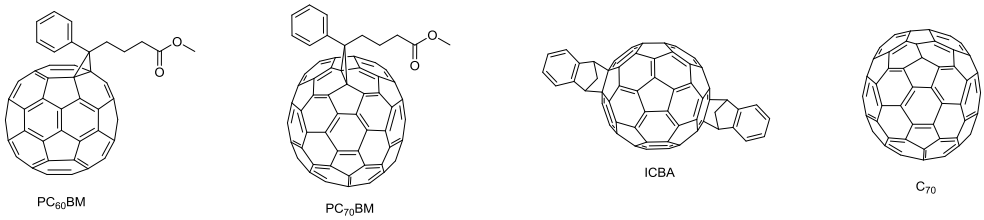

Figure 5. Fullerene acceptors used in tandem solar cells covered by this chapter. The references for publications describing these materials are provided in Table 1.

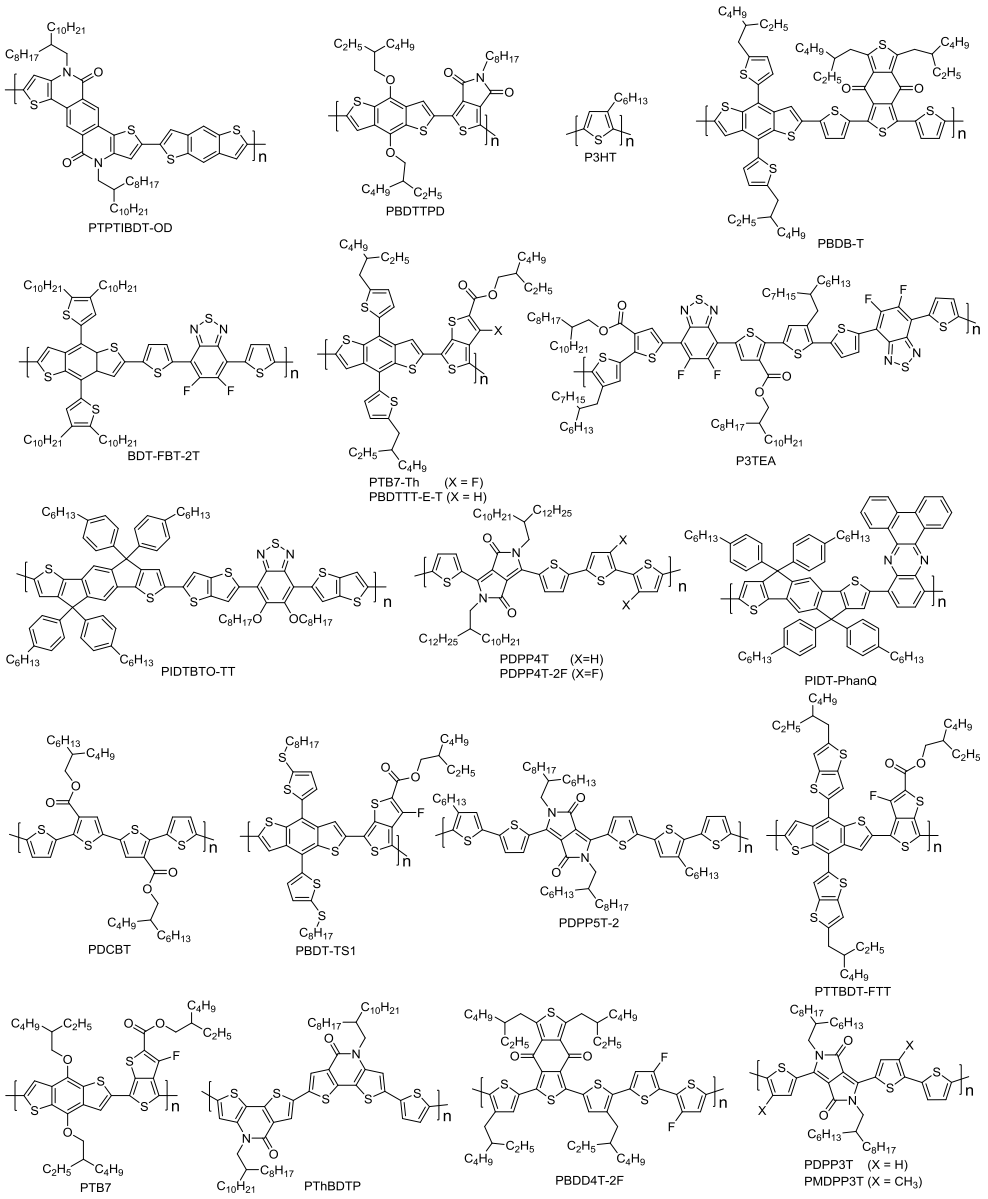

Figure 6. Polymer donor materials used in tandem solar cells covered by this chapter. The references for publications describing these materials are provided in Table 1.

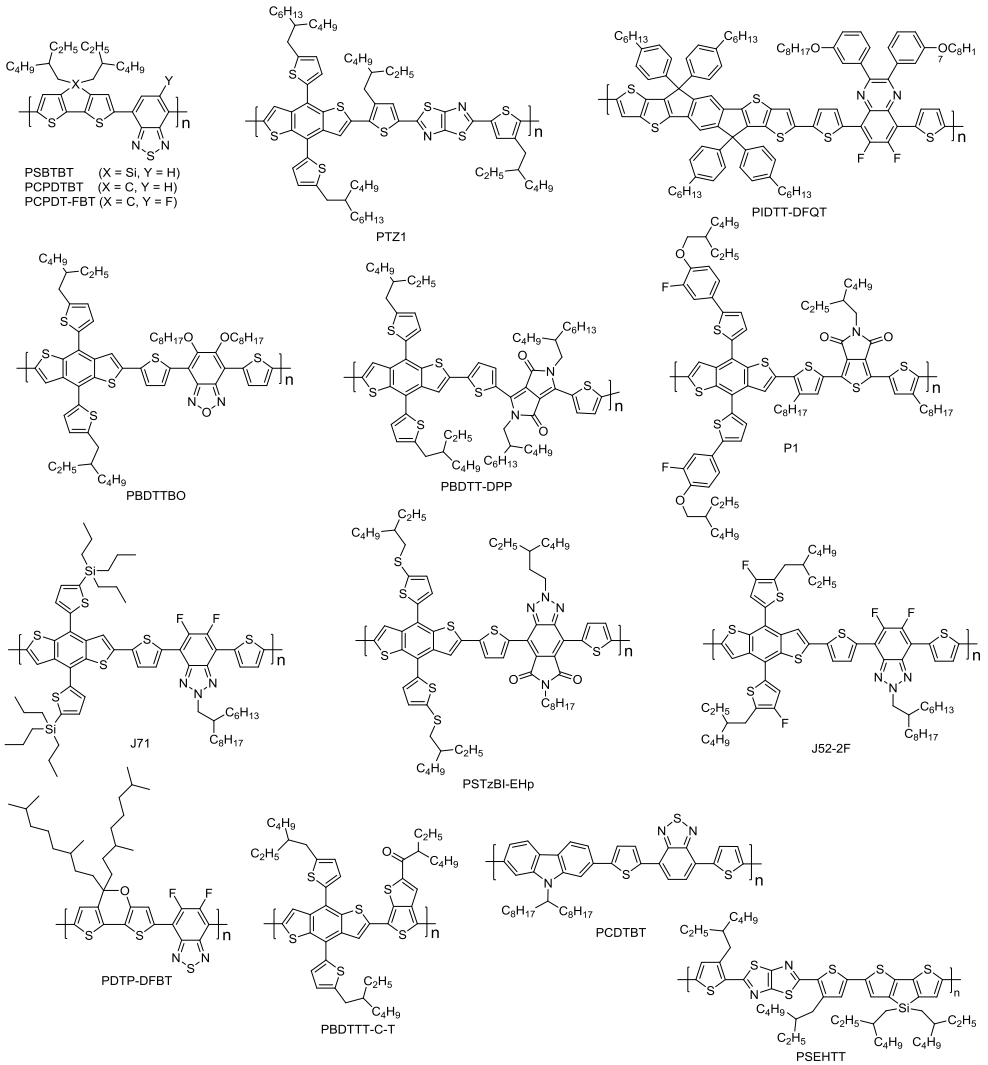

Figure 7. Additional polymer donor materials used in tandem solar cells covered by this chapter. The references for publications using these materials are provided in Tables 1 and 2.

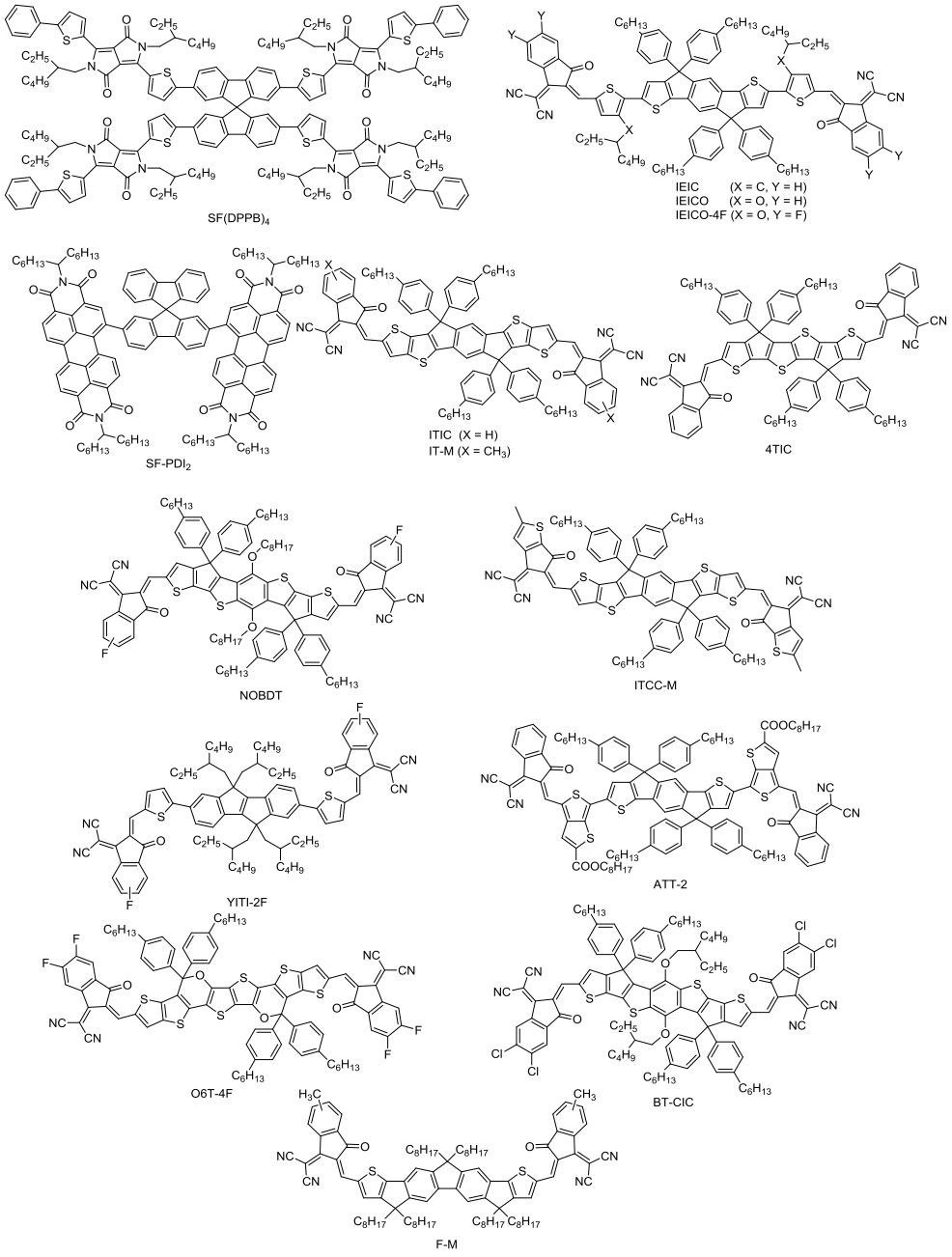

Figure 8. Non-fullerene acceptor materials used in tandem solar cells covered by this chapter. The references for publications using these materials are provided in Table 1.

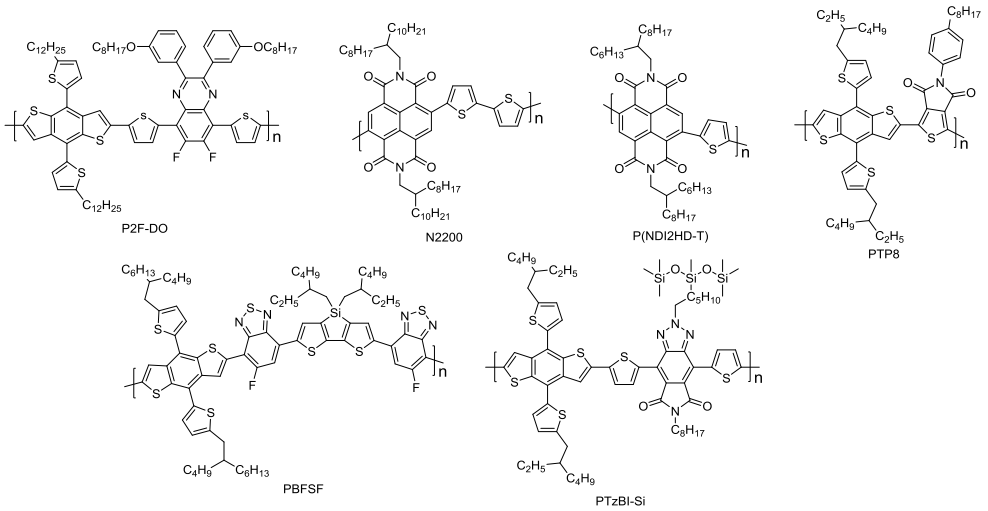

Figure 9. Donor and acceptor materials for all-polymers blends reported in tandem solar cells covered by this chapter. The references for publications using these materials are provided in Table 1.

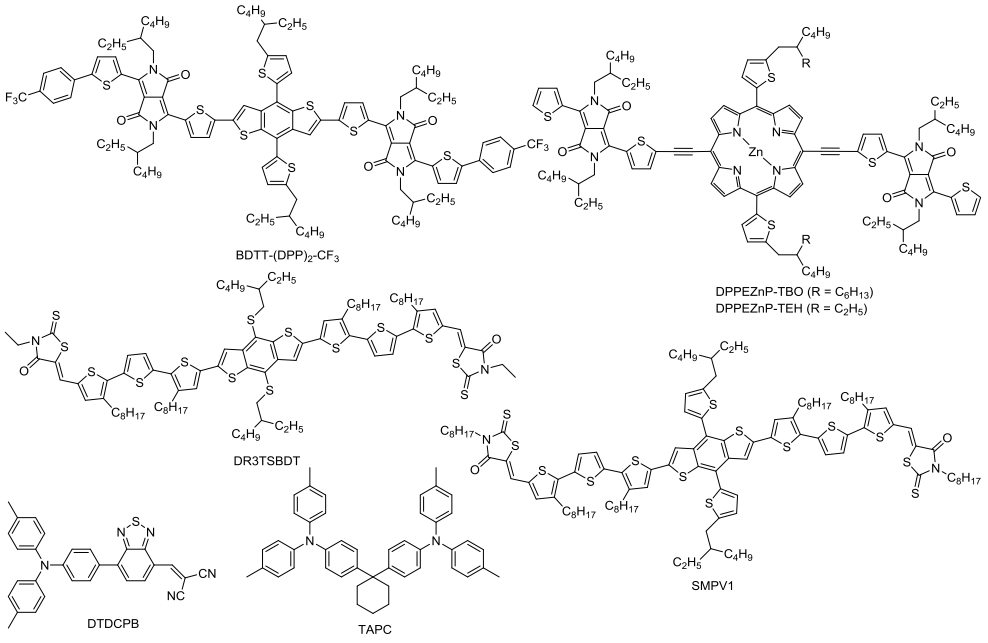

Figure 10. Small molecular donor materials used in tandem solar cells covered by this chapter. The references for publications using these materials are provided in Table 1.

Photoactive blends based on PCBM were traditionally the most diffused and studied. Benefiting from its isotropy, PCBM works reasonably well with a wide range of polymer donors. PTB7-Th represents a benchmark donor material for polymer-fullerene blends in the last years, especially for tandem solar cells. With a band gap of 1.58 V, a single-junction device based on this material and $PC_{70}BM$ features a V_{OC} around 0.8 V and efficiency up to 10% or more.[53] When blended with $PC_{70}BM$, an efficiency of 11.3% was reported for a homo-tandem device with this active layer, despite the lack of complementarity in the absorption due to the use of the same absorber for both the front and back subcells.[9] More groups reported similar efficiencies for tandem cells featuring this blend at least in one of the two subcells.[34,54,55] In 2015 Zheng et al. combined the polythiophene PDCBT and the benzodithiophene-based PBDT-TS1, blended with $PC_{70}BM$ and $PC_{60}BM$, respectively in a tandem device.[56] The first one has a wide band gap of 1.90 eV and the second one has a band gap of 1.51 eV. Both possessed maximum EQEs around 70% in optimal single-junction devices and V_{OC}s of 0.80 V. The authors fabricated a tandem by using the PDCBT blend for the front cell and the PBDT-TS1 blend as back cell. A PCE of 10.2% was reported for this device. Besides a moderate FF of 0.55, the device showed a correct addition of the V_{OC} of the subcells (V_{OC} = 1.60 V) and a remarkable J_{SC} of 11.7 mA cm^{-2}. This high value of J_{SC} derived from the EQE spectrum of the subcells, being as high as almost 70% (back cell) and ca. 75% (front cell). Nevertheless some concern arises because the summed EQE of the subcells goes above 100% around 450 nm. In 2016 the same group synthesized a new low band gap polymer[57] by introducing fluorine atoms in the structure of the already reported PDPP4T.[58] Compared to PDPP4T, the fluorinated version PDPP4T-2F showed a slightly broader absorption spectrum, the onset being at ca. 900 nm. The main advantage of this new version consists in the high V_{OC} it can give, when mixed with $PC_{60}BM$, thanks to the lower HOMO level (0.12 eV lower). The difference in V_{OC} of the single-junction cells reflected perfectly the difference in HOMO: 0.78 V vs 0.66 V for PDPP4T-2F and PDPP4T, respectively. A tandem with PBDD4T-2F:$PC_{60}BM$ (V_{OC} = 0.90 V) as front cell and PDPP4T-2F:$PC_{70}BM$ as back cell afforded a high V_{OC} of 1.68 V, together with a J_{SC} of 11.3 mA cm^{-2} and PCE 11.6%. Benefitting from the successful development of benzodithiophene (BDT) based polymers, Duan et al. reported in 2015 a thienyl-substituted BDT copolymerized with fluorine-substituted benzothiadiazole (BT) and two thiophenes (BDT-FBT-2T).[59] The optical band gap of this polymer amounted to 1.72 eV. Single-junction solar cells with a blend of this polymer with $PC_{70}BM$ showed no loss of performance at increasing thickness of the active layer up to 250 nm. Both these characteristics make it suitable as front cell wide band gap donor material in a tandem device. Using PMDPP3T:$PC_{60}BM$ as back cell, a tandem with PCE of 8.9% was fabricated, for which the main limiting factor was the V_{OC} (1.42 V), due to the significant minimum photon energy loss ($E_{loss} = E_g - eV_{OC}$ = 0.85 eV) in the front cell. Furthering on the BDT unit as leitmotif, PTZ1 was synthesized in 2016 by Guo et al. by copolymerization with the electron deficient thiazolothiazole unit.[60] Thanks to both the wide band gap of 1.97 eV and the relatively deep-lying HOMO level of −5.31 eV, a high V_{OC} of

1.01 V was measured for the pristine PTZ1:$PC_{70}BM$ single-junction solar cell, which lowered to 0.94 V after optimization of the processing conditions. These materials were adopted in a tandem as front cell, with a blend of the low band gap (1.58 eV) PBDTTT-C-T and $PC_{70}BM$ in the back cell. The latter was reported to give a V_{OC} of 0.74 V. The measurement of the tandem returned a PCE of 10.3%, with a nearly ideal addition of the V_{OC} (1.65 V), FF of 0.65 and J_{SC} of 9.6 mA cm^{-2}. Integration of the EQE of the subcells returned 8.15 and 9.80 mA cm^{-2} for the front and back subcells, respectively. Indacenodithiophene (IDT) is an interesting donor unit for donor-acceptor (D-A) copolymers given the planarity of its structure. A new copolymer of IDT with BT units was reported in 2017 by Ma et al. (PIDTBTO-TT).[55] The authors copolymerized these units using thienothiophene (TT) as π-bridges. After optimization of the morphology using $PC_{70}BM$ as acceptor and diiodooctane as co-solvent, a PCE of 8.15% was recorded. Since the polymer had a band gap of 1.87 eV and gave V_{OC} of 0.91 V, it was used as front cell of a tandem, in combination with PTB7-Th:$PC_{70}BM$ in the back cell. A V_{OC} of 1.70 V and PCE of 11.2% were achieved for the best device. More BDT-based donor polymers were reported by Song et al. in 2017, P1 and P2.[61] For an optical band gap of 1.82 eV, 0.91 V and 1.00 V of V_{OC} were achieved in single-junction devices with $PC_{70}BM$, thanks to deep-lying HOMO levels of −5.43 and −5.50 eV, respectively. The single junctions were also characterized by EQE spectra of 70%. These materials were used as front cell for two different tandem solar cells, in combination with PTB7-Th:$PC_{70}BM$ (V_{OC} = 0.81 V) in the back cell. From the measurements, V_{OC} values of 1.64 (with P1) and 1.72 V (with P2) were achieved, respectively. The measured J_{SC}s were 10.1 (P1) and 9.3 mA cm^{-2} (P2) and lower J_{SC}s were integrated from the EQE spectra of the subcells.

In recent years increasing focus in the OPV field is on non-fullerene acceptors (NFAs).[62-65] NFA molecules allow more freedom to engineer the energy levels (and optical band gap) to achieve high V_{OC}. Different from fullerene-based acceptors, a reduced offset in the HOMO-HOMO and LUMO-LUMO of donor and acceptor does not occur at the expense of efficient charge separation.[66] Studies suggested a different nature of the exciton separation process in this class of systems. In addition, the photocurrent can benefit from their substantial absorption coefficient. Although the anisotropy limits the number of successful donor-acceptor combinations, an increasing number of relevant results have been reported in the last few years, with important consequences on the efficiency not only of single-junction but also of tandem solar cells. The review paper by Cheng et al. provides a good picture of recent results about non-fullerene polymer solar cells and the direction to further advance in this field. Hou et al. also analyzed the opportunities and challenges of NFAs. For a more in-depth discussion of the topic, the reader is referred to recent review papers.[62-65] A first demonstration of how a high V_{OC} can be achieved in tandems with NFAs was given by Liu et al. in 2016.[67] Two polymer:NFA systems with high V_{OC} and complementary absorption were selected for their tandem: P3HT:$SF(DPPB)_4$ (the band gaps are 1.90 and 1.77 eV,

respectively) and PTB7-Th:IEIC (band gaps of 1.58 and 1.50 eV, respectively). The first one delivered a V_{OC} of 1.11 V, while the second one gave 0.95 V. The best tandem device (PCE = 8.48%) afforded a V_{OC} as high as 1.97 V. The performance in this case was mainly limited by the FF (0.52), largely determined by the FF of the corresponding single-junction cells (0.54 and 0.47 for the front and back subcells). The highest V_{OC} for a NFA tandem was reported in 2017 by Chen et al.[38] With P3TA (band gap = 1.72 eV) and SF-PDI$_2$ (band gap = 2.07 eV) as polymer donor and NFA, respectively, a low minimum voltage loss could be achieved (0.6 eV). Due to the limited absorption in the optimal single-junction device, combining the same active layer blend as both front and back subcells in a homo tandem allowed to boost the efficiency from 9.5% (single junction) to 10.8% (tandem), accompanied by a remarkable V_{OC} of 2.13 V. In 2017 multiple NFA systems introduced in tandem solar cells allowed to break the 12% efficiency threshold, surpassing the current state-of-the-art for fullerene-based tandems. In 2017 Shi et al. reported an efficient low band gap NFA by combining a central fused rings electron-donating unit, thiophene-thienothiophene-thiophene (4T), with a terminal electron-accepting part, 3-(dicyanomethylidene)indan-1-one (IC), resulting in 4TIC.[68] Given the shallower HOMO level and slightly deeper LUMO level than the benchmark NFA named ITIC (band gap of 1.59 eV), the 4TIC is characterized by an energy gap of 1.40 eV. Blended with PTB7-Th as donor, 4TIC demonstrated 10% efficiency in a single-junction cell, owing to a J_{SC} of 18.4 mA cm^{-2}, together with V_{OC} of 0.78 V and FF of 0.72, which makes it suitable as back cell for tandems. Therefore, the authors combined it with PBDB-T:ITIC (PBDB-T has a band gap of 1.80 eV) as front cell, which is capable of 0.92 V of V_{OC}, and J_{SC} and FF of 16.1 mA cm^{-2} and 0.71, respectively. The tandem afforded a V_{OC} of 1.65 V, high FF of 0.71 and J_{SC} of 10.6 mA cm^{-2} (PCE = 12.6%). No EQE spectrum was reported to support this value. In 2017 Qin et al. profited of the even lower band gap of the IEICO acceptor (1.34 eV), which together with PBDTTT-E-T (1.55 eV) as donor showed PCE over 9% in single-junction configuration, with V_{OC} of 0.81 V.[69] In a tandem with this blend as back cell and PBDD4T-2F:PC$_{70}$BM as wide band gap front cell (V_{OC} = 0.90 V), a PCE of 12.8% could be obtained at best, with a V_{OC} of 1.71 V and J_{SC} of 11.51 mA cm^{-2}. The EQE of both subcells in particular was over 60%, and extended to ca. 900 nm. To achieve instead wider band gap than ITIC, Cui et al. synthesized its derivative ITCC-M, for which the band gap was 1.68 eV.[10] Single-junction cells of PBDB-T:ITCC-M were characterized by a V_{OC} of 1.03 V, in addition to a J_{SC} of 14.5 mA cm^{-2}, reflecting the EQE up to ca. 75%. Again using PBDTTT-E-T:IEICO as back cell and the blend of the new NFA in the front cell, the authors could push the PCE to 13%, where the V_{OC} was 1.79 V and the J_{SC} was 11.4 mA cm^{-2}. In 2018, the same group improved the efficiency with respect to the latter result by carefully choosing more suitable materials for the active layers.[70] In place of PBDB-T:ITCC-M in the front cell, they adopted the wide band gap (1.94 eV) polymer J52-2F (also known as PFBZ), blended with IT-M, for which the band gap is 1.60 eV. Due to the wider and lower band gap of J52-F and IT-M, respectively, the EQE featured higher values in the range where the polymer absorbs and it was extended up to almost 800 nm thanks to the

acceptor. At the same time, the minimum photon energy loss was also decreased from 0.69 to 0.64 eV and the FF remarkably increased to 0.73. For the back cell, the spectral response was upshifted to 1000 nm by using the NFA IEICO-4F, which has a lower band gap of 1.24 eV (instead of 1.34 eV of IEICO). This one was blended with the donor PTB7-Th and together in a single-junction device, they gained a higher EQE over the whole spectral range, without drop in FF (0.69). The combination of these two active layers yielded a tandem with best efficiency close to 15% (14.0% certified), thanks to a slightly lower minimum photon energy loss, significantly higher current (J_{SC} = 13.3 mA cm^{-2}) deriving from the broader absorption, and improved FF of 0.68 (V_{OC} = 1.65 V). Another reported tandem featuring PTB7-Th:IEICO-4F as low band gap back cell was demonstrated by Shi et al. again in 2018.[71] A high PCE of 14.1% was also reported by Zhang et al. in 2018 for a NFA-based tandem.[72] Two new NFAs were synthesized ad-hoc, F-M (band gap 1.65 eV) and NOBDT (band gap 1.39 eV) and blended with PBDB-T (1.80 eV) and PTB7-Th (1.58 eV), respectively. Both these blends in single-junction cells showed generally very good photovoltaic performance. To notice is that both returned EQE values ≥ 70%. The F-M blend and the NOBDT blend were used as front and back subcells in a tandem cell, respectively. This device yielded high V_{OC} (1.71), high FF (0.70) and J_{SC} of 11.72 mA cm^{-2} at the same time. In 2018 Yue et al. reported a newly developed NFA with medium band gap (1.64 eV) based on the indenoindene core, named YITI-2F.[73] This NFA was blended with PBDB-T, reaching an efficiency of 9.7% in single junction, with V_{OC} of 0.93 V, J_{SC} of 15.5 mA cm^{-2} and FF of 0.70. They adopted this system as front cell of a tandem. For the back cell, PTB7-Th:ATT-2 was selected, ATT-2 being a previously reported NFA with band gap of 1.32 eV. In a single junction, the latter gave PCE of 9.52%. The tandem reached an efficiency of 11.9% at best, mainly limited by the intensity of the EQE, with maxima of ca. 50% and 60% for the front and back subcells, respectively, and the spectral coverage up to ca. 950 nm. Up to today, the highest efficiency ever reported for organic solar cells corresponds to an all-solution-processed (apart from the top electrode) tandem device featuring polymer:NFA blends in both front and back cells. In 2018 Meng et al. reported a combination of photoactive materials leading to a significantly higher PCE of 17.4%.[74] With respect to the previous work from reference [72], the single-junction devices of the front and back cells could afford a substantially higher J_{SC}, at the expense of only a modest drop in V_{OC}. One of the main reasons for this simultaneous improvement could derive from the use of the inverted architecture, in which the silver top contact has better reflectivity than aluminum, used in the precedent work (**Figure 11**). In the inverted configuration, the same PBDB-T:F-M single-junction cell featured a higher EQE of 0.80. For the back cell, a ternary blend of PTB7-Th:O6T-4F:$PC_{70}BM$ was adopted, where O6T-4F is a NFA (also known as CO_i8DFIC) with band gap of 1.26 eV. With respect to the binary PTB7-Th:O6T-4F system, the ternary blend has a red-shifted absorption up to 1050 nm ca., maybe induced by a morphological change due to the presence of PCBM. Consequently, its single junction returned an outstanding J_{SC} of 28 mA cm^{-2}. In the tandem, these high and broad EQEs of the corresponding single junctions

permitted to redistribute the amount of light from the solar spectrum between the subcells, leading to a balanced J_{SC} of 14.2 mA cm^{-2} from both of them. This record value of J_{SC} for OPV tandems largely overcompensated the 60 mV loss of V_{OC} with respect to reference [72], holding at the same time a FF of 0.74.

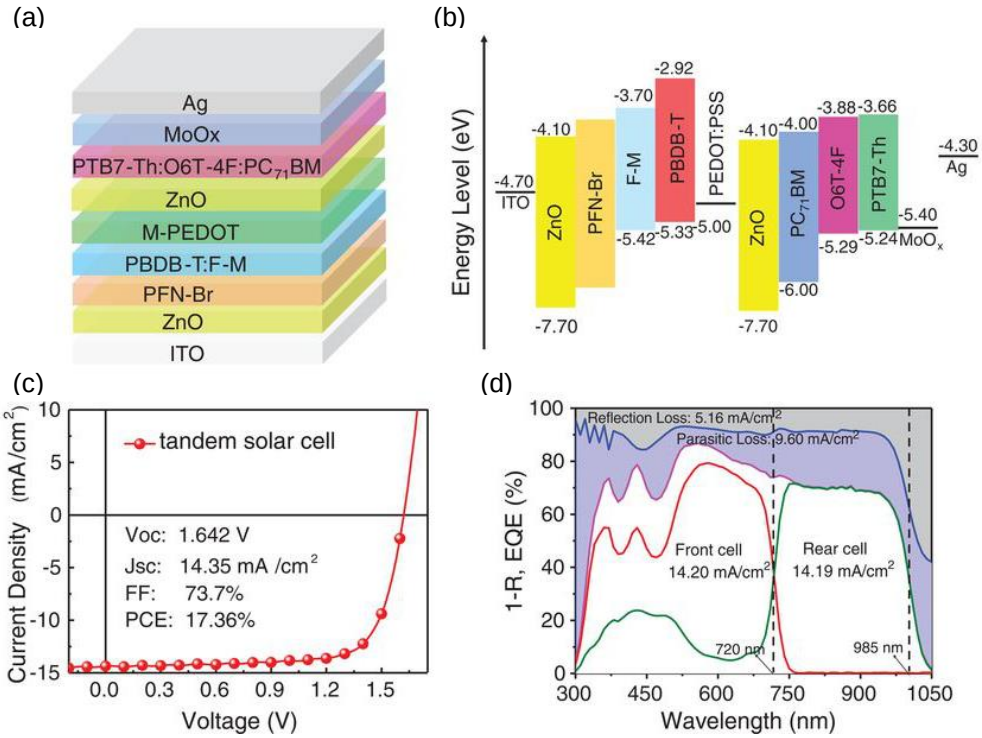

Figure 11. Record efficiency (17.4%) tandem organic solar cell. Device stack (a), energy levels diagram (b), *J*−*V* characteristic curve with device metrics (c), and EQE of the subcells measured under relevant light and voltage bias conditions (d). From Ref. 74. Reprinted with permission from AAAS.

Very few examples of small-molecular donor materials blended with PCBM in combination with a tandem cell configuration have been reported in the period considered. In 2015 Kim et al. optimized the performance of a benzodithiophene-diketopyrrolopyrrole based small molecule by introducing trifluoromethylbenzene end groups, resulting in BDTT-(DPP)$_2$-CF$_3$.[75] This molecule has a band gap of 1.55 eV and returned a PCE of 6% at best in single junction, blended with PC$_{70}$BM (V_{OC} = 0.70 V). This active layer was incorporated as back cell in a tandem solar cell, where P3HT:ICBA was used in the front cell. The tandem

showed a V_{OC} of 1.53 V, with a FF of 0.68 and J_{SC} of 8.0 mA cm^{-2}, resulting in a PCE of 8.11%. The main limit to the efficiency of the tandem was the low EQE of the back cell (max. 60%). In 2016 Zhang et al. reported the application of a high performing, wide band gap, small molecular donor material, named DR3TSBDT in tandem cells.[76] This molecule has a band gap of 1.74 eV and when blended with $PC_{70}BM$ it showed very interesting properties in single-junction cells: V_{OC} = 0.91 V, J_{SC} = 14.3 mA cm^{-2} and FF = 0.71 (best PCE of 9.5%). This makes it interesting as front cell for tandem solar cells. As back cell, the authors chose PTB7-Th:$PC_{70}BM$ (V_{OC} of 0.80 V). The tandem yielded a best PCE of 11.5%, corresponding to a FF of 0.65, V_{OC} of 1.69 V and J_{SC} of 10.51 mA cm^{-2}. The spectral overlap with the PTB7-Th cell leaves room for improvement, provided a lower band gap back cell is adopted instead. In 2017 the same DR3TSBDT:$PC_{70}BM$ active layer was integrated in a tandem with another small molecular donor:$PC_{60}BM$ blend by Li et al.[77] The latter was a zinc porphyrin based molecule, DPPEZnP-TBO, with a low band gap of 1.37 eV. Thanks to a low minimum photon energy loss, DPPEZnP-TBO:$PC_{60}BM$ had a V_{OC} of 0.73 V in single-junction cells, and EQE up to ca. 900 nm (maximum of ca. 60%). By combining the latter in a tandem as back cell, with DR3TSBDT:$PC_{70}BM$ as front cell, a best efficiency of 12.5% was demonstrated, the highest for solution-processed small-molecular donor systems.

It is certainly also worth to mention the first example of an all-polymer (i.e. polymer donor and polymer acceptor) tandem solar cell, reported in 2016 by Yuan et al.[78] P2F-DO and N2200 were blended as donor and acceptor polymers, respectively. The first one has a band gap of 1.60 eV while the second one has a band gap of 1.45 eV. The optimal single-junction cell absorbed up to ca. 800 nm and had a V_{OC} of 0.80 V. The PCE was limited to 4.7% because of the low EQE (ca. 40%). To improve the light absorption, a homo tandem with this materials was manufactured. This one showed the same FF (0.58) and almost twice the V_{OC} (1.58 V) of the single-junction device. Recently Yuan et al. reported an improved all-polymer tandem, using complementary absorber layers.[79] For the front cell, a combination of polymers with similar wide band gap was used: the BDT-based PTP8 (band gap of 1.80 eV) as electron-donating species, and P(NDI2HD-T) (band gap of 1.85 eV) as electron-accepting component. For the back cell, a newly synthesized ternary conjugated polymer, PBFSF (band gap of 1.55 eV) was used as donor, while N2200 was the acceptor. The J_{SC} of the tandem was almost 8 mA cm^{-2} and the V_{OC} was 1.77 V, together with a FF of 0.59. The PCE was then 8.3%. A new record PCE for all-polymer tandem cells was established in 2018 by Zhang et al.[14] Again a homo tandem was fabricated, adopting PTzBI-Si as donor and N2200 as acceptor. The first one has a band gap of 1.78 eV, and when blended with N2200 it returned a V_{OC} of 0.86 V in a single-junction configuration, together with a remarkable FF above 0.7, and J_{SC} of 15.4 mA cm^{-2}. The tandem cell was characterized by an improved overall absorption, according to the J_{SC} (8.6 mA cm^{-2}) of the current-limiting subcell, while V_{OC} and FF were in agreement with the expectation from the single-junction cell, affording a PCE of 11%.

2.2.5 Upscaling

For the commercial success of solution-processed tandem organic solar cells, it is important to further develop manufacturing techniques and device configurations that allow for large area and roll-to-roll production. Many reported high-efficiency tandem solar cells require the processing of some layers, especially the photoactive ones, in an inert atmosphere environment. This constraint severely limits the large-scale production. In 2015, Li and Brabec reported air-processed tandem solar cells with efficiency exceeding 10%.[80] Not only the ZnO, PEDOT:PSS and PEI charge transport and interconnecting layers were deposited in ambient air by blade coating, but also the photoactive layers. For the front cell a commercial polymer (GEN-2) blended with $PC_{60}BM$ was adopted, while for the back cell, the well-known PTB7-Th:$PC_{70}BM$ was used. In their work, the authors pointed out the critical drop in performance of the back cell due to the manufacturing in ambient air. A solvent treatment with ethanol was observed to recover the performance, which they speculate could remove residual diiodooctane, used as co-solvent for the active layer.

Another important factor to scale the technology up is the achievement of good efficiency on large area devices. Tandem modules of 1.3 and 2.1 cm^2 with PCEs of 5.2% and 4.7% were reported in 2015 by Hanisch et al.[81] In the two cases, 3 and 5 cells were connected in series, respectively. Also in this work, all the layers but the electrodes were deposited in ambient air by doctor blade coating, a technique in which the drying is close to slot-die coating. For the active layers, they used PCDTBT and Si-PCPDTBT (also known as PSBTBT) for the front and back subcells, respectively, and $PC_{70}BM$ as acceptor. For the ICL, ZnO nanoparticles and pH-neutral PEDOT:PSS/Nafion were adopted. A combination of laser and mechanical scribing was used for the patterning at the lines interconnecting the cells. Although the series resistance of the electrodes increases with the size of the cell, the shunt resistance can benefit from the increased number of layers in a tandem, with respect to a single-junction structure, as demonstrated in 2017 by Mao et al.[82] In their work they created single-junction and tandem solar cells with size of 0.73 and 1 cm^2, respectively. They intentionally created ca. 1 mm^2-size defects either in the front cell or the interconnecting layer. Consequently, they detected only a modest drop in performance for the tandem, while the single-junction cell underwent a more dramatic loss in performance. On a flexible polyethersulfone (PES) substrate, they built a 10.5 cm^2-size tandem cell, which afforded an efficiency of 6.5%, fairly close to the PCE of 7.7% of the small size reference tandem (0.05 cm^2). The PES substrate was coated with evaporated silver, followed by a thin layer of PEI. P3HT:ICBA and PTB7-Th:$PC_{60}BM$ were used as active layers for the front and back subcells and modified PEDOT:PSS/PEI formed the ICL. PEDOT:PSS (modified PH1000) was also used as top electrode, followed by evaporation of silver grid lines with 5% shadowing loss. All the non-metallic layers were deposited by spin-coating. The optimization of the front and back cell layer thickness can be done either via opto(-electrical) modeling or experimentally, by realizing multiple tandem cells with different thickness of the active layers. In 2018 Glaser

et al. proposed a simple method to optimize the time consuming experimental screening of the optimal thicknesses of the subcells.[83] To do so they manufactured tandem solar cells on a single 4 × 4 cm^2 substrate by blade coating technique. PTB7:$PC_{70}BM$ was used as active layer for both the front and back subcells. For the front cell, they created a wedge-shape thickness profile in one direction. The substrate was then rotated by 90 ° and the back cell deposited with a similar thickness wedge. In this way a grid of different thickness combinations for the front and back subcells was determined. The substrate was illuminated through a small aperture, which was moved along a grid of positions to map the photocurrent. Upscaling one specific combination of thicknesses to a 4-cells-module of 24 cm^2 afforded a PCE of 5.2%, with geometric fill factor of 84%.

Indium-doped tin oxide is undoubtedly the most used and best performing transparent electrode for organic solar cells. Unfortunately, the coating of this material requires low-throughput vacuum-based techniques, such as sputtering. In addition, its application on flexible substrates is limited by its brittleness. On top of this, the availability and in turn the price of indium significantly raise the production costs. In this sense, some works explored the potential of using silver instead of ITO, deposited as a semitransparent grid or as a nanowire layer.[82,84,85] Guo et al. in 2015 demonstrated a fully solution-processed tandem polymer solar cell using silver nanowires from a commercially available dispersion for the semitransparent contact.[85] Interestingly, also the opaque contact was deposited from a commercially available silver ink, which was cured at relatively low temperature (130 °C), compatible with flexible substrates. It is worth to mention this since the reference opaque contact in almost every work on OPV consists of a metal deposited by thermal evaporation in high vacuum. By depositing all the layers by doctor-blade coating in ambient conditions, the authors presented a 5.81% tandem on glass and a 4.85% tandem on flexible polyethylene terephthalate substrates. The commercially available GEN-2 and PDPP5T-2 blended with PCBM were used a front and back subcells, respectively. The ICL was made of zinc oxide nanoparticles and pH-neutral PEDOT:PSS. Another interesting semitransparent electrode from solution is the highly conductive formulation of PEDOT:PSS. In 2015 Tong et al. provided an example where they used such a highly conductive PEDOT:PSS (PH1000) as a transparent top electrode for tandem solar cells, deposited by film transfer.[86] Their tandem device consisted of P3HT:ICBA as both front and back subcells and PH1000/PEI as ICL. For the top electrode, first a piece of polydimethylsiloxane (PDMS) was attached on a glass substrate. Before depositing a modified PH1000 dispersion, the PDMS surface was treated with oxygen plasma to improve the wetting. Once formed, the layer of PEDOT:PSS was dried at room temperature. Then the surface of top cell was also treated with oxygen plasma for 5 seconds. The PDMS/PEDOT:PSS was applied on this active layer, with the PEDOT:PSS in contact with it, and the PDMS stamp was peeled off. In 2016 the same group reported the use of transfer printed PEDOT:PSS top electrode on a fully solution-processed tandem solar cell on flexible PES substrate.[87] A modified PH1000 dispersion was used as

bottom electrode, patterned by selective surface treatment of the substrate with oxygen plasma. To build an inverted tandem, the PH1000 surface was modified with PEI, for the bottom electrode. P3HT:ICBA and PTB7-Th:$PC_{70}BM$ were used as front and back cell active layers, and a modified PEDOT:PSS (mixture of Al4083 and PH1000) followed by PEI was used as ICL. The PCE reached by the device was 6.1%, limited mainly in current because of the absence of a reflecting electrode.

Related to future technology development, a few publications evaluated the stability of tandem solar cells.[88,89] Few more studies focused on the process control of the manufacturing by imaging/probing techniques.[90,91,92]

Table 1. Overview of the relevant data concerning solution-processed organic tandem solar cells covered by this chapter.

Front subcell			Back subcell			Tandem		Interconnecting layer		Ref
Material	E_g [a] [eV]	V_{OC} [V]	Material	E_g [a] [eV]	V_{OC} [V]	Type[b]	PCE [%]	Contact to front subcell	Contact to back subcell	
PTB7-Th:$PC_{70}BM$	1.58	0.78	PTB7-Th:$PC_{70}BM$	1.58	0.78	C	11.3	ZnO np	CPEPh-Na	9
DR3TSBDT:$PC_{70}BM$	1.74	0.90	DPPEZnP-TBO:$PC_{60}BM$	1.37	0.73	C	12.5	ZnO np	pH-neutral PEDOT:PSS	77
PBDB-T:ITCC-M	1.68	1.00	PBDTTT-E-T:IEICO	1.34	0.82	C	13.8	ZnO np	PCP-Na	10
PDCBT:$PC_{70}BM$	1.90	0.80	PBDT-TS1:$PC_{60}BM$	1.51	0.80	I	10.2	MoO_3/Ag	ZnO np/PFN	56
GEN-2:PCBM	1.76	0.78	PTB7-Th:$PC_{70}BM$	1.58	0.78	I	10.0	PEDOT:PSS(HIL3.3)	ZnO np/PEI	80
PBDD4T-2F:$PC_{60}BM$	1.78	0.90	PDPP4T-2F:$PC_{70}BM$	1.37	0.79	I	11.6	MoO_3/Ag	PFN	57
PThBDTP:$PC_{70}BM$	1.86	0.95	DPPEZnP-TEH:$PC_{60}BM$	1.37	0.78	C	11.4	PF3N-2TNDI/Ag	PEDOT:PSS	12
PIDT-PhanQ:$PC_{70}BM$	1.67	0.86	PTB7:$PC_{70}BM$	1.61	0.73	I	11.0	MoO_3/Ag	PFN	15
PTB7-Th:$PC_{70}BM$	1.58	0.79	PTB7-Th:$PC_{70}BM$	1.58	0.79	I	10.8	PEDOT:PSS(PH1000,surfactant)	PEI	35
BDT-FBT-2T:$PC_{70}BM$	1.72	0.84	PMDPP3T:$PC_{60}BM$	1.30	0.61	C	8.9	ZnO np	pH-neutral PEDOT:PSS	59
P3HT:$PC_{60}BM$	1.90	0.58	PDPP5T-2:$PC_{70}BM$	1.46	0.56	I	4.4	PEDOT:PSS	ZnO np\$Ba(OH)_2$	89
P3HT:SF$(DPPB)_4$	1.77	1.11	PTB7-Th:IEIC	1.50	0.95	I	8.5	MoO_3/Ag	PFN	67
GEN-2:$PC_{60}BM$	1.75	0.75	PDPP5T-2:$PC_{60}BM$	1.46	0.56	C	6.5	ZnO np	pH-neutral PEDOT:PSS	85
PBDD4T-2F:$PC_{70}BM$	1.78	0.90	PBDTTT-E-T:IEICO	1.34	0.81	C	12.8	ZnO np	PCP-Na	69
SMPV1:$PC_{70}BM$	1.63	0.88	PTTBDT-FTT:$PC_{70}BM$	1.55	0.74	C	8.5	ZnO	PEDOT:PSS	93
P3HT:ICBA	1.90	0.77	PTB7-Th:$PC_{70}BM$	1.58	0.77	I	9.0	PEDOT:PSS(Al4083:PH1000)	PEIE	87
DR3TSBDT:$PC_{70}BM$	1.74	0.91	PTB7-Th:$PC_{70}BM$	1.58	0.80	C	11.5	ZnO np	pH-neutral PEDOT:PSS	76
PIDTBTO-TT:$PC_{70}BM$	1.87	0.91	PTB7-Th:$PC_{70}BM$	1.58	0.80	C	11.2	PDIN:PFN/Al	MoO_3	55
P3TEA:SF-PDI_2	1.72	1.11	P3TEA:SF-PDI_2	1.72	1.11	I	10.8	PEDOT:PSS (HTL)	ZnO sol-gel	38

Front subcell			Back subcell			Tandem		Interconnecting layer		Ref
Material	E_g [a] [eV]	V_{OC} [V]	Material	E_g [a] [eV]	V_{OC} [V]	Type[b]	PCE [%]	Contact to front subcell	Contact to back subcell	
P3HT:$PC_{60}BM$	1.90	0.60	P3HT:$PC_{60}BM$	1.90	0.60	I	3.6	PEDOT:PSS(CPP105D)	AZO sol-gel/PEIE	24
P3HT:ICBA	1.90	0.83	PSBTBT:$PC_{70}BM$	1.50	0.63	I	9.3	PEDOT:PSS(surfactant)	TBAI-doped C-$PCBN_3$	32
P2F-DO:N2200	1.45	0.80	P2F-DO:N2200	1.45	0.80	I	6.7	PEDOT:PSS(PH500 mod)	ZnO np	78
PBDTTT-C-T:$PC_{70}BM$	1.58	0.77	PBDTTT-C-T:$PC_{70}BM$	1.58	0.77	I	8.1	MoO_3 bronze/PF6N25Py	TiO_2 np	17
PBDB-T:ITIC	1.59	0.92	PTB7-Th:4TIC	1.40	0.78	I	12.6	MoO_3/Ag	PFN	68
P3HT:ICBA	1.90	0.83	BDTT-$(DPP)_2$-CF_3: $PC_{70}BM$	1.55	0.70	I	8.3	PEDOT:PSS(surfactant)	PEIE	75
PBDTTPD:$PC_{70}BM$	1.85	0.92	PBDTTPD:$PC_{70}BM$	1.85	0.92	C	8.4	ZnO np/Al	MoO_3	94
PTB7:$PC_{70}BM$	1.61	0.73	PTB7:$PC_{70}BM$	1.61	0.73	I	8.1	PEDOT:PSS(HTL mod)	ZnO np	95
PTB7:$PC_{70}BM$	1.61	0.74	PTB7:$PC_{70}BM$	1.61	0.72	I	8.2	MoO_3/Ag	PFN	16
PTB7-Th:4TIC	1.40	0.76	PTB7-Th:4TIC	1.40	0.76	I/P	11.1	PEDOT:PSS/Ag	Au/MoO_3	46
PTZ1:$PC_{70}BM$	1.97	0.94	PBDTTT-C-T:$PC_{70}BM$	1.58	0.74	I	10.3	MoO_3/Ag	PFN	60
P3HT:ICBA	1.90	0.84	PBDTTT-C-T:$PC_{70}BM$	1.58	0.77	I	8.2	PEDOT:PSS(surfactant)	a-Zr(acac)/PF6N25Py	27
P3HT:ICBA	1.90	0.79	P3HT:ICBA	1.90	0.83	I	3.6	PEDOT:PSS(PH1000)	PEI	86
P3HT:ICBA	1.90	n.a. [c]	PTB7-Th:$PC_{60}BM$	1.58	n.a. [c]	I	7.7	PEDOT:PSS(Al4083:PH1000)	PEI	82
PTB7-Th:$PC_{70}BM$	1.58	0.77	PTB7-Th:$PC_{70}BM$	1.58	0.77	C	10.2	ZnO np	PEDOT-SO_3Na/p-PFP-O	11
PTB7-Th:$PC_{70}BM$	1.58	0.76	PTB7-Th:$PC_{70}BM$	1.58	0.76	I	9.1	PEDOT:PSS(surfactant)	PEI	36
PIDTT-DFQT:$PC_{70}BM$	n.a. [c]	0.91	PCPDT-FBT:$PC_{70}BM$	1.44	0.74	C/T	7.4	C_{60}-SAM/ZnO sol-gel	PEDOT:PSS(PH1000/mod)	48
PBDTT-DPP:$PC_{60}BM$	1.44	0.73	TAPC:C_{70}	1.66	0.84	I/P	5.6	MoO_3/Ag	MoO_3	45
PThBDTP:$PC_{70}BM$	1.86	0.92	PTB7-Th:$PC_{60}BM$	1.58	0.78	I	8.7	PEDOT:PSS:MoO_3 np	ZnO np/PEI	25
HBG1:$PC_{60}BM$	1.80	0.77	PMDPP3T:$PC_{60}BM$	1.30	0.58	I	7.8	PEDOT:PSS(surfactant)	ZnO np	39

Front subcell			Back subcell			Tandem		Interconnecting layer		Ref
Material	*Eg* [a] [eV]	V_{OC} [V]	Material	*Eg* [a] [eV]	V_{OC} [V]	Type[b]	PCE [%]	Contact to front subcell	Contact to back subcell	
PCDTBT:$PC_{70}BM$	1.88	0.88	PSBTBT:$PC_{70}BM$	1.45	0.63	C	6.9	ZnO np	pH-neutral PEDOT:PSS\ Nafion	81
PTPTIBDT-OD:$PC_{70}BM$	2.04	0.90	PTPTIBDT-OD:$PC_{70}BM$	2.04	0.90	C	5.3	ZnO np	pH-neutral PEDOT:PSS\MoO_3	96
PCDTBT:$PC_{70}BM$	1.88	0.88	PBDTT-DPP:$PC_{70}BM$	1.44	0.74	I	9.0	PEDOT:PSS:GO	LZO sol-gel	33
P3HT:$PC_{70}BM$	1.90	0.62	PTB7:$PC_{70}BM$	1.61	0.67	I/P	3.7	PEDOT:PSS(surfactant)/Au	PEDOT:PSS	97
PTB7:$PC_{70}BM$	1.61	0.70	PTB7:$PC_{70}BM$	1.61	0.73	I/4T	6.1	ZnO sol-gel	ZnO sol-gel	47
PTB7-Th:$PC_{70}BM$	1.58	0.78	PTB7-Th:$PC_{70}BM$	1.58	0.78	I	8.1	MoO_3/Ag	TIPD	29
P1:$PC_{70}BM$	1.82	0.91	PTB7-Th:$PC_{70}BM$	1.58	0.81	C	11.4	ZnO np	pH-neutral PEDOT:PSS	61
PTB7:$PC_{70}BM$	1.61	n.a. [c]	PTB7:$PC_{70}BM$	1.61	n.a. [c]	I	7.0	PEDOT:PSS(FHC/HTL mod)	ZnO np	50
P3HT:ICBA	1.90	0.86	PTB7-Th:$PC_{70}BM$	1.58	0.77	I	8.3	PEDOT:PSS(Al4083:PH1000)	PEIE	52
PTB7:$PC_{70}BM$	1.61	0.76	PTB7-Th:$PC_{70}BM$	1.58	0.81	I	10.8	MoO_3/Ag	PFN	98
P3HT:$PC_{60}BM$	1.90	0.59	P3HT:$PC_{60}BM$	1.90	0.59	C	2.9	TiO_2 sol-gel	PEDOT:PSS:Ag np	26
PBDB-T:$PC_{70}BM$	1.80	0.80	PTB7-Th:IEICO-4F	1.24	0.71	I	9.7	MoO_3/Ag	PFN-Br	71
DTDCPB:C_{70}	1.68	0.90	PTB7-Th:BT-CIC	1.38	0.69	C	15.0	BPhen:C_{60}/Ag	PEDOT:PSS	44
PCDTBT:$PC_{70}BM$	1.88	0.85	PDPP3T:$PC_{60}BM$	1.33	0.63	I	8.0	MoO_3	SnO_X (ALD)	20
PTB7:$PC_{70}BM$	1.61	0.72	PDPP4T-2F:$PC_{70}BM$	1.37	0.76	I	10.3	PMA/pH-neutral PEDOT:PSS(mod)	ZnO np	30
PTB7:$PC_{70}BM$	1.61	0.75	PDPP4T-2F:$PC_{70}BM$	1.37	0.76	C	10.5	ZnO np	pH-neutral PEDOT:PSS(mod)/PMA	30
P3HT:$PC_{60}BM$	1.90	0.59	P3HT:$PC_{60}BM$	1.90	0.59	I	3.0	PEDOT:PSS(surfactant)/MoO_3/ Au/Al	ZnO sol-gel	99
PBDTTBO:$PC_{70}BM$	1.80	0.86	PDTP-DFBT:$PC_{70}BM$	1.30	0.66	I	10.1	MoO_3/PEDOT:PSS(mod)	Zr-acac	28
PSTzBI-EHp:$PC_{70}BM$	n.a. [c]	0.93	PBDTTT-E-T:IEICO	1.34	0.82	C	12.6	PF3N-2TNDI:PEI	PEDOT:PSS	13

Front subcell			Back subcell			Tandem		Interconnecting layer		Ref
Material	*E*g [a] [eV]	V_{OC} [V]	Material	*E*g [a] [eV]	V_{OC} [V]	Type[b]	PCE [%]	Contact to front subcell	Contact to back subcell	
PTB7:$PC_{70}BM$	1.61	0.74	PTB7:$PC_{70}BM$	1.61	0.74	I	7.4	PEDOT(CPP105D/HTL mod)	ZnO np	83
PBDB-T:F-M	1.65	0.98	PTB7-Th:NOBDT	1.39	0.77	C	14.1	ZnO np	pH-neutral PEDOT:PSS	72
PTB7-Th:$PC_{70}BM$	1.58	0.77	PTB7-Th:$PC_{70}BM$	1.58	0.77	I	12.1	PEDOT:PSS(surfactant)	CQD:PEI	34
PTB7-Th:$PC_{70}BM$	1.58	0.78	PTB7-Th:$PC_{70}BM$	1.58	0.78	C	9.5	ZnO np	pH-neutral PEDOT:PSS	49
P3HT:$PC_{60}BM$	1.90	0.61	P3HT:$PC_{60}BM$	1.90	0.62	I	3.5	PEDOT:PSS(surfactant)/MoO_3/ Au/Al	ZnO sol-gel	100
PCDTBT:$PC_{60}BM$	1.88	0.90	PDPP5T-2:$PC_{70}BM$	1.46	0.55	I	3.5	MoO_3/PEDOT:PSS	PEI	101
TAPC:C_{70}	1.66	0.89	PCPDTBT:$PC_{70}BM$	1.38	0.59	C	6.3	PTCBI:C_{70}/PTCBI/Ag	HAT-CN	42
J52-2F:IT-M	1.60	0.95	PTB7-Th:IEICO-4F	1.24	0.71	C	14.9	ZnO np	PCP-Na	70
PBDB-T:F-M	1.65	0.94	PTB7-Th:O6T-4F: $PC_{70}BM$	1.26	0.69	I	17.4	PEDOT:PSS(surfactant)	ZnO np	74
PBDB-T:YITI-2F	1.64	0.93	PTB7-Th:ATT-2	1.32	0.72	C	11.9	ZnO np	pH-neutral PEDOT:PSS	73
PTP8:P(NDI2HD-T)	1.80	0.97	PBFSF:N2200	1.45	0.82	I	8.3	MoO_3/Ag	ZnO np	79
P3HT:$PC_{60}BM$	1.90	0.60	PCPDTBT:$PC_{70}BM$	1.38	0.60	C	5.7	BCP:Ag/Ag	HAT-CN	43
PTzBI-Si:N2200	1.45	0.86	PTzBI-Si:N2200	1.45	0.86	C	11.2	PF3N-2TNDI:PEI	PEDOT:PSS	14
PTB7-Th:$PC_{70}BM$	1.58	0.79	PMDPP3T:$PC_{60}BM$	1.30	0.61	I	8.7	PEDOT:PSS	ZnO np	40
J71:ITIC	1.59	0.93	PMDPP3T:$PC_{60}BM$	1.30	0.60	C	10.2	SnO_2 np	PEDOT:PSS	23
J71:ITIC	1.59	0.92	PMDPP3T:$PC_{60}BM$	1.30	0.61	I	10.4	PEDOT:PSS	SnO_2 np	23

[a] *E*g is the lowest optical band gap of the materials blended in the active layer, with exception of fullerene derivatives, for which it was omitted. [b] C = conventional structure, I = inverted structure, P = parallel connection, 4T = four-terminal connection, T = illuminated from the top. [c] not available.

2.3 Three- and four-fold junction solar cells

On the theoretical level, increasing the number of junctions in a many-fold solar cell would allow to progressively increase the efficiency.[102] In the practice this idea is very difficult to pursue, especially when the manufacturing is performed via solutions. Developing highly performing active materials with complementary absorption also poses enormous limits to its practical realization. In the period 2015-2018 only few triple-junction solar cells from solution processing have been reported, mainly those presented in Chapter 3.[40]

As mentioned in Chapter 1, the highest efficiency published until the end of 2014 for all-solution-processed triple-junction solar cells was 11.6%, by Chen et al.[103] In 2015 bin Mohd Yusoff et al. developed another triple cell, aiming at achieving a higher efficiency.[104] In their report, PSEHTT (band gap of 1.82 eV) blended with ICBA was used as wide band gap front cell, while PTB7 (band gap of 1.61 eV) and PMDPP3T (band gap of 1.30 eV) were adopted as middle and low band gap polymers for the middle and back subcells, respectively, both blended with $PC_{70}BM$. The device structure was inverted, and the interconnection of the subcells was obtained by means of a stack made of pH-neutral PEDOT:PSS, followed by lithium-doped zinc oxide (LZO) from a sol-gel route and a self-assembled monolayer of C_{60}, also from solution. The measurement of their triple cell returned a V_{OC} of 2.24 V, J_{SC} = 7.83 mA cm^{-2} and FF of 0.68, pointing towards a PCE of 11.8%. Regrettably, the characterization of this triple cell is not completely consistent, because the summed EQE of the subcells exceeds 100%. In 2016 Gao et al. reported both double- and triple-junction solar cells using PBDTTPD:$PC_{70}BM$ as absorber material for all the subcells.[94] The aim was to use these cells for photoelectrochemical water splitting. The homo tandem and triple can potentially not only afford the high photovoltage required, but they can also increase the efficiency by increasing the light absorption, which was limited in their optimal single junction. They fabricated the multi-junction cells with a conventional structure, with a solution-processed zinc oxide nanoparticles layer, followed by thermally evaporated Al and MoO_3 as ICL. The bottom contact was ITO/PEDOT:PSS and the top contact was Ca/Al. The triple featured a V_{OC} of 2.75 V, in perfect agreement with the V_{OC} of 0.92 V (at best) of the single junction, and a FF of 0.68. With respect to the tandem cell, the efficiency of the triple-junction cells was lower (PCE of 8.35% for the tandem and of 7.42% for the triple), likely due to the fact that the tandem already afforded a nearly complete absorption of light. Two additional examples about the use of triple-junction polymer solar cells for water splitting will be discussed in Section 2.6.[105,106] The results reported in Chapter 3 and published in 2018[40] show three triple-junction solar cells fabricated using the same PEDOT:PSS/zinc oxide ICL, also discussed in Section 2.2.2. Briefly, the commercial PEDOT:PSS dispersion was diluted with 1-propanol and deposited in inert atmosphere on one active layer, a film of ZnO nanoparticles was stacked on top of it by processing from isoamyl alcohol. These devices were made with an inverted device structure, using sol-gel zinc oxide on the ITO bottom

contact and evaporated molybdenum oxide/silver as top contact (**Figure 12**). A first device used PCDTBT:$PC_{70}BM$, PDPPTPT:$PC_{60}BM$ and PDPP5T:$PC_{60}BM$ for the front, middle and back subcells, respectively. These absorbers have different and complementary band gap of, in order, 1.88, 1.53 eV and 1.46 eV. The triple junction featured a V_{OC} of 2.26 V, perfectly matched to the sum of the single-junction cells: 0.88, 0.79 and 0.57 V, in the stack. A second device with PDCBT:$PC_{60}BM$ (front cell), PDPPTPT:$PC_{70}BM$ (middle cell) and PMDPP3T:$PC_{60}BM$ (back cell) was fabricated. PDCBT and PMDPP3T are better performing materials with band gaps of 1.90 and 1.30 eV, respectively. The band gap of 1.30 eV of PMDPP3T created a red-shifted absorption compared to PDPP5T. The use of $PC_{60}BM$ in the front and back subcells and of $PC_{70}BM$ in the middle cell was aimed at improving the light absorption by the middle cell, which is usually penalized in the triple configuration. In fact the front cell can absorb light at its first pass and the back cell can benefit from the reflection from the metal back contact. For this triple, the thickness of the active layers was optimized via opto-electrical modeling. The optimal device returned a PCE of 8.7%, with a small loss of V_{OC} (from 2.26 V expected to 2.20 V), and FF of 0.66. Despite the measures to increase the current of the middle cell, the EQE was still lagging behind, resulting in a J_{SC} of 6.0 mA cm^{-2} (integrated from its EQE). By changing the middle band gap (1.58 eV) material to PTB7-Th instead of PDPPTPT, the necessary improvement in EQE was obtained, pushing the J_{SC} up to 6.9 mA cm^{-2}. The FF was 0.68 and the V_{OC} was 2.15 V, giving an overall PCE of 10%.

In Chapter 5 and in reference [41], the first example of a solution-processed quadruple-junction solar cell with four complementary absorber layers is reported. This complex device was manufactured like the aforementioned triple-junction cell with PDCBT, PTB7-Th and PMDPP3T, by adding another back cell with an ultra-low band gap (1.1 eV): PDPPSDTPS:$PC_{60}BM$. By doing so the spectral coverage was extended up to 1150 nm ca. (**Figure 13**). The diluted PEDOT:PSS/zinc oxide nanoparticles recombination layer proved to work efficiently also for this complex stack, made out of 14 functional layers, of which 11 are deposited sequentially from solutions. The V_{OC} (2.45 V) and J_{SC} (5.23 mA cm^{-2}) were perfectly matched to the expected values from modeling, and the FF was close to the expected one (0.59 instead of 0.63, respectively), corresponding to a PCE of 7.6%. The EQE spectrum of each subcell individually was accurately measured using representative light and voltage bias conditions, returning a general very good agreement with the modeled spectra. From an analysis of the optical losses, it emerged that the efficiency was mainly limited by bimolecular recombination in OPV materials, which limits the use of thick active layers to absorb more light.

An overview of the relevant features of the three- and four-fold junction solar cells published in the covered period is collected in **Table 2**.

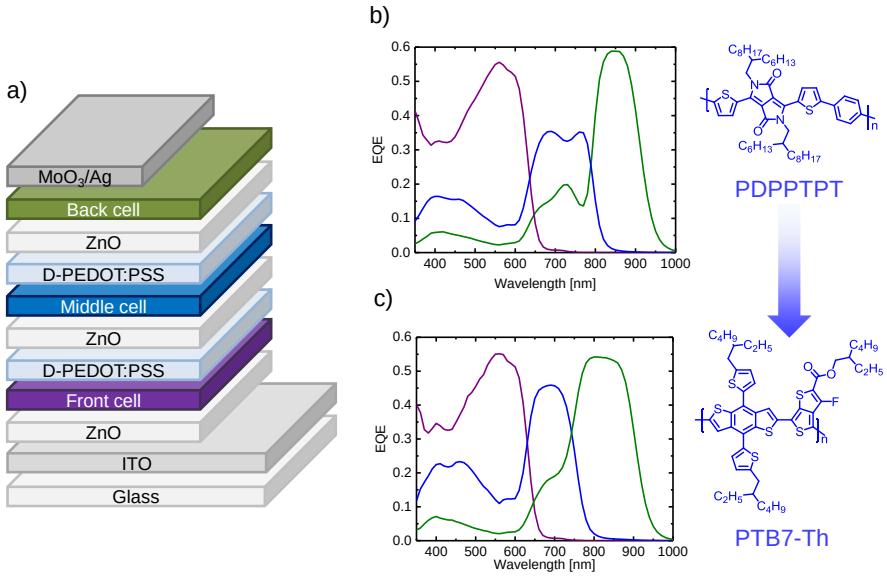

Figure 12. Device structure of a triple-junction solar cell (a), EQE spectra of triples with PDCBT and PMDPP3T front and back cells, with PDPPTPT (b) or PTB7-Th (c) as middle cell. Chemical formulas of the middle cell polymers are reported.

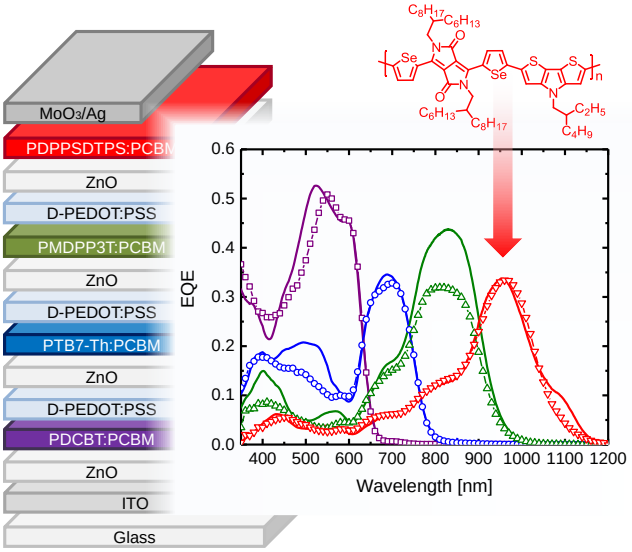

Figure 13. Quadruple-junction polymer solar cell with four complementary absorber layers and chemical structure of PDPPSDTPS.

Table 2. Overview of the relevant data concerning solution-processed organic three- and four-fold junction solar cells covered by this chapter.

Cell configuration [a]	*Eg* [b] [eV]	V_{OC} [V]	Type [c]	PCE [%]	Interconnecting layer Front|Back	Ref
PSEHTT:ICBA (1) PTB7:$PC_{70}BM$ (2) PMDPP3T:$PC_{70}BM$ (3)	1.82 1.61 1.30	2.24	3-fold I	11.8	pH-neutral PEDOT:PSS|LZO sol-gel/C_{60}-SAM	104
PCDTBT:$PC_{70}BM$ (1) PMDPP3T:$PC_{60}BM$ (2,3)	1.88 1.30	2.03	3-fold C	6.7	ZnO np|pH-neutral PEDOT:PSS	105
PBDTTPD:$PC_{70}BM$ (1-3)	1.85	2.75	3-fold C	7.4	ZnO np|Al/MoO_3	94
PTB7:$PC_{70}BM$ (1-3)	1.61	2.13	3-fold I	8.7	MoO_3/Ag|PFN	106
PCDTBT:$PC_{70}BM$ (1) PDPPTPT:$PC_{60}BM$ (2) PDPP5T:$PC_{60}BM$ (3)	1.88 1.53 1.46	2.26	3-fold I	6.0	PEDOT:PSS|ZnO np	40
PDCBT:$PC_{60}BM$ (1) PDPPTPT:$PC_{70}BM$ (2) PMDPP3T:$PC_{60}BM$ (3)	1.90 1.53 1.30	2.20	3-fold I	8.7	PEDOT:PSS|ZnO np	40
PDCBT:$PC_{60}BM$ (1) PTB7-Th:$PC_{70}BM$ (2) PMDPP3T:$PC_{60}BM$ (3)	1.90 1.58 1.30	2.15	3-fold I	10.0	PEDOT:PSS|ZnO np	40
PDCBT:$PC_{60}BM$ (1) PTB7-Th:$PC_{70}BM$ (2) PMDPP3T:$PC_{60}BM$ (3) PDPPSDTPS:$PC_{60}BM$ (4)	1.90 1.58 1.30 1.13	2.45	4-fold I	7.6	PEDOT:PSS|ZnO np	41

[a] The numbers in parentheses refer to the subcell number in the stack, with (1) being the front cell. [b] *Eg* is the lowest optical band gap of the materials blended in the active layer, with exception of fullerene derivatives, for which it was omitted. [c] C = conventional structure, I = inverted structure.

2.4 Accurate characterization

The OPV community has been actively putting a tremendous effort to increase the efficiency of solution-processed organic tandem solar cells, as can be argued by reading the previous sections. For a reliable development of this technology, it is important to carefully define suitable characterization methods. In this way a fair and accurate mean of comparison of the different works would be available. These methods should take into account for the peculiarity of organic tandem solar cells, differentiating them from traditional silicon-based solar cells. To this end, in 2015 Timmreck et al. analyzed the characterization practices adopted in literature on OPV tandem cells from January 2009 to September 2014.[107] Their alarming conclusion was that 51% of the published papers provided no EQE measurement of the subcells and no comment on the mismatch factor. 45% of the references reported the EQE measurement for the subcells but provided no comment about the mismatch factor (*M*) or they did not use it at all. Only the remaining 4% performed a characterization according to the standard ASTM E2236. In their correspondence, Timmreck et al. proposed a series of

general rules for characterizing OPV tandem cells. Without going into details, which the reader can find in reference [107], they summarized in four points how the characterization should be performed. First, the bias lights should be selected according to the absorption spectrum of the active layer absorbers, with a special remark for homo-tandem solar cells, for which optical simulations should be involved to ensure constant biasing of one subcell all-over the spectral range of measurement. Second, the necessary voltage bias (V_{bias}) should be determined, according to the expected electric field induced by the application of the light bias. For this, the V_{OC} of the single-junction solar cells can be used as approximation. Third, the spectral response measurement should be performed according to the ASTM E2236 standard test methods, using chopped monochromatic light and a lock-in technique, while applying both light and voltage bias. Fourth, the intensity of a two sources solar simulator should be adjusted to correct for the mismatch of the subcells. Under such a calibrated light source, the *J–V* characteristic can be measured, putting emphasis on the correct determination of the effective area of the solar cell. In addition, the authors recommended a detailed description of all the experimental procedures and setups involved in the characterization.

Herein a similar research as the one of Timmreck et al. was repeated on Web of Science, using the keywords and criteria reported in Section 2.1. From this, the papers considered "highly cited papers" were selected, repeating the research for different time periods: 2015-2018 (i), 2016-2018 (ii), and 2017-2018 (iii). In addition, recently published papers claiming high efficiency tandems were included. The research on Web of Science returned 11 articles (13 total) in the period (i), 7 (8 total) in the period (ii) and 5 (6 total) for the period (iii). Two entries in period (i) and one entry in period (ii) and (iii) were excluded, being out of topic. All the entries in list (iii) overlapped with those in list (ii) and similarly for those in list (ii) with the ones in list (i). Two papers recently published[72,74] and one not covered by the keywords[70] were included because of the high efficiencies reported. Among other papers found, not covered by the keywords, one with high number of citations[108] was excluded for the high complexity of the device structure (series/parallel triple-junction cell), and the others were not considered because of a lower number of citations. Some of the characteristics of the EQE measurement there adopted were selected, and are presented in **Table 3**.

Table 3. Literature survey on solution-processed multi-junction organic tandem solar cells in the period: January 2015−August 2018. Please refer to the main text for a detailed description of the criteria.

EQE tandem	Light bias	V_{bias}	δJ_{SC}^{EQE} [%][a)]	Ref.
+ [b)]	−	−	n.a. [c)]	9
+ [b)]	−	−	n.a. [c)]	38
+	+	−	+2.2	12
+	+	−	+3.8	55
+ [d)]	+	−	+4.8	56
+	+	−	+8.7	57
+	+	−	+0.7	69
+	+	n.m. [e)]	+1.5	70
+	+	−	+3.8	72
+	+	−	−0.7	77
+	+	−	n.a. [c)]	80
+ [d)]	+ [f)]	−	+8.3	104
+	+	+ [g)]	+8.7	10
+	+	+	+1.1	74

[a)] Relative deviation of the J_{SC} measured under solar simulator with respect to the J_{SC} from integration of the EQE spectrum of the current-limiting subcell with the reference AM1.5G solar spectrum (J_{SC}^{EQE}). [b)] Homo-tandem. [c)] J_{SC}^{EQE} Not available. [d)] Summed EQE of the subcells exceeds 100% at some wavelengths. [e)] Not mentioned. [f)] No details provided [g)] No explanation of the choice.

From this list of sensible publications it appears that researchers gave greater consideration to the importance of EQE measurement, which was neglected in half of the published papers before the aforementioned correspondence. Although not always described in detail, a light bias is provided in all the references in Table 3. Two cases[9,38] where homo-tandem cells were studied, limit themselves to report the EQE measurement without any bias. Provided that leakage paths in the subcells do no contribute significantly, this should correspond to the lower envelope of the EQEs of the two subcells.[107] For what concerns the application of a voltage bias during the EQE measurement, only reference [10] and [74] report the use of this correction, necessary to not overestimate the efficiency. Although the correspondence by Timmreck et al. recommends to put effort in the determination of the exact effective area, neither of the cited publications in Table 3 mentions this for the EQE measurement. Reference [55] mentions that the size of the beam of the probe light was smaller than the cell area. This might affect the accuracy of the measurement, especially because of the high conductivity of many formulations of PEDOT:PSS, largely used to fabricate tandems.[109,110,111] The overlap of the area of the bottom and top electrodes defines the effective area in the dark. When light shines on the sample, the lateral region around this

intersection photogenerates charges which can be collected by a highly conductive interlayer, leading to overestimation of the real current (the entity depends on the lateral conductivity of the interlayer(s) in question). In addition, the manufacturing of both semitransparent ITO electrode and the metal contact are subject to limited accuracy, possibly leading to substantial deviations in their areas and overlap from the nominal values. Therefore, measuring not only the $J-V$ characteristic but also the EQE (and also for the calibrated reference cell) through an opaque, non-reflecting mask with an accurately determined aperture area represents a good practice to avoid such issue. Only reference [10] and [74] report the mismatch factor of the subcells and only [74] comments on how it was determined. Given the fact that in a series-connected tandem solar cell the current is limited by the subcell generating less current, it is interesting to compare the J_{SC} of the tandem measured under simulated solar radiation (AM1.5G spectrum) with the J_{SC} of the current-limiting subcell ($^{lim}J_{SC}^{EQE}$). The latter can be derived from its corresponding EQE spectrum, integrated with the tabulated reference AM1.5G solar spectrum. In Table 3 the relative deviations between J_{SC} and $^{lim}J_{SC}^{EQE}$ is indicated with δJ_{SC}^{EQE}. Another easy operation for a quick check that gives more information about the EQE measurement consists in adding up the EQEs of the individual subcells. Although this in not always done in this sample of literature, we note that in references [56] and [104] the summed EQE locally exceeds 100%. No comment was given on possible reasons for this remarkable outcome.

The correspondence by Timmreck et al. provided a rigorous method to accurately determine the efficiency of OPV devices. Possibly due to the limited experimental availability and/or the intricate nature of some of the steps enumerated, the application of this vade mecum is never fully rigorously performed (following the sensible sample of the recent literature here considered). Nevertheless, what discussed in this section about the EQE measurement can likely improve the accuracy, without introducing experimental complications. In particular, (1) the usage of the proper voltage bias (or the readily available V_{OC} of the single-junction cells as approximation), (2) the use of a shadow mask with an accurately determined aperture area, (3) the comparison of the J_{SC} of the tandem as measured under simulated solar radiation with the EQE-integrated J_{SC} of the current-limiting subcell, (4) and adding up the EQEs of the subcells over the spectral range of measurement.

Concerning homo-tandem solar cells, Bahro et al. addressed the problem of measuring the individual subcells by using an intermediate electrode in the ICL zone.[95] In their study, they fabricated homo tandems based on PTB7:$PC_{70}BM$ as active layer. A combination of modified PEDOT:PSS and ZnO nanoparticles was involved as ICL. For the creation of the intermediate electrode, another formulation of highly conductive PEDOT:PSS was deposited before the ICL on top of the front cell, and structured laterally to avoid effects due to its high lateral conductivity. The thickness of the PEDOT:PSS bilayer in the three-terminal device was controlled to match the one in the reference two-terminal tandem, without the extra PEDOT:PSS electrode. The authors showed that the ICL based on the extra electrode implied

no difference in the optoelectronic performance of the device. Therefore, the EQE of both front and back subcells could be directly measured, by simply contacting the intermediate electrode.

Chapter 4 covers an accurate characterization protocol for triple-junction polymer solar cells, also published in reference [112]. The triple was the same already presented in Section 2.3 from reference [40], with PDCBT, PTB7-Th and PMDPP3T blended with PCBM as front, middle, and back subcells, respectively. Besides the measurement of its $J-V$ characteristic curve, the focus was given on the EQE measurement of each individual subcell. The latter was isolated and acquired by optically biasing the other two subcells. For the purpose, high power light-emitting diodes with wavelength (in nm) of 530, 730, and 940 nm were used, which matched the absorption spectra of the subcells. By performing optical modeling calculations, the amount of current generated by each subcell under different (combinations of) light bias was predicted. Due to the partial spectral overlap, this was aimed at ensuring with enough confidence that only one subcell is current-limiting over the whole range of wavelengths of the measurement. In this prediction, the different IQEs of the subcells were taken into account. In addition, the predicted light intensity experienced by the subcells under light bias was recreated on single-junction cells representative of the subcells and their $J-V$ characteristic was measured. In this way, the necessary voltage bias correction was determined for each subcell. Without this correction, the EQE of the subcells was seen to substantially overestimate the correct EQE. The measured EQEs matched remarkably well the predicted spectra via opto-electrical modeling, validating the whole procedure.

2.5 Unusual device architectures

Besides the series and parallel connected tandem solar cells, few works presented new unusual device architectures. In a series connection the V_{OC}s add up and the current is determined by the current-limiting subcell, while in a parallel connection, the currents add up and the V_{OC} is close to the lowest one of the two subcells (usually the active layer with lowest band gap). Both these factors complicate achieving high PCE values. In 2015 Guo et al. proposed a new concept to alleviate these stringent criteria,[108] by connecting in series two times the low band gap absorber, therefore adding up their V_{OC}s, and connecting this homo tandem in parallel to the wide band gap absorber, which has a higher V_{OC} (**Figure 14**). Going from the bottom to the top, first the low band gap (1.46 eV) homo tandem was realized, using PDPP5T-2:$PC_{60}BM$ in the active layers. The ICL of the tandem consisted of zinc oxide/pH-neutral PEDOT:PSS, which was also used on top of the back cell. Then, silver nanowires were casted on the PEDOT:PSS film to provide the internal contact for the parallel connection. The parallel subcell was fabricated starting from zinc oxide nanoparticles on the silver nanowire layer, followed by the wide band gap top cell of either PCDTBT:$PC_{70}BM$

(band gap = 1.88 eV) or the commercial OPV12:$PC_{60}BM$ (band gap = 1.73 eV), and completed by the MoO_3/Ag top electrode. The V_{OC}s of the PDPP5T-2 single cell and the PCDTBT and OPV12 subcells were: 0.56, 0.82 and 0.77 V, respectively. The bottom homo tandem gave almost twice the V_{OC} of the DPP cell (1.08 V). The series-parallel solar cell demonstrated V_{OC}s of 0.89 and 0.82 V for the PCDTBT- and the OPV12-based devices, respectively. In accordance with the expectations, these values are much higher than the V_{OC} of the DPP single cell and close to the V_{OC} of the wide band gap cells. Moreover, the J_{SC} of the subcells nicely summed up, as expected. The complete stack returned J_{SC}s of 9.67 and 9.55 mA cm^{-2}, with PCDTBT and OPV12, respectively. In both cases the PCE was 5.4%.

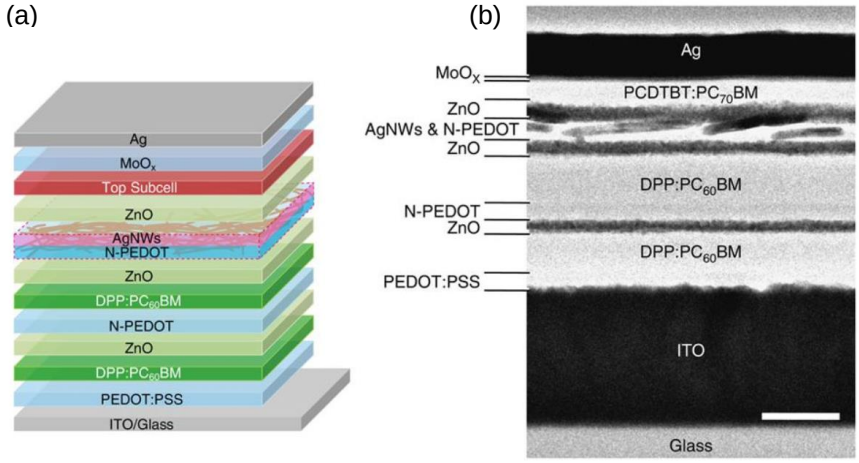

Figure 14. Series/parallel connected triple-junction cell. Device scheme (a) and cross-sectional transmission electron microscopy image (b), for which the scale bar is 200 nm. Please referrer to the man text for a description. Reproduced from Ref. 108 under the CC BY 4.0 License. Copyright 2015 Macmillan Publishers Limited.

2.6 Use of multi-junction polymer solar cells for photoelectrochemical water splitting

In Chapter 1 the concept and working mechanisms of tandem organic solar cells were introduced. The direct conversion of solar energy into readily available electrical energy is pushing the development of devices capable of higher power conversion efficiency (PCE). Another appealing advantage of these devices comes from the possibility to achieve high V_{OC}, to be used for photoelectrochemical water splitting. The standard potential for water splitting is E^0_{H2O} = 1.23 V, which in practice is further increased to 1.4−1.8 V due to

overpotentials for oxygen/hydrogen formation at the electrodes. Provided that enough operating voltage is delivered by the solar cell, there is a direct proportionality between photocurrent and hydrogen evolution. Assuming 100% Faradaic efficiency, the solar-to-hydrogen evolution efficiency (η_{STH}) follows the relation $\eta_{STH} = J_{op} \times E^0_{H2O} / P_{in}$, where J_{op} is the operating current density delivered by the cell during water splitting. Preferably the cell and electrode materials are designed in such a way that the cell operates in its maximum power point, i.e. $J_{op} = J_{max}$ and $V_{op} = V_{max}$, in which case η_{STH} = PCE × (E^0_{H2O} / V_{op}). In 2013 Esiner et al. demonstrated for the first time the possibility of using triple-junction solar cells for water splitting.[113] In 2015 Esiner et al. used a more efficient triple-junction solar cell for photoelectrochemical water splitting, comprising PCDTBT:$PC_{70}BM$ as wide band gap front cell and PMDPP3T:$PC_{60}BM$ as both middle and back cells.[105] The interconnection of the subcells was realized with ZnO nanoparticles and pH-neutral PEDOT:PSS. The study shed light on the effect of the nature and surface area of the catalyst connected to a triple-junction cell on the η_{STH} efficiency. In particular, a η_{STH} of 5.4% was afforded with RuO_2-coated Ti substrates as catalysts for both hydrogen and oxygen evolution, with a surface area 15 times the one of the solar cell used. They also fabricated a water splitting device by replacing the RuO_2 catalyst by the earth-abundant Co_3O_4/NiMoZn catalysts, which yielded a η_{STH} of 4.9%. When the surface area of the catalyst was reduced to ca. 0.7 times the area of the solar cell, the higher current density in the catalyst caused an increase in overpotential, which shifted the operating voltage V_{op} from 1.49 to 1.67 V, i.e. away from the maximum power point of the solar cell. Consequently, η_{STH} decreased to 3.6%. Because the photon flux is distributed over only two instead of three absorber layers a tandem solar cell can generate a higher current density than a triple-junction cell at the same optical band gap. Hence, provided that the required operating voltage can be reached, a tandem cell can give a high η_{STH}. In 2016 Esiner et al. reported a wide band gap donor polymer containing a pentacyclic lactam unit, PTPTIBDT-OD.[96] The optical band gap of this material is 2.04 eV and in combination with $PC_{70}BM$ as acceptor it can afford a V_{OC} of 0.90 V in a single-junction solar cell. This active layer was used for both the front and back subcells of a homo-tandem device. To avoid voltage losses, the ICL was carefully designed using a ZnO/pH-neutral PEDOT:PSS/MoO_3 stack, allowing a V_{OC} of 1.74 V. For the water splitting reaction, the authors connected the solar cell to a RuO_2-coated Ti substrate catalytic electrode for oxygen and hydrogen evolution or a Pt plate catalyst for hydrogen evolution, in a KOH solution. The operating voltage for water splitting of this system was 1.5 V. In virtue of the high fill factor (FF) of 0.73 for this tandem, a η_{STH} of 4.3% could be achieved, assuming 100% Faradaic efficiency. Also in 2016, Gao et al. reported a homo-tandem polymer solar cell adopting PBDTTPD as a wide band gap donor material in combination with $PC_{70}BM$.[94] This donor material has a band gap of 1.85 eV and can deliver a V_{OC} of 0.92 V in a single-junction device, together with an internal quantum efficiency (IQE) around 0.9. The homo tandem affords J_{op} = 5.4 mA cm^{-2} during water splitting at V_{op} = 1.5 V, using an aqueous NaOH solution and platinum and nickel foam for hydrogen and oxygen evolution electrodes, respectively. The cell thus affords η_{STH} of

6.6% when assuming 100% Faradaic efficiency. In the same year Elias et al. presented a homo-triple junction for water splitting, i.e. using the same absorber in all the three subcells, PTB7:$PC_{70}BM$.[106] The structure of this device was inverted, with the successful MoO_3/Ag/PFN stack as ICL. The triple was characterized by a V_{OC} of 2.13 V, which together with an outstanding FF of 0.76 (certainly considering the number of layers in the stack) ensured a high value of J_{op}. A 6% in η_{STH} was achieved at neutral pH, by connecting the triple cell to a cathode of NiMoZn on stainless steel and an anode of RuO_2 on glassy carbon. The choice of the catalysts is particularly valuable since the first one is made of relatively abundant materials and the second one was manufactured with a minimal content of RuO_2. As already addressed before, polymer blends with non-fullerene acceptors (NFAs) can provide in general significantly higher V_{OC}s than fullerene-based cells. In 2016 Liu et al.[67] and in 2017 Chen et al.[38] reported V_{OC}s of 1.97 V and 2.16 V for these two NFA-based tandem cells, respectively, and demonstrated the evolution of gasses at the catalytic electrodes (platinum and nickel foam in a NaOH solution).

2.7 Conclusions

The results reported in this chapter point towards a very active research community on solution-processed multi-junction organic solar cells. The top efficiency for tandems with polymer:NFA photoactive blends reached the outstanding record PCE of 17.4%, and for tandems featuring small molecular donors blended with PCBM the highest PCE is 12.5%. Worth to mention is a remarkable PCE of 15% for hybrid evaporated small molecules (front cell) and solution-processed (back cell) tandems. Also all-polymer tandem cells underwent a significant improvement of the performance up to 11.2%, despite a small number of investigations addressing these cells. Polymer:PCBM-based tandems were reported multiple times capable of PCE > 11%. The PTB7-Th donor was adopted in many cases of efficient tandem solar cells, irrespective of whether PCBM and/or NFA acceptors were blended with it. In addition to the high efficiency, the high V_{OC} (especially of NFA systems) make OPV tandems suitable for photoelectrochemical water splitting application. From the point of view of the ICL, PEDOT:PSS and ZnO nanoparticles are still widely used in research, with interesting developments to improve their processing. A significant focus lied on the use of conjugated polyelectrolytes charge transport layers in the ICL. Among these, the use of PFN was reported by multiple groups, especially in the stack: MoO_3/Ag/PFN. The latter allowed achieving high FF values as well as an intriguing solution to tune the optical electric field in the device, improving the balance of photocurrent in the subcells. The thickness-dependent performance of single-junction cells, deriving from bimolecular recombination, was tackled in some papers by adopting the same absorber system in a homo-tandem solar cell, demonstrating improved absorption of light, accompanied by an increase in efficiency. All these recent developments might pave the way towards better performing triple-junction solar

cells, which were developed in a very limited number of studies due to their intricate requirements in terms of current matching and more elaborate processing and characterization. From the modeling, manufacturing, and characterization aspects, even a quadruple-junction polymer solar cell with complementary absorber layers was demonstrated, expanding the previous toolbox. A critical analysis on the procedure to follow to correctly characterize OPV tandems was presented in the early 2015. So far few relevant papers followed the guidelines rigorously, but the awareness of correct characterization has certainly been increased in recent years. In view of the high efficiencies now reported, the currently available studies stability on upscaling the technology should be continued, to meet the requirements for industrial manufacturing and reaching the market.

2.8 References

[1] A. Furlan, R. A. J. Janssen, *RSC Polym. Chem. Ser.* **2016**, *17*, 310.

[2] Z. Hong, L. Dou, G. Li, Y. Yang, *Top. Appl. Phys.*, **2015**, *130*, 315.

[3] N. Li, T. Ameri, C. J. Brabec, in *Organic Solar Cells*, (Ed. Q. Qiao) CRC Press, Boca Raton, Florida (USA) **2015**, Ch. 12, pp 337-377.

[4] O. Adebanjo, B. Vaagensmith, Q. Qiao, *J. Mater. Chem. A* **2014**, *2*, 10331.

[5] K. Glaser, A. Puetz, J. Mescher, D. Bahro, A. Colsmann, in *Organic Photovoltaics*, 2nd Ed. (Eds. J. C Brabec, U. Scherf, Ullrich, V. Dyakonov) Wiley-VCH, Weinheim, Germany **2014**, Ch. 14, pp 445-463.

[6] J. You, L. Dou, Z. Hong, G. Li, Y. Yang, *Prog. Polym. Sci.* **2013**, *38*, 1909.

[7] T. Ameri, N. Li, C. J. Brabec, *Energy Environ. Sci.* **2013**, *6*, 2390.

[8] T. Ameri, G. Dennler, C. Lungenschmied, C. J. Brabec, *Energy Environ. Sci.* **2009**, *2*, 347.

[9] H. Zhou, Y. Zhang, C.-K. Mai, S. D. Collins, G. C. Bazan, T.-Q. Nguyen, A. J. Heeger, *Adv. Mater.* **2015**, *27*, 1767.

[10] Y. Cui, H. Yao, B. Gao, Y. Qin, S. Zhang, B. Yang, C. He, B. Xu, J. Hou, *J. Am. Chem. Soc.* **2017**, *139*, 7302.

[11] J. Lee, H. Kang, S. Kee, S. H. Lee, S. Y. Jeong, G. Kim, J. Kim, S. Hong, H. Back, K. Lee, *ACS Appl. Mater. Interfaces* **2016**, *8*, 6144.

[12] K. Zhang, K. Gao, R. Xia, Z. Wu, C. Sun, J. Cao, L. Qian, W. Li, S. Liu, F. Huang, X. Peng, L. Ding, H.-L. Yip, Y. Cao, *Adv. Mater.* **2016**, *28*, 4817.

[13] K. Zhang, B. Fan, R. Xia, X. Liu, Z. Hu, H. Gu, S. Liu, H.-L. Yip, L. Ying, F. Huang, Y. Cao, *Adv. Energy Mater.* **2018**, *8*, 1703180.

[14] K. Zhang, R. Xia, B. Fan, X. Liu, Z. Wang, S. Dong, H.-L. Yip, L. Ying, F. Huang, Y. Cao, *Adv. Mater.* **2018**, DOI:10.1002/adma.201803166.

[15] L. Zuo, C.-Y. Chang, C.-C. Chueh, S. Zhang, H. Li, A. K.-Y. Jen, H. Chen, *Energy Environ. Sci.* **2015**, *8*, 1712.

[16] A. Martínez-Otero, Q. Liu, P. Mantilla-Perez, M. M. Bajo, J. Martorell, *J. Mater. Chem. A* **2015**, *3*, 10681.

[17] S. Lu, X. Guan, X. Li, W. E. I. Sha, F. Xie, H. Liu, J. Wang, F. Huang, W. C. H. Choy, *Adv. Energy Mater.* **2015**, *5*, 1500631.

[18] C.-H. Chou, W. L. Kwan, Z. Hong, L.-M. Chen, Y. Yang, *Adv. Mater.* **2011**, *23*, 1282.

[19] D. W. Zhao, L. Ke, Y. Li, S. T. Tan, A. K. K. Kyaw, H. V. Demir, X. W. Sun, D. L. Carroll, G. Q. Lo, D. L. Kwong, *Sol. Energy Mater. Sol. Cells* **2011**, *95*, 921.

[20] T. Becker, S. Trost, A. Behrendt, I. Shutsko, A. Polywka, P. Görrn, P. Reckers, C. Das, T. Mayer, D. Di Carlo Rasi, K. H. Hendriks, M. M. Wienk, R. A. J. Janssen, T. Riedl, *Adv. Energy Mater.* **2018**, *8*, 1702533.

[21] J. Yang, R. Zhu, Z. Hong, Y. He, A. Kumar, Y. Li, Y. Yang, *Adv. Mater.* **2011**, *23*, 3465.
[22] F. Verbakel, S. C. J. Meskers, R. A. J. Janssen, *Appl. Phys. Lett.* **2006**, *89*, 102103.
[23] D. Di Carlo Rasi, P. M. J. G. van Thiel, H. Bin, K. H. Hendriks, G. H. L. Heintges, M. M. Wienk, R. A. J. Janssen, submitted.
[24] A. F. Mitul, L. Mohammad, S. Venkatesan, N. Adhikari, S. Sigdel, Q. Wang, A. Dubey, D. Khatiwada, Q. Qiao, *Nano Energy* **2015**, *11*, 56.
[25] X. Du, O. Lytken, M. S. Killian, J. Cao, T. Stubhan, M. Turbiez, P. Schmuki, H.-P. Steinrück, L. Ding, R. H. Fink, N. Li, C. J. Brabec, *Adv. Energy Mater.* **2017**, *7*, 1601959.
[26] N. Torabi, A. Behjat, M. Shahpari, S. Edalati, *J. Nanophotonics* **2015**, *9*, 093049.
[27] S. Lu, X. Guan, X. Li, J. Liu, F. Huang, W. C. H. Choy, *Nano Energy* **2016**, *21*, 123.
[28] S.-Y. Chang, Y.-C. Lin, P. Sun, Y.-T. Hsieh, L. Meng, S.-H. Bae, Y.-W. Su, W. Huang, C. Zhu, G. Li, K.-H. Wei, Y. Yang, *Sol. RRL* **2017**, *1*, 1700139.
[29] Z. Shi, H. Liu, L. Xia, Y. Bai, F. Wang, B. Zhang, T. Hayat, A. Alsaedi, Z. Tan, *Chin. J. Chem.* **2018**, *36*, 194.
[30] S. Lu, H. Lin, S. Zhang, J. Hou, W. C. H. Choy, *Adv. Energy Mater.* **2017**, *7*, 1701164.
[31] S. Esiner, H. Van Eersel, M. M. Wienk, R. A. J. Janssen, *Adv. Mater.* **2013**, *25*, 2932.
[32] C.-Y. Chang, W.-K. Huang, Y.-C. Chang, K.-T. Lee, H.-Y. Siao, *Chem. Mater.* **2015**, *27*, 1869.
[33] W. J. da Silva, F. K. Schneider, A. R. bin Mohd Yusoff, J. Jang, *Sci. Rep.* **2015**, *5*, 18090.
[34] R. Kang, S. Park, Y. K. Jung, D. C. Lim, M. J. Cha, J. H. Seo, S. Cho, *Adv. Energy Mater.* **2018**, *8*, 1702165.
[35] H. Kang, S. Kee, K. Yu, J. Lee, G. Kim, J. Kim, J.-R. Kim, J. Kong, K. Lee, *Adv. Mater.* **2015**, *27*, 1408.
[36] S. Kim, H. Kang, S. Hong, J. Lee, S. Lee, B. Park, J. Kim, K. Lee, *Adv. Funct. Mater.* **2016**, *26*, 3563.
[37] Q. Wei, T. Nishizawa, K. Tajima, K. Hashimoto *Adv. Mater.* **2008**, *20*, 2211.
[38] S. Chen, G. Zhang, J. Liu, H. Yao, J. Zhang, T. Ma, Z. Li, H. Yan, *Adv. Mater.* **2017**, *29*, 1604231.
[39] M. Prosa, M. Tessarolo, M. Bolognesi, T. Cramer, Z. Chen, A. Facchetti, B. Fraboni, M. Seri, G. Ruani, M. Muccini, *Adv. Mater. Interfaces* **2016**, *3*, 1600770.
[40] D. Di Carlo Rasi, K. H. Hendriks, G. H. L. Heintges, G. Simone, G. H. Gelinck, V. S. Gevaerts, R. Andriessen, G. Pirotte, W. Maes, W. Li, M. M. Wienk, R. A. J. Janssen, *Sol. RRL* **2018**, *2*, 1800018.

[41] D. Di Carlo Rasi, K. H. Hendriks, M. M. Wienk, R. A. J. Janssen, *Adv. Mater.* **2018**, doi.org/10.1002/adma.201803836.
[42] Y. Ka, H. Hwang, C. Kim, *Sci. Rep.* **2017**, *7*, 1942.
[43] Y. Ka, H. Kim, S. Han, C. Kim, *Nanoscale* **2018**, *10*, 12588.
[44] X. Che, Y. Li, Y. Qu, S. R. Forrest, *Nat. Energy* **2018**, *3*, 422.
[45] S. Lee, T. E. Kang, D. Han, H. Kim, B. J. Kim, J. Lee, S. Yoo, *Sol. Energy Mater. Sol. Cells* **2015**, *137*, 34.
[46] L. Zuo, J. Yu, X. Shi, F. Lin, W. Tang, A. K.-Y. Jen, *Adv. Mater.* **2017**, *29*, 1702547.
[47] P. Mantilla-Perez, A. Martinez-Otero, P. Romero-Gomez, J. Martorell, *ACS Appl. Mater. Interfaces* **2015**, *7*, 18435.
[48] L. Zuo, C.-Y. Chang, C.-C. Chueh, Y. Xu, H. Chen, A. K.-Y. Jen, *J. Mater. Chem. A* **2016**, *4*, 961.
[49] J. A. Mayer, T. Offermans, M. Chrapa, M. Pfannmöller, S. Bals, R. Ferrini, G. Nisato, *Opt. Express* **2018**, *26*, A240.
[50] A. Mertens, J. Mescher, D. Bahro, M. Koppitz, A. Colsmann, *Opt. Express* **2016**, *24*, A898.
[51] M. Riede, C. Uhrich, J. Widmer, R. Timmreck, D. Wynands, G. Schwartz, W.-M. Gnehr, D. Hildebrandt, A. Weiss, J. Hwang, S. Sundarraj, P. Erk, M. Pfeiffer, K. Leo, *Adv. Funct. Mater.* **2011**, *21*, 3019.
[52] B. Luo, Y. Jiang, L. Mao, W. Meng, F. Jiang, Y. Xu, Y. Zhou, *J. Mater. Chem. C* **2017**, *5*, 7884.
[53] S.-H. Liao, H.-J. Jhuo, P.-N. Yeh, Y.-S. Cheng, Y.-L. Li, Y.-H. Lee, S. Sharma, S.-A. Chen, *Sci. Rep.* **2015**, *4*, 6813.
[54] Q. Zhang, X. Wan, F. Liu, B. Kan, M. Li, H. Feng, H. Zhang, T. P. Russell, Y. Chen, *Adv. Mater.* **2016**, *28*, 7008.
[55] Y. Ma, S.-C. Chen, Z. Wang, W. Ma, J. Wang, Z. Yin, C. Tang, D. Cai, Q. Zheng, *Nano Energy* **2017**, *33*, 313.
[56] Z. Zheng, S. Zhang, M. Zhang, K. Zhao, L. Ye, Y. Chen, B. Yang, J. Hou, *Adv. Mater.* **2015**, *27*, 1189.
[57] Z. Zheng, S. Zhang, J. Zhang, Y. Qin, W. Li, R. Yu, Z. Wei, J. Hou, *Adv. Mater.* **2016**, *28*, 5133.
[58] W. Li, K. H. Hendriks, A. Furlan, W. S. C. Roelofs, M. M. Wienk, R. A. J. Janssen, *J. Am. Chem. Soc.* **2013**, *135*, 18942.
[59] C. Duan, A. Furlan, J. J. van Franeker, R. E. M. Willems, M. M. Wienk, R. A. J. Janssen, *Adv. Mater.* **2015**, *27*, 4461.
[60] B. Guo, X. Guo, W. Li, X. Meng, W. Ma, M. Zhang, Y. Li, *J. Mater. Chem. A* **2016**, *4*, 13251.

[61] S. Song, K. Kranthiraja, J. Heo, T. Kim, B. Walker, S.-H. H. Jin, J. Y. Kim, *Adv. Energy Mater.* **2017**, *7*, 1700782.
[62] J. Hou, O. Inganäs, R. H. Friend, F. Gao, *Nat. Mater.* **2018**, *17*, 119.
[63] P. Cheng, G. Li, X. Zhan, Y. Yang, *Nat. Photonics* **2018**, *12*, 131.
[64] A. Wadsworth, M. Moser, A. Marks, M. S. Little, N. Gasparini, C. J. Brabec, D. Baran, I. McCulloch, *Chem. Soc. Rev.* **2018**, DOI 10.1039/C7CS00892A.
[65] G. Zhang, J. Zhao, P. C. Y. Chow, K. Jiang, J. Zhang, Z. Zhu, J. Zhang, F. Huang, H. Yan, Chem. Rev. **2018**, *118*, 3447.
[66] J. Liu, S. Chen, D. Qian, B. Gautam, G. Yang, J. Zhao, J. Bergqvist, F. Zhang, W. Ma, H. Ade, O. Inganäs, K. Gundogdu, F. Gao, H. Yan, *Nat. Energy* **2016**, *1*, 16089.
[67] W. Liu, S. Li, J. Huang, S. Yang, J. Chen, L. Zuo, M. Shi, X. Zhan, C.-Z. Li, H. Chen, *Adv. Mater.* **2016**, *28*, 9729.
[68] X. Shi, L. Zuo, S. B. Jo, K. Gao, F. Lin, F. Liu, A. K.-Y. Jen, *Chem. Mater.* **2017**, *29*, 8369.
[69] Y. Qin, Y. Chen, Y. Cui, S. Zhang, H. Yao, J. Huang, W. Li, Z. Zheng, J. Hou, *Adv. Mater.* **2017**, *29*, 1606340.
[70] Y. Cui, H. Yao, C. Yang, S. Zhang, J. Hou, *Acta Polym. Sin.* **2018**, *2*, 223.
[71] Z. Shi, H. Liu, J. Li, F. Wang, Y. Bai, X. Bian, B. Zhang, A. Alsaedi, T. Hayat, Z. Tan, *Sol. Energy Mater. Sol. Cells* **2018**, *180*, 1.
[72] Y. Zhang, B. Kan, Y. Sun, Y. Wang, R. Xia, X. Ke, Y.-Q.-Q. Yi, C. Li, H.-L. Yip, X. Wan, Y. Cao, Y. Chen, *Adv. Mater.* **2018**, *30*, 1707508.
[73] Q. Yue, Z. Zhou, S. Xu, J. Zhang, X. Zhu, *J. Mater. Chem. A* **2018**, *6*, 13588.
[74] L. Meng, Y. Zhang, X. Wan, C. Li, X. Zhang, Y. Wang, X. Ke, Z. Xiao, L. Ding, R. Xia, H.-L. Yip, Y. Cao, Y. Chen, *Science* **2018**, *361*, 1094.
[75] J.-H. Kim, J. B. Park, H. Yang, I. H. Jung, S. C. Yoon, D. Kim, D.-H. Hwang, *ACS Appl. Mater. Interfaces* **2015**, *7*, 23866.
[76] Q. Zhang, X. Wan, F. Liu, B. Kan, M. Li, H. Feng, H. Zhang, T. P. Russell, Y. Chen, *Adv. Mater.* **2016**, *28*, 7008.
[77] M. Li, K. Gao, X. Wan, Q. Zhang, B. Kan, R. Xia, F. Liu, X. Yang, H. Feng, W. Ni, Y. Wang, J. Peng, H. Zhang, Z. Liang, H.-L. Yip, X. Peng, Y. Cao, Y. Chen, *Nat. Photonics* **2017**, *11*, 85.
[78] J. Yuan, J. Gu, G. Shi, J. Sun, H.-Q. Wang, W. Ma, *Sci. Rep.* **2016**, *6*, 26459.
[79] J. Yuan, M. J. Ford, Y. Xu, Y. Zhang, G. C. Bazan, W. Ma, *Adv. Energy Mater.* **2018**, *8*, 1703291.
[80] N. Li, C. J. Brabec, *Energy Environ. Sci.* **2015**, *8*, 2902.
[81] J. Hanisch, T. Wahl, C. D. Wessendorf, E. Ahlswede, *J. Mater. Chem. A* **2016**, *4*, 4771.

[82] L. Mao, J. Tong, S. Xiong, F. Jiang, F. Qin, W. Meng, B. Luo, Y. Liu, Z. Li, Y. Jiang, C. Fuentes-Hernandez, B. Kippelen, Y. Zhou, *J. Mater. Chem. A* **2017**, *5*, 3186.

[83] K. Glaser, P. Beu, D. Bahro, C. Sprau, A. Pütz, A. Colsmann, *J. Mater. Chem. A* **2018**, *6*, 9257.

[84] D. Angmo, T. R. Andersen, J. J. Bentzen, M. Helgesen, R. R. Søndergaard, M. Jørgensen, J. E. Carlé, E. Bundgaard, F. C. Krebs, *Adv. Funct. Mater.* **2015**, *25*, 4539.

[85] F. Guo, N. Li, V. V. Radmilović, V. R. Radmilović, M. Turbiez, E. Spiecker, K. Forberich, C. J. Brabec, *Energy Environ. Sci.* **2015**, *8*, 1690.

[86] J. Tong, S. Xiong, Z. Li, F. Jiang, L. Mao, W. Meng, Y. Zhou, *Appl. Phys. Lett.* **2015**, *106*, 053306.

[87] J. Tong, S. Xiong, Y. Zhou, L. Mao, X. Min, Z. Li, F. Jiang, W. Meng, F. Qin, T. Liu, R. Ge, C. Fuentes-Hernandez, B. Kippelen, Y. Zhou, *Mater. Horiz.* **2016**, *3*, 452.

[88] F. Livi, R. R. Søndergaard, T. R. Andersen, B. Roth, S. Gevorgyan, H. F. Dam, J. E. Carlé, M. Helgesen, G. D. Spyropoulos, J. Adams, T. Ameri, C. J. Brabec, M. Legros, N. Lemaitre, S. Berny, O. R. Lozman, S. Schumann, A. Scheel, P. Apilo, M. Vilkman, E. Bundgaard, F. C. Krebs, *Energy Technol.* **2015**, *3*, 423.

[89] J. Adams, G. D. Spyropoulos, M. Salvador, N. Li, S. Strohm, L. Lucera, S. Langner, F. Machui, H. Zhang, T. Ameri, M. M. Voigt, F. C. Krebs, C. J. Brabec, *Energy Environ. Sci.* **2015**, *8*, 169.

[90] E. B. L. Pedersen, D. Angmo, H. F. Dam, K. T. S. Thydén, T. R. Andersen, E. T. B. Skjønsfjell, F. C. Krebs, M. Holler, A. Diaz, M. Guizar-Sicairos, D. W. Breiby, J. W. Andreasen, *Nanoscale* **2015**, *7*, 13765.

[91] H. F. Dam, T. R. Andersen, E. B. L. Pedersen, K. T. S. Thydén, M. Helgesen, J. E. Carlé, P. S. Jørgensen, J. Reinhardt, R. R. Søndergaard, M. Jørgensen, E. Bundgaard, F. C. Krebs, J. W. Andreasen, *Adv. Energy Mater.* **2015**, *5*, 1400736.

[92] T. T. Larsen-Olsen, T. R. Andersen, H. F. Dam, M. Jørgensen, F. C. Krebs, *Sol. Energy Mater. Sol. Cells* **2015**, *137*, 154.

[93] A. R. bin Mohd Yusoff, D. Kim, F. K. Schneider, W. J. da Silva, J. Jang, *Energy Environ. Sci.* **2015**, *8*, 1523.

[94] Y. Gao, V. M. Le Corre, A. Gaïtis, M. Neophytou, M. A. Hamid, K. Takanabe, P. M. Beaujuge, *Adv. Mater.* **2016**, *28*, 3366.

[95] D. Bahro, M. Koppitz, A. Mertens, K. Glaser, J. Mescher, A. Colsmann, *Adv. Energy Mater.* **2015**, *5*, 1501019.

[96] S. Esiner, G. W. P. van Pruissen, M. M. Wienk, R. A. J. Janssen, *J. Mater. Chem. A* **2016**, *4*, 5107.

[97] H. Y. Han, H. Yoon, C. S. Yoon, *Sol. Energy Mater. Sol. Cells* **2015**, *132*, 56.

[98] S.-C. Chen, Q. Zheng, Z. Yin, D. Cai, Y. Ma, *Org. Electron.* **2017**, *47*, 79.
[99] F. Yang, D.-W. Kang, Y.-S. Kim, *Sol. Energy* **2017**, *155*, 552.
[100] F. Yang, D.-W. Kang, Y.-S. Kim, *Sol. Energy* **2018**, *163*, 434.
[101] M. Prosa, N. Li, N. Gasparini, M. Bolognesi, M. Seri, M. Muccini, C. J. Brabec, *Adv. Mater. Interfaces* **2017**, *4*, 1700776.
[102] A. Brown, M. Green, *Prog. Photovolt: Res. Appl.* **2002**, *10*, 299.
[103] C.-C. Chen, W.-H. Chang, K. Yoshimura, K. Ohya, J. You, J. Gao, Z. Hong, Y. Yang, *Adv. Mater.* **2014**, *26*, 5670.
[104] A. R. bin Mohd Yusoff, D. Kim, H. P. Kim, F. K. Shneider, W. J. da Silva, J. Jang, *Energy Environ. Sci.* **2015**, *8*, 303.
[105] S. Esiner, R. E. M. Willems, A. Furlan, W. Li, M. M. Wienk, R. A. J. Janssen, *J. Mater. Chem. A* **2015**, *3*, 23936.
[106] X. Elias, Q. Liu, C. Gimbert-Suriñach, R. Matheu, P. Mantilla-Perez, A. Martinez-Otero, X. Sala, J. Martorell, A. Llobet, *ACS Catal.* **2016**, *6*, 3310.
[107] R. Timmreck, T. Meyer, J. Gilot, H. Seifert, T. Mueller, A. Furlan, M. M. Wienk, D. Wynands, J. Hohl-Ebinger, W. Warta, R. A. J. Janssen, M. Riede, K. Leo, *Nat. Photonics* **2015**, *9*, 478.
[108] F. Guo, N. Li, F. W. Fecher, N. Gasparini, C. O. R. Quiroz, C. Bronnbauer, Y. Hou, V. V. Radmilović, V. R. Radmilović, E. Spiecker, K. Forberich, C. J. Brabec, *Nat. Commun.* **2015**, *6*, 7730.
[109] A. Cravino, P. Schilinsky, C. J. Brabec, *Adv. Funct. Mater.* **2007**, *17*, 3906.
[110] M.-S. Kim, M.-G. Kang, L. J. Guo, J. Kim, *Appl. Phys. Lett.* **2008**, *92*, 133301.
[111] S. Sista, M.-H. Park, Z. Hong, Y. Wu, J. Hou, W. L. Kwan, G. Li, Y. Yang, *Adv. Mater.* **2010**, *22*, 380.
[112] D. Di Carlo Rasi, K. H. Hendriks, M. M. Wienk, R. A. J. Janssen, *Adv. Energy Mater.* **2017**, *7*, 1701664.
[113] S. Esiner, H. Van Eersel, M. M. Wienk, R. A. J. Janssen, *Adv. Mater.* **2013**, *25*, 2932.

Chapter 3

A Universal Route to Fabricate n-i-p Multi-Junction Polymer Solar Cells via Solution Processing*

Abstract

The interconnection layer (ICL) that connects adjacent subcells electrically and optically in solution-processed multi-junction polymer solar cells must meet functional requirements in terms of work functions, conductivity, and transparency, but also be compatible with the multiple layer stack in terms of processing and deposition conditions. Using a combination of poly(3,4-ethylenedioxythiophene):polystyrene sulfonate, diluted in near azeotropic water/n-propanol dispersions as hole transport layer, and ZnO nanoparticles, dispersed in isoamyl alcohol as electron transport layer, a novel, versatile ICL has been developed for solution-processed tandem and triple-junction solar cells in an n-i-p architecture. The ICL has been incorporated in six different tandem cells and three different triple-junction solar cells, employing a range of different polymer-fullerene photoactive layers. The new ICL provided an essentially lossless contact in each case, without the need of adjusting the formulations or deposition conditions. The approach permitted realizing complex devices in good yields, providing a power conversion efficiency up to 10%.

* This chapter has been published as: D. Di Carlo Rasi, K. H. Hendriks, G. H. L. Heintges, G. Simone, G. H. Gelinck, V. S. Gevaerts, R. Andriessen, G. Pirotte, W. Maes, W. Li, M. M. Wienk, R. A. J. Janssen, *Sol. RRL* **2018**, *2*, 1800018.

3.1 Introduction

The main challenge in developing a procedure for making multi-junction solar cells from solution is the fabrication of the interconnecting layer (ICL). The ICL is composed of charge-selective interlayer materials that ensure the recombination of opposite charges from two adjacent active layers, without energy loss. This is done by stacking an electron transport material and a hole transport material (Chapter 1). Efficient, solution-processable ICLs should satisfy a number of requirements:

(1) The Fermi levels of the ICL must match with the relevant highest occupied molecular orbital (HOMO) and lowest unoccupied molecular orbital LUMO energy levels of the organic materials in the adjacent active layers that are sandwiching the ICL to create Ohmic contacts.

(2) The materials in the ICL should possess sufficient Ohmic conductance to enable fast recombination of charges and to avoid loss of potential energy or fill factor.

(3) The parasitic absorption of sunlight should be low.

(4) The temperatures at which the processing and any post-treatment are performed should not deteriorate the performance of the active layers in the device.

(5) The formulation of the solutions from which the ICL is cast should not interfere with the underlying materials in the sequence of the device stack.

(6) The ICL should prevent that the solvents that are used to deposit subsequent layers in the stack, penetrate and dissolve underlying layers.

(7) The processing of the ICL should be versatile, so that it can be used for many combinations of active layers from different materials.

In recent years, several different combinations of materials have been proposed as ICL, involving either organic materials or transparent semiconducting metal oxides[1-15] (refer also to Chapter 2). For the selective extraction of holes from the photoactive layers poly(3,4-ethylenedioxythiophene):polystyrene sulfonate (PEDOT:PSS) is widely used but also metal oxides such as MoO_3,[16] V_2O_5,[17] and WO_3,[18] or graphene oxide (GO)[19] can be used for the purpose. For selective electron extraction, solution-processed metal oxides such as ZnO nanoparticles,[20] sol-gel TiO_2,[1] or Li-doped ZnO[21] are popular. These metal oxides can be covered by self-assembled monolayers[22] or poly[(9,9-bis(3'-(*N*,*N*-dimethylamion)propyl)-2,7-fluorene)-*alt*-2,7-(9,9-dioctyl)-fluorene] (PFN)[23] to improve charge selectivity. Also polyamines such as ethoxylated polyethylenimine (PEIE)[24] and polyethylenimine (PEI)[25] have been used to modify the work function of PEDOT:PSS or metal oxides to create an effective low work function, electron selective contact. One of the reasons for the large

variety of ICLs stems from the fact that the proposed materials or their processing conditions are often quite specific to the nature of the photoactive layers. A universal, solution-based method that works in combination with a large number of different active layers does not exist at present. The choice of ICL and the details of its casting conditions (mainly the formulation of the solutions) do vary substantially according to the particular stack of materials under consideration, to ensure the so-called orthogonality of casting solvents (related to requirements (5) and (6) above). The match of the surface energy of the inks from which we process the ICL to the surface energy of the organic active layer plays a major role in the formation of the film.[26] Regarding requirement (4), we note that for some of the materials used in this work even mild temperatures like 60 °C decrease the photovoltaic performance of the photoactive layer, probably due to morphology changes. Hence, a universal route to fabricate multi-junction polymer solar cells via solution processing at mild temperatures is in great demand.

Herein, we describe a combination of interlayers and processing conditions that fulfill the entire list of requirements. We developed new formulations for dispersions of PEDOT:PSS and ZnO nanoparticles in solvents that enable orthogonal processing of the ICL on any photoactive layer in an inverted (n-i-p) configuration we have tested. The reasons to choose for PEDOT:PSS and ZnO are their favorable work functions, and room temperature deposition conditions from benign solvents. To demonstrate this, we combined photoactive layers based on polymer-fullerene blends of different nature to fabricate six tandem and three triple-junction solar cells. A total of eight different active layers were tested in varying configurations, as front or back subcells in tandems, or as a middle subcell in triple junctions. The performance characteristics of these multi-junction devices were, in general, in good agreement with the expected performance based on the properties of corresponding single-junction devices. As proof of concept, triple-junction solar cells with a power conversion efficiency of 10% were realized with excellent statistical relevance (yield 94%).

3.2 Results and Discussion

3.2.1 Materials and device architectures

To develop a versatile method for coating the ICL in different device stacks we decided to develop and test ICL formulations on active layer materials of different chemical nature and with different opto-electrical properties, suitable for different roles in tandem and triple-junction cells. We adopted an inverted (n-i-p) device configuration in which the electron transporting layer (ETL) is deposited first, followed by the active layer and the hole transport layer (HTL). There are several reasons to prefer an inverted (n-i-p) over a conventional (p-i-n) device architecture, mainly related to the use of PEDOT:PSS as HTL. In the conventional structure, the HTL is positioned between the light source and the photoactive layer, which

leads to parasitic absorption by the polaron/bipolaron absorption bands of PEDOT:PSS in the near infrared.[27] Further, the acidic nature of the commercial PEDOT:PSS dispersions in water causes that it cannot be deposited on ZnO without deteriorating this layer or even washing it away completely. Increasing the pH of the dispersion can mitigate this, but lowers the work function of the resulting PEDOT:PSS layer. In turn this limits the open-circuit voltage (V_{OC}) that can be reached and necessitates the use of additional MoO_3 or Nafion layers to compensate for this loss.[28] Reversing the processing order of the ZnO and PEDOT:PSS layers avoids these complications. Finally, the Ag back electrode that is commonly used in the n-i-p configuration is more reflective than the Al back contact in most p-i-n structures.[29] The general sequence of layers in single, double and triple-junction devices used in this work is shown in **Figure 1**.

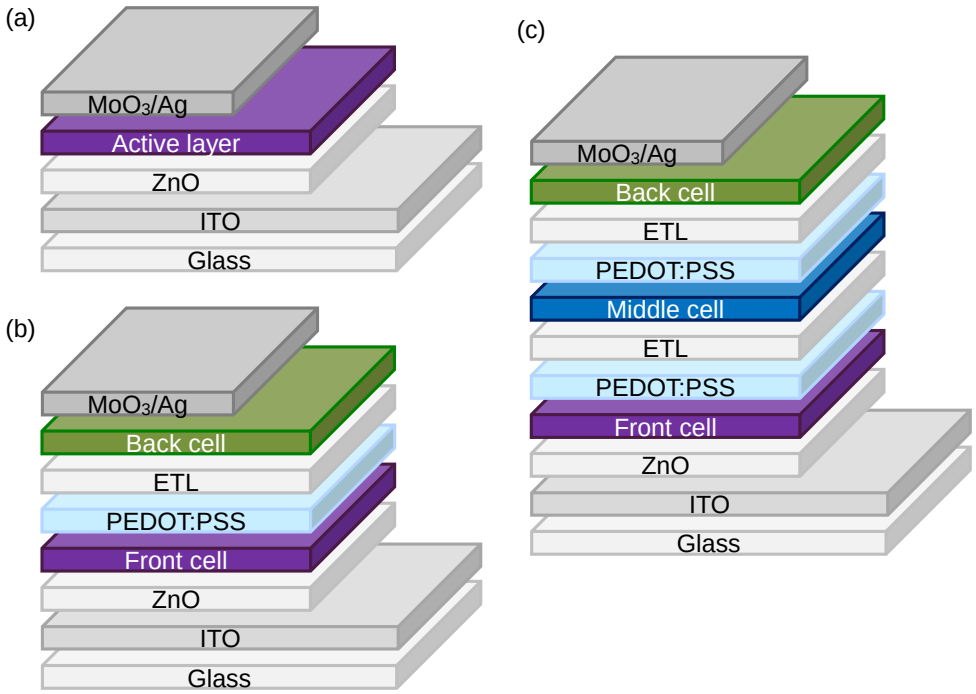

Figure 1. Device architecture of n-i-p (a) single, (b), double, and (c) triple-junction solar cells adopted in this work.

The optimal position of an organic semiconductor layer in a multi-junction stack is dictated by its optical band gap: wide band gap materials are preferably close to the

transparent electrode (front subcell), while low band gap materials are close to the reflecting back contact (back subcell). This generally represents an optimal choice because the high energy of photons from the blue part of the solar spectrum would be lost by thermalization if these were absorbed by the low band gap material. Materials with an intermediate band gap can be conveniently used in various positions, especially as middle cell in triple-junction solar cells.

Figure 2 and **Table 1** show the donor polymers tested in this study. We used PCDTBT (E_g = 1.88 eV), PBDTTPD (E_g = 1.85 eV), and PDCBT (E_g = 1.90 eV) as wide band gap donors in the front subcells.[30,31,32] For the back subcells we selected PDPP5T (E_g = 1.46 eV), PDPP3T (E_g = 1.33 eV), and its methylated version PMDPP3T (E_g = 1.30 eV) as donors.[4,33,34] Donors that were used either in the front, middle, or back subcells were PDPPTPT (E_g = 1.53 eV) and PTB7-Th (E_g = 1.58 eV).[35,36] All donors were used in combination with [6,6]-phenyl-C_{61}-butyric acid methyl ester ($PC_{60}BM$) or [6,6]-phenyl-C_{71}-butyric acid methyl ester ($PC_{70}BM$).

Table 1. Systematic names of the donor polymers used.

PCDTBT	poly[*N*-9″-heptadecanyl-2,7-carbazole-*alt*-5,5-(4′,7′-di-2-thienyl-2′,1′,3′-benzothiadiazole)])
PBDTTPD	poly[bis(2′-ethylhexyloxy)benzo[1,2-*b*:4,5-*b*′]dithiophene-*alt*-*N*-octylthieno[3,4-*c*]pyrrole-4,6-dione]
PDCBT	poly[5,5′-bis(2-butyloctyl)-(2,2′-bithiophene)-4,4′-dicarboxylate-*alt*-5,5′-2,2′-bithiophene]
PDPP5T	poly[[2,5-bis(2-hexyldecyl)-2,3,5,6-tetrahydro-3,6-dioxopyrrolo[3,4-*c*]pyrrole-1,4-diyl]-*alt*-(3‴,4′-dihexyl[2,2′:5′,2″:5″,2‴:5‴,2⁗-quinquethiophene]-5,5⁗-diyl)]
PDPP3T	poly[[2,5-bis(2-hexyldecyl)-2,3,5,6-tetrahydro-3,6-dioxopyrrolo[3,4-*c*]pyrrole-1,4-diyl]-*alt*-[2,2′:5′,2″-terthiophene]-5,5″-diyl]
PMDPP3T	poly[[2,5-bis(2-hexyldecyl)-2,3,5,6-tetrahydro-3,6-dioxopyrrolo[3,4-*c*]pyrrole-1,4-diyl]-*alt*-[3′,3″-dimethyl-2,2′:5′,2″-terthiophene]-5,5″-diyl]
PDPPTPT	poly[{2,5-bis(2-hexyldecyl)-2,3,5,6-tetrahydro-3,6-dioxopyrrolo[3,4-c]pyrrole-1,4-diyl}-*alt*-{[2,2′-(1,4-phenylene)bisthiophene]-5,5′-diyl}]
PTB7-Th	poly[4,8-bis(5-(2-ethylhexyl)thiophen-2-yl)benzo[1,2-*b*:4,5-*b*′]dithiophene-*co*-3-fluorothieno[3,4-*b*]thiophene-2-carboxylate]

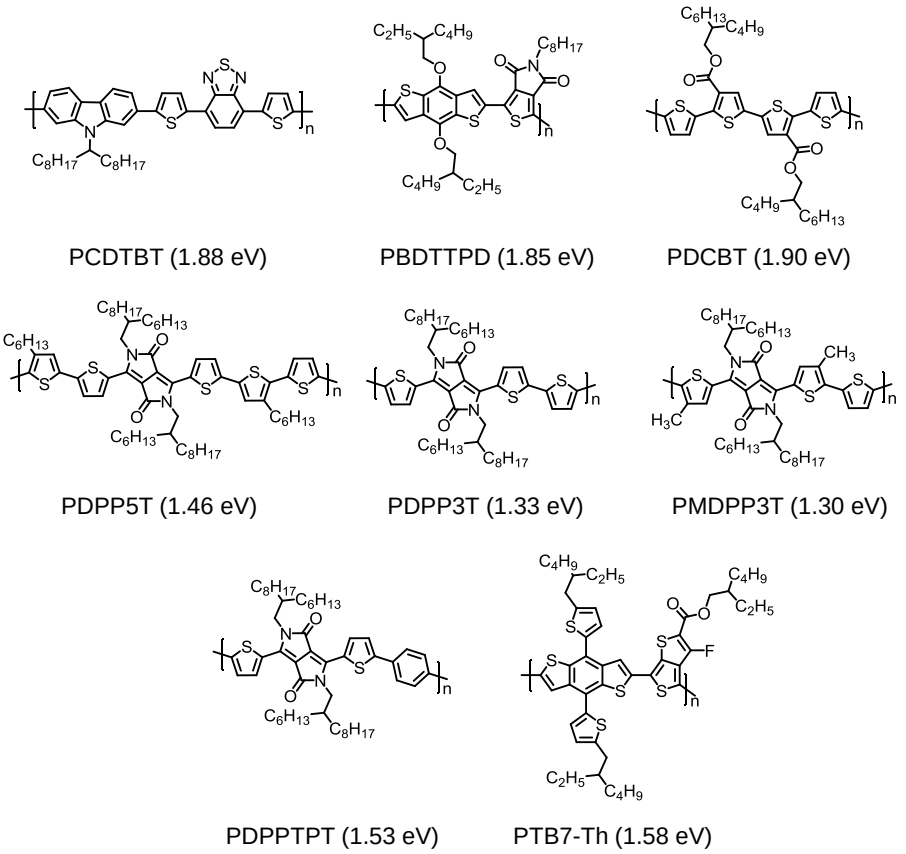

Figure 2. Chemical structures of the donor polymers used in this study. The corresponding optical band gaps are shown in parenthesis. Systematic names of the polymers are collected in Table 1.

Table 2 lists the optimized photovoltaic performance under simulated air mass 1.5 (AM1.5G) solar radiation of each of the eight donor polymers in combination with either $PC_{60}BM$ or $PC_{70}BM$ as acceptor in an n-i-p device configuration using sol-gel ZnO as ETL and MoO_3 as HTL with indium tin oxide (ITO) and silver as electrodes. We labelled each blend as BHJ*n*, *n* being a number for further reference. Details on the processing conditions for each cell can be found in the Experimental Section 3.4 of this chapter.

Table 2. Photovoltaic performance of the inverted single-junction solar cells with optimized thickness.

	Blend	V_{OC} [V]	J_{SC} [mA cm^{-2}]	FF	PCE [%]
BHJ1	PCDTBT:$PC_{70}BM$	0.88	9.04	0.63	5.0
BHJ2	PBDTTPD:$PC_{70}BM$	0.90	11.9	0.66	7.1
BHJ3	PDCBT:$PC_{60}BM$	0.86	8.73	0.71	5.3
BHJ4	PDPPTPT:$PC_{60}BM$	0.79	12.1	0.64	6.3
BHJ5	PTB7-Th:$PC_{70}BM$	0.79	16.9	0.69	9.2
BHJ6	PDPP5T:$PC_{60}BM$	0.57	14.6	0.65	5.4
BHJ7	PDPP3T:$PC_{60}BM$	0.68	11.8	0.68	5.4
BHJ8	PMDPP3T:$PC_{60}BM$	0.61	15.6	0.63	5.7

3.2.2 PEDOT:PSS as HTL

PEDOT:PSS is used in many organic solar cells as HTL. PEDOT:PSS is generally deposited from a dispersion in water at low pH. In principle the use of water is advantageous because it is an orthogonal solvent to the organic photoactive layers. On the other hand, the surface energy of water (72.8 mN m^{-1}) is so high that the PEDOT:PSS dispersion poorly wets the surface of organic semiconductors and mostly flies off during the spin-coating. Different modifications of commercial PEDOT:PSS dispersions have been proposed to improve the deposition of PEDOT:PSS on top of a photoactive layer, while preserving the functional properties. Examples are the use of isopropanol[22,25,37,38] or surfactants[39-44] to change the wettability, or sodium polystyrene sulfonate (SPS) to change the viscosity.[26] Modifications that involve solid and liquid additives can also alter properties of PEDOT:PSS like the conductivity and the work function.

In this work, we introduce a novel formulation of PEDOT:PSS based on adding *n*-propanol. We found that dropwise addition of *n*-propanol to the commercial PEDOT:PSS (Clevios P VPAl 4083) dispersion in water over 15 minutes under vigorous stirring results in a stable dispersion. *n*-Propanol has a much lower surface energy (23.7 mN m^{-1}), which improves the wetting of the diluted dispersion on organic surfaces. Furthermore the 1:2 volume ratio of water to *n*-propanol (0.38:0.62 w/w) is fairly close to the azeotropic composition (0.28:0.72 w/w). This ensures that during evaporation the evaporating layer will contain an appreciable amount of *n*-propanol, such that de-wetting during drying is prevented.[45] The use of *n*-propanol has a distinct advantage over the use of isopropanol. The water-isopropanol azeotrope (0.12:0.88 w/w) is much richer in the alcohol, implying that more isopropanol than *n*-propanol must be added to the aqueous PEDOT:PSS dispersion to reach (near) azeotropic evaporation. This results in thinner PEDOT:PSS layers. In the

following we refer to this new formulation as D-PEDOT:PSS (diluted in *n*-propanol). We remark that *n*-propanol evaporates virtually completely during spin-coating, leaving nothing more than just PEDOT:PSS in the layer.

We optimized the amount of *n*-propanol that is necessary to uniformly cover the active layer. **Figure 3** shows pictures taken with a camera of three different bulk-heterojunction layers, before and after spin-coating of D-PEDOT:PSS on top. For the deposition we used spin-coating at 500 rpm in a nitrogen filled glove box, which was found to improve the wetting. Figure 3 shows that dilution of PEDOT:PSS with *n*-propanol improved the film formation properties. On a PCDTBT:$PC_{70}BM$ layer, a ratio of water/*n*-propanol 1:1 (v/v) seemed sufficient to form a uniform film of PEDOT:PSS on top. For PDPPTPT:$PC_{60}BM$ and PDPP5T:$PC_{60}BM$, however, the PEDOT:PSS 1:1 (v/v) diluted dispersion in water/*n*-propanol only partially covered the surface, possibly due to a larger difference in surface energy of these substrates. By further diluting to 1:2 (v/v), the coverage turned uniform for each of the cases considered. The same 1:2 (v/v) formulation turned out to deposit well on many other active layers. As explained, the 1:2 mixture corresponds to a mass fraction of *n*-propanol of 0.62, close to the azeotropic composition of 0.72. Hence in the last stages of the drying process, mostly water is present in the layer, which is the native medium of PEDOT:PSS, but the viscosity at this point has increased because of the increased PEDOT:PSS concentration such that dewetting or material flying off from the substrate does not occur. After spin-coating the D-PEDOT:PSS layers were kept in a vacuum of ~10^{-2} mbar for 30 minutes to remove residual solvents, and no further treatment was performed.

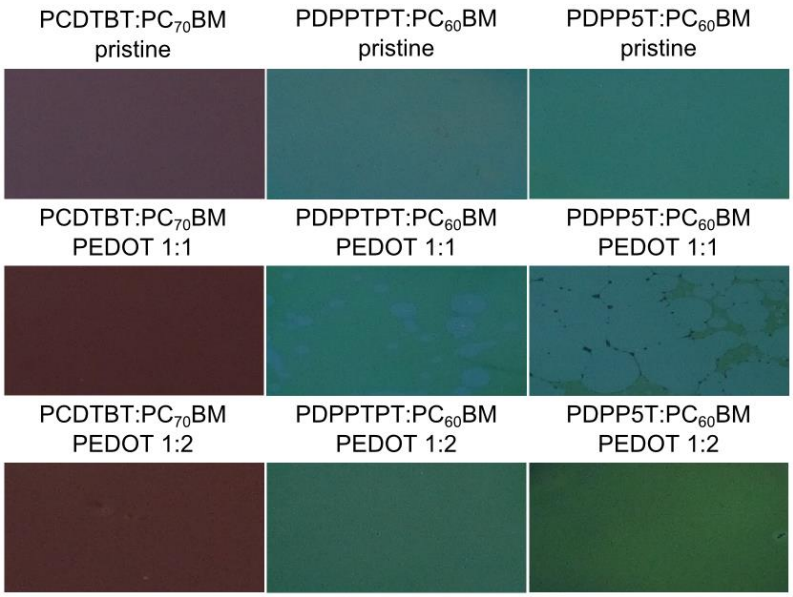

Figure 3. Photographs of glass substrates coated with different bulk-heterojunction layers without and with an additional layer of PEDOT:PSS processed from water/*n*-propanol mixtures with different volume ratios.

To optimize the performance of D-PEDOT:PSS as HTL, we made single-junction solar cells based on BHJ1 with a ITO/PEIE/BHJ1/D-PEDOT:PSS/Ag architecture, using PEIE as an ETL.[46] Different dilutions with *n*-propanol were compared and the photovoltaic parameters determined under simulated solar illumination are collected in **Table 3** and compared to a reference cell in which D-PEDOT:PSS was replaced by a layer of MoO_3. Dilution with *n*-propanol reduces the thickness of the D-PEDOT:PSS films. Table 3 reveals that the amount of *n*-propanol mainly affected the short-circuit current density (J_{SC}) and the fill factor (FF). Starting from 1:2 dilution, the power conversion efficiency (PCE) remains constant. The difference in J_{SC} with respect to the reference device is related to optical cavity effects as inferred from optical modeling. Apart from this, only minor differences in the FF occurred. Table 3 shows that going beyond 1:2 of dilution brings no improvement. Therefore, we adopted the 1:2 (v/v) water/*n*-propanol ratio as the standard for D-PEDOT:PSS.

Table 3. Photovoltaic parameters of ITO/PEIE/PCDTBT:$PC_{70}BM$/D-PEDOT:PSS/Ag solar cells with a PEDOT:PSS layer processed from different water/*n*-propanol (v/v) dispersions.

PEDOT:PSS:*n*-propanol	V_{OC} [V]	J_{SC} [mA cm^{-2}]	FF	PCE [%]
Reference [a)]	0.87	8.2	0.56	4.0
1:1 (70 nm)	0.86	6.1	0.61	3.2
1:2 (40 nm)	0.89	7.2	0.61	3.9
1:3 (30 nm)	0.88	7.8	0.57	3.9
1:4 (25 nm)	0.87	7.8	0.58	3.9
1:5 (20 nm)	0.88	7.8	0.57	3.8

[a)] ITO/PEIE/PCDTBT:$PC_{70}BM$/MoO_3/Ag.

3.2.3 PEIE and ZnO nanoparticles as ETL

To create an ICL for tandem solar cells the optimized D-PEDOT:PSS layer must be combined with an ETL (Figure 1). We decided to test both PEIE and ZnO nanoparticles on top of the D-PEDOT:PSS film. The function of PEIE is to create a thin (< 10 nm) layer in which the presence of dipoles or ions at the interface lowers the work function of PEDOT:PSS, permitting the tunneling of electrons.[46] PEIE is commercially available as an aqueous solution, but water is not a suitable solvent for processing on top of PEDOT:PSS layers. Following the procedure of Lee et al. [25] for the non-ethoxylated version of polyethylenimine (PEI), we diluted PEIE with a significant amount of isopropanol (IPA) to reach concentrations in IPA around 0.2 wt%. By doing so the content in water reduced to a marginal amount (in the same order of magnitude as PEIE), avoiding the dissolution of the PEDOT:PSS layer. PEIE is an insulating material and therefore an optimal coverage of the substrates is required in order to have correctly working devices. **Figure 4** shows how the *J*−*V* characteristics of ITO/D-PEDOT:PSS/PEIE/BHJ7/MoO_3/Ag single-junction devices change in relation to the concentration of PEIE in IPA. If the concentration is too low, the layer is too thin and, eventually, discontinuous, leading to a reduced FF. On the opposite, a too high concentration yields a too thick layer, which hinders tunneling of electrons and creates a barrier at this interface resulting in a lower J_{sc} and FF. At 0.2 wt% PEIE in IPA the device performance of the ITO/D-PEDOT:PSS/PEIE/BHJ7/MoO_3/Ag cells is very similar to that of the reference ITO/ZnO/BHJ7/MoO_3/Ag cell (Figure 4).

The ZnO nanoparticles were synthesized according to the procedure described in detail in the Experimental Section 3.4 of this chapter and were re-dispersed in isoamyl alcohol. Spin-coating the ZnO nanoparticles from isoamyl alcohol on top of a PEDOT:PSS layer is straightforward.

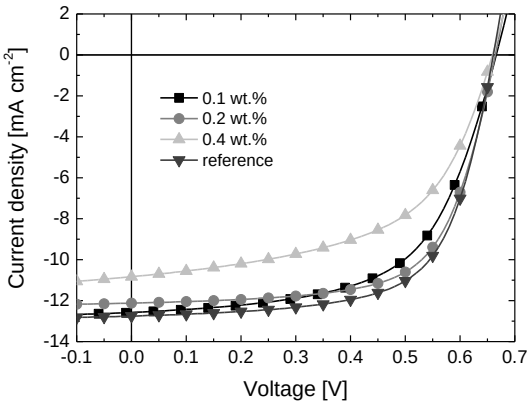

Figure 4. *J*−*V* characteristics of ITO/D-PEDOT:PSS/PEIE/BHJ7/MoO_3/Ag fabricated using different concentrations of PEIE in IPA in wt.%. The reference device with sol-gel ZnO on ITO instead of D-PEDOT:PSS/PEIE is shown for a comparison.

3.2.4 Tandem solar cells

The combination of D-PEDOT:PSS and PEIE or ZnO was used to realize a series of tandem solar cells featuring different active layer materials (**Table 4**). Given the complexity of a full thickness optimization of all layers, we used the optimum thickness of the photoactive layers of the single-junction cells. By doing so it was still possible to evaluate the quality of the ICL by checking the addition of the V_{OC}'s of the subcells. Also the FF of the tandem is determined by the *J*−*V* characteristics of both the subcells, and can be found from the mathematical sum of the *J*−*V* curves along the voltage axis, i.e. at constant current density. In practice the FF of the tandem cell is comparable to that of the current-limiting subcell. If the processing of the complete stack would degrade any of the layers, it would unavoidably lower the FF of the tandem cell.

The experimental V_{OC}'s generally agree within a few tens of mV with the value calculated from the sum of the corresponding single-junction devices (V_{OC}^{sum}). Only for the two tandem cells featuring BHJ3 (PDCBT:PC_{60}BM) in the front cell a substantial loss in V_{OC} was found. In general a 10 to 20 mV loss can be expected because the effective light intensity in each of the subcells of a tandem is less than in a single-junction cell under AM1.5G illumination. This expected loss can be estimated using $\Delta V_{OC} = (kT/q)\ln[J_{SC}(\text{tandem})/J_{SC}(\text{single})]$, i.e. assuming that the ideality factor of diode is unity.

Table 4. Photovoltaic performance of ITO/ZnO/BHJ/D-PEDOT:PSS/ETL/BHJ/MoO_3/Ag tandem solar cells with different active layer materials.

Tandem (Front-Back)	ETL	V_{OC} [a] [V]	V_{OC}^{sum} [b] [V]	J_{SC} [a] [mA cm^{-2}]	FF [a]	PCE [a] [%]	Yield
BHJ1-BHJ6	PEIE	1.47 (1.47)	1.45	6.3 (6.22)	0.62 (0.60)	5.7 (5.48)	4/4
BHJ2-BHJ4	PEIE	1.66 (1.66)	1.69	7.1 (7.04)	0.61 (0.60)	7.2 (7.05)	3/4
BHJ4-BHJ6	PEIE	1.33 (1.33)	1.36	6.9 (6.38)	0.63 (0.62)	5.7 (5.19)	7/8
BHJ7-BHJ7	PEIE	1.32 (1.30)	1.36	6.0 (5.98)	0.77 (0.70)	6.1 (5.46)	16/16
BHJ1-BHJ4 [c]	ZnO	1.68 (1.68)	1.67	7.1 (6.58)	0.62 (0.62)	7.3 (6.75)	6/8
BHJ4-BHJ6	ZnO	1.34 (1.34)	1.36	5.8 (5.36)	0.64 (0.61)	5.0 (4.36)	8/8
BHJ3-BHJ4 [d]	ZnO	1.54 (1.54)	1.65	6.8 (6.70)	0.66 (0.61)	6.9 (6.25)	3/4
BHJ4-BHJ8 [d]	ZnO	1.36 (1.37)	1.40	6.8 (6.81)	0.59 (0.55)	5.5 (5.10)	4/4
BHJ3-BHJ5	ZnO	1.57 (1.58)	1.65	7.8 (7.63)	0.61 (0.60)	7.4 (7.17)	4/4
BHJ5-BHJ8 [e]	ZnO	1.39 (1.39)	1.40	10.1 (9.98)	0.62 (0.62)	8.7 (8.61)	8/8

[a] Values in parenthesis are average values over the number of working devices tested.
[b] Sum of V_{OC}'s of the corresponding single-junction cells (Table 3).
[c] ITO/ZnO/BHJ1/D-PEDOT:PSS/ZnO/BHJ4/D-PEDOT:PSS/MoO_3/Ag.
[d] $PC_{70}BM$ was used instead of $PC_{60}BM$ for BHJ4.
[e] ITO/D-PEDOT:PSS/ZnO/BHJ5/D-PEDOT:PSS/ZnO/BHJ8/MoO_3/Ag.

For BHJ3, the loss is evidently much larger (up to 110 mV). We found that in a single-junction BHJ3 device, the V_{OC} is reduced by about 30 mV when a D-PEDOT:PSS/MoO_3/Ag top contact is used instead of MoO_3/Ag. Apparently the V_{OC} of BHJ3 is sensitive to the details of the processing or the nature of the top contact. Further evidence of the sensitivity of the V_{OC} of BHJ3 was provided by comparison of the $J-V$ characteristics of single-junction devices with thermal annealing either before or after evaporating the MoO_3/Ag top contact (data not shown here). The difference in V_{OC} is 100 mV. Presently, we cannot offer a consistent explanation for this difference, but apparently subtle changes in interface morphology or composition of BHJ3 in the two annealing procedures have a large effect on V_{OC}.

The quality of the tandem solar cells can also be evaluated by considering the FF. In a multi-junction device, the FF is influenced by the FF of each subcell, in particular by the subcell that limits the photocurrent. Comparing Table 2 and Table 4, we can see that the FF of the tandems BHJ1-BHJ6, BHJ4-BHJ6 (both with PEIE and ZnO), BHJ1-BHJ4, BHJ3-BHJ4 and BHJ5-BHJ8 is comparable ($\leq \pm 0.01$) with at least one of the corresponding single-junction cells. For BHJ2-BHJ4, BHJ4-BHJ8 and BHJ3-BHJ5 the corresponding loss in FF is larger, but the FF never went below 0.59. A special case is the BHJ7-BHJ7 tandem cell where

the FF (0.77) was significantly higher than for the single-junction cell (0.68). A possible cause is the reduced light intensity experienced by each subcell (*e.g.* lower bimolecular recombination).

Measuring the external quantum efficiency (EQE) spectrum of a tandem cell gives insight in the current generated by each subcell, but also in the structural integrity of the layers, especially on the presence of current leakage paths in one or more photoactive layers. In an ideal tandem cell, the EQE measured without bias light should follow the lower envelope of the EQEs of the subcells, determined using representative bias light.[47] In case of a leakage, the EQE without bias light can be substantially higher.[47] **Figure 5** shows that the EQEs of BHJ2-BHJ4 (best tandem with PEIE as ETL) and BHJ5-BHJ8 (best tandem with ZnO as ETL) measured without light bias are very close to the expected behavior.

By comparison of V_{OC} and FF values and measuring EQE, we conclude that the D-PEDOT:PSS/PEIE and D-PEDOT:PSS/ZnO ICLs are suitable for use in a range of tandem cell configurations.

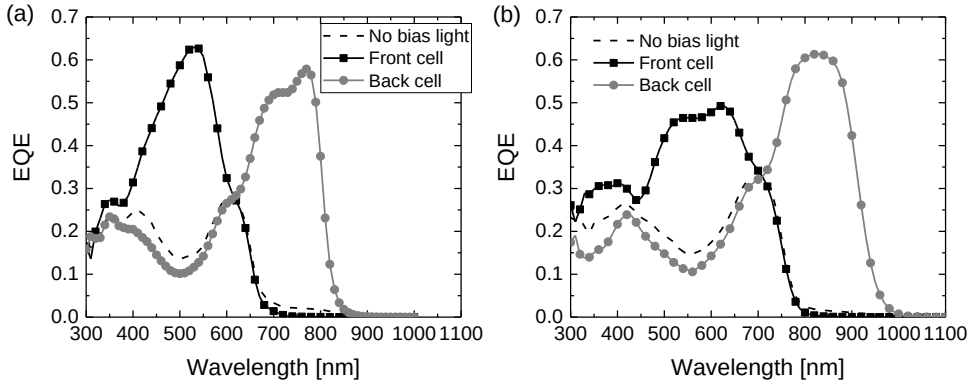

Figure 5. EQE spectra of (a) BHJ2-BHJ4 (PEIE as ETL) and (b) BHJ5-BHJ8 (ZnO as ETL) recorded with (solid lines) and without (dashed lines) bias light; for the nomenclature refer to Table 1. LED sources (530 and 730 nm (a) or 530 and 940 nm (b)) were used to optically bias the front and back subcells, respectively.

3.2.5 ICL for triple-junction solar cells: need for second order orthogonality

After demonstrating tandem solar cells using D-PEDOT:PSS/PEIE and D-PEDOT:PSS/ZnO as ICL, we studied the application of the same layers to fabricate triple-junction cells. To make triple-junction cells, the ICL must withstand the deposition of a BHJ

as well as a subsequent ICL. To test the compatibility of the layers with the solvents necessary for processing, we made ITO/D-PEDOT:PSS/PEIE/BHJ4/MoO_3/Ag single-junction cells and compared their performance with and without rinsing the BHJ4 layer with water/*n*-propanol (1:2), before evaporating the top contact. BHJ4 (PDPPTPT:$PC_{60}BM$) represents an attractive option as middle cell active layer. **Figure 6**a demonstrates that the water/*n*-propanol (1:2 v/v) mixture has a detrimental effect on the device performance. We observed similar behavior also with BHJ1 and BHJ6 as photoactive layer (data not shown here), implying that the effect is not related to the specific choice of the photoactive layer. To better understand the problem, we performed a similar experiment in which we used a ITO/D-PEDOT:PSS/ZnO/BHJ4/(D-PEDOT:PSS)/MoO_3/Ag cell, with and without the second layer of D-PEDOT:PSS on top of the active layer. Figure 6b shows that with ZnO on top of D-PEDOT:PSS the problem does not occur. We thus see that the water/*n*-propanol (1:2 v/v) mixture disrupts the interface between PEDOT:PSS and PEIE, beneath the BHJ layer on which the water/*n*-propanol mixture is processed. Fortuitously, this problem does not occur between D-PEDOT:PSS and the ZnO nanoparticles, such that a D-PEDOT:PSS layer can be processed on a D-PEDOT:PSS/ZnO/BHJ stack. This is remarkable because ZnO is sensitive to the acidic nature of the D-PEDOT:PSS dispersion and we speculate that acidic water does not penetrate the BHJ layer but *n*-propanol does. Given the suitability of the ZnO nanoparticle layer, we adopted this option instead of PEIE to fabricate triple-junction solar cells.

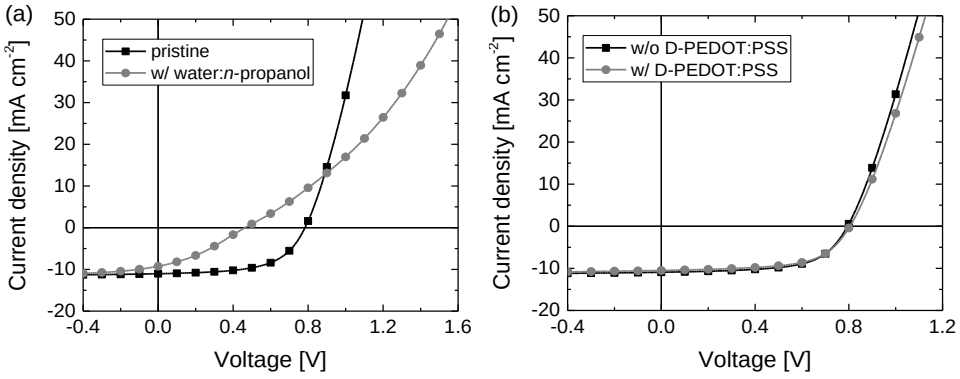

Figure 6. (a) *J*−*V* characteristics of an ITO/D-PEDOT:PSS/PEIE/BHJ4/MoO_3/Ag cell with and without rinsing the active layer with water/*n*-propanol (1:2) before evaporating the top contact. (b) *J*−*V* characteristics of an ITO/D-PEDOT:PSS/ZnO/BHJ4/(D-PEDOT:PSS)/MoO_3/Ag cell with and without the second layer of D-PEDOT:PSS on top of the active layer.

3.2.6 Triple-junction solar cells

We used D-PEDOT:PSS and ZnO nanoparticles to fabricate the ICLs of n-i-p triple-junction polymer solar cells (Figure 1) and first used BHJ1, BHJ4, and BHJ6 in the front, middle, and back subcells, respectively (**Table 5**) using the optimal thicknesses of the single-junction cell for each layer.

Table 5. Photovoltaic performance of ITO/ZnO/BHJ/D-PEDOT:PSS/ZnO/BHJ/D-PEDOT:PSS/ZnO/BHJ/MoO_3/Ag triple-junction solar cells with different active layer materials.

Triple (Front-Middle-Back)	V_{OC} [a] [V]	V_{OC}^{sum} [b] [V]	J_{SC} [a] [mA cm^{-2}]	FF [a]	PCE [a] [%]	Yield
BHJ1-BHJ4-BHJ6	2.26 (2.24)	2.24	4.4 (3.41)	0.61 (0.64)	6.0 (4.89)	12/12
BHJ3-BHJ4-BHJ8 [c]	2.20 (2.19)	2.26	6.0 (5.77)	0.66 (0.60)	8.7 (7.57)	12/12
BHJ3-BHJ5-BHJ8	2.15 (2.15)	2.26	6.9 (6.58)	0.68 (0.69)	10.0 (9.77)	15/16

[a] Values in parenthesis are average values over the number of working devices tested.
[b] Sum of V_{OC}'s of corresponding single-junction cells (Table 3).
[c] $PC_{70}BM$ was used instead of $PC_{60}BM$ for BHJ4.

By adding the values of V_{OC}'s of the single-junction cells from Table 2, a perfect match with the experimental value for the triple cells was found. Also the average FF is consistent with the FFs of the reference cells. The triple cells were fabricated with an excellent yield of 12 good devices out of 12 fabricated. Both the choice of the materials and the optical interference effects dramatically limited the best PCE (about 6%).

To improve the performance, we applied improved materials in the front (BHJ3) and back (BHJ8) subcells. The use of $PC_{60}BM$ in BHJ3 and BHJ8 of the front and back cells was aimed at sacrificing some of the light absorbed by the front and back cell in favor of the middle cell, which is usually current limiting. Again to favor the middle cell, $PC_{70}BM$ instead of $PC_{60}BM$ was adopted in the BHJ4. We further optimized the thickness of the active layers via semi-empirical opto-electrical modeling.[48] The procedure consists of three steps. First we determined the wavelength-dependent refractive index (n) and extinction coefficient (k) of each layer and determined the maximum current generated in single-junction cells using transfer matrix (TM) optical modeling and the AM1.5G spectrum. Next, we fabricated single-junction cells using a range of different active layer thicknesses and measured the $J-V$ characteristics and the EQE. The internal quantum efficiency (IQE) of the single junction at each thickness was determined as the ratio between the J_{SC} obtained by integrating the EQE with the AM1.5G spectrum and the maximum predicted J_{SC} according to the optical

modeling. Finally, we scaled the experimental *J*−*V* characteristics of single-junction cells by the modeled, IQE-corrected J_{SC} value of each subcell and we combined these according to Kirchhoff's law to give the expected *J*−*V* characteristics of the triple-junction cell.[49] The last step is re-iterated for all thickness combinations of interest. All the relevant data are shown in **Appendix 1-3** and **Figure 7**.

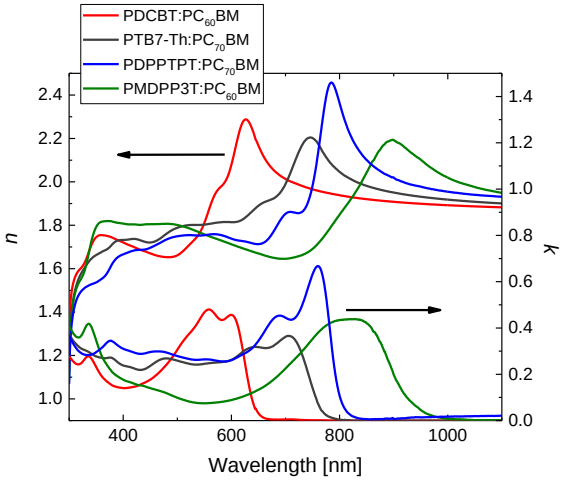

Figure 7. *n* and *k* values of PDCBT:PC_{60}BM (red), PTB7-Th:PC_{70}BM (black), PDPPTPT:PC_{70}BM (blue) and PMDPP3T:PC_{60}BM (green) as a function of the wavelength.

In the optimization, the thickness of the D-PEDOT:PSS (30 nm) and ZnO (20 nm) in the interconnection layer was kept constant. The results of the optimization are summarized in **Figure 8**a.

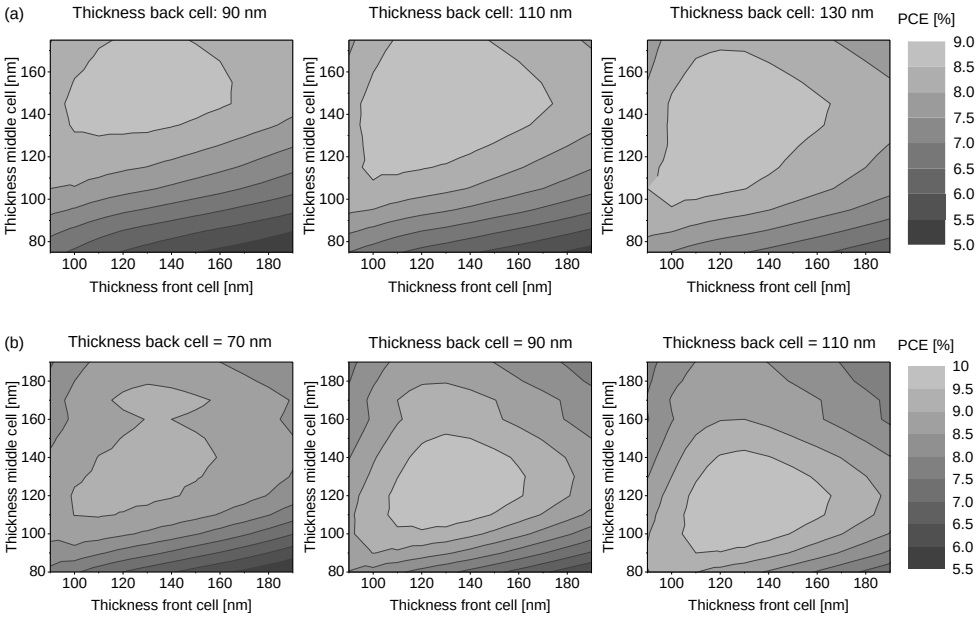

Figure 8. Expected PCE for an ITO/ZnO/BHJ3/D-PEDOT:PSS/ZnO/Middle cell/D-PEDOT:PSS/ZnO/BHJ8/MoO_3/Ag triple-junction solar cell as a function of the thickness of each active layer, according to opto-electrical modeling optimization. The middle cell is PDPPTPT:$PC_{70}BM$ (a) or PTB7-Th:$PC_{70}BM$ (b).

On the basis of the modeling, we selected 130, 145, and 110 nm, respectively, for the front, middle, and back subcells. By using this combination of thicknesses, a PCE of around 9% was expected. Table 5 reveals that the PCE (8.7%) of the best cell is close to the predicted PCE. The difference is acceptable, considering the approximations adopted in the optimization. Similarly to the tandems with BHJ3, a 60 mV loss in the V_{OC} appeared also in this triple. The best FF (0.66) nicely lies in the middle of the range reported for the references.

The EQE of the triple-junction cell was measured using appropriate light bias, voltage bias and light intensity corrections following a protocol which will be described in detail in Chapter 4. From the EQE spectra in **Figure 9**a, it can be seen that the middle cell (PDPPTPT:$PC_{70}BM$) gave a low EQE signal, limiting the total current extracted from the device. Integration of the three EQEs with the AM1.5G spectrum gave 7.13, 5.70 and 6.63 mA cm^{-2}. The low current generated by the middle cell is due to the modest IQE = 0.64 at the optimal thickness (145 nm).

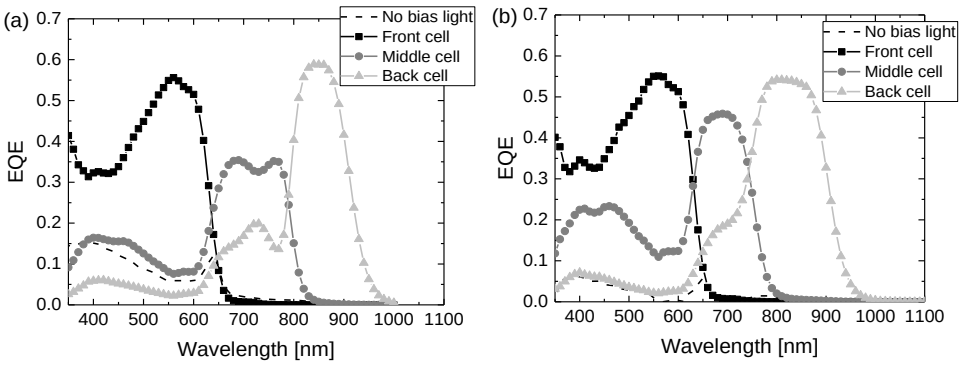

Figure 9. (a) EQE measurements of the best BHJ3-BHJ4-BHJ8 triple-junction device (with $PC_{70}BM$ instead of $PC_{60}BM$ in BHJ4). Conditions for light and voltage bias: Front cell: 730 nm LED at 87 mW cm^{-2} and V_{bias} = 1.29 V; Middle cell: 530 nm LED at 44 mW cm^{-2} with 940 nm LED at 78 mW cm^{-2} and V_{bias} =1.36 V; (signal was scaled by the light-intensity-dependence factor 0.95); Back cell: 530 nm LED at 67 mW cm^{-2} and V_{bias} = 1.45 V. (b) EQE of the best BHJ3-BHJ5-BHJ8 triple-junction device. Conditions for light and voltage bias: Front cell: 730 nm LED at 86 mW cm^{-2} and V_{bias} = 1.36 V; Middle cell: 530 nm LED at 42 mW cm^{-2} with 940 nm LED at 76 mW cm^{-2} and V_{bias} =1.40 V; (signal was scaled by the light-intensity-dependence factor 0.96); Back cell: 530 nm LED at 67 mW cm^{-2} and V_{bias} = 1.51 V.

To improve the performance of the triple-junction cell, we used PTB7-Th instead of PDPPTPT as the absorber layer for the middle cell. PTB7-Th:$PC_{70}BM$ (BHJ5) has opto-electronic properties close to PDPPTPT:$PC_{70}BM$ but has a significantly higher IQE of 0.84 (at 145 nm, see Appendix 4), opening up the possibility of a higher current in a triple-junction solar cell. We optimized the triple device with BHJ3, BHJ5, and BHJ8 as front, middle, and back subcells using the semi-empirical method described above. The input data for BHJ5 is reported in **Appendix 4** and Figure 7. The results are reported in Figure 8b. The optimal thicknesses found were 130, 140, and 90 nm for the front, middle, and back subcells, respectively. For this combination, a PCE of 10% was predicted and the corresponding experimental results are reported in Table 5. The EQE in Figure 9b reveals that the BHJ5 middle cell provides a significantly enhanced performance compared to PDPPTPT:$PC_{70}BM$ as middle cell (Figure 9a). Because of the small blue-shift in the absorption of BHJ5 compared to BHJ4, also the back cell received more light, increasing the width of its peak in the EQE spectrum. Consequently, the EQE-integrated J_{SC} values for the front, middle and back subcells were, respectively: 7.16, 6.61, and 7.53 mA cm^{-2}. In addition to this, a remarkable FF of 0.68 was determined for such a complex stack of 8 layers sequentially processed by spin-coating and 2 additional layers by thermal evaporation.

3.2.7 Synopsis

By considering the results for the tandem and triple-junction cells, we find that the combination of D-PEDOT:PSS/nanoparticle ZnO allowed us to use the same coating techniques to make a wide variety of layer stacks with different active layers in multi-junction devices. Besides its versatility for processing, the D-PEDOT:PSS/nanoparticle ZnO ICL matches the energy levels of the active layers adopted with very few exceptions where the V_{OC} dropped by more than 50 mV (partially due to contact issues of one of the chosen materials, PDCBT). Regarding the FF, only a small loss was observed for some of the tandems compared to the individual subcell devices. Using opto-electrical optimization and by fabricating triple-junction cells, we demonstrated that the D-PEDOT:PSS/nanoparticle ZnO combination provides an almost loss-less ICL. State-of-the-art triple-junction polymer solar cell with 10% power conversion efficiency were fabricated in excellent yields (15/16) where the PCE is limited by the photoactive layers.

3.3 Conclusions

We developed novel ink formulations to deposit virtually loss-less interconnecting layers for solution-processed n-i-p multi-junction polymer solar cells, using PEDOT:PSS, ZnO or PEIE. By selecting suitable co-solvents, we improved the film-forming properties of the dispersions and solutions from which these materials were processed, while preserving their optical, electrical and structural properties. The formulations are relatively simple and can be used with a wide range of active layer materials of different chemical nature without adjustments.

For tandem cells both ZnO and PEIE are convenient as ETL of an ICL. We reported the results of six different tandem cells with nearly loss-less ICL performance. For fabricating triple-junction solar cells we find that PEIE is not suitable in the bottom ICL because it deteriorates upon deposition of the top ICL. We hypothesize that the very thin layer of PEIE (< 10 nm) in the bottom ICL might intermix with the PEDOT:PSS at their interface as a consequence of the processing of another layer of PEDOT:PSS on top of the middle cell. This problem is avoided by using ZnO nanoparticles. By a more judicious choice of the active layer materials and opto-electrical optimization, the efficiency of the triple-junction cells was improved to 10%, with very good reproducibility, demonstrating that the ICL allows to achieve state-of-the-art performance.

The new formulations of PEDOT:PSS, diluted in a near azeotropic water/*n*-propanol mixture, and ZnO nanoparticles, dispersed in isoamyl alcohol, represent a versatile combination to fabricate a nearly loss-less ICL for solution-processed multi-junction n-i-p polymer solar cells. It alleviates the tedious task of developing and adjusting the ICL for each

specific case. We encourage researchers to adopt these layers for optimizing future multi-junction devices with novel and improved active layer materials.

3.4 Experimental Section

Materials: Pre-patterned ITO (150 nm) on glass substrates were purchased from Naranjo Substrates. Molybdenum trioxide powder (99.97%) was purchased from Sigma Aldrich. The ZnO was either made by a sol-gel route or from pre-formed nanoparticles with average diameter of 4 nm, as confirmed by dynamic light scattering measurements (see the corresponding paragraph for the synthesis). The sol-gel consisted of a solution 0.5 M $Zn(CH_3COO)_2 \cdot 2H_2O$ (98 %, Acros Organics) and 0.5 M ethanolamine in 2-methoxyethanol. The suspension of D-PEDOT:PSS was prepared starting from the commercial formulation Clevios P VPAl 4083. After filtering it with a PVDF 0.45 μm filter we diluted it with *n*-propanol while vigorously stirring. For the optimal dilution ratio of 1:2 we added *n*-propanol (1 mL) to VPAl 4083 (0.5 mL) in 15 minutes. The suspension was prepared fresh every time, right before depositing PEDOT:PSS, and no further additives were used. PEIE was purchased from Sigma Aldrich (batch 04814BGV). Starting from the pristine concentration in water, which was 37 wt.%, we diluted in isopropanol until the total mass fraction of PEIE became 0.2 wt.% (tandems BHJ1-BHJ6, BHJ2-BHJ4 and BHJ7-BHJ7) or 0.1 wt.% (single-junction cell of BHJ1 in Table 3 and tandem BHJ4-BHJ6). No particular stirring or additional operation were used after the addition and the solution was stable for more than 3 weeks. $PC_{60}BM$ and $PC_{70}BM$ were purchased from Solenne B.V. PCDTBT was purchased from 1-Material (batch YY7276) and blended with $PC_{70}BM$ in a 1:4 (w/w) ratio in chlorobenzene at a polymer concentration of 7 mg mL^{-1}. PBDTTPD[50] was mixed with $PC_{70}BM$ in a 1:1.5 (w/w) ratio in chlorobenzene with 5 vol.% of 1-chloronaphthalene at a polymer concentration of 8 mg mL^{-1}. PDCBT[32] was blended with $PC_{60}BM$ in a 1:1 (w/w) ratio in chloroform containing 1 vol.% of *o*-dichlorobenzene at a polymer concentration of 10 mg mL^{-1}. PDPP5T[33] was combined with $PC_{60}BM$ in 1:2 (w/w) ratio in chloroform with 10 vol.% *o*-dichlorobenzene at a polymer concentration of 6 mg mL^{-1}. PDPP3T[51] was blended with $PC_{60}BM$ 1:2 (w/w) and dissolved in chloroform with 7 vol.% *o*-dichlorobenzene at a polymer concentration of 5 mg mL^{-1}. The methylated derivative PMDPP3T[4] was blended with $PC_{60}BM$ 1:3 (w/w) and dissolved in chloroform containing 7 vol.% *o*-dichlorobenzene at a polymer concentration of 4 mg mL^{-1}. PDPPTPT[51] was blended with $PC_{60}BM$ 1:2 (w/w) or $PC_{70}BM$ 1:2 (w/w) in chloroform with 6 vol.% *o*-dichlorobenzene at a polymer concentration of 5 mg mL^{-1}. PTB7-Th was purchased from 1-Material, mixed with $PC_{70}BM$ (1:1.5 w/w) and dissolved in chlorobenzene containing 3 vol.% diiodooctane at a concentration of 9 mg mL^{-1}(reference and tandem cells) or 12 mg mL^{-1} (triple junction cells) of polymer.[36]

Synthesis of ZnO nanoparticles: Zinc acetate dehydrate (98%, Acros Organics) (26.53 g) was weighted in a round bottom flask and dissolved in methanol (475 mL) by stirring for 10 min. A mild argon supply was plugged to the flask as well as a reflux cooler and a dropping funnel. The flask was set in a water bath with controllable temperature. Demineralized water (4 mL) was added to the solution and the water bath set to 30 °C. KOH (13.26 g) was dissolved in methanol (200 mL) and transferred to the dropping funnel. The KOH solution was added dropwise over 15 min while vigorously stirring. After the addition the reaction mixture appeared milky white. The temperature of the water bath was increased to 67 °C and after 2 h, the water bath was removed and methanol (200 mL) was added to the round bottom flask, stirring for 5 min more. At the end, the mixture looked greyish white. Stirring was stopped and the particles were allowed to sediment for 2.5 h (a mild Ar flow was maintained). The upper liquid was carefully removed using a pipette. Then methanol (400 mL) was added and the suspension was stirred for 10 min. Again, stirring was stopped and the particles were allowed to sediment for 2.5 h, under Ar flow. The clear upper liquid was removed carefully and methanol (300 mL) was added again. Then all methanol was decanted by centrifuging and the ZnO nanoparticles sediment was re-dispersed directly in acetone. The new dispersion was sonicated for 3 days and filtered using a 0.2 μm PTFE filter, resulting in a clear, translucent ZnO dispersion. The suspension was again re-dispersed in isoamyl alcohol to achieve a ZnO concentration of 10 mg mL^{-1}. 2-(2-Methoxyethoxy)acetic acid was added as stabilizer to the acetone dispersion in a round bottom flask, with a concentration of 0.47 μL mL^{-1}. Ultra-sonication for 5 min followed and then the lower boiling point acetone was removed by rotary evaporation at ~70 °C under vacuum.

Device fabrication: Pre-patterned ITO-coated glass substrates were cleaned by sonication in acetone, followed by water and sodium dodecyl sulfate in water. After rinsing in water they were again sonicated in isopropanol. To finish the cleaning, 30 min of UV-ozone treatment preceded the spin-coating of the first layer. Sol-gel ZnO was cast directly on clean ITO substrates by spin-coating in ambient air and annealed at 150 °C for 5 min on a hotplate. The D-PEDOT:PSS dispersion was processed by spin-coating (45 nm for BHJ1-BHJ6 and 60 nm for BHJ2-BHJ4 and BHJ4-BHJ6 with PEIE) or dynamic spin-coating (45 nm for BHJ1-BHJ4, BHJ7-BHJ7, BHJ3-BHJ5, BHJ5-BHJ8 tandems and the BHJ3-BHJ5-BHJ8 triple, and 30 nm for all the other tandems and triples) in a nitrogen filled glove box for improved wetting. The layer was kept in the vacuum at ~10^{-2} mbar for 30 min right after spin-coating to remove residual solvents and no further treatment was performed. The PEIE solution was cast by spin-coating in air to form a very thin (~10 nm) layer. The ZnO nanoparticle dispersion was dynamically spin-coated in ambient air to give a 20 nm thick layer, without any post treatment. The last step in the fabrication of each of these devices was the evaporation of the top contact. In all cases this was accomplished by evaporating MoO_3 (10 nm), followed by Ag (100 nm) in a vacuum chamber at ca. 6×10^{-7} mbar, through a shadow mask. On each substrate, the intersection of the ITO pattern with the evaporated top

contact formed two squares of 9 mm^2 area and two squares of 16 mm^2 area. The thickness of each layer was measured using a Veeco Dektak profilometer.

Single-junction cells: Cleaned ITO substrates were covered with 40 nm of sol-gel ZnO. Subsequently, the active layer was spin-coated following different procedures. BHJ1 (85 nm) was spin-coated in a glove box and annealed at 70 °C for 10 min. BHJ2 (50 nm) was also spin-coated in a glove box and used without thermal annealing. BHJ3 (130 nm) was deposited in a glove box and annealed at 100 °C for 5 min and again at 105 °C for 5 min after evaporation of the top contact to improve the V_{OC}. Spin-coating of BHJ4 (85 nm) was performed in air. BHJ5 (85 nm) was cast in a glove box and the samples were kept at ~10^{-2} mbar for 2 h after spin-coating. BHJ6 (100 nm), BHJ7 (130 nm) and BHJ8 (110 nm) were spin-coated in air without any post-treatment. After depositing the active layer, all cells were completed by evaporating the top contact.

For the BHJ1 devices reported in Table 3, PEIE was deposited on ITO, followed by the BHJ1 layer as reported. D-PEDOT:PSS was deposited by spin-coating in a nitrogen filled glovebox from 1:1, 1:2, 1:3, 1:4 and 1:5 (v/v) dispersions in water/*n*-propanol. The top contact in this case was Ag (100 nm).

For the single-junction cells shown in Figure 4, D-PEDOT:PSS was deposited by spin-coating on clean ITO substrates to form a 45 nm thick layer and the samples were dried at ~10^{-2} mbar for 30 min. PEIE was spin-coated from solutions with different solid content (0.1, 0.2 and 0.4 wt.%). BHJ7 (130 nm) was then spin-coated in air without any post treatment. The top contact was thermally evaporated.

For the solar cells of BHJ4 shown in Figure 6, D-PEDOT:PSS was spin-coated in a glove box directly on clean ITO substrates to form a 45 nm thick layer. The samples were kept in vacuum at ~10^{-2} mbar for 30 min. PEIE or ZnO nanoparticles were then spin-coated, followed by the active layer of BHJ4 (85 nm). The water/*n*-propanol (1:2 v/v) mixture or another layer of D-PEDOT:PSS was spin-coated on top of the active layer, followed by the evaporation of the top contact.

Tandem cells: Cleaned ITO substrates were covered with 40 nm sol-gel ZnO. The active layer of the front cell was processed as described for the single-junctions cells, except for the tandem BHJ4-BHJ8 (Table 4), where the BHJ4 layer was 145 nm thick and $PC_{70}BM$ substituted $PC_{60}BM$. Then D-PEDOT:PSS was processed as described before. For the BHJ3-BHJ4 and BHJ3-BHJ5 tandem cells a second annealing step of the front cell was performed at 105 °C for 5 min to improve the V_{OC}. To complete the ICL, either PEIE or the ZnO nanoparticles were deposited as reported. Deposition of the back cells followed the same procedure as for the single cells, except for the BHJ3-BHJ4 tandem (Table 4), where the back cell of BHJ4 was 145 nm thick and $PC_{70}BM$ substituted $PC_{60}BM$. The top contact was formed by evaporation.

The tandem BHJ1-BHJ4 differed from the others by an additional layer of D-PEDOT:PSS (30 nm) between the BHJ4 back cell and the top contact. Also the tandem BHJ5-BHJ8 differed from the others, using another layer of D-PEDOT:PSS between ITO and the first layer of ZnO nanoparticles.

Triple-junction devices: For all the triple-junction cells, the fabrication started from sol-gel ZnO (40 nm) on clean ITO substrates, followed by the first active layer as described above. Subsequently D-PEDOT:PSS was deposited with a thickness of 30 nm (BHJ1-BHJ4-BHJ6 and BHJ3-BHJ4-BHJ8) or 45 nm (BHJ3-BHJ5-BHJ8). Whenever the front cell was BHJ3, a post annealing at 105 °C for 5 min was performed. After this, ZnO nanoparticles were deposited. For the middle cell, the same thickness of BHJ4 as for the single cells was used in the first, non-optimal triple of Table 5. In the second triple $PC_{70}BM$ replaced $PC_{60}BM$, and as a consequence of the optimization, a thicker active layer was used, in order to absorb more light: 145 nm. Also for the last triple a thicker active layer of BHJ5 was adopted: 140 nm. On top of the middle cell, another layer of D-PEDOT:PSS was processed in the same way as in the bottom ICL of each triple. Then ZnO nanoparticles followed to complete the second ICL. After this, the top cell was spin-coated as described for single-junction cells, with the only difference that the thickness of BHJ8 in the last triple was 90 nm. To finish, the top contact was evaporated.

Characterization: All measurements were performed under N_2 atmosphere. In order to photodope the ZnO and MoO_3 layers, 6 min of UV exposition were performed right before the measurement for all cells. The characteristic $J-V$ curve was measured from −2 V to +2 V for single and double-junction cells and to +2.6 V for triples. The number of voltage steps was 401, with an integration time of 20 ms at each point. Simulated solar light from a tungsten-halogen lamp filtered with a UV filter and daylight filter (Hoya LB120) was shined on the cells during the measurement of the $J-V$ characteristics. The color of the spectrum and the intensity of it were adjusted to match the EQE-integrated J_{SC} of the single-junction cells, to warrant that the PCE can be determined from the $J-V$ characteristics. To accurately define the active area of the cells, the 4 squares from the intersection of top and bottom contact were masked with an aperture slightly smaller than their size: 6.76 and 12.96 mm^2 for the 9 and 16 mm^2 squares, respectively.

The EQE was measured using a custom-made setup consisting of the following: a tungsten-halogen lamp, a chopper, a monochromator (Oriel, Cornerstone 130), a pre-amplifier (Stanford Research Systems SR570) and a lock-in amplifier (Stanford Research Systems SR830 DSP). Although the setup was in ambient air, the substrates were constantly kept sealed in a N_2 filled box equipped with a quartz window. For this measurement, a circular aperture size of 2 mm of diameter was used to define the active area. To convert the current signal from the cell into an EQE value, a comparison was made with a reference calibrated silicon solar cell. In the range of wavelengths 350-1050 nm, the standard deviation

of this setup is less than 0.005 electrons/photons. As bias light, a 530, 730, and 940 nm high power LEDs from Thorlabs were involved. The voltage bias correction was applied directly from the pre-amplifier.

Optical modeling: This was done using the transfer matrix (TM) method using Setfos 3.2 software (Fluxim AG). By measuring transmission and reflection of each layer, we estimated the *n* and *k* values as a function of the wavelength (see Chapter 1). To optimize the thickness of each active layer in the triples, we used an extension of a procedure already published for tandems.[48] This consisted in modeling iteratively the current generation of each subcell, correcting it for the corresponding IQE. The combination of this data with the normalized $J-V$ characteristics of the subcells returned the $J-V$ characteristics of the triple for each of the tested combination of thicknesses. The determination of the voltage bias correction for the EQE of the two optimized triples followed the procedure developed in Chapter 4.

3.5 References

[1] Y. Cui, H. Yao, B. Gao, Y. Qin, S. Zhang, B. Yang, C. He, B. Xu, J. Hou, *J. Am. Chem. Soc.* **2017**, *139*, 7302.

[2] J. Y. Kim, K. Lee, N. E. Coates, D. Moses, T.-Q. Nguyen, M. Dante, A. J. Heeger, *Science* **2007**, *317*, 222.

[3] L. Dou, J. You, J. Yang, C.-C. Chen, Y. He, S. Murase, T. Moriarty, K. Emery, G. Li, Y. Yang, *Nat. Photonics* **2012**, *6*, 180.

[4] W. Li, A. Furlan, K. H. Hendriks, M. M. Wienk, R. A. J. Janssen, *J. Am. Chem. Soc.* **2013**, *135*, 5529.

[5] S. Sista, M.-H. Park, Z. Hong, Y. Wu, J. Hou, W. L. Kwan, G. Li, Y. Yang, *Adv. Mater.* **2010**, *22*, 380.

[6] J. Yang, J. You, C.-C. Chen, W.-C. Hsu, H. Tan, X. W. Zhang, Z. Hong, Y. Yang, *ACS Nano* **2011**, *5*, 6210.

[7] H. Zhou, Y. Zhang, C. K. Mai, S. D. Collins, G. C. Bazan, T. Q. Nguyen, A. J. Heeger, *Adv. Mater.* **2015**, *27*, 1767.

[8] K. Zhang, K. Gao, R. Xia, Z. Wu, C. Sun, J. Cao, L. Qian, W. Li, S. Liu, F. Huang, X. Peng, L. Ding, H.-L. Yip, Y. Cao, *Adv. Mater.* **2016**, *28*, 4817.

[9] Z. Zheng, S. Zhang, J. Zhang, Y. Qin, W. Li, R. Yu, Z. Wei, J. Hou, *Adv. Mater.* **2016**, *28*, 5133.

[10] Y. Gao, V. M. Le Corre, A. Gaïtis, M. Neophytou, M. A. Hamid, K. Takanabe, P. M. Beaujuge, *Adv. Mater.* **2016**, *28*, 3366.

[11] Y. Ma, S.-C. Chen, Z. Wang, W. Ma, J. Wang, Z. Yin, C. Tang, D. Cai, Q. Zheng, *Nano Energy* **2017**, *33*, 313.

[12] S. Esiner, H. Van Eersel, M. M. Wienk, R. A. J. Janssen, *Adv. Mater.* **2013**, *25*, 2932.

[13] T. Becker, S. Trost, A. Behrendt, I. Shutsko, A. Polywka, P. Görrn, P. Reckers, C. Das, T. Mayer, D. Di Carlo Rasi, K. H. Hendriks, M. M. Wienk, R. A. J. Janssen, T. Riedl, *Adv. Energy Mater.* **2018**, *8*, 1702533.

[14] A. R. b. M. Yusoff, H. P. Kim, J. Jang, *Energy Technol.* **2013**, *1*, 212.

[15] X. Du, O. Lytken, M. S. Killian, J. Cao, T. Stubhan, M. Turbiez, P. Schmuki, H.-P. Steinrück, L. Ding, R. H. Fink, N. Li, C. J. Brabec, *Adv. Energy Mater.* **2017**, *7*, 1601959.

[16] X. Guo, F. Liu, W. Yue, Z. Xie, Y. Geng, L. Wang, *Org. Electron.* **2009**, *10*, 1174.

[17] S. Sista, Z. Hong, M.-H. Park, Z. Xu, Y. Yang, *Adv. Mater.* **2010**, *22*, E77.

[18] C.-C. Chen, W.-H. Chang, K. Yoshimura, K. Ohya, J. You, J. Gao, Z. Hong, Y. Yang, *Adv. Mater.* **2014**, *26*, 5670.

[19] V. C. Tung, J. Kim, L. J. Cote, J. Huang, *J. Am. Chem. Soc.* **2011**, *133*, 9262.

[20] J. Gilot, M. M. Wienk, R. A. J. Janssen, *Appl. Phys. Lett.* **2007**, *90*, 143512.

[21] A. R. B. M. Yusoff, S. J. Lee, J. Kim, F. K. Shneider, W. J. da Silva, J. Jang, *ACS Appl. Mater. Interfaces* **2014**, *6*, 13079.

[22] S. K. Hau, H.-L. Yip, K.-S. Chen, J. Zou, A. K.-Y. Jen, *Appl. Phys. Lett*., 2010, **97**, 253307.

[23] Z. Zheng, S. Zhang, M. Zhang, K. Zhao, L. Ye, Y. Chen, B. Yang, J. Hou, *Adv. Mater*. **2015**, *27*, 1189.

[24] Y. Zhou, C. Fuentes-Hernandez, J. W. Shim, T. M. Khan, B. Kippelen, *Energy Environ. Sci*. **2012**, *5*, 9827

[25] J. Lee, H. Kang, J. Kong, K. Lee, *Adv. Energy Mater.* **2014**, *4*, 1301226.

[26] J. Yang, R. Zhu, Z. Hong, Y. He, A. Kumar, Y. Li, Y. Yang, *Adv. Mater.* **2011**, *23*, 3465.

[27] J. C. Gustafsson, B. Liedberg, O. Inganäs, *Solid State lonics* **1994**, *69*, 145.

[28] S. Esiner, G. W. P. van Pruissen, M. M. Wienk, R. A. J. Janssen, *J. Mater. Chem. A*, **2016**, *4*, 5107.

[29] C. Tao, S. Ruan, X. Zhang, G. Xie, L. Shen, X. Kong, W. Dong, C. Liu, W. Chen, *Appl. Phys. Lett.* **2008**, *93*, 193307.

[30] N. Blouin, A. Michaud, M. Leclerc, *Adv. Mater.* **2007**, *19*, 2295.

[31] C. Dyer-Smith, I. A. Howard, C. Cabanetos, A. El Labban, P. M. Beaujuge, F. Laquai, *Adv. Energy Mater.* **2015**, *5*, 1401778.

[32] M. Zhang, X. Guo, W. Ma, H. Ade, J. Hou, *Adv. Mater.* **2014**, *26*, 5880.

[33] M. Dueggeli, M. Zaher Eteish, P. Hayoz, O. F. Aebischer, M. Fonrodona Turon, M. G. R. Turbiez, *PCT Int Appl.* **2010**, WO 2010049323

[34] J. C. Bijleveld, A. P. Zoombelt, S. G. J. Mathijssen, M. M. Wienk, M. Turbiez, D. M. de Leeuw, R. A. J. Janssen, *J. Am. Chem. Soc.* **2009**, *131*, 16616.

[35] J. C. Bijleveld, V. S. Gevaerts, D. Di Nuzzo, M. Turbiez, S. G. J. Mathijssen, D. M. de Leeuw, M. M. Wienk, R. A. J. Janssen, *Adv. Mater.* **2010**, *22*, E242.

[36] S. H. Liao, H. J. Jhuo, Y. S. Cheng, S. A. Chen, *Adv. Mater.* **2013**, *25*, 4766.

[37] S. Kouijzer, S. Esiner, C. H. Frijters, M. Turbiez, M. M. Wienk, R. A. J. Janssen, *Adv. Energy Mater*. **2012**, *2*, 945.

[38] J. Jo, J.-R. Pouliot, D. Wynands, S. D. Collins, J. Y. Kim, T. L. Nguyen, H. Y. Woo, Y. Sun, M. Leclerc, A. J. Heeger, *Adv. Mater.* **2013**, *25*, 4783.

[39] J.-H. Kim, C. E. Song, H. U. Kim, A. C. Grimsdale, S.-J. Moon, W. S. Shin, S. K. Choi, D.-H. Hwang, *Chem. Mater.* **2013**, *25*, 2722

[40] P.-N. Yeh, T.-H. Jen, Y.-S. Cheng, S.-A. Chen, *Sol. Energy Mater. Sol. Cells* **2014**, *120*, 728.

[41] J.-H. Kim, C. E. Song, B. S. Kim, I.-N. Kang, W. S. Shin, D.-H Hwang, *Chem. Mater.* **2014**, *26*, 1234.

[42] C.-Y. Chang, L. Zuo, H.-L. Yip, C.-Z. Li, Y. Li, C.-S. Hsu, Y.-J. Cheng, H. Chen, A. K.-Y. Jen, *Adv. Energy Mater.* **2014**, *4*, 1301645.

[43] D. Gupta, M. M. Wienk, R. A. J. Janssen, *ACS Appl. Mater. Interfaces* **2014**, *6*, 13937.

[44] S. Lu, H. Lin, S. Q. Zhang, J. H. Hou, W. C. H. Choy, *Adv. Energy Mater*. **2017**, *21*, 1701164.

[45] S. M. Rowan, M. I. Newton, F. W. Driewer, G. McHale, *J. Phys. Chem. B* **2000**, *104*, 8217.

[46] Y. Zhou, C. Fuentes-Hernandez, J. Shim, J. Meyer, A. J. Giordano, H. Li, P. Winget, T. Papadopoulos, H. Cheun, J. Kim, M. Fenoll, A. Dindar, W. Haske, E. Najafabadi, T. M. Khan, H. Sojoudi, S. Barlow, S. Graham, J.-L. Brédas, S. R. Marder, A. Kahn, B. Kippelen, *Science* **2012**, *336*, 327.

[47] R. Timmreck, T. Meyer, J. Gilot, H. Seifert, T. Mueller, A. Furlan, M. M. Wienk, D. Wynands, J. Hohl-Ebinger, W. Warta, R. A. J. Janssen, M. Riede, K. Leo, *Nat. Photonics* **2015**, *9*, 478.

[48] J. Gilot, M. M. Wienk, R. A. J. Janssen, *Adv. Mater.* **2010**, *22*, 67.

[49] A. Hadipour, B. de Boer, P. W. M. Blom, *Org. Electron*. **2008**, *9*, 617.

[50] G. Pirotte, J. Kesters, P. Verstappen, S. Govaerts, J. Manca, L. Lutsen, D. Vanderzande, W. Maes, *ChemSusChem* **2015**, *8*, 3228.

[51] K. H. Hendriks, G. H. L. Heintges, V. S. Gevaerts, M. M. Wienk, R. A. J. Janssen, *Angew. Chemie Int. Ed.* **2013**, *52*, 8341.

Chapter 4

Accurate Characterization of Triple-Junction Polymer Solar Cells*

Abstract

Triple-junction device architectures represent a promising strategy to highly efficient organic solar cells. Accurate characterization of such devices is challenging, especially with respect to determining the external quantum efficiency (EQE) of the individual subcells. The specific light bias conditions that are commonly used to determine the EQE of a subcell of interest cause an excess of charge generation in the two other subcells. This results in the build-up of an electric field over the subcell of interest, which enhances current generation and leads to an overestimation of the EQE. A new protocol, involving optical modeling, is developed to correctly measure the EQE of triple-junction organic solar cells. Apart from correcting for the build-up electric field, the effect of light intensity is considered with the help of representative single-junction cells. The short-circuit current density (J_{SC}) determined from integration of the EQE with the AM1.5G solar spectrum differs by up to 10% between corrected and un-corrected protocols. The results are validated by comparing the EQE experimentally measured to the EQE calculated via optical-electronic modeling, obtaining an excellent agreement.

* This chapter has been published as: D. Di Carlo Rasi, K. H. Hendriks, M. M. Wienk, R. A. J. Janssen, *Adv. Energy Mater.* **2017**, *7*, 1701664.

4.1 Introduction

Referring to Chapter 2, it strikes that most of the studies have focused on the tandem architecture, in which identical or different absorber layers are used, resulting in maximum efficiencies up to 17.3%.[1] At least conceptually, stacking three absorber layers in a triple-junction solar cell can lead to a further increase in efficiency. There are few examples of triple-junction organic solar cells.[2-20] The gain in efficiency achieved by these triple-junction devices was not always accompanied by a critical analysis of the measured performance. In Chapter 2 a recent publication by Timmreck et al. was mentioned, which methodically analyzed the literature on tandem organic solar cells, shedding light on the fact that the vast majority of the publications on organic tandem cells lacked a proper characterization.[21] The follow-up analysis given in Chapter 2 showed that there are still some criticalities in recent articles on multi junctions. Although the paper focused attention on the tandem structure, the argumentations provided can reasonably be extended to the case of triple junctions. At present, the characterization of organic triple junctions is often limited to measuring the $J-V$ characteristics under simulated solar radiation and determining the EQE using different light sources to optically bias the subcells.[2-20] Nevertheless, organic materials commonly employed for solar cells feature peculiar characteristics that necessitate special attention for their EQE measurement.[21-23] An accurate analysis of the effect of bias light and bias voltage on the EQE of triple-junction organic solar cells is necessary.

Detailed protocols for the characterization of triple-junction solar cells are available in the literature.[24] For many inorganic triple-junction solar cells the effect of bias voltage on the spectral response is very small, which makes correction for bias voltage not critical.[24] The aim of this work is to provide a characterization protocol for organic triple-junction solar cells that takes into account the uniqueness of these particular materials. In order to do so, we combine optical and electrical modeling, use representative single-junction cells, and perform EQE measurements with appropriate light and voltage bias. We used a representative highly efficient (~10%) triple-junction organic solar cell to develop the procedure. We found a significant overestimation, by up to 10%, of the current generated by the subcells and the overall efficiency, when the EQE was measured with bias light but without the correct bias voltage. The opto-electrical modeling of the expected EQE provided a remarkably good agreement with the experimental results, when measured correctly.

4.2 Results and Discussion

4.2.1 The design of the triple-junction cell

Three photoactive polymers with different optical band gaps were selected for the triple-junction device. Poly[5,5′-bis(2-butyloctyl)-(2,2′-bithiophene)-4,4′-dicarboxylate-*alt*-5,5′-2,2′-bithiophene] (PDCBT) is a wide band-gap polymer (1.90 eV) that was first presented by Zhang et al. as a polythiophene derivative with photovoltaic properties superior to those of poly[3-hexylthiophene] (P3HT).[25] This material was blended with [6,6]-phenyl-C_{61}-butyric acid methyl ester ($PC_{60}BM$) as acceptor to form the active layer of the front subcell. For the middle subcell we used poly[4,8-bis(5-(2-ethylhexyl)thiophen-2-yl)benzo[1,2-*b*:4,5-*b*′]dithiophene-*co*-3-fluorothieno[3,4-*b*]thiophene-2-carboxylate] (PTB7-Th) with a medium band gap (1.58 eV). PTB7-Th performs remarkably well in single-,[26] double-,[27] and triple-junction[11] solar cells. PTB7-Th was blended with [6,6]-phenyl-C_{71}-butyric acid methyl ester ($PC_{70}BM$) to improve the current generation for the middle subcell. For the back subcell we used poly[[2,5-bis(2-hexyldecyl-2,3,5,6-tetrahydro-3,6-dioxopyrrolo[3,4-*c*]pyrrole-1,4-diyl]-*alt*-[3′,3″-dimethyl-2,2′:5′,2″-terthiophene]-5,5″-diyl] (PMDPP3T). This polymer absorbs light up to 960 nm (1.30 eV) and was previously successfully used in tandem and triple-junction solar cells with estimated efficiencies up to 9.6%.[6] PMDPP3T was blended with $PC_{60}BM$, to minimize absorption of high-energy photons in the back cell. The complete stack is shown in **Figure 1**.

The triple-junction cell was constructed in an inverted device geometry on a glass substrate with patterned indium tin oxide (ITO) and a bottom electron-collecting contact consisting of sol-gel ZnO (40 nm) and a top hole-collecting contact made from MoO_3 (10 nm) covered with Ag (100 nm). For the recombination of holes and electrons between two adjacent subcells we used an interconnecting layer, consisting of a stack of poly(3,4-ethylenedioxythiophene) polystyrene sulfonate (PEDOT:PSS, 45 nm) and ZnO nanoparticles (20 nm). The thickness of each photoactive layer was optimized by optical modeling based on the transfer matrix (TM) method, combined with an empirical electrical modeling, as described elsewhere.[28] The input for this optimization are the experimentally determined wavelength-dependent refractive index (n) and extinction coefficient (k), the internal quantum efficiency (IQE) of each photoactive layer as function of layer thickness, and the normalized shape of the current density – voltage ($J-V$) characteristics of the three photoactive layers, also as function of thickness.[28] The relevant data are collected in Appendix 1, 3, 4, and Figure 1. In the optimization we kept the interconnecting layer thickness constant and varied the thickness of the photoactive layers to find the optimal thickness combination in terms of power conversion efficiency (PCE) (**Figure 2**): front cell 130 nm, middle cell 140 nm, and back cell 90 nm.

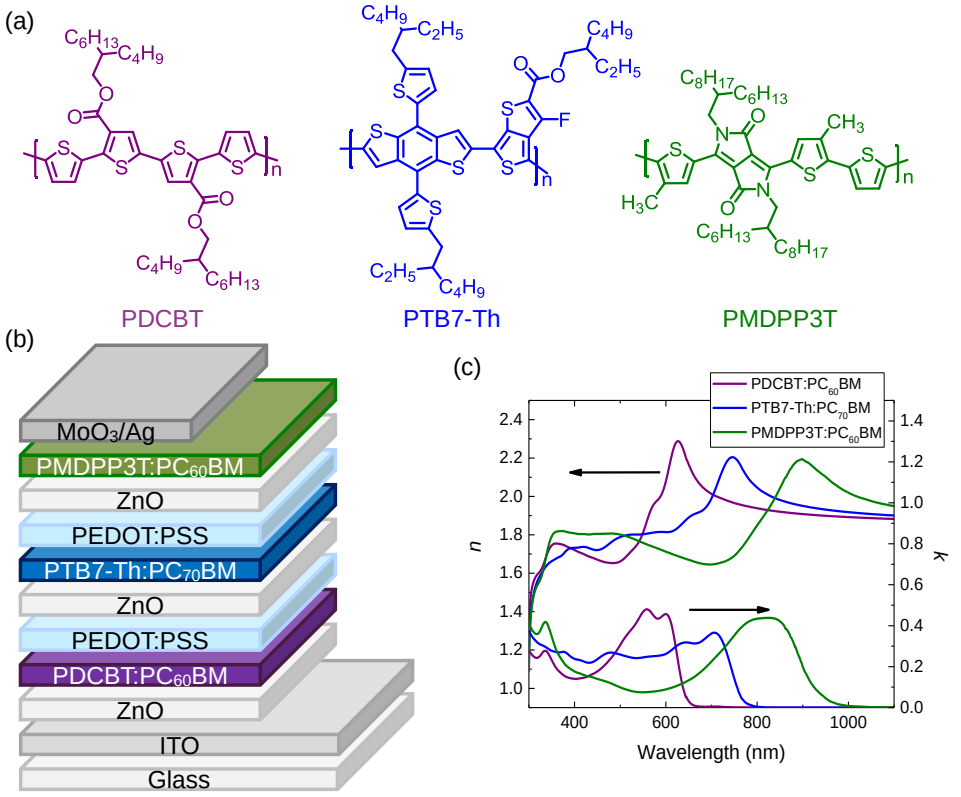

Figure 1. (a) Structures of the semiconductor polymers used in the absorber layers. (b) Device layout of the triple-junction polymer solar cell. Please refer to the text for a description of the thickness values. (c) *n* and *k* values of PDCBT:$PC_{60}BM$ (purple), PTB7-Th:$PC_{70}BM$ (blue) and PMDPP3T:$PC_{60}BM$ (green) as a function of the wavelength.

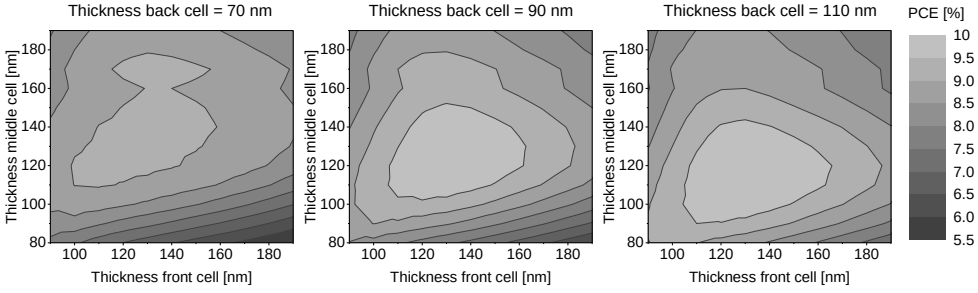

Figure 2. Predicted PCEs of the triple-junction solar cell as function of the thickness of the front, middle and back cells based on optical-electrical modeling.

4.2.2 Measuring the performance under simulated AM1.5G light

The $J-V$ characteristic of a solar cell is generally measured under simulated AM1.5G light. For this purpose, we used filtered light from a tungsten-halogen lamp as described in the Experimental Section 4.4 of this chapter. To calibrate the illumination we used representative single-junction cells for each photoactive layer in the triple-junction cell. These single-junction cells used the same electron and hole transporting materials as present in the triple-junction solar cell (**Figure 3**) and they were fabricated using identical processing conditions. We also checked if the layers adjacent to these charge-transport layers have an effect. We found that the V_{OC} and fill factor (FF) of the middle cell differ when the bottom contact is either ITO/ZnO or ITO/PEDOT:PSS/ZnO, while such difference does not occur for the back cell (data not reported here). To exclude this effect, we used the layouts of the representative single-junction cells as shown in Figure 3. The voltage supplied to the lamp could be tuned to change the color of the emission spectrum, and the distance between lamp and cell was varied to tune the intensity of the light. These parameters were adjusted to provide the best possible correspondence between the J_{SC} determined from the $J-V$ characteristics and the J_{SC}^{EQE}, determined from integrating the EQE with the tabulated AM1.5G spectrum for three single-junction cells simultaneously. In the ideal case J_{SC} and J_{SC}^{EQE} are identical for each of the three subcells. This would provide a perfect match of the spectral irradiance of the light source used with the AM1.5G spectrum. In practice this ideal scenario is not achieved, because the simulated and the official AM1.5G spectrum differ.

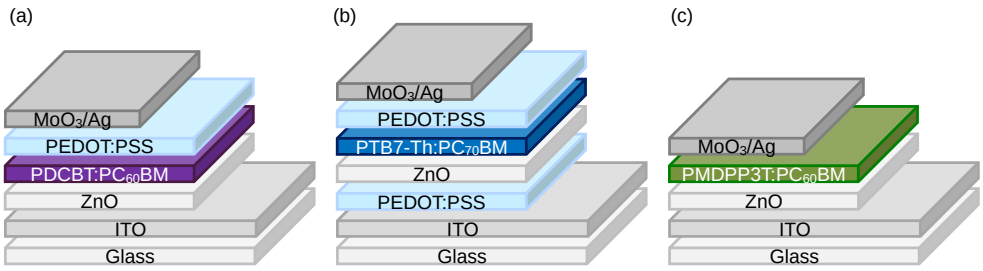

Figure 3. Structure of the representative single-junction cells. (a) Front cell. (b) Middle cell. (c) Back cell.

As will be shown below, the middle subcell is crucial because it is the current-limiting subcell of the triple-junction device. Therefore, it is important to match the current-limiting subcell to the AM1.5G spectrum as best as possible, even if this results in a small offset on the match of the other subcells with the AM1.5G spectrum. Consequently we used a lamp

setting in which the current limiting middle cell of the triple-junction provides a close correspondence between J_{SC} and J_{SC}^{EQE}, while the front and back cells are slightly underestimated (**Table 1**).

Table 1. Photovoltaic parameters of representative single-junction cells and the corresponding triple-junction cell.

Device [a]	V_{OC} [V]	J_{SC} [mA cm^{-2}]	FF	P_{max} [mW cm^{-2}]	J_{SC}^{EQE} [b] [mA cm^{-2}]	δJ_{SC} [c] [%]	PCE [d] [%]
PDCBT	0.83 ± 0.01	8.34 ± 0.14	0.72 ± 0.02	4.96 ± 0.18	8.89 ± 0.20	−6.20	5.30 ± 0.14
PTB7-Th	0.74 ± 0.01	13.3 ± 0.1	0.52 ± 0.01	5.13 ± 0.15	13.14 ± 0.03	+1.40	5.15 ± 0.01
PMDPP3T	0.62 ± 0.01	14.8 ± 0.2	0.66 ± 0.02	5.98 ± 0.25	15.2 ± 0.3	−3.20	6.37 ± 0.01
Triple	2.15 ± 0.01	6.58 ± 0.19	0.69 ± 0.01	9.77 ± 0.29			

[a] The average and standard deviation are over 15 devices for the $J-V$ measurement and over 4 devices for the EQE measurements. [b] J_{SC} determined by integrating the EQE over the AM1.5G spectrum. [c] Difference between J_{SC} and J_{SC}^{EQE}. [d] Determined using J_{SC}^{EQE}.

4.2.3 EQE of the triple junction using bias light

The EQE of the triple-junction solar cells was first measured using only the low intensity monochromatic probe light without any additional bias illumination. For a properly working multi-junction solar cell, the EQE under this condition should follow the lower envelope of the EQE of all the subcells. The presence of a low shunt resistance in one or more subcells would result in a higher EQE.[21] The EQE of the triple measured without bias light is shown in **Figure 4** with black triangles, and nicely follows the lower envelope of the EQE of the subcells.

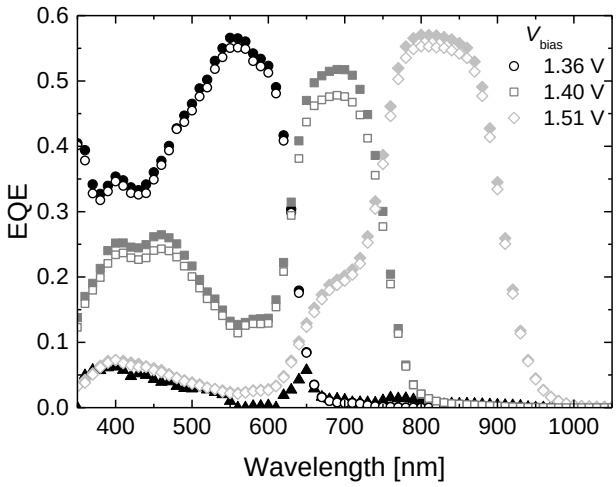

Figure 4. EQE measurements of the best triple-junction solar cell under different light and voltage bias conditions. Without bias light (black solid triangles) and with bias light from LEDs of specific wavelengths 730 nm (85.7 mW cm^{-2}) (black circles), 530 nm (67.0 mW cm^{-2}) (light grey symbols), and 530 nm (42.4 mW cm^{-2}) plus 940 nm (75.8 mW cm^{-2}) (dark grey symbols), without (closed markers) or with (open markers) voltage bias (V_{bias}) as indicated.

The EQE of each of the three individual subcells was measured while simultaneously illuminating the other two subcells with high intensity monochromatic bias light to ensure that the subcell of interest is current limiting in the entire spectral range. We used three light-emitting diodes (LEDs) with emissions centered at 530, 730, and 940 nm. These wavelengths represent a good set to illuminate selectively one or two subcells, but not all of them at the same time. The intensity of the emission of each of these light sources could be tuned by controlling the driving current and the resulting power was measured with a calibrated silicon solar cell. The LEDs were used standalone or combined to reach the desired bias light conditions. We used optical modeling to predict which subcells are biased with specific LED settings. While for tandem cells this might not be necessary, we found that for triple-junction cells it is more difficult to predict the effect of (combinations of) monochromatic bias light without optical modeling. This step differentiates this work from the procedure for analyzing tandem cells.[22] The emission spectrum of the LEDs was scaled by the intensity determined using a calibrated silicon reference cell and this data was used as input for the modeling. **Table 2** shows the maximum current generation (J_{SC}^{max}) of each subcell when the triple-junction device is illuminated with specific settings of the LEDs. These currents were then

scaled by the IQE of each subcell to estimate the actual current generated (J_{SC}^{IQE}). These IQEs were determined using representative single-junction cells as the ratio between J_{SC}^{EQE} and the corresponding maximum J_{SC} evaluated by optical modeling.

Table 2. Predicted J_{SC}^{max} and J_{SC}^{IQE} for each subcell according to the TM model for different bias illumination conditions. The bold-faced rows indicate the current-limiting subcell.

λ_{LED} [nm]	P_{LED} [mW cm^{-2}]	Subcell	J_{SC}^{max} [mA cm^{-2}]	J_{SC}^{IQE} [mA cm^{-2}]
		Front cell	**0.35**	**0.27**
730	86	Middle cell	23.2	19.5
		Back cell	20.0	14.0
		Front cell	11.5	8.78
530 + 940	42 + 76	**Middle cell**	**3.88**	**3.26**
		Back cell	17.5	12.2
		Front cell	17.9	13.7
530	67	Middle cell	5.93	4.98
		Back cell	**1.24**	**0.87**

As can be seen in Table 2, with the three selected settings it is possible to turn each of the subcells current limiting. Excluding the triangles, the other solid symbols in Figure 4 represent the EQEs of the front, middle, and back subcells measured using the specified sets of light bias.

4.2.4 Corrections to the EQE measurement

There are, however, important corrections to take into account when measuring the EQE. The first is the effect of (combinations of) monochromatic bias light on the internal electric field over the three subcells. This has been addressed in detail by Gilot et al. for organic tandem solar cells, and the reasoning for triple-junction cells is analogous.[22] The critical issue is that bias light causes a large difference in charge generation between the subcells. Because the current is limited by the subcell of which the EQE is being probed and the total triple-junction cell is held at short circuit, each of the three subcells will be at a different bias such that $V_{tot} = V_f + V_m + V_b = 0$, but with $V_f \neq V_m \neq V_b \neq 0$. In general, the illumination conditions will be such that the two light-biased subcells will be under forward bias ($V > 0$), while the cell of interest is under reverse bias ($V < 0$). The latter condition increases the measured photocurrent and hence results in an overestimated EQE.

To assess the effect of bias light we measured the J–V characteristics of the three representative single-junction cells under the same light intensity as the corresponding

subcell would experience inside the light-biased triple-junction solar cell. Via optical modeling we already established the expected short-circuit currents in each subcell under the three different bias illumination conditions (J_{SC}^{IQE} in Table 2). **Figure 5** shows the measured *J*−*V* characteristics of the representative single-junction cells, where the illumination intensity was adjusted to give $J_{SC} = J_{SC}^{IQE}$ (Table 2). Figure 5 shows how we could estimate the reverse bias experienced by the subcell of which the EQE is measured. To perform a correct EQE measurement, we had to apply a compensating forward bias to the triple-junction cell. Figure 5 shows that the corrections were 1.36 V for the front subcell, 1.40 V for the middle cell, and 1.51 V for measuring the back cell. We note that, at least in first approximation, the bias voltage correction is close to the sum of the V_{OC}'s of the optically biased subcells. The resulting EQE under appropriate light and voltage bias are shown in Figure 4 (open markers).

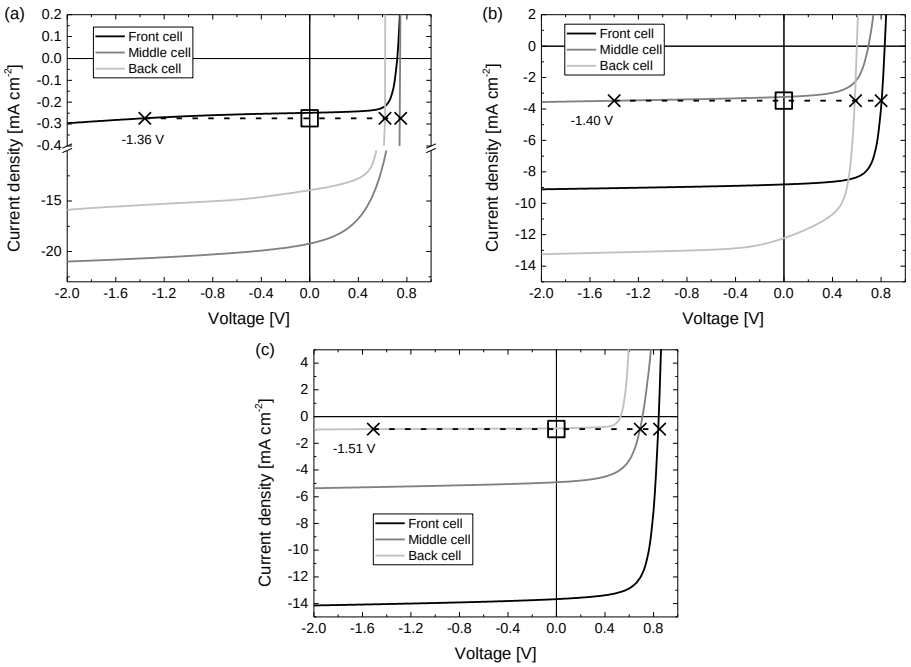

Figure 5. *J*−*V* characteristics of the representative single-junction cells illuminated to give $J_{SC} = J_{SC}^{IQE}$ as determined by optical modeling and corrected for IQE (Table 2). The current-limiting subcell is the front cell (a), middle cell (b), and back cell (c).

As a final remark we note that applying a voltage bias is particularly important for subcells that have a lower fill factor. In an optimized triple junction the middle cell is typically thicker than the other subcells because it competes with the front and back cells for absorbing photons. Thicker cells result in lower fill factors, and hence the correction is most relevant for the current limiting, middle cell.

The second correction to consider is the non-linearity of the current generation by the organic solar cells with increasing light intensity.[23] To estimate the effect, we measured each representative single-junction cell and evaluated the average ratio of the EQE measured with and without bias light to give the current expected for 100 mW cm^{-2} AM1.5G illumination. We note that this overestimates the correction because the subcells of the triple junction effectively receive less light than 100 mW cm^{-2} AM1.5G and the bias light used for measuring the triple cell can be substantial, even for the current limiting cell (Table 2). The average light intensity correction factors (*f*) for the front, middle, and back representative cells are 0.996, 0.962 and 0.984, respectively (**Table 3**), showing that the effects are small.

Table 3. Statistics on J_{SC}^{EQE} for single-junction cells measured with and without bias light.

Device	J_{SC}^{EQE} w/ bias [mA cm^{-2}]	J_{SC}^{EQE} w/o bias [mA cm^{-2}]	*f*
PDCBT:PC_{60}BM	8.81	8.84	0.997
	8.66	8.67	0.997
	8.93	8.98	0.997
	9.15	9.20	0.994
PTB7-Th:PC_{70}BM	13.17	13.81	0.963
	13.12	13.65	0.961
	13.11	13.64	0.962
	13.17	13.68	0.961
PMDPP3T:PC_{60}BM	15.14	15.22	0.994
	14.91	15.35	0.973
	15.22	15.66	0.973
	15.70	15.74	0.997

Table 4 summarizes the results of the applied corrections and reveals that the J_{SC}'s of the front, middle and back subcells are reduced by 3%, 10%, and 5% respectively. The most important correction is the voltage bias, which is the strongest for the middle subcell. The reason is related to the low FF of 0.52 of the middle cell, which causes a significant bias dependent photocurrent. The light intensity correction has a small effect for all subcells.

Table 4. J_{SC}^{EQE} (mA cm^{-2}) of the triple-junction solar cell under representative light and voltage bias.

	Front cell	Middle cell	Back cell
Light bias [a)]	7.35	7.38	7.91
Light bias [a)] and voltage bias [b)]	7.19	6.87	7.65
Light bias [a)], voltage bias [b)], and intensity correction [c)]	7.16	6.61	7.53

[a)] Light bias as in Table 2. [b)] V_f = 1.36 V, V_m = 1.40 V, V_b = 1.51 V. [c)] f_{front} = 0.996, f_{middle} = 0.962, f_{back} = 0.984.

We now reconsider the white light illumination conditions used for measuring the $J-V$ characteristics (Table 1). Because the middle subcell is limiting the current of the triple-junction cell, the illumination conditions should assure that for the corresponding single-junction cell the J_{SC} is close to J_{SC}^{EQE}. At the same time the J_{SC}'s of the front and back cells should not be overestimated because this would increase the photocurrent. Hence, by matching J_{SC} to J_{SC}^{EQE} for the representative middle-junction cell, and having $J_{SC} < J_{SC}^{EQE}$ for the front and back cells (conditions chosen in Table 1) we assure an illumination close to 100 mW cm^{-2} AM1.5G. The resulting PCE is 9.77 ± 0.29 % when averaged over 15 devices.

4.2.5 Reconstructing the $J-V$-curve

Using the EQE data of the triple-junction solar cell and the $J-V$ characteristics of the representative single-junction solar cells it is possible to construct the expected $J-V$ curve of the triple solar cell. The reconstruction is performed by scaling the current under illumination for each of the three representative single-junction solar cells, such that the J_{SC} matches the J_{SC}^{EQE} (Table 4) and then adding the voltages of the three cells for each current value. When using the J_{SC}^{EQE} determined without applying the voltage bias (first line Table 4), the reconstructed $J-V$ curve of the triple junction (Construction 1) grossly overestimates the experimental performance (**Figure 6**), but with the appropriate corrections (last line in Table 4) there is a very good correspondence (Construction 2), although small deviations can be seen at open circuit, short circuit and in the maximum power point. (Figure 6 and **Table 5**).

The overestimation of the V_{OC} by 50 mV is mainly the result of the fact that the light intensity in each of the subcells is less than 100 mW cm^{-2} AM1.5G. This effect can be estimated from $\Delta V_{OC} = (kT/q)\ln[J_{SC}(\text{triple})/J_{SC}(\text{single})]$, where J_{SC}(triple) and J_{SC}(single) are the J_{SC} of the triple and single-junction solar cells as given in Table 1. Summing the values for the three subcells results in a combined loss of 45 mV, in fair agreement with the 50 mV difference found experimentally.

The deviations at short-circuit and in the maximum power point are caused by the fact that the reconstruction does not take into account the increase of FF at lower light intensity in each subcell. To assess the magnitude of this effect, we recorded $J-V$ characteristics of the representative single junction for the middle subcell, which is current limiting and has a low FF, under the reduced light intensity that is expected in the triple-junction cell **(Figure 7**). At reduced light intensity the FF of the single junction increases from 0.52 to 0.58 and for the reconstructed triple junction the FF goes from 0.63 to 0.65 (Construction 3 in Figure 6 and Table 5). The small deviation remaining compared to the experimental value of 0.68, is attributable to the light intensity dependence of the FF in the other two cells and the unavoidable small differences between the representative single junction configurations and the corresponding subcells in the triple.

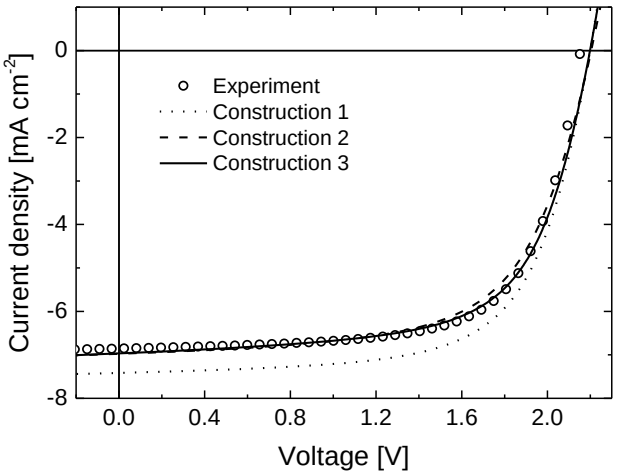

Figure 6. Experimental $J-V$ characteristics of the triple-junction solar cell measured under simulated solar radiation, and reconstructed $J-V$ curves from the measured EQE data and the representative single-junction cells (see text for details).

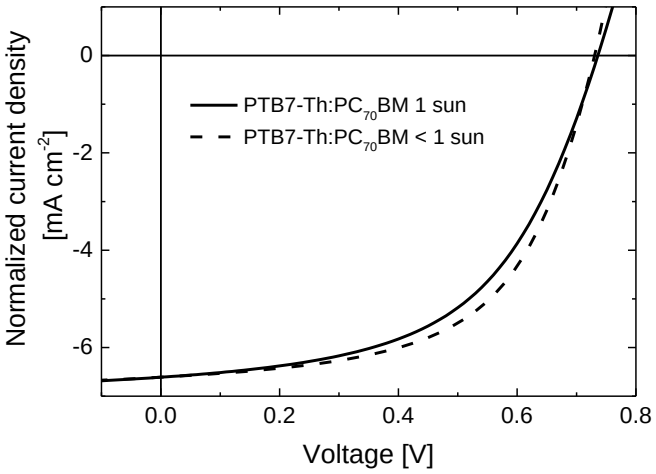

Figure 7. Normalized *J*–*V* characteristics of a PTB7-Th:$PC_{70}BM$ single-junction solar cell measured under 1 sun light intensity (solid line) and under reduced light intensity, such that the current generated was similar to the one inside the triple-junction solar cell under 1 sun light intensity (dashed line). To provide an easier comparison of the difference in FF, the J_{SC} of the cell illuminated at 1 sun intensity was normalized to match the value of the cell illuminated under reduced intensity.

Table 5. Experimental and reconstructed solar cell parameters of the best triple-junction solar cell.

J–*V* characteristic	V_{OC} [V]	J_{SC} [mA cm^{-2}]	FF	PCE [%]
Measured	2.15	6.86	0.68	10.03
Construction 1	2.20	7.42	0.66	10.77
Construction 2	2.20	6.98	0.63	9.71
Construction 3	2.20	6.97	0.65	9.96

Another important check is to compare the EQE of the subcells to the one predicted by optical modeling. **Figure 8** compares the experimental EQE with the absorption efficiency, determined from the TM modeling, multiplied with the IQE determined for the corresponding representative single-junction cells. We consider the agreement to be excellent, both in spectral shape as well as in absolute intensity. The exceptional correspondence validates all the steps taken in the characterization.

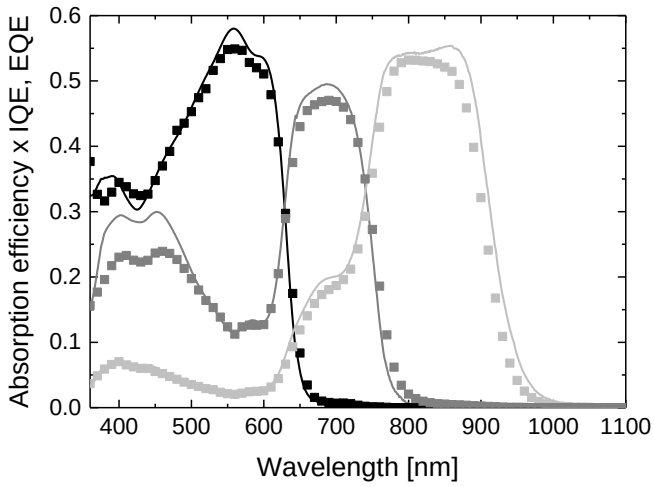

Figure 8. Comparison of the experimental EQE (markers) and expected EQE (solid lines) as determined from the product of the absorption efficiency (from TM modeling) and the IQE (from the representative single-junction cells).

4.3 Conclusions

We developed a characterization protocol to characterize triple-junction organic solar cells and measure the EQE of the individual subcells accurately. By using (combinations of) three monochromatic high-power LEDs we sequentially optically biased two of the three subcells of a polymer triple-junction solar cell to ensure that the spectral response corresponds to the particular subcell of interest. We demonstrated that the optical bias must be combined with an appropriate voltage bias over the triple junction in order not to overestimate the performance. Using the modeled currents as input for the voltage bias correction is significantly different from the approach we proposed for the tandem characterization.[22] Without this step it is impossible to characterize the triple-junction cell properly. The required bias voltage can be accurately determined from the J–V characteristics of representative single-junction cells,[21,22] and lies generally within −0.1 V from the sum of the V_{OC}'s of the optically biased subcells. A second adjustment accounts for the non-linearity of the photocurrent with light intensity. By combining these two corrections, the J_{SC}^{EQE} integrated from the EQE and the AM1.5G solar spectrum reduced by as much as 3%, 10%, and 5% for the front, middle, and back subcells, respectively. The J–V curve constructed using the J_{SC}^{EQE} from the only-light-biased measurement lead to an overestimation of the PCE by 8% with respect to the construction in which all corrections

were used. The reconstructed PCE = 9.96% differed by 0.07 percent point from the experimental PCE = 10.03%. Likewise, the experimental EQE of the subcells in the triple-junction cell and the EQE estimated from optical TM modeling and IQE of the single-junction cells, show excellent agreement. The EQE analyses also give credence to our adjustment procedure of the white light illumination to match the AM1.5G spectrum for this triple-junction cell. By adjusting the light source to match the EQE-integrated J_{SC} of each individual absorber in the multi junction, we found optimal conditions in which the illumination approaches the AM1.5G response. Measuring the PCE under these conditions gave a PCE = 9.77 ± 0.29 %. The procedure provides internally consistent results and represents a reliable method to characterize triple-junction polymer solar cells.

We note that the magnitudes of the voltage and light intensity correction will generally depend on the nature of the photoactive layers in the subcells of the triple-junction cell and on the intensity and spectrum of the adopted bias illumination. With respect to the solar simulator used for recording the $J-V$ characteristics, a close match with the AM1.5G spectrum must be established.[21] In this work this was achieved by adjusting the spectral radiance to match the correct AM1.5G short-circuit current density of the three representative single-junction cells with the same illumination conditions.

We realize that characterizing triple-junction organic solar cells via this protocol requires considerable additional effort, but stress that without proper and critical analysis a considerable overestimation of the PCE is almost inevitable.

4.4 Experimental Section

Materials: Pre-patterned ITO (150 nm) on glass substrates were purchased from Naranjo Substrates. Molybdenum trioxide powder (99.97%) was purchased from Sigma Aldrich. The ZnO layers were made via a sol-gel route or by spin-coating a suspension of pre-formed nanoparticles (see Chapter 3 for their synthesis). The former consisted of a solution 0.5 M $Zn(CH_3COO)_2 \cdot 2H_2O$ (98 %, Acros Organics) and 0.5 M ethanolamine in 2-methoxyethanol.[29] The suspension of PEDOT:PSS (Clevios P, VP Al 4083) was filtered with a 0.45 μm PVDF filter and diluted in 1-propanol 1:2 (v/v) right before use, hereafter referred to as D-PEDOT. For the preparation of D-PEDOT, 1-propanol (1 mL) was added dropwise to the commercial PEDOT:PSS dispersion in water (0.5 mL) over 15 minutes under vigorous stirring. No further additives were used. Poly[5,5′-bis(2-butyloctyl)-(2,2′-bithiophene)-4,4′-dicarboxylate-*alt*-5,5′-2,2′-bithiophene] (PDCBT) was synthesized according to the procedure reported in literature and blended with $PC_{60}BM$ with a 1:1 weight ratio.[25] The two components were dissolved in chloroform containing 1 vol.% of *o*-dichlorobenzene at a concentration of 10 mg mL^{-1} of polymer. Poly[4,8-bis(5-(2-ethylhexyl)thiophen-2-yl)benzo[1,2-*b*:4,5-*b*′]dithiophene-*co*-3-fluorothieno [3,4-

b]thiophene-2-carboxylate] (PTB7-Th) was purchased from 1-Material (batch YY10228), mixed with $PC_{70}BM$ (1:1.5 weight ratio) and dissolved in chlorobenzene, containing 3 vol.% diiodooctane at a concentration of 12 mg mL^{-1} of polymer.[30] Poly[[2,5-bis(2-hexyldecyl-2,3,5,6-tetrahydro-3,6-dioxopyrrolo[3,4‐*c*]pyrrole-1,4-diyl]-*alt*-[3′,3″-dimethyl-2,2′:5′,2″-terthiophene]-5,5″-diyl] (PMDPP3T) was synthesized following the reported procedure.[6] PMDPP3T was blended with $PC_{60}BM$ (1:3 weight ratio) and dissolved in a solution of chloroform, containing 7 vol.% *o*-dichlorobenzene. The concentration of polymer was 3 mg mL^{-1}.

Device fabrication: The patterned ITO substrates were cleaned by sonication in acetone, followed by a solution of sodium dodecyl sulfate in water. They were then rinsed in water and sonicated in isopropanol, before being treated under a UV/Ozone lamp to complete the cleaning. In the following paragraphs the processing of all the layers made from solution is described. Wherever mentioned, the sol-gel ZnO was cast directly on clean ITO substrates by spin-coating in ambient air and annealed at 150 °C for 5 min on a hotplate. The D-PEDOT solution was always processed by dynamic spin-coating (90 µL per sample) in a nitrogen filled glove box for improved wetting to form a 45 nm thick layer. The layer was kept in the vacuum of the antechamber for 30 min. right after spin-coating to remove residual solvents and no further treatment was performed. The ZnO nanoparticles dispersion was dynamically spin-coated (70 µL per sample) in ambient air to give a 20 nm thick layer, without any post treatment. The last step in the fabrication of each of these devices was the evaporation of the top contact. In all cases this was accomplished by evaporating MoO_3 (10 nm), followed by Ag (100 nm) in a vacuum chamber at ca. 6×10^{-7} mbar, through a shadow mask. On each substrate, the intersection of the ITO pattern with the evaporated top contact formed two squares of 9 mm^2 area and two squares of 16 mm^2 area. The thickness of each layer was measured using a Veeco Dektak profilometer.

PDCBT:$PC_{60}BM$ single-junction cells: The clean ITO substrates were covered with ZnO from the sol-gel route. Subsequently the solution of PDCBT:$PC_{60}BM$ was spin-coated in a N_2 filled glove box to form a layer with a thickness of 130 nm. The substrates were then annealed in the glove box for 5 min at 100 °C. After this step, the D-PEDOT solution was spin-coated and the samples annealed again at 105 °C for 10 min.

PTB7-Th:$PC_{70}BM$ single-junction cells: D-PEDOT was processed directly on clean ITO substrates and annealed at 105 °C for 10 min in glove-box. Then the ZnO nanoparticles were deposited as previously described, followed by the casting of the PTB7-Th:$PC_{70}BM$ blend in the glove box to form a 140 nm thick layer. The substrates were then kept in vacuum in the antechamber of the glove box for 2 hours. Subsequently, another D-PEDOT layer was deposited.

PMDPP3T single-junction cells: Sol-gel ZnO was processed on the clean ITO substrate. Afterwards, the solution of PMDPP3T:$PC_{60}BM$ was spin-coated in ambient air to obtain a layer of 90 nm in thickness.

Triple-junction solar cells: Sol-gel ZnO was spin-coated on clean ITO substrates. A layer of 130 nm of PDCBT:$PC_{60}BM$ was processed on top in a glovebox and annealed at 100 °C for 5 min. Subsequently, the first layer of D-PEDOT was spin-coated and annealed in a glovebox, at 105 °C for 10 min. To finish the first ICL, ZnO nanoparticles were spin-coated on D-PEDOT, followed by 140 nm of PTB7-Th:$PC_{70}BM$. After this step, the samples were dried in vacuum for 2 hours. For the second ICL, D-PEDOT was spin-coated again. Then, the ZnO nanoparticles layer was deposited, followed by 90 nm of PMDPP3T:$PC_{60}BM$. The cell was completed by the thermal evaporation of MoO_3 (10 nm) and Ag (100 nm) at ca. 6×10^{-7} mbar.

Characterization: Both the measurement of the $J-V$ curve and the EQE were performed under nitrogen atmosphere. The substrates were treated under a UV-lamp for 6 minutes before measuring, in order to photodope the ZnO and MoO_3 layers. Subsequently, the $J-V$ characteristics were measured with a Keithley 2400 source meter from −2 to +2V (single-junction cells) and from −2 V to +2.6 V (triple-junction cells). 401 points per scan were acquired, each with 20 ms integration time. The lamp used for this measurement was a tungsten-halogen lamp which was filtered with a UV filter and a daylight filter (Hoya LB120), calibrated to match the current integrated from the EQE spectrum of each single-junction cell, as shown in the text. The measurements were performed through an illumination mask with aperture sizes of 6.76 and 12.96 mm^2, corresponding to the 9 mm^2 and 16 mm^2 nominal device areas, respectively. This defined the active area of the devices.

The EQE measurement was performed in a home-made setup, consisting of a tungsten-halogen lamp, a chopper, a monochromator (Oriel, Cornerstone 130), a pre-amplifier (Stanford Research Systems SR570) and a lock-in amplifier (Stanford Research Systems SR830 DSP). The substrates were kept in a N_2-filled box with a quartz window during the duration of the measurement. The device of interest on each substrate was aligned through a circular aperture with 2 mm of diameter, defining the active area. The signal response to the modulated light was transformed into an EQE value by comparison with the measurement on a calibrated silicon reference solar cell. The average standard deviation in measuring the wavelength dependent EQE in this setup is less than 0.005 in electrons/photons for wavelengths in the range of 350–1050 nm. The 530, 730 and 940 nm bias lights were high power LEDs obtained from Thorlabs. The additional voltage bias was applied directly from the pre-amplifier.

Optical modeling: Optical modeling based on the transfer matrix (TM) method was performed using Setfos 3.2 (Fluxim). The wavelength dependent n and k values of each active

layer were determined by transmission and reflection measurements (Chapter 1) using an integrating sphere attachment on a Perkin-Elmer Lambda 1050 spectrophotometer. The optimization based on IQE correction of the modeled current densities and the construction of the $J-V$ characteristics was performed according to a procedure previously reported and extended for triple junction cells.[28] The same tools were used to predict the current generation of each subcell in the triple-junction under the different light bias conditions. As described in the main text, this was done by measuring the power density of the light sources at a different driving current with the calibrated silicon reference cell of the EQE setup and scaling the power profile of each LED (provided by the manufacturer) by those values. The latter spectra were used as input for the TM calculation.

4.5 References

[1] L. Meng, Y. Zhang, X. Wan, C. Li, X. Zhang, Y. Wang, X. Ke, Z. Xiao, L. Ding, R. Xia, H.-L. Yip, Y. Cao, Y. Chen, *Science* **2018**, DOI: 10.1126/science.aat2612.

[2] A. Yakimov, S. R. Forrest, *Appl. Phys. Lett.* **2002**, *80*, 1667

[3] J. Gilot, M. M. Wienk, R. A. J. Janssen, *Appl. Phys. Lett.* **2007**, *90*, 143512.

[4] D. W. Zhao, X. W. Sun, C. Y. Jiang, A. Kyaw, G. Q. Lo, D. L. Kwong, *IEEE Electron Device Lett.* **2009**, *30*, 490.

[5] S. K. Hau, H.-L. Yip, K.-S. Chen, J. Zou, A. K.-Y. Jen, *Appl. Phys. Lett.* **2010**, *97*, 53307.

[6] W. Li, A. Furlan, K. H. Hendriks, M. M. Wienk, R. A. J. Janssen, *J. Am. Chem. Soc.* **2013**, *135*, 5529.

[7] S. Esiner, H. Van Eersel, M. M. Wienk, R. A. J. Janssen, *Adv. Mater.* **2013**, *25*, 2932.

[8] N. Li, D. Baran, K. Forberich, M. Turbiez, T. Ameri, F. C. Krebs, C. J. Brabec, *Adv. Energy Mater.* **2013**, *3*, 1597.

[9] R. Meerheim, C. Körner, K. Leo, *Appl. Phys. Lett.* **2014**, *105*, 63306.

[10] X. Che, X. Xiao, J. D. Zimmerman, D. Fan, S. R. Forrest, *Adv. Energy Mater.* **2014**, *4*, 1400568.

[11] C.-C. Chen, W.-H. Chang, K. Yoshimura, K. Ohya, J. You, J. Gao, Z. Hong, Y. Yang, *Adv. Mater.* **2014**, *26*, 5670.

[12] A. R. Bin Mohd Yusoff, D. Kim, H. P. Kim, F. K. Shneider, W. J. da Silva, J. Jang, *Energy Environ. Sci.* **2015**, *8*, 303.

[13] F. Guo, N. Li, F. W. Fecher, N. Gasparini, C. O. R. Quiroz, C. Bronnbauer, Y. Hou, V. V. Radmilović, V. R. Radmilović, E. Spiecker, K. Forberich, C. J. Brabec, *Nat. Commun.* **2015**, *6*, 7730.

[14] S. Esiner, R. E. M. Willems, A. Furlan, W. Li, M. M. Wienk, R. A. J. Janssen, *J. Mater. Chem. A* **2015**, *3*, 23936.

[15] X. Xiao, K. Lee, S. R. Forrest, *Appl. Phys. Lett.* **2015**, *106*, 213301.

[16] J. Tong, S. Xiong, Y. Zhou, L. Mao, X. Min, Z. Li, F. Jiang, W. Meng, F. Qin, T. Liu, R. Ge, C. F.-Hernandez, B. Kippelen, Y. Zhou, *Mater. Horiz.* **2016**, *3*, 452.

[17] R. Meerheim, C. Körner, B. Oesen, K. Leo, *Appl. Phys. Lett.* **2016**, *108*, 103302.

[18] X. Zhang, L. Chen, T. Yuan, H. Huang, Z. Sui, R. Du, X. Li, Y. Lu, Q. Li, *Mater. Horizons* **2016**, *3*, 452.

[19] X. Elias, Q. Liu, C. G.-Suriñach, R. Matheu, P. M.-Perez, A. M.-Otero, X. Sala, J. Martorell, A. Llobet, *ACS Catal.* **2016**, *6*, 3310.

[20] H. Zhang, B. Niesen, E. Hack, S. Jenatsch, L. Wang, A. C. Véron, M. Makha, R. Schneider, Y. Arroyo, R. Hany, F. Nüesch, *Org. Electron.* **2016**, *30*, 191.

[21] R. Timmreck, T. Meyer, J. Gilot, H. Seifert, T. Mueller, A. Furlan, M. M. Wienk, D. Wijnands, J. H.-Hebinger, W. Warta, R. A. J. Janssen, M. Riede, K. Leo, *Nat. Photonics* **2015**, *9*, 478.

[22] J. Gilot, M. M. Wienk, R. A. J. Janssen, *Adv. Funct. Mater.* **2010**, *20*, 3904.

[23] D. J. Wehenkel, K. H. Hendriks, M. M. Wienk, R. A. J. Janssen, *Org. Electron*. **2012**, *13*, 3284.

[24] M. Meusel, C. Baur, G. Létay, A. W. Bett, W. Warta, E. Fernandez, *Prog. Photovolt: Res. Appl.* **2003**, *11*, 499.

[25] M. Zhang, X. Guo, W. Ma, H. Ade, J. Hou, *Adv. Mater.* **2014**, *26*, 5880.

[26] S.-H. Liao, H.-J. Jhuo, P.-N. Yeh, Y.-S. Cheng, Y.-L. Li, Y.-H. Lee, S. Sharma, S.-A. Chen, *Sci. Rep.* **2014**, *4*, 6813.

[27] H. Zhou, Y. Zhang, C. K. Mai, S. D. Collins, G. C. Bazan, T. Q. Nguyen, A. J. Heeger, *Adv. Mater.* **2015**, *27*, 1767.

[28] J. Gilot, M. M. Wienk, R. A. J. Janssen, *Adv. Mater.* **2010**, *22*, E67.

[29] Y. Sun, J. H. Seo, C. J. Takacs, J. Seifter, A. J. Heeger, *Adv. Mater.* **2011**, *23*, 1679.

[30] S. H. Liao, H. J. Jhuo, Y. S. Cheng, S. A. Chen, *Adv. Mater.* **2013**, *25*, 4766.

Chapter 5

Quadruple-Junction Polymer Solar Cells with Four Complementary Absorber Layers*

Abstract

A monolithic two-terminal solution-processed quadruple-junction polymer solar cell in a n-i-p (inverted) configuration with four complementary polymer:fullerene active bulk-heterojunction layers is presented. The subcells possess different optical band gaps ranging from 1.90 to 1.13 eV. Optical modeling using the transfer matrix formalism enables to predict the fraction of absorbed photons from sunlight in each subcell and determine the optimal combination of layer thicknesses. The quadruple-junction cell, features an open-circuit voltage of 2.45 V and has a power conversion efficiency of 7.6%, only slightly less than the modeled value of 8.2%. The external quantum efficiency spectrum, determined with appropriate light and voltage bias conditions, exhibits in general an excellent agreement with modeled spectrum. The device performance is presently limited by bimolecular recombination, which prevents using thick photoactive layers that could absorb light more efficiently.

* This chapter has been published as: D. Di Carlo Rasi, K. H. Hendriks, M. M. Wienk, R. A. J. Janssen, *Adv. Mater.* **2018**, *30*, 1803836.

5.1 Introduction

The efficiency of multi-junction solar cells can be progressively increased by stacking an increasing number of absorbers.[1] Following this approach, crystalline semiconductor quintuple-junction solar cells and quadruple-junction thin film solar cells using amorphous silicon have reached PCEs of 38.8% and 15.0%, respectively.[2,3]

Several solution-processed monolithic tandem and triple-junction organic solar cells have been reported, [4,5] of which the most recent ones were discussed in Chapter 2. Solution-processed multi-junction organic solar cells with more than three active layers have been reported in very few occasions, in which cases the same absorber layer was repeated along the stack.[6,7] Given the lack of complementarity in the absorption spectra of the subcells, these multi-junction cells did not offer the opportunity to achieve a high efficiency.

Here we report a first example of a quadruple-junction polymer solar cell that features four complementary band gap absorber layers (**Figure 1**a). The device comprises 14 functional layers of which 11 are processed consecutively from solution. The subcells were fabricated using four different polymer:fullerene active layers with optical band gaps (E_g) ranging from 1.90 to 1.13 eV and a combination of poly(3,4-ethylenedioxythiophene): polystyrene sulfonate (PEDOT:PSS) and ZnO as interconnection layer in a n-i-p (inverted) configuration (Figure 1a). The quadruple-junction solar cells reached a power conversion efficiency of 7.6% with an open-circuit voltage of 2.45 V. The external quantum efficiency (EQE) of the quadruple-junction solar cells was measured using bias light of different wavelengths, following the protocol presented in Chapter 4 involving optical modeling and correcting for the build-up electric field.[8]

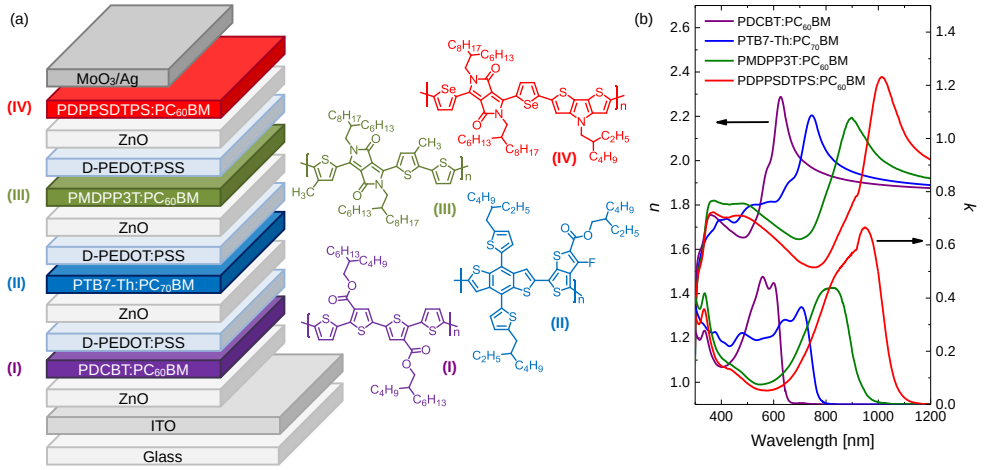

Figure 1. (a) Device structure of the quadruple-junction solar cell and chemical structure of the photoactive polymers featured in each subcell: (**I**) PDCBT:$PC_{60}BM$, (**II**) PTB7-Th:$PC_{70}BM$, (**III**) PMDPP3T:$PC_{60}BM$, and (**IV**) PDPPSDTPS:$PC_{60}BM$. (b) Wavelength-dependent *n* and *k* optical constants of the active layers used for the quadruple junction.

5.2 Results and discussion

5.2.1 Layers stack and optimization

The first cell on top of the transparent indium tin oxide (ITO)/ZnO contact consists of poly[5,5′-bis(2-butyloctyl)-(2,2′-bithiophene)-4,4′-dicarboxylate-alt-5,5′-2,2′-bithiophene] (PDCBT) with E_g = 1.90 eV as donor,[9] blended with [6,6]-phenyl-C_{61}-butyric acid methyl ester ($PC_{60}BM$) as acceptor. The second photoactive layer is poly[4,8-bis(5-(2-ethylhexyl)thiophen-2-yl)benzo[1,2-*b*:4,5-*b*′]dithiophene-co-3-fluorothieno[3,4-*b*]thiophene-2-carboxylate] (PTB7-Th) having E_g = 1.58 eV in combination with [6,6]-phenyl-C_{71}-butyric acid methyl ester ($PC_{70}BM$).[10] The third subcell comprises poly[[2,5-bis(2-hexyldecyl-2,3,5,6-tetrahydro-3,6-dioxopyrrolo[3,4-*c*]pyrrole-1,4-diyl]-*alt*-[3′,3″-dimethyl-2,2′:5′,2″-terthiophene]-5,5″-diyl] (PMDPP3T) with a E_g = 1.30 eV together with $PC_{60}BM$.[11] Finally the device is completed with a subcell consisting of poly[[4-(2-ethylhexyl)-4*H*-dithieno[3,2-*b*:2',3'-*d*]pyrrole-2,6-diyl]-*alt*-2,5-selenophenediyl[2,5-bis(2-ethylhexyl)-2,3,5,6-tetrahydro-3,6-dioxopyrrolo[3,4-*c*]pyrrole-1,4-diyl]-2,5-selenophenediyl] (PDPPSDPTS), having a small band gap of E_g = 1.13 eV, combined with $PC_{60}BM$ as acceptor.[12] To interconnect these cells we use layers of PEDOT:PSS, deposited from the commercial dispersion diluted with *n*-propanol to near azeotropic composition (referred to as D-PEDOT:PSS), as hole transport layer and ZnO nanoparticles, dispersed in

isoamyl alcohol, as electron transport layer.[13] Details about the processing are in the Experimental Section 5.4 of this chapter and were already introduced in Chapter 3.

The efficiency of the quadruple-junction solar cell strongly depends on the appropriate matching of the current generation in each of the individual subcells. To determine the optimal layer thicknesses for the quadruple-junction solar cell we used a combination of experiments on representative single-junction cells (**Figure 2**) together with optical modeling using the transfer matrix formalism.

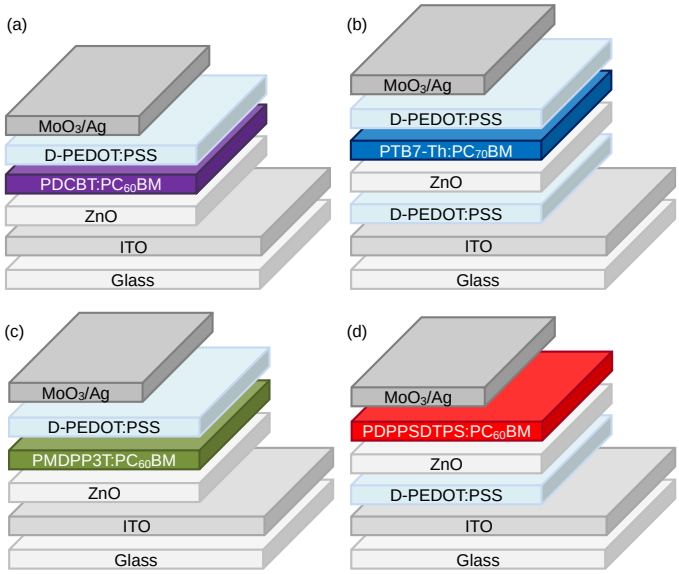

Figure 2. Device scheme of representative single-junction cells of (a) PDCBT:$PC_{60}BM$, (b) PTB7-Th:$PC_{70}BM$, (c) PMDPP3T:$PC_{60}BM$, (d) PDPPSDTPS:$PC_{60}BM$.

To this end, we determined the wavelength-dependent refractive index $n(\lambda)$ and extinction coefficient $k(\lambda)$ for each photoactive layer (Figure 1b), the charge transport layers (D-PEDOT:PSS, MoO_3 and ZnO), and the electrodes (ITO, Ag). Second, the photovoltaic performance of the four individual photoactive layers was determined as a function of the layer thickness using single-junction cells. The details of these experiments can be found in Appendix 1, 4-6. By using optical simulations for the single-junction cells, it is possible to model the fraction of photons absorbed by the photoactive layers ($f_A(\lambda)$) and by combining this with the corresponding experimental EQE(λ), we determined the internal quantum efficiency (IQE(λ)) for each layer. With these data it is possible to predict the performance

of the quadruple solar cell for each thickness combination under AM1.5G illumination. In the optical simulations we used a 45 nm thick D-PEDOT:PSS layer and a 15 nm layer of ZnO nanoparticles, which correspond to the experimentally used thicknesses. The simulations reveal that for a layer thickness combination of 110, 100, 170 and 160 nm for the front, front-middle, back-middle, and back cells, respectively, a PCE of 8.2% can be expected (**Table 1**). **Figure 3** shows the corresponding fraction of photons absorbed by the photoactive layers, the parasitic absorption by the charge transport layers and the electrodes, and the fraction of unused (i.e. reflected) photons. The spectrum of the fraction of absorbed photons is a combination of absorption and interference effects. Figure 3 shows that the parasitic absorption is largely situated in near-IR region and dominated by the three D-PEDOT:PSS layers and the ITO electrode. The appreciable absorption of light in the UV region by ITO and ZnO is less relevant for the device performance, because the sun's photon flux is small in the UV region. **Table 2** shows the expected current generation in each of the four subcells under AM1.5G (100 mW cm^{-2}) illumination. These currents were determined from the modeled EQE spectra (**Figure 4**b) that were calculated by multiplying the modeled fraction of absorbed photons, $f_A(\lambda)$, in each photoactive layer with the IQE(λ) of that layer. Subsequent integration with the AM1.5G spectrum over all wavelengths afforded the expected short-circuit current densities (J_{SC}) values. Table 2 reveals that the J_{SC}s of the subcells are similar, but not perfectly matched, and that the back cell is current limiting.

Table 1. Modeled and experimental device metrics of the quadruple-junction solar cell under AM1.5G (100 mW cm^{-2}) illumination.

	J_{SC} [mA cm^{-2}]	V_{OC} [V]	FF	PCE [%]
Modeling	5.26	2.46	0.63	8.2
Experiment	5.23	2.45	0.59	7.6

Table 2. EQE-integrated J_{SC} [mA cm^{-2}] of the subcells of the quadruple-junction device.

	Front cell	Middle-front cell	Middle-back cell	Back cell
Modeling	6.45	5.25	6.68	4.57
Experiment	6.21	4.77	5.17	4.55

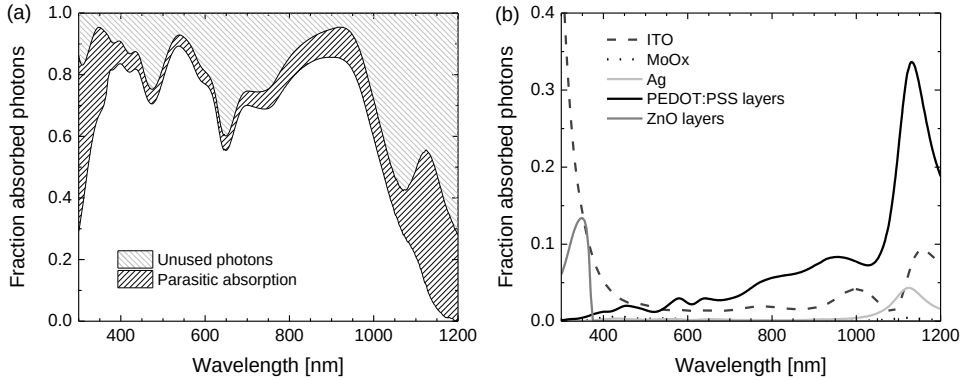

Figure 3. (a) Fraction of photons absorbed by the active layers (white background), parasitic absorption by non-photoactive layers (black hatched area), and fraction of unused (i.e. reflected) photons (grey hatched area) as determined by optical modeling calculations using the transfer matrix method. (b) Individual contributions of the different non-photoactive layers to the parasitic absorption.

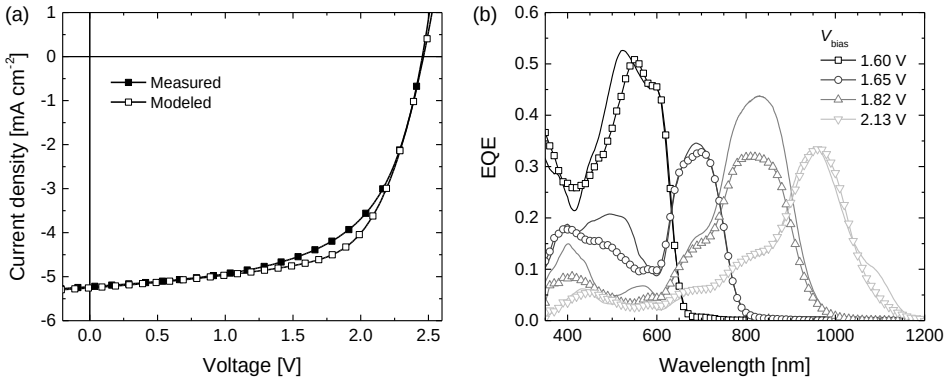

Figure 4. Modeled and experimental device characteristics of the quadruple-junction solar cell. (a) *J*−*V* characteristics under simulated AM1.5G (100 mW cm^{-2}) illumination. (b) Modeled (solid lines) and experimental (lines with open markers) EQEs. The experimental EQEs were measured under representative light and voltage bias conditions.

5.2.2 Performance of the quadruple-junction solar cell

To ensure sufficient accuracy in measuring the $J-V$ characteristic, we matched the light source of our solar simulator in such a way that, at the thicknesses used in the quadruple-junction device, the corresponding four single-junction cells generated virtually the same J_{SC} under solar simulator as the value obtained by integration of their EQE spectrum with the AM1.5G solar spectrum. The photovoltaic performance characteristics of the representative cells, fabricated in the same run of the quadruples, are collected in **Table 3**.

Table 3. Photovoltaic parameters of the reference single-junction devices. Average values are in parentheses.

Device [a]	V_{OC} [V]	J_{SC} [mA cm^{-2}]	FF	P_{max} [mW cm^{-2}]	J_{SC}^{EQE} [b] [mA cm^{-2}]	δJ_{SC} [c] [%]	PCE [d] [%]
PDCBT	0.83 (0.84)	7.81 (7.50)	0.72 (0.71)	4.67 (4.44)	7.58	+3.0	4.53
PTB7-Th	0.76 (0.76)	12.2 (12.0)	0.51 (0.51)	4.73 (4.64)	11.1	+9.5	4.32
PMDPP3T	0.60 (0.60)	15.2 (14.5)	0.52 (0.51)	4.74 (4.44)	15.8	-3.6	4.92
PDPPSDTPS	0.30 (0.30)	13.7 (13.0)	0.48 (0.49)	1.97 (1.90)	13.8	-0.9	1.99

[a] The average is over 8 devices for the $J-V$ measurement (7 devices for PTB7-Th) while the EQE was measured on one device. [b] J_{SC} determined by integrating the EQE over the AM1.5G spectrum. [c] Difference between J_{SC} and J_{SC}^{EQE}. [d] Determined using J_{SC}^{EQE}.

The measurement of the quadruple-junction devices under the calibrated light source returned in the best case a V_{OC} of 2.45 V, a J_{SC} of 5.23 mA cm^{-2} and a FF of 0.59. Together, these corresponded to a PCE of 7.6%, which matches the expected efficiency of 8.2% rather well. There is an excellent match between the modeled and experimental values for J_{SC} and V_{OC} and only the FF is slightly less than expected (0.59 vs. 0.63, see Table 1). Hence, the interconnecting contact of D-PEDOT:PSS/ZnO does not lead to voltage losses. The slightly lower FF can be due to small resistive losses in the interconnecting layers, which are not accounted for in the modeling. Due to the intricate device fabrication, involving 11 solution-processed layers, the yield of efficient quadruple solar cells is moderate: 6 out of 16 devices had efficiencies above 7% with an average of 7.3 ± 0.2%. **Figure 5**a shows the distribution of PCEs among all 16 devices.

To obtain more insight on the device operation, we measured the EQEs of each subcell. Measuring the EQE of a specific subcell in a two-terminal quadruple-junction solar cell requires that this subcell is current limiting over the entire wavelength range over which it is measured. This can be accomplished by using appropriate bias illumination for the remaining three subcells. Optically biased subcells, however, induce an electric field in the device which brings the current-limiting subcell in the reverse bias regime.[14] Because the photocurrent in

polymer solar cells depends on the applied voltage, this can result in an overestimation of the short-circuit current density and EQE. To correct for this, a suitable bias voltage should be applied to the quadruple-junction solar cell to compensate for this optically induced electric field over the subcell of interest. To determine the correct bias illumination conditions we used opto-electrical modeling,[8] and the results are collected in **Table 4**. This method represents an extension of the one already developed for triple-junction cells in Chapter 4. We approximated the bias voltage corrections as the sum of the V_{OC}s of the representative single-junction cells measured under AM1.5G illumination (see the Experimental Section 5.4 of this chapter). In practice this differs by only few tens of mV from the actual values.[8] Figure 4b shows the EQE measurements of the quadruple device measured under representative light and voltage bias conditions (open markers). Figure 5b-d shows three additional EQE spectra for nominally identical quadruple-junction cells fabricated on different substrates. Thanks to the judiciously selected light bias conditions, it possible to measure the EQE of each individual subcell. Figure 5b-d demonstrates that the voltage correction during the EQE measurement is important to not overestimate the EQEs. The measurement without any light bias nicely follows the lower envelope of the EQEs and suggests that leakage paths are not significant (Figure 5b-d).[15]

To give credence to these measurements, the EQE spectra in Figure 4b are compared to the curves expected from the fraction of absorbed photons from the AM1.5G spectrum multiplied by the wavelength-dependent IQE of each photoactive layer. With the exception of the PMDPP3T:$PC_{60}BM$ middle-back cell, the agreement between experiment and modeling is outstanding.

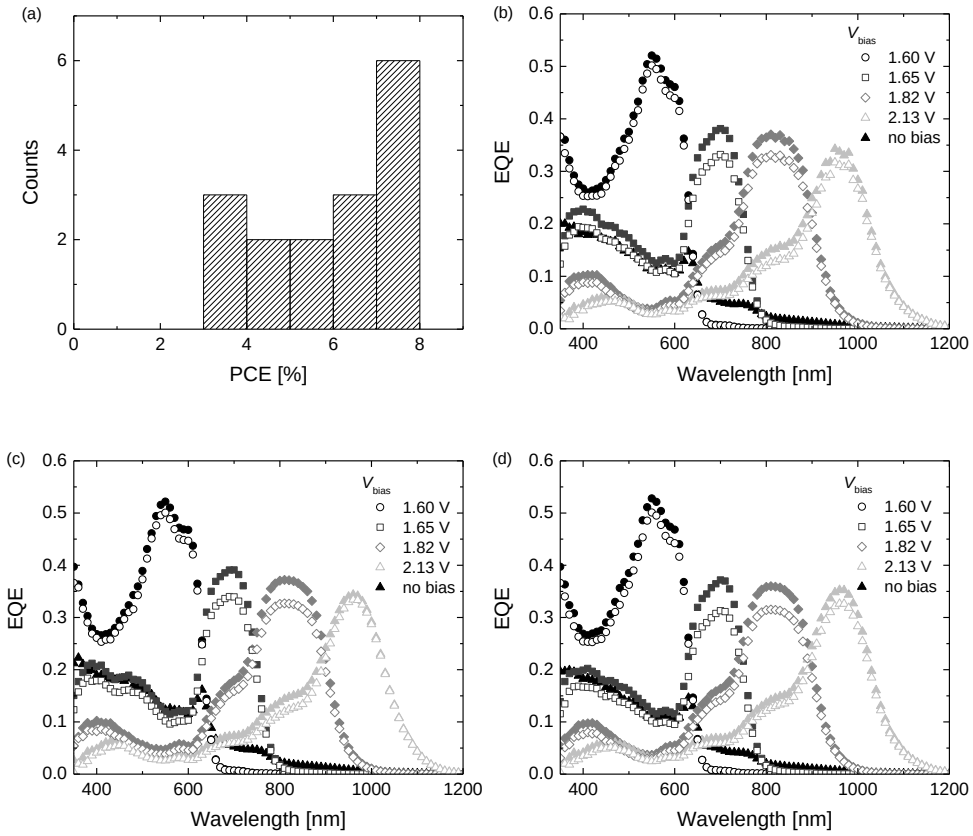

Figure 5. (a) Distribution of the PCE values of the quadruple-junction devices measured under simulated AM1.5G solar spectrum. Average PCE = 5.9 ± 1.5 %. (b-d) EQE spectra of the second, third and fourth best quadruple-junction devices, each from different substrates, acquired under representative light bias conditions, with (empty symbols) and without (filled symbols) a voltage correction (indicated in the legend).

Table 4. Predicted J_{SC}^{max} and J_{SC}^{IQE} for each subcell according to the transfer matrix optical modeling for different bias illumination conditions. The same IQE values as in tables in Appendix 1, 4-6 have been used for calculating J_{SC}^{IQE}. The bold-faced rows indicate the current-limiting subcell.

λ_{LED} [nm]	P_{LED} [mW cm^{-2}]	Subcell	J_{SC}^{max} [mA cm^{-2}]	J_{SC}^{IQE} [mA cm^{-2}]
730	48	**Front cell**	**0.20**	**0.16**
		Front-middle cell	8.27	7.44
		Back-middle cell	8.11	6.16
		Back cell	4.07	2.20
530 + 940	29 + 76	Front cell	6.98	5.58
		Front-middle cell	**2.23**	**2.01**
		Back-middle cell	6.44	4.89
		Back cell	39.66	21.41
530 + 940	65 + 14.8	Front cell	15.64	12.51
		Front-middle cell	5.01	4.51
		Back-middle cell	**2.95**	**2.24**
		Back cell	8.79	4.75
530 + 730	42 + 30	Front cell	10.23	8.19
		Front-middle cell	8.40	7.56
		Back-middle cell	6.27	4.76
		Back cell	**3.29**	**1.78**

For the deviating middle-back cell, we investigated whether the internal quantum efficiency of that active layer was affected by the processing of the back cell. To this end we fabricated different single-junction devices with the structure: ITO/ZnO/PMDPP3T:PC_{60}BM/Top contact. For the top contact we compared different stacks like: MoO_3/Ag (1), D-PEDOT:PSS/MoO_3/Ag (2), and D-PEDOT:PSS/ZnO/Ag (3). For device (2) a second version (2') was made in which the D-PEDOT:PSS layer was rinsed first with butanol and then with a mixture of chloroform with 5 vol.% *o*-dichlorobenzene, from which the top back-cell of PDPPSDTPS:PC_{60}BM in the quadruple was processed. For the device (3') the top ZnO layer was rinsed only with the same chloroform/*o*-dichlorobenzene mixture as for (2'). **Figure 6**a shows the $J-V$ characteristic of these cells under simulated AM1.5G light. No difference can be noticed between the pristine devices and the rinsed ones. A minor loss in J_{SC} from configuration (1) to (2) to (3) appears, due to D-PEDOT:PSS and ZnO, which act as optical spacers. Given these results, we cannot confirm that the processing conditions used for the back cell, deteriorates the performance of the middle-back cell.

With a PCE of 7.6% the quadruple-junction cell has an efficiency that is lower than that of the best single, tandem, and triple-junction cells reported to date. Several factors contribute

to this. Apart from reflection losses and parasitic absorption, the EQE data in Figure 4b clearly show that the middle-front, middle back, and back cell all use photons that should have been absorbed by the previous layer in the stack. At the layer thicknesses used (100 – 170 nm), the photoactive materials are unable to have unit absorption. Single-junction cells are more forgiving in this sense, because photons that are not absorbed in their first pass will be reflected by the metal back electrode, and can be absorbed in the second pass. For multi-junction cells, these photons are more likely to be absorbed by a subsequent layer. At present the only way to increase the absorption efficiency of individual layers is to increase the thickness. Unfortunately, the performance of organic bulk-heterojunction cells is affected by bimolecular recombination, which increase with layer thickness and lowers the fill factor (Figure 6b) and in turn, the efficiency. Hence, while multi-junction polymer solar cells offer the perspective of reaching PCEs in excess of 20%, accomplishing such goal hinges on developing photoactive layers which absorb more efficiently and provide less bimolecular recombination.

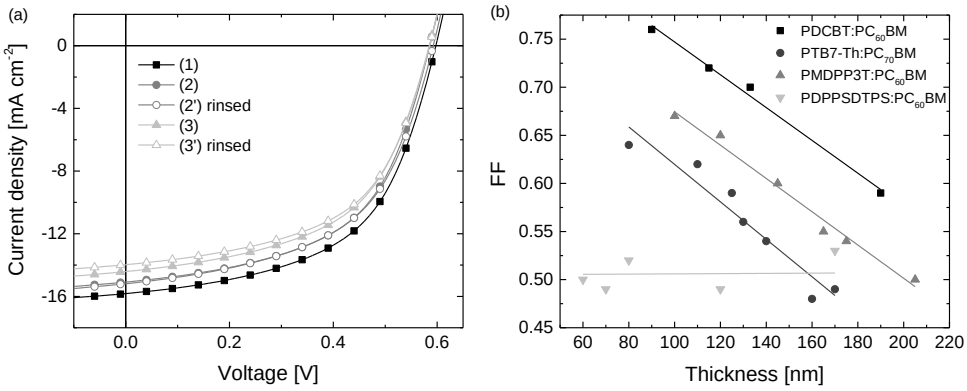

Figure 6. (a) *J*−*V* characteristics of ITO/ZnO/PMDPP3T:$PC_{60}BM$ cells with different top contacts: (1) MoO_3/Ag; (2) D-PEDOT:PSS/MoO_3/Ag; (3) D-PEDOT:PSS/ZnO/Ag as top contact. Device (2') is similar to (2) but was rinsed first with butanol and subsequently with a mixture of chloroform with 5 vol.% *o*-dichlorobenzene before depositing MoO_3/Ag. Device (3') is similar to (3) but was rinsed with a mixture of chloroform with 5 vol.% *o*-dichlorobenzene before depositing MoO_3/Ag. (b) FF of representative single-junction cells as a function of the thickness of the active layer. Lines are guides to the eye.

5.3 Conclusions

In conclusion, we combined four different photoactive polymers with complementary absorption spectra to fabricate a first example of a quadruple-junction polymer solar cell via solution processing. The quadruple-junction solar cell provided a PCE of 7.6 % under simulated AM1.5G sunlight. The results were validated by a comparison with modeling, using the $J-V$ characteristics of representative single-junction cells and optical modeling to determine the fraction of absorbed photons in each individual layer. The correspondence between the measured and modeled EQE was excellent in terms of predicting the spectral shapes and height, except for the middle-back cell were the experimental EQE was lower. The efficiency of the quadruple-junction polymer cell is limited by bimolecular recombination in the photoactive layers, which prevents the use of thick (>200 nm) layers to absorb light more efficiently. Improving the efficiency of multi-junction cells, therefore hinges on developing materials that are efficient also for thick layers. From the perspective of the device fabrication, the present work demonstrates that it possible to process complex device stacks (in this case 14 individual layers of which 11 are processed from solution) in a reliable fashion with photovoltaic properties that are in very good agreement with the expected values. This provides the framework for the development of efficient complex multi-junction solar cells from solution.

5.4 Experimental Section

Materials: Pre-patterned ITO (170 nm) on glass substrates were purchased from Naranjo Substrates. Molybdenum trioxide (MoO_3) powder (99.97%) was purchased from Sigma Aldrich. The ZnO layers were made via a sol-gel route or by spin-coating a suspension of pre-formed nanoparticles in isoamyl alcohol (see Chapter 3 for their synthesis).[13] The former consisted of a solution 0.5 M $Zn(CH_3COO)_2{\cdot}2H_2O$ (98 %, Acros Organics) and 0.5 M ethanolamine in 2-methoxyethanol. The suspension of PEDOT:PSS (Clevios P, VP Al 4083) was diluted in 1-propanol 1:2 (v/v) right before use, referred to in the main text as D-PEDOT:PSS (discussed in Chapter 3).[13] PDCBT,[9] PMDPP3T,[11] and PDPPSDTPS[12] were synthesized according to procedures reported in literature. PTB7-Th was purchased from 1-Material (batch YY10228).

Device fabrication: The patterned ITO substrates were cleaned by sonication in acetone, followed by a solution of sodium dodecyl sulfate in water. They were then rinsed in water and sonicated in isopropanol, before being treated under a UV/ozone lamp to complete the cleaning. In the following paragraphs the processing of all the layers made from solution is described. Wherever mentioned, the sol-gel ZnO was cast directly on clean ITO substrates by spin-coating in ambient air and annealed at 150 °C for 5 min on a hotplate. The D-

PEDOT:PSS solution was always processed by dynamic spin-coating (90 µL per sample) in a nitrogen filled glove box for improved wetting to form a 45 nm thick layer. The layer was kept in the vacuum of the antechamber for 30 min. right after spin-coating to remove residual solvents and no further treatment was performed. The ZnO nanoparticle dispersion was dynamically spin-coated (70 µL per sample) in ambient air to give a 15 nm thick layer, without any post treatment. The last step in the fabrication of each of these devices was the evaporation of the top contact. In all cases this was accomplished by evaporating MoO_3 (10 nm), followed by Ag (100 nm) in a vacuum chamber at ca. 6×10^{-7} mbar, through a shadow mask. On each substrate, the intersection of the ITO pattern with the evaporated top contact formed two squares of 9 mm^2 area and two squares of 16 mm^2 area. The thickness of each layer was measured using a Veeco Dektak profilometer.

PDCBT:$PC_{60}BM$ single-junction cells: The clean ITO substrates were covered with ZnO from the sol-gel route. The two components blended in a 1:1 weight ratio were dissolved in chloroform containing 1 vol.% of *o*-dichlorobenzene at a concentration of 10 mg mL^{-1} of polymer. Subsequently the solution of PDCBT:$PC_{60}BM$ was spin-coated in a N_2 filled glove box to form a layer with a thickness of 110 nm. The substrates were then annealed in the glove box for 5 min at 100 °C. After this step, the D-PEDOT:PSS solution was spin-coated and the samples annealed again at 105 °C for 10 min.

PTB7-Th:$PC_{70}BM$ single-junction cells: D-PEDOT:PSS was processed directly on clean ITO substrates and annealed at 105 °C for 10 min in glove-box. Then the ZnO nanoparticles were deposited as previously described, PTB7-Th was mixed with $PC_{70}BM$ (1:1.5 weight ratio) and dissolved in chlorobenzene, containing 3 vol.% diiodooctane at a concentration of 12 mg mL^{-1} of polymer and cast in the glove box to form a 100 nm thick layer. The substrates were then kept in a vacuum of $\approx 10^{-2}$ mbar for 2 hours. Subsequently, another D-PEDOT:PSS layer was deposited.

PMDPP3T:$PC_{60}BM$ single-junction cells: Sol-gel ZnO was processed on the clean ITO substrate. PMDPP3T was blended with $PC_{60}BM$ (1:3 weight ratio) and dissolved in a solution of chloroform, containing 7 vol.% *o*-dichlorobenzene. The concentration of polymer was 3 mg mL^{-1}. The solution of PMDPP3T:$PC_{60}BM$ was spin-coated in ambient air to obtain a layer of 170 nm in thickness. After this, a layer D-PEDOT:PSS was spin-coated on top.

PDPPSDTPS:$PC_{60}BM$ single-junction cells: D-PEDOT:PSS was processed directly on clean ITO substrates, followed by a layer of ZnO nanoparticles. PDPPSDTPS was blended with $PC_{60}BM$ (1:2 weight ratio) and together dissolved in chloroform, containing 5 vol.% *o*-dichlorobenzene. The concentration of the polymer was 4 mg mL^{-1}.The active layer was spin-coated in the glovebox, with a thickness of 160 nm.

Quadruple-junction solar cells: Sol-gel ZnO was spin-coated on clean ITO substrates. A layer of 110 nm of PDCBT:$PC_{60}BM$ was processed on top in a glovebox and annealed at

100 °C for 5 min. Subsequently, the first layer of D-PEDOT:PSS was spin-coated and annealed in a glovebox, at 105 °C for 10 min. To finish the first interconnecting layer (ICL), ZnO nanoparticles were spin-coated on D-PEDOT:PSS, followed by 100 nm of PTB7-Th:$PC_{70}BM$. After this step, the samples were dried in a vacuum of $\approx 10^{-2}$ mbar for 2 hours. For the second ICL, D-PEDOT:PSS was spin-coated again. Then, the ZnO nanoparticles layer was deposited, followed by 170 nm of PMDPP3T:$PC_{60}BM$. The third ICL was again fabricated with a D-PEDOT:PSS layer, followed by the ZnO nanoparticles. The last active layer was deposited in glovebox with a thickness of 160 nm. The cell was completed by the thermal evaporation of MoO_3 (10 nm) and Ag (100 nm) at ca. 6×10^{-7} mbar.

Characterization: Both the measurement of the $J-V$ curve and the EQE were performed under nitrogen atmosphere. The substrates were treated under a UV-lamp for 8 minutes before measuring, in order to photodope the ZnO and MoO_3 layers. Subsequently, the $J-V$ characteristics were measured with a Keithley 2400 source meter from −2 to +2V (single-junction cells) and from −2 V to +3 V (quadruple-junction cells). 401 points per scan were acquired, each with 20 ms integration time. The lamp used for this measurement was a tungsten-halogen lamp which was filtered with a UV filter and a daylight filter (Hoya LB120), calibrated to match the current integrated from the EQE spectrum of each single-junction cell, as shown in the text. The measurements were performed through an illumination mask with aperture sizes of 6.76 and 12.96 mm^2, corresponding to the 9 mm^2 and 16 mm^2 nominal device areas, respectively. This defined the active area of the devices.

The EQE measurement was performed in a home-made setup, consisting of a tungsten-halogen lamp, a chopper, a monochromator (Oriel, Cornerstone 130), a pre-amplifier (Stanford Research Systems SR570) and a lock-in amplifier (Stanford Research Systems SR830 DSP). The substrates were kept in a N_2-filled box with a quartz window during the duration of the measurement. The device of interest on each substrate was aligned through a circular aperture with 2 mm of diameter, defining the active area. The signal response to the modulated light was transformed into an EQE value by comparison with the measurement on a calibrated silicon reference solar cell. The average standard deviation in measuring the wavelength dependent EQE measurement in this setup is less than 0.005 in electrons/photons for wavelengths in the range of 350–1050 nm. The 530, 730 and 940 nm bias lights were high power LEDs obtained from Thorlabs. The additional voltage bias was applied directly from the pre-amplifier. We measured the V_{OC} of the representative single-junction cells under simulated AM1.5G spectrum and we used those values to estimate the voltage bias needed for each light bias condition. In particular, the voltage correction was the sum of the V_{OC}s of the optically biased subcells for each case. Since the aperture for the measurement of the EQE was smaller (3.14 mm^2) than the apertures used for the measurement of the $J-V$ characteristic (6.76 and 12.96 mm^2), we used another mask with a 3.14 mm^2 aperture to measure again the representative single-junction cells. The measurement returned V_{OC}s of

0.80, 0.75, 0.58 and 0.27 V for the PDCBT, PTB7-Th, PMDPP3T and the PDPPSDTPS single cells.

Optical modeling: Optical modeling based on the transfer matrix (TM) method was performed using Setfos 3.2 (Fluxim). The wavelength dependent *n* and *k* values of each active layer were determined by transmission and reflection measurements using an integrating sphere attachment on a Perkin-Elmer Lambda 1050 spectrophotometer. More details about the procedure are provided in Chapter 1. The optimization based on IQE correction of the modeled current densities and the construction of the $J-V$ characteristics were performed according to a procedure previously reported and extended for quadruple-junction cells.[16] In order to fine tune the prediction with a more accurate estimate of the J_{SC} generated in each subcell, the IQE was determined as a function of the wavelength (λ). To calculate IQE(λ), we divided the EQEs of the representative single-junction cells (Appendix 1, 4-6) by the corresponding fractions of absorbed photons ($f_A(\lambda)$) of the active layers, estimated by means of optical modeling. Again using the optical modeling, we then calculated $f_A(\lambda)$ for each active layer in the quadruple-junction cell and we multiplied these spectra by the corresponding IQE(λ), obtaining an estimated EQE value. The calculation of the J_{SC} value then followed by integration with the AM1.5G reference spectrum. The same tools were used to predict the current generation of each subcell in the quadruple-junction cell under the different light bias conditions, similarly to the procedure developed in Chapter 4. This was done by measuring the power density of the light sources at a different driving current with the calibrated silicon reference cell of the EQE setup and scaling the power profile of each LED (provided by the manufacturer) by those values. The latter spectra were used as input for the TM calculation.

5.5 References

[1] A. Brown, M. Green, *Prog. Photovolt: Res. Appl.* **2002**, *10*, 299.

[2] P. T. Chiu, *D. C Law, R. L. Woo, S. B. Singer, D. Bhusari, W. D. Hong, A. Zakaria, J. Boisvert, S. Mesropian*, R. R. King, N. H. Karam, *Proc. 2014 IEEE 40th Photovoltaic Specialist Conference (PVSC)*, Institute of Electrical and Electronics Engineers Inc., Denver, CO, USA **2014**, pp. 0011.

[3] B. Liu, L. Bai, T. Li, C. Wei, B. Li, Q. Huang, D. Zhang, G. Wang, Y. Zhao, X. Zhang, *Energy Environ. Sci.* **2017**, *10*, 1134.

[4] A. Furlan, R. A. J. Janssen, In *Polymer Photovoltaics: Materials, Physics, and Device Engineering*, F. Huang, H.-L. Yip and Y. Cao (Eds.), Royal Society of Chemistry, **2015**, Chapter 11, p. 310-351.

[5] G. Li, W. H. Chang, Y. Yang, *Nat. Rev. Mater.* **2017**, *2*, 1.

[6] N. Li, D. Baran, K. Forberich, M. Turbiez, T. Ameri, F. C. Krebs, C. J. Brabec, *Adv. Energy Mater.* **2013**, *3*, 1597.

[7] J. Gilot and R. A. J. Janssen, In *Organic Solar Cells: Fundamentals, Devices, and Upscaling*, (Eds: B. P. Rand, H. Richter), Pan Stanford Publishing Pte. Ltd, Singapore **2014**, Ch. 6, pp. 277−313.

[8] D. Di Carlo Rasi, K. H. Hendriks, M. M. Wienk, R. A. J. Janssen, *Adv. Energy Mater.* **2017**, *7*, 1701664.

[9] M. Zhang, X. Guo, W. Ma, H. Ade, J. Hou, *Adv. Mater.* **2014**, *26*, 5880.

[10] S. H. Liao, H. J. Jhuo, Y. S. Cheng, S. A. Chen, *Adv. Mater.* **2013**, *25*, 4766.

[11] W. Li, A. Furlan, K. H. Hendriks, M. M. Wienk, R. A. J. Janssen, *J. Am. Chem. Soc.* **2013**, *135*, 5529.

[12] K. H. Hendriks, W. Li, M. M. Wienk, R. A. J. Janssen, *J. Am. Chem. Soc.* **2014**, *136*, 12130.

[13] D. Di Carlo Rasi, K. H. Hendriks, G. H. L. Heintges, G. Simone, G. H. Gelinck, V. S. Gevaerts, R. Andriessen, G. Pirotte, W. Maes, W. Li, M. M. Wienk, R. A. J. Janssen, *Sol. RRL* **2018**, *2*, 1800018.

[14] J. Gilot, M. M. Wienk, R. A. J. Janssen, *Adv. Funct. Mater.* **2010**, *20*, 3904.

[15] R. Timmreck, T. Meyer, J. Gilot, H. Seifert, T. Mueller, A. Furlan, M. M. Wienk, D. Wynands, J. Hohl-Ebinger, W. Warta, R. A. J. Janssen, M. Riede, K. Leo, *Nat. Photonics* **2015**, *9*, 478.

[16] J. Gilot, M. M. Wienk, R. A. J. Janssen, *Adv. Mater.* **2010**, *22*, E67.

Chapter 6

Solution-Processed Tin Oxide-PEDOT:PSS Interconnecting Layers for Efficient Inverted and Conventional Tandem Polymer Solar Cells*

Abstract

Tin oxide nanoparticles are employed as electron transporting layer in solution-processed polymer solar cells. Tin oxide based devices give excellent performance and can interchangeably be used in conventional and inverted device configurations. In combination with poly(3,4-ethylenedioxythiophene):polystyrene sulfonate (PEDOT:PSS) as hole transporting layer, tin oxide forms an effective interconnecting layer (ICL) for tandem solar cells. Conventional and inverted tandem cells with this ICL provide efficiencies up to 10.4% in good agreement with optical-electrical modeling simulations. The critical advantage of tin oxide in an ICL in a conventional tandem structure over the commonly used zinc oxide is that the latter requires the use of a pH-neutral formulation of PEDOT:PSS to fabricate the ICL, limiting the open-circuit voltage (V_{OC}) because of its low work function. The SnO_2/PEDOT:PSS ICL, on the other hand, provides a nearly loss-free V_{OC}.

* This chapter has been submitted for publication as: D. Di Carlo Rasi, P. M. J. G. van Thiel, H. Bin, K. H. Hendriks, G. H. L. Heintges, M. M. Wienk, T. Becker, Y. Li, T. Riedl, R. A. J. Janssen. Solution-Processed Tin Oxide-PEDOT:PSS Interconnecting Layers for Efficient Inverted and Conventional Tandem Polymer Solar Cells.

6.1 Introduction

Chapter 3 introduced a versatile processing of the ICL for inverted multi-junction polymer solar cells.[1] The ICL consisted of a combination of PEDOT:PSS in a nearly azeotropic water:1-propanol mixture as HTL and zinc oxide nanoparticles dispersed in isoamyl alcohol as ETL. Several double-, triple- and even a quadruple-junction cells could be realized using the same processing conditions. Unfortunately, the same materials are not suitable to fabricate tandem devices in the conventional configuration. Due to its strong acidity ($1 < pH < 2$) the PEDOT:PSS dispersion would unavoidably dissolve a previously deposited zinc oxide layer. A workaround consists in replacing the standard acidic formulation of PEDOT:PSS with a pH-neutral one,[2] but this is accompanied by a loss in the work function of PEDOT:PSS from 5.05 to 4.65 eV.[3] This in turns results in a non-optimal alignment between the Fermi level of PEDOT:PSS and the HOMO level of the electron-donating polymer in the adjacent active layer, if this is particularly deep. As a consequence, a loss in the open-circuit voltage (V_{OC}) occurs.[4] First, Moet et al. proposed the use of Nafion deposited on top of the pH-neutral PEDOT:PSS layer to recover the work function.[4] More recently Lu et al. introduced the usage of phosphomolybdic acid as surface modifier (see Chapter 2).[5] Although this approach was successful, it involves an additional functional layer in the ICL, further complicating the fabrication process. Ideally, an alternative ETL with enough chemical stability to withstand the processing of acidic PEDOT:PSS would be required.

Solution-processed tin oxide nanoparticles have emerged as an ETL in the field of perovskite solar cells.[6] Also sol-gel tin oxide has been used for organic photovoltaic devices.[7,8] Recently, Becker et al. presented a tandem polymer solar cell with a molybdenum oxide/tin oxide ICL, where these layers were deposited by thermal evaporation and atomic layer deposition, respectively.[9] Here we demonstrate the use of commercially available tin oxide colloidal dispersions as ETL for the solution processing of efficient single-junction and tandem polymer solar cells with both the inverted and the conventional configuration. For the tandems, tin oxide was used in combination with PEDOT:PSS in the ICL. Two tin oxide formulations were considered in our study, one in water and one in a 1:1 (v/v) mixture of 1- and 2-butanol. In single-junction cells the performance of tin oxide as ETL compares well with a perylene diimide with amino *N*-oxide terminal substituents (PDINO), used as reference ETL.[10] For the ICL in the inverted tandem configuration a SnO_2 nanoparticles formulation in butanol was used because butanol does not affect a PEDOT:PSS layer. In conventional tandems the tin oxide layer did not dissolve during the deposition of the acidic PEDOT:PSS dispersion. The tandem solar cells with tin oxide afforded efficiencies up to 10.4%, in good agreement with optical-electrical modeling. To further highlight the advantage of solution-processed SnO_2 layers over the ubiquitously used ZnO layers in ICLs of conventional tandem solar cells, we demonstrate that the tandem open-circuit voltage loss

for polymers with deep HOMO energy levels can be reduced from 200 to 20 mV when using SnO_2.

6.2 Results and Discussion

6.2.1 Single-junction Cells with SnO_2 Charge Transport Layers

We fabricated single-junction cells in conventional and inverted cell configurations using poly[(4,8-bis(5-(tripropylsilyl)thiophen-2-yl)benzo[1,2-*b*:4,5-*b'*]dithiophene)-*alt*-(5,6-difluoro-2-(2-hexyldecyl)-4,7-di(thiophen-2-yl)-2H-benzo[*d*][1,2,3]triazole)] (J71) blended with 2,2'-[[6,6,12,12-tetrakis(4-hexylphenyl)-6,12-dihydrodithieno[2,3-*d*:2′,3′-*d'*]-s-indaceno[1,2-*b*:5,6-*b'*]dithiophene-2,8-diyl]bis[methylidyne(3-oxo-1H-indene-2,1(3H)-diylidene)]]bis[propanedinitrile] (ITIC) (**Figure 1**).[11] For inverted devices we deposited SnO_2 nanoparticles from water (5 wt.%) on ITO as ETL (with work function (WF) of 4.0 eV) and PEDOT:PSS as HTL from a water:1-propanol 1:2 (v/v) mixture on the bulk heterojunction layers. For the conventional configuration we used PEDOT:PSS from water on ITO and SnO_2 nanoparticles from a mixture of 1- and 2-butanol 1:1 (v/v) on the active layers. Further details are provided in the Experimental Section 6.4 of this chapter. Layers of SnO_2 nanoparticles have negligible optical absorption in the visible range and show an optical band gap at 3.8-3.9 eV. As a reference, we used a device with PDINO as ETL as published by Bin et al.[11] (Figure 1a). The photovoltaic performance of the three devices under simulated air mass 1.5 (AM1.5G, 100 mW cm^{-2}) solar illumination is reported in **Table 1**. For 75 nm thick active layer films, the short-circuit current density is fairly close for the three devices ($14.8 < J_{SC}^{EQE} < 15.6$ mA cm^{-2}). Compared to the PCE of 11.4% reported by Bin et al.[11] the reference device had unfortunately a lower performance because of a lower FF and J_{SC}. The FF of the conventional cell with SnO_2 is slightly lower than the reference device (0.58 vs 0.60, respectively), while it increases for the inverted cell to 0.63. The results in Table 1 demonstrate that solution-processed SnO_2 layers can be used as effective ETL in single-junction polymer cells.

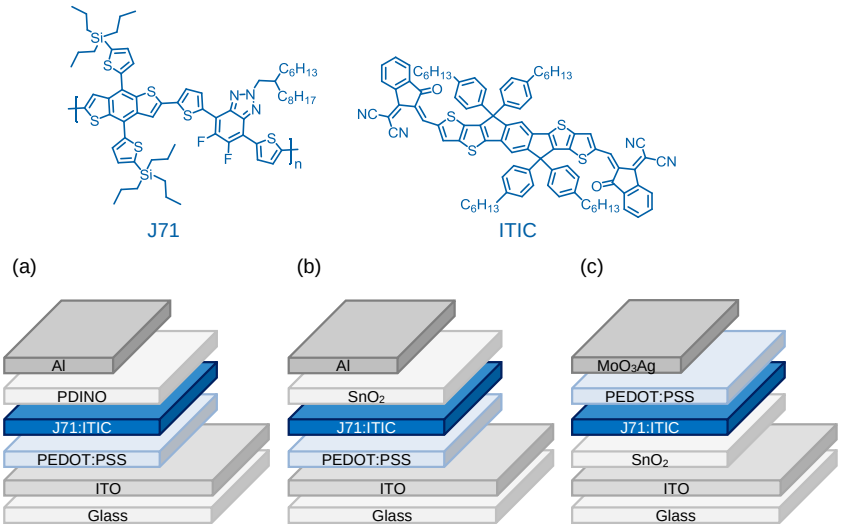

Figure 1. Chemical structures of J71 and ITIC. (a) Reference device. (b) Conventional device. (c) Inverted device.

Table 1. Photovoltaic parameters of J71:ITIC single-junction cells determined with simulated AM1.5G (100 mW cm^{-2}) illumination.

Configuration [a]	V_{OC} [b] [V]	J_{SC} [mA cm^{-2}]	FF	P_{max} [mW cm^{-2}]	J_{SC}^{EQE} [c] [mA cm^{-2}]	PCE [d] [%]
Reference	0.92 (0.92)	15.1 (14.9)	0.60 (0.60)	8.34 (8.13)	15.2	8.39
Conventional	0.93 (0.93)	14.9 (14.7)	0.58 (0.58)	8.04 (7.88)	14.8	7.98
Inverted [e]	0.92 (0.91)	16.1 (15.8)	0.63 (0.61)	9.33 (8.85)	15.6	9.04

[a] Thickness of active layers is 75 nm. [b] Values are reported for best cells with average performance over 4 cells in parentheses. [c] By integrating the EQE with the AM1.5G spectrum. [d] Calculated using J_{SC}^{EQE}. [e] Prior to the measurement, the devices were exposed to UV-light.

6.2.2 Tandem Solar Cells with SnO_2 and PEDOT:PSS Interconnecting Layer

Prior to making tandem cells in the conventional configuration we tested the integrity of the SnO_2 layer against the subsequent deposition of an acidic aqueous PEDOT:PSS dispersion. A SEM cross-section image shows a closed SnO_2 nanoparticle layer after depositing a PEDOT:PSS layer on top from an acidic aqueous dispersion **(Figure 2)**. This demonstrates that the acidic PEDOT:PSS dispersion does not deteriorate the SnO_2 layer.

Kelvin probe experiments showed a WF of 5.0 eV for the ITO/SnO_2/PEDOT:PSS stack, close to the WF of 5.1 eV for ITO/PEDOT:PSS.

For the inverted configuration, SnO_2 from butanol was spin-coated on top of PEDOT:PSS. The WF of an ITO/PEDOT:PSS/SnO_2 stack determined from Kelvin probe is 4.1 eV, compared to 4.0 eV for a ITO/SnO_2 layer.

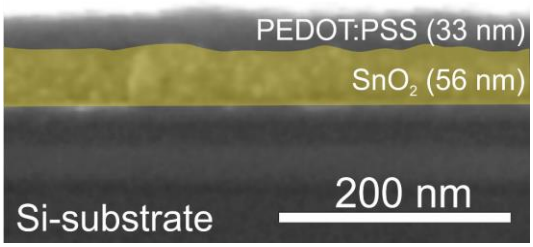

Figure 2. Colored SEM cross-section of a PEDOT:PSS layer spin-coated on a SnO_2 nanoparticle layer on a Si substrate.

Next, both conventional and inverted tandem devices were fabricated, adopting complementary active layer absorbers for the subcells. J71 blended with ITIC was used as wide band gap front cell absorber, while poly[[2,5-bis(2-hexyldecyl-2,3,5,6-tetrahydro-3,6-dioxopyrrolo[3,4-*c*]pyrrole-1,4-diyl]-*alt*-[3′,3″-dimethyl-2,2′:5′,2″-terthiophene]-5,5″-diyl] (PMDPP3T) [12] in combination with [6,6]-phenyl-C_{61}-butyric acid methyl ester ($PC_{60}BM$) was used as active layer for the small band gap back cell. **Figure 3** shows a schematic of the device stack adopted for both configurations and the chemical structures of PMDPP3T and $PC_{60}BM$.

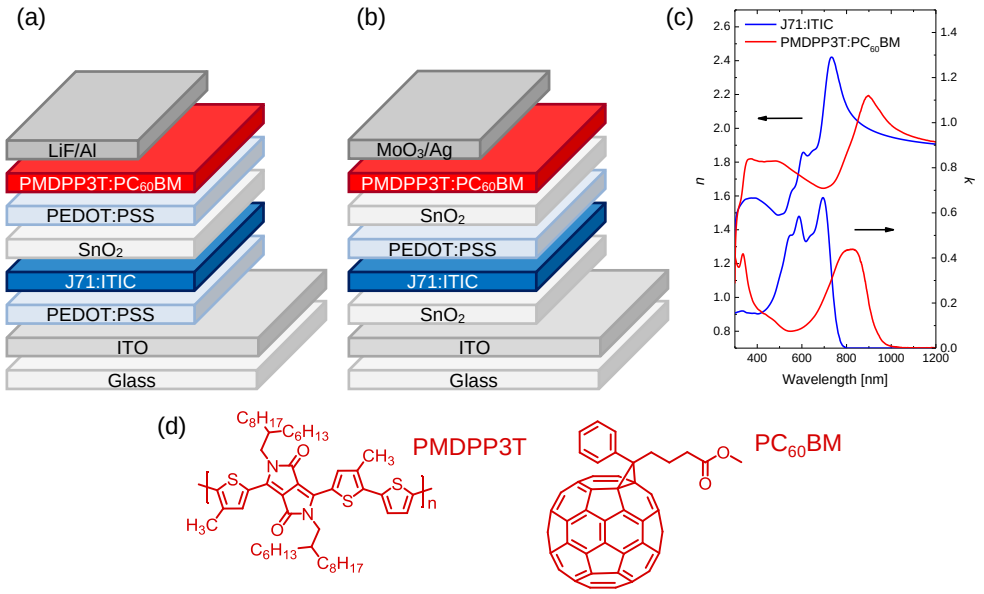

Figure 3. Tandem solar cells in the conventional (a) and the inverted (b) configurations. Wavelength-dependent *n* and *k* optical constants of the active layers (c). Chemical structures of PMDPP3T and $PC_{60}BM$ (d).

In order to maximize and balance the light absorption in the subcells of the tandem devices, we performed optical simulations using the transfer matrix method on the entire device stacks using the experimentally determined refractive index and extinction coefficients of all layers in the stack. The wavelength-dependent refractive index ($n(\lambda)$) and extinction coefficient ($k(\lambda)$) of the active layers are shown in Figure 3c. These optical simulations were then combined with electrical performance data, acquired from a set of representative single-junction devices of both the subcells, at different thickness of the active layer to obtain the expected current density – voltage (*J*–*V*) characteristics of the tandem cells from which the relevant expected device metrics can be determined. The details of this method are described in the literature and in the remainder we refer to it as optical-electrical modeling.[13] The precise device structure and photovoltaic parameters of the single-junction cells are reported in the Experimental Section 6.4 of this chapter and Appendix 3, 7 and 8. **Figure 4** shows the contour plots of the predicted PCE for the conventional and inverted tandem cells obtained from the optical-electrical modeling.

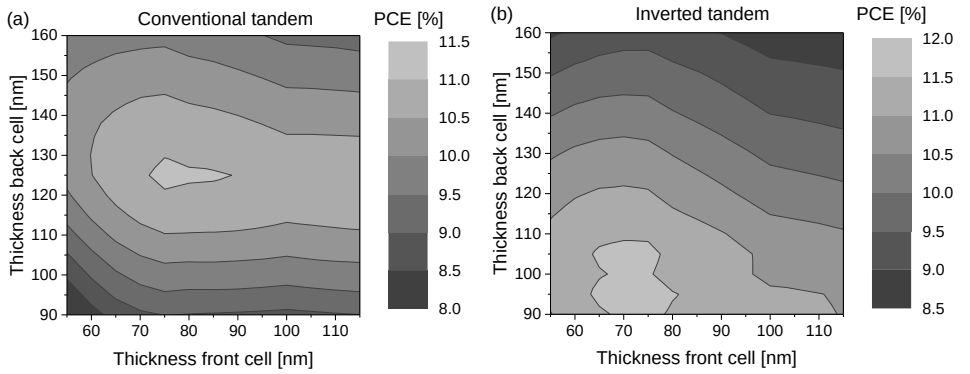

Figure 4. Contour plots of the PCE predicted by optical-electrical modeling as a function of the thicknesses of both the front and the back subcells of the conventional (a) and inverted (b) tandem cells.

The highest efficiency predicted for the conventional tandem is 11.1% and corresponds to a thickness combination of 75 nm for the front cell and 125 nm for the back cell. For the inverted tandem the highest PCE expected is 11.7%, and corresponds again to 75 nm for the front cell and 95 nm for the back cell. Because initial experiments on inverted tandem cells gave lower performance than the optical-electrical modeling suggested, we verified experimentally the exact location of the optimum point in the inverted structure. For this we fabricated inverted tandem cells in which the thickness of the front cell was 75 nm, and the thickness of the back cell was increased from 95 nm to 110 nm and 125 nm and we compared the experimental EQE with the optical-electrical modeling (**Figure 5)**. While the experimental EQE of the front cell closely follows the predicted spectral shift with thickness, the experimental EQE of the back cell maximizes at 125 nm, while the optical-electrical modeling suggested 95 nm. For this reason we chose 125 nm for the thickness of the back cell as the experimental optimum. According to the optical-electrical modeling, this should correspond to a PCE of 10.8%. For the conventional configuration layer stack the PCE of the tandem cell did not improve when changing the thickness compared to the optimum found in the optical-electrical modeling. It is presently not clear what causes the small differences between the modeling and experiments for the inverted tandem cells, but not for the conventional cells. The *J-V* characteristics of the optimized tandem cells measured under simulated AM1.5G (100 mW cm^{-2}) solar light are shown in **Figure 6** and the relevant parameters are summarized in **Table 2**.

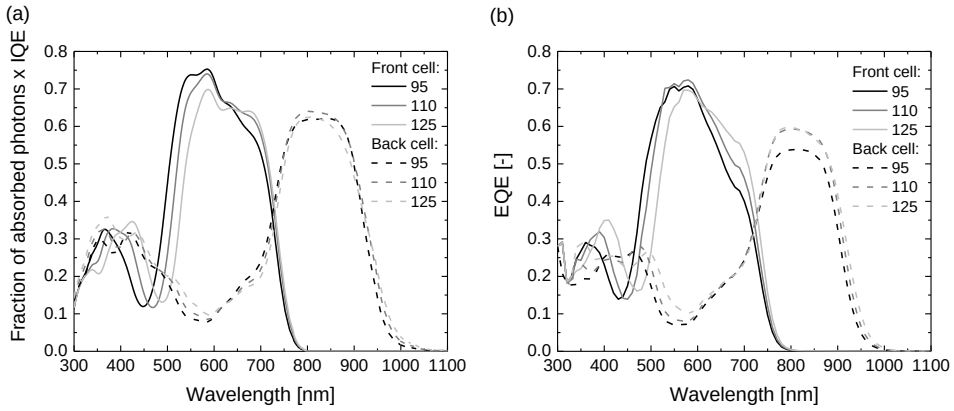

Figure 5. EQE spectra of the inverted tandem cell with thickness of the front cell of 75 nm and thickness of the back cell of 95, 110, and 125 nm. (a) Predicted EQE from optical-electrical modeling as fraction of absorbed photons × IQE. (b) Experimentally measured EQE.

Table 2. Photovoltaic parameters of tandem solar cells shown in Figure 3 determined with simulated AM1.5G (100 mW cm^{-2}) illumination.

Configuration [a]		V_{OC} [V]	J_{SC} [mA cm^{-2}]	FF	PCE [%]
conventional	experiment	1.51 (1.51)	10.10 (9.91)	0.67 (0.66)	10.22 (9.88)
	modeling	1.54	11.05	0.65	11.07
inverted	experiment	1.48 (1.48)	11.10 (10.95)	0.63 (0.63)	10.35 (10.18)
	modeling	1.53	11.38	0.62	10.80

[a] Values are reported for best cells with average performance over 8 cells in parentheses. All tandems were exposed to UV light prior to the measurement.

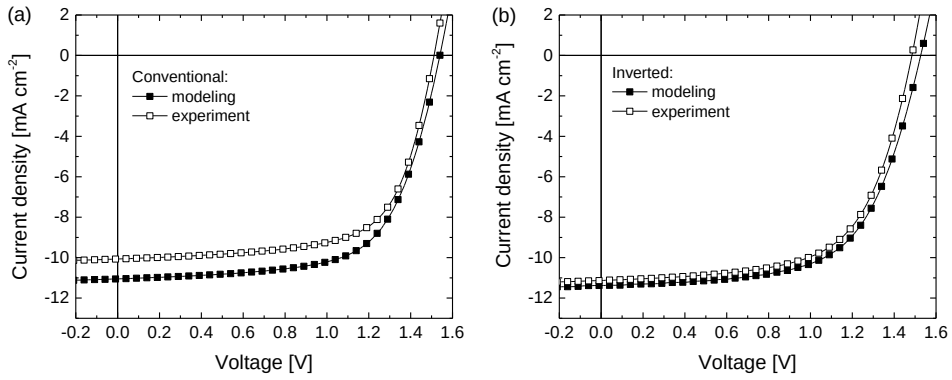

Figure 6 *J-V* characteristics of optimized conventional (a) and inverted (b) tandem devices measured under simulated AM1.5G light (100 mW cm^{-2}) (open symbols) and corresponding predicted optical-electrical modeling (solid symbols).

With respect to the optical-electrical modeling, the V_{OC} is only 2% lower for the conventional structure (1.51 vs 1.54 V) and 3% lower for the inverted one (1.48 vs 1.53 V). The fill factor (FF) is in general slightly higher than the modeling: 0.67 vs 0.65 for the conventional cell and 0.63 vs 0.62 for the inverted tandem cell. The experimental and modeled J_{SC} of the conventional cell deviate by 1 mA cm^{-2} (10.10 vs 11.05 mA cm^{-2}). For the inverted tandem the experimental J_{SC} matches rather well with the optical-electrical modeling (11.10 vs 11.38 mA cm^{-2}). To understand the origin of these deviations and to get in general a better insight, we measured the external quantum efficiency (EQE) spectra of the tandem cells. The EQEs were measured under representative light and voltage bias conditions. The light bias is meant to isolate the response of the individual front and the back cells, while the voltage bias corrects for the electric field induced in the device by the light bias.[14] Light emitting diodes (LEDs) centered at 530 and 940 nm were used for optical biasing the front and the back subcells, respectively. The required voltage bias (V_{bias}) was approximated as the V_{OC} of the representative single-junction cells, i.e. V_{bias} = 0.92 V for the front cell and V_{bias} = 0.61 V for the back cell (Appendix 7 and 8). **Figure 7** shows the EQE under the different bias conditions. The EQE without light bias follows the lower envelope of the EQE of the subcells, pointing that the contribution of leakage paths is relatively low.[15] The effect of the voltage bias is relatively small, and more significant for the back cell of the inverted tandem. The experimental and optically modeled EQE spectra for both tandem cell configurations are shown in **Figure 8**. The agreement between optical-electrical modeling and experiment is generally good for both the front and back cells. Minor differences account

for the 1 mA cm^{-2} drop in the J_{SC} for the conventional tandem, with respect to the modeling (Table 2).

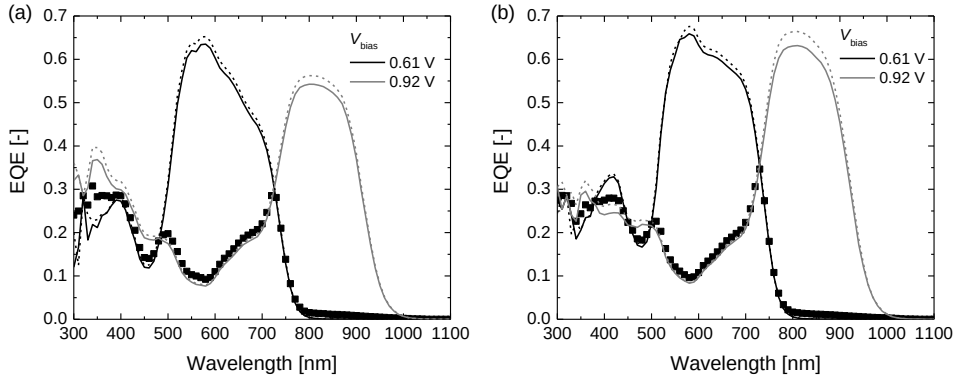

Figure 7. EQE spectrum of the conventional (a) and the inverted (b) tandem, as measured under a 530 nm LED bias (grey lines), a 940 nm LED bias (black lines), with (solid lines) or without (dashed lines) a voltage bias, indicated in the legend. The measurement without any bias is reported with black squares.

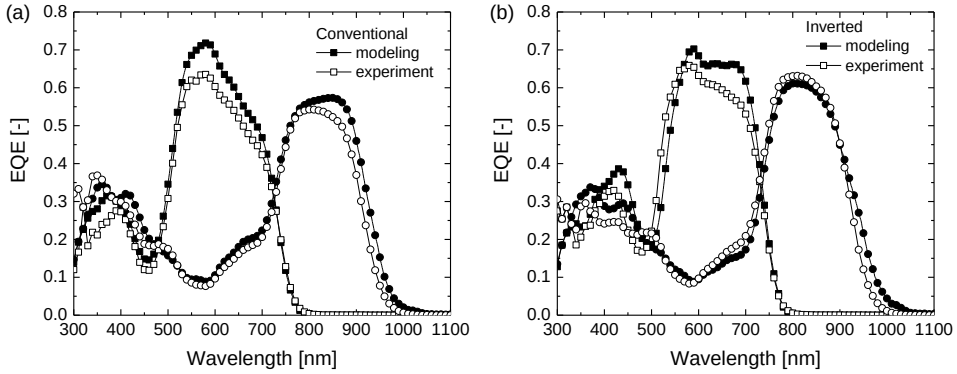

Figure 8. Experimental (open symbols) and modeled (solid symbols) EQE spectra of (a) conventional and (b) inverted tandem cells. The EQEs of the front cells are represented with squares while the back cells are reported using circles.

Table 3. J_{SC} values (in mA cm^{-2}) obtained by integration of the EQE spectrum of the subcells of the conventional and inverted tandems cells with the AM1.5G spectrum (100 mW cm^{-2}).

	Conventional		Inverted	
	Front cell	Back cell	Front cell	Back cell
Modeling	11.09	10.91	11.76	11.15
Experiment	9.99	9.93	11.03	11.16

6.2.3 Advantage of SnO_2 over ZnO

The possibility of fabricating a conventional tandem with tin oxide has an important consequence wherever a polymer with a deep-lying HOMO level is used in the back cell to increase the V_{OC}. One such example is poly[{2,5-bis(2-hexyldecyl)-2,3,5,6-tetrahydro-3,6-dioxopyrrolo[3,4-c]pyrrole-1,4-diyl}-*alt*-{[2,2′-(1,4-phenylene)bisthiophene]-5,5′-diyl}] (PDPPTPT) which has a HOMO energy level of 5.48 eV.[16] We previously reported that in a conventional tandem cell with zinc oxide and pH-neutral PEDOT:PSS a V_{OC} loss of 200 mV occurs because of the mismatch between the HOMO of PDPPTPT and the work function of the pH-neutral PEDOT:PSS.[17] To confirm that this loss does not occur for the new SnO_2/PEDOT:PSS ICL, we fabricated a PDPPTPT:$PC_{70}BM$ homo-tandem cell, i.e. using the same active layer for both subcells. Here $PC_{70}BM$ is the [6,6]-phenyl-C_{71}-butyric acid methyl ester. The device structure was identical to that in Figure 3a, using PDPPTPT:$PC_{70}BM$ as active layers. For simplicity, the same layer thickness (100 nm) was used in both subcells. An ITO/PEDOT:PSS/PDPPTPT:$PC_{70}BM$/LiF/Al single-junction cell with 100 nm thickness was used as reference. **Table 4** shows the photovoltaic metrics of these devices under simulated AM1.5G solar radiation.

Table 4. Photovoltaic parameters of single and homo-tandem cells based on PDPPTPT:$PC_{70}BM$ in a conventional structure determined with simulated AM1.5G (100 mW cm^{-2}) illumination.

Configuration [a]	V_{OC} [V]	J_{SC} [mA cm^{-2}]	FF	PCE [%]
Single junction	0.80 (0.79)	14.4 (14.4)	0.63 (0.62)	7.23 (7.03)
Single junction [b]	0.78 (0.78)	7.34 (7.37)	0.66 (0.65)	3.77 (3.72)
Tandem	1.54 (1.54)	7.59 (7.48)	0.58 (0.58)	6.82 (6.69)

[a] See the main text for a description. Values are reported for best cells with average performance in parentheses. The statistics is over 4 identical cells for the single-junction devices and 8 cells for tandems. [b] These measurements were performed under reduced light intensity to mimic the behavior of the subcells in the tandem.

Having the same active layer in both subcells, the V_{OC} of the tandem is expected to be twice that of the single-junction cell (1.60 V). Experimentally, the tandem cells had a V_{OC} of 1.54 V, which is 4% lower than expected. Part of this loss is due to the reduced light intensity experienced by the subcells. This loss can be estimated from $\Delta V_{OC} = (kT/q)\ln[J_{SC}(\text{tandem})/J_{SC}(\text{single})]$, where J_{SC}(tandem) and J_{SC}(single) are the J_{SC} values of the tandem and the single-junction cells (Table 4), and k Boltzmann constant, T the temperature, and q the elementary charge. Since the same absorber is used in both subcells, J_{SC}(tandem) roughly corresponds to half the J_{SC}(single) value, as confirmed by the results in Table 4 (7.59 vs 14.4 mA cm^{-2}, respectively). Therefore, we can expect an 18 mV loss at each junction, accounting in total to 36 mV. To confirm this, the reference single-junction cell was also measured at reduced light intensity, such that it was giving a similar J_{SC} as the tandem cell. The V_{OC} measured in this way was 20 mV lower, very close to the predicted loss of 18 mV. The V_{OC} loss of the tandem which is not directly attributable to the reduced light intensity is then only 20 mV. This result is significantly better than what reported earlier for a similar tandem using zinc oxide and pH-neutral PEDOT:PSS, where the V_{OC} loss was 200 mV.[17] This confirms that a SnO_2/acidic-PEDOT:PSS ICL gives superior performance compared to a ZnO/pH-neutral-PEDOT:PSS ICL for polymers with deep HOMO levels.

6.3 Conclusions

Commercially available tin oxide nanoparticles dispersions in water or butanol are adopted in the fabrication of polymer solar cells. Both conventional (p-i-n) and inverted (n-i-p) solar cells can be build using tin oxide as ETL and PEDOT:PSS as HTL in the interconnecting layer. The two materials are not only chemically compatible with each other, but they also provide an effective interconnection of the subcells, as demonstrated by two high efficiency tandems with PCEs of 10.2% (conventional) and 10.4% (inverted), in good agreement with the performance predicted by optical-electrical modeling. The use of SnO_2 and its resilience against acidic aqueous PEDOT:PSS dispersions compared to the traditionally used ZnO, has an important advantage when donor materials with deep-lying HOMO energy level are involved. As an example, a homo-tandem cell with two PDPPTPT:PC_{70}BM active layers shows nearly a negligible voltage loss (20 mV) when compared to the 200 mV loss reported for a similar device based on zinc oxide and pH-neutral PEDOT:PSS.[17] In conclusion, SnO_2 and PEDOT:PSS can be used as ICL for efficient conventional and inverted tandem cells, without the need of additional layers to reach optimal performance. Together, these results pave the way to new possibilities in the framework of manufacturing efficient multi-junction organic solar cells.

6.4 Experimental Section

Materials: Pre-patterned ITO (190 nm) on glass substrates were purchased from Naranjo Substrates. Molybdenum trioxide powder (99.97%) was purchased from Sigma Aldrich. The tin oxide layers were made by spin-coating a suspension of pre-formed nanoparticles. These were either tin oxide in water (15 wt.%, Alfa Aesar) or in a mixture of 1- and 2-butanol 1:1 (v/v) (N31, 2.5 wt.%, Avantama). The concentration was adapted by diluting the stock dispersion with water or 1-butanol, respectively. The suspension of PEDOT:PSS (Clevios P, VP Al 4083) was filtered with a 0.45 µm PVDF filter and directly used or diluted with 1-propanol while vigorously stirring (referred to as D-PEDOT:PSS, see Chapter 3).[1] A dilution ratio of 1:2 (v/v) was used by adding n-propanol (1 mL) to VP Al 4083 (0.5 mL) in 15 minutes under constant vigorous stirring. The suspension was prepared right before depositing D-PEDOT:PSS, and no further additives were used. PDINO was synthesized according to the procedure reported in literature and dissolved in methanol with a concentration of 1 mg mL^{-1}.[10] $PC_{60}BM$ and $PC_{70}BM$ were purchased from Solenne while ITIC was purchased from Solarmer. Poly[(4,8-bis(5-(tripropylsilyl)thiophen-2-yl)benzo[1,2-*b*:4,5-*b'*]dithiophene)-*alt*-(5,6-difluoro-2-(2-hexyldecyl)-4,7-di(thiophen-2-yl)-2H-benzo[*d*][1,2,3]triazole)] (J71) was synthesized according to the procedure reported in literature and blended with ITIC with a 1:1 weight ratio.[11] The two components were dissolved in chloroform at a concentration of 6 mg mL^{-1} of polymer. Poly[[2,5-bis(2-hexyldecyl-2,3,5,6-tetrahydro-3,6-dioxopyrrolo[3,4‑*c*]pyrrole-1,4-diyl]-*alt*-[3′,3″-dimethyl-2,2′:5′,2″-terthiophene]-5,5″-diyl] (PMDPP3T) was synthesized following the reported procedure.[12] PMDPP3T was blended with $PC_{60}BM$ (1:3 weight ratio) and dissolved in a solution of chloroform, containing 7 vol.% *o*-dichlorobenzene. The concentration of polymer was 3 mg mL^{-1}. Poly[{2,5-bis(2-hexyldecyl)-2,3,5,6-tetrahydro-3,6-dioxopyrrolo[3,4-*c*]pyrrole-1,4-diyl}-*alt*-{[2,2′-(1,4-phenylene)bisthiophene]-5,5′-diyl}] (PDPPTPT) was synthesized according to the procedure reported in literature.[16] This polymer was blended with $PC_{70}BM$ 1:2 (w/w) in chloroform with 6 vol.% *o*-dichlorobenzene at a polymer concentration of 5 mg mL^{-1}.

Device Fabrication: The patterned ITO substrates were cleaned by sonication in acetone, followed by a solution of sodium dodecyl sulfate in water. They were then rinsed in water and sonicated in isopropanol, before being treated under a UV/Ozone lamp to complete the cleaning. Molybdenum oxide (10 nm), silver (100 nm), lithium fluoride (1 nm) and aluminum (100 nm) were thermally evaporated in a vacuum chamber at $\approx 6 \times 10^{-7}$ mbar, through a shadow mask. On each substrate, the intersection of the ITO pattern with the evaporated top contact formed two squares of 9 mm^2 area and two squares of 16 mm^2 area. The thickness of each layer was measured using a Veeco Dektak profilometer. The fabrication of the various device stacks described in this study is detailed in the following paragraphs.

J71:ITIC Single-Junction Cell (Conventional) (1): The filtered PV Al 4083 was coated on clean ITO substrates with a thickness value of 50 nm and annealed at 140 °C for 10 min. The J71:ITIC blend was deposited in a N_2 filled glove box to form a layer with thickness of 75 nm and annealed at 150 °C for 10 min. After this, a different ETL was deposited for the reference device and the tin oxide based device. In one case, PDINO was deposited in glovebox, with a thickness of 3 nm. In the other case, tin oxide in butanol (2.5 wt.%) was deposited by dynamic spin-coating in glove box and dried at $\approx 10^{-2}$ mbar for 2 hours. This layer served as wetting layer for the subsequent deposition of tin oxide in water (2.5 wt.%) by dynamic spin-coating in ambient air. Also this layer was dried at $\approx 10^{-2}$ mbar for 30 min. The final thickness of the tin oxide layer was 35 nm. We encountered a suboptimal performance of the device when using only the first layer of tin oxide in butanol, possibly due to an unfavorable morphology of the layer. For this reason we opted for the combination of the two formulations, here reported. At last, both the reference and the tin oxide device were completed by evaporating the aluminum top contact.

J71:ITIC Single-Junction Cell (Inverted) (2): Clean ITO substrates were covered with tin oxide from water (5 wt.%) to form a 40 nm thick layer and annealed at 150 °C for 30 min. Subsequently the solution of J71:ITIC was spin-coated in a N_2 filled glove box. The thickness of the active layer was varied by changing the rotational speed. The substrates were then annealed in the glove box for 10 min at 150 °C. After this step, the D-PEDOT:PSS solution was dynamically spin-coated in the same environment and the samples dried at $\approx 10^{-2}$ mbar for 30 min. To finish the device, molybdenum oxide and silver were evaporated on top. MoO_3 prevents the formation of silver filaments that can reach the active layer and that occasionally form when silver is deposited directly on PEDOT:PPS.

PMDPP3T:PC_{60}BM Single-Junction Cell (Conventional) (3): Clean ITO substrates were coated with VP Al 4083 to form a 50 nm thick layer and annealed at 140 °C for 10 min. The PMDPP3T:PC_{60}BM solution was deposited in ambient air without any post treatment. The thickness of this layer was controlled by varying the rotational speed. At last, lithium fluoride and aluminum were evaporated on top.

J71:ITIC-PMDPP3T:PC_{60}BM Tandem Cell (Conventional) (4): The filtered PV Al 4083 was coated on clean ITO substrates to form a layer with thickness value 50 nm and annealed at 140 °C for 10 min. The J71:ITIC blend was deposited in a N_2 filled glove box to form a layer with a thickness of 75 nm and annealed at 150 °C for 10 min. After this, tin oxide in butanol (2.5 wt.%) was deposited by dynamic spin-coating in glove box and dried at $\approx 10^{-2}$ mbar for 2 hours. This layer served as wetting layer for the subsequent deposition of tin oxide in water (2.5 wt.%) by dynamic spin-coating in ambient air, analogously to what reported for device (1). Also this layer was dried at $\approx 10^{-2}$ mbar for 30 min. The final thickness of the tin oxide layer was 35 nm. VP Al 4083 was deposited by dynamic spin-coating in ambient air to form a 50 nm thick layer and dried at $\approx 10^{-2}$ mbar for 30 min. The

PMDPP3T:PC_{60}BM solution was deposited in ambient air without any post treatment. The thickness of this layer was 125 nm. At last, lithium fluoride and aluminum were evaporated on top.

J71:ITIC-PMDPP3T:PC_{60}BM Tandem Cell (Inverted) (5): The clean ITO substrates were covered with tin oxide from water (5 wt.%) to form a 40 nm thick layer, i.e. without using wetting layer, and annealed at 150 °C for 30 min. Subsequently the solution of J71:ITIC was spin-coated in a N_2 filled glove box, to form a film with a thickness of 75 nm. The substrates were then annealed in the glove box for 10 min at 150 °C. After this step, the D-PEDOT:PSS solution was dynamically spin-coated in the same environment to make a 45 nm thick layer and the samples annealed again at 150 °C for 5 min. Tin oxide in butanol (2.5 wt.%) was dynamically coated in ambient air to form a 55 nm thick layer. The layer was dried in a vacuum of $\approx 10^{-2}$ mbar for 30 min. The solution of PMDPP3T:PC_{60}BM was spin-coated in ambient air, returning a layer thickness of 125 nm. No further treatment was performed before the evaporation of the molybdenum oxide/silver top contact.

PDPPTPT:PC_{70}BM Single-Junction Cell (Conventional) (6): The clean ITO substrates were covered with P VP Al 4083 PEDOT:PSS dispersion to form a layer of 50 nm in thickness. The substrates were then annealed at 140 °C for 10 min. The PDPPTPT:PC_{70}BM solution was deposited by spin-coating in ambient air to make a layer with thickness 100 nm. No post-treatment was performed before the evaporation of lithium fluoride and aluminum at last.

PDPPTPT:PC_{70}BM Homo-Tandem Cell (Conventional) (7): Clean ITO substrates were coated with PEDOT:PSS to form a layer with 50 nm of thickness and annealed at 140 °C for 10 min. PDPPTPT:PC_{70}BM was deposited in ambient conditions on top of this to form a layer of 100 nm in thickness, without any post-treatment. Subsequently, tin oxide in butanol (2.5 wt.%) was deposited by dynamic spin-coating in glove box and dried in a vacuum of $\approx 10^{-2}$ mbar for 2 hours. This layer served as wetting layer for the subsequent deposition of tin oxide in water (2.5 wt.%) by dynamic spin-coating in ambient air, similarly to devices (1) and (4). Also this layer was dried in a vacuum of $\approx 10^{-2}$ mbar for 30 min. The final thickness of the tin oxide layer was 35 nm. VP Al 4083 was deposited by dynamic spin-coating in ambient air to form a 50 nm thick layer and dried in a vacuum of $\approx 10^{-2}$ mbar for 30 min. The top PDPPTPT:PC_{70}BM active layer was deposited using the same conditions as for the front cell. To complete the stack, lithium fluoride and aluminum were thermally evaporated.

Characterization: Both the measurement of the $J-V$ curve and the EQE were performed under nitrogen atmosphere. Devices with MoO_3 were treated under a UV-lamp before the measurements. For these devices we found that this UV treatment gives more reproducible and occasionally better device performance. For the conventional tandem device we found a UV-treatment to be beneficial for the FF (+3%). Probably a similar photodoping mechanism

can occur for tin oxide as well, although we did not investigate the mechanism. The $J-V$ characteristics were measured with a Keithley 2400 source meter from –2 to +2V (inverted cells) or +2 to −2V (conventional cells). 401 points per scan were acquired, each with 20 ms integration time. The lamp used for this measurement was a tungsten-halogen lamp which was filtered with a UV filter and a daylight filter (Hoya LB120). The color and intensity of the light were tuned in a way to match the EQE-integrated J_{SC} of representative single-junction cells of the two subcells at the same time. The measurements were performed through an illumination mask with aperture sizes of 6.76 and 12.96 mm^2, corresponding to the 9 mm^2 and 16 mm^2 nominal device areas, respectively. This defined the active area of the devices.

The EQE measurement was performed in a home-made setup, consisting of a tungsten-halogen lamp, a chopper, a monochromator (Oriel, Cornerstone 130), a pre-amplifier (Stanford Research Systems SR570) and a lock-in amplifier (Stanford Research Systems SR830 DSP). The substrates were kept in a N_2-filled box with a quartz window during the duration of the measurement. The device of interest on each substrate was aligned through a circular aperture with 2 mm of diameter, defining the active area. The signal response to the modulated light was transformed into an EQE value by comparison with the measurement on a calibrated silicon reference solar cell. The average standard deviation in measuring the wavelength-dependent EQE in this setup is less than 0.005 electrons/photons for wavelengths in the range of 350-1050 nm. The 530 and 940 nm bias lights were high power light-emitting diodes obtained from Thorlabs. The additional voltage bias was applied directly from the pre-amplifier. The voltage bias correction needed for the EQE of the tandems cells was approximated as the V_{OC} of the reference single-junction cells: 0.92 and 0.61 V for biasing the front and back subcells, respectively.

Optical-Electrical Modeling: Optical simulations based on the transfer matrix method was performed using Setfos 3.2 (Fluxim). The wavelength dependent n and k values of each active layer were determined by transmission and reflection measurements (see Chapter 1) using an integrating sphere attachment on a Perkin-Elmer Lambda 1050 spectrophotometer. The optimization based on IQE correction of the modeled current densities and the construction of the $J-V$ characteristics was performed according to a procedure previously reported.[13] According to the results discussed in Section 6.2.1, the performance of J71:ITIC in the conventional and inverted structure is more or less comparable. Therefore, the data series of the representative conventional cell of J71:ITIC was approximated with the dataset of the inverted representative cell, reported in Appendix 8. The performance of the PMDPP3T:$PC_{60}BM$ series in the inverted configuration was taken from Appendix 3, where zinc oxide instead of tin oxide was used. We then calculated the spectrally resolved fraction of absorbed photons from the subcells and we scaled this by the corresponding IQE (reported in Appendix 3, 7 and 8). The result can be considered as an estimated EQE spectrum of the subcells. Integration with the reference AM1.5G solar spectrum follows to derive the J_{SC} of

the subcells. At last, the construction of the *J-V* characteristic of the tandem was performed as described in the referenced article.[13]

Scanning electron microscopy: For the SEM cross-section studies, layers on Si substrates were investigated using a Philips XL30S FEG microscope with a field emission cathode.

Kelvin Probe: The measurements of the surface potential were done with a McAllister KP6500 Kelvin-Probe (KP) system in vacuum (10^{-6} mbar). Highly ordered pyrolytic graphite with a work function of 4.5 eV was used as reference.

6.5 References

[1] D. Di Carlo Rasi, K. H. Hendriks, G. H. L. Heintges, G. Simone, G. H. Gelinck, V. S. Gevaerts, R. Andriessen, G. Pirotte, W. Maes, W. Li, M. M. Wienk, R. A. J. Janssen, *Sol. RRL* **2018**, *2*, 1800018.

[2] J. Gilot, M. M. Wienk, R. A. J. Janssen, *Appl. Phys. Lett.* **2007**, *90*, 143512.

[3] J. Gilot, Polymer Tandem Solar Cells, Ph.D thesis, Eindhoven University of Technology, **2010**, ISBN: 978-90-386-2279-8.

[4] D. J. D. Moet, P. de Bruyn, P. W. M. Blom, *Appl. Phys. Lett.* **2010**, *96*, 153504.

[5] S. Lu, H. Lin, S. Zhang, J. Hou, W. C. H. Choy, *Adv. Energy Mater.* **2017**, *7*, 1701164.

[6] Q. Jiang, L. Zhang, H. Wang, X. Yang, J. Meng, H. Liu, Z. Yin, J. Wu, X. Zhang, J. You, *Nat. Energy* **2016**, *2*, 16677.

[7] S. Trost, K. Zilberberg, A. Behrendt, T. Riedl, *J. Mater. Chem.* **2012**, *22*, 16224.

[8] S. Trost, T. Becker, A. Polywka, P. Görrn, M. F. Oszajca, N. A. Luechinger, D. Rogalla, M. Weidner, P. Reckers, T. Mayer, T. Riedl, *Adv. Energy Mater.* **2016**, *6*, 1600347.

[9] T. Becker, S. Trost, A. Behrendt, I. Shutsko, A. Polywka, P. Görrn, P. Reckers, C. Das, T. Mayer, D. Di Carlo Rasi, K. H. Hendriks, M. M. Wienk, R. A. J. Janssen, T. Riedl, *Adv. Energy Mater.* **2018**, *8*, 1702533.

[10] Z.-G. Zhang, B. Qi, Z. Jin, D. Chi, Z. Qi, Y. Li, J. Wang, *Energy Environ. Sci.* **2014**, *7*, 1966.

[11] H. Bin, L. Gao, Z. G. Zhang, Y. Yang, Y. Zhang, C. Zhang, S. Chen, L. Xue, C. Yang, M. Xiao, Y. Li, *Nat. Commun.* **2016**, *7*, 13651.

[12] W. Li, A. Furlan, K. H. Hendriks, M. M. Wienk, R. A. J. Janssen, *J. Am. Chem. Soc.* **2013**, *135*, 5529.

[13] J. Gilot, M. M. Wienk, R. A. J. Janssen, *Adv. Mater.* **2010**, *22*, E67.

[14] J. Gilot, M. M. Wienk, R. A. J. Janssen, *Adv. Funct. Mater.* **2010**, *20*, 3904.

[15] R. Timmreck, T. Meyer, J. Gilot, H. Seifert, T. Mueller, A. Furlan, M. M. Wienk, D. Wynands, J. Hohl-Ebinger, W. Warta, R. A. J. Janssen, M. Riede, K. Leo, *Nat. Photonics* **2015**, *9*, 478.

[16] K. H. Hendriks, G. H. L. Heintges, V. S. Gevaerts, M. M. Wienk, R. A. J. Janssen, *Angew. Chem., Int. Ed.* **2013**, *52*, 8341.

[17] S. Esiner, H. Van Eersel, M. M. Wienk, R. A. J. Janssen, *Adv. Mater.* **2013**, *25*, 2932.

Summary

Tandem, Triple, and Quadruple Junction Polymer Solar Cells

Chapter 1 reports a global energy scenario characterized by a growing demand, which until now strongly relies on the availability of traditional energy sources like oil. As the consumption of these has dramatic consequences for climate changes, other renewable sources need to be harnessed. Solar energy is the most abundant one, and the development of solar cells based on crystalline silicon has resulted in the enormous progress in the conversion of solar energy. Manufacturing such crystalline silicon solar cell requires materials with high purity. Moreover, in order to absorb efficiently light the use of thick layers is required, which limits the number of potential applications. Therefore a number of alternative technologies have been developed to comply with solving these limitations. Among these, organic photovoltaics (OPV) emerged as an attractive alternative. OPV technology is based on non-toxic organic semiconductor molecules, which can eventually be deposited by low-cost printing techniques. Characteristics of the devices like low weight, semi-transparency, customizable color and mechanical flexibility attract a significant attention on this future technology. Efficiencies of OPV devices are so far lower than for crystalline silicon. Nevertheless multi-junction architectures offer the possibility to reduce thermalization and transmission losses, and increase the efficiency. Multi-junction devices consist of the combination of more photoactive layers with complementary absorption, connected in series via an interconnecting layer (ICL). The ICL is made out of a stack of a hole and an electron transporting layers. Research on organic multi-junction solar cells yielded significant improvements since the first devices obtained by thermal evaporation of small molecules. An important step came with the development of all-solution-processed multi-junction cells.

The recent period (from early 2015 to middle 2018) was characterized by important accomplishments in the framework of such solution-processed multi-junction devices, which are systematically reviewed and discussed in **Chapter 2**. The efficiency of tandems increased steadily up to the current record PCE at an outstanding value of 17.3%. This accomplishment was possible by the introduction of small molecular non-fullerene acceptors (NFA) in the active layer of the subcells. The reduced minimum energy loss afforded by blends of photoactive polymers and NFA is the crucial factor determining their improved performance, compared to fullerene-derivatives-based blends. Tandems with polymer:PCBM blends were

still actively developed (best PCE > 11%), followed by materials combinations like small-molecular donor:PCBM (best PCE = 12.5%) and polymer:polymer blends (best PCE = 11.2%). Besides the active layer, also the ICL is of crucial importance in a multi-junction device. Chapter 2 presents developments spanning from the use of new combinations of functional materials (e.g. conjugated polyelectrolytes) to processing techniques (e.g. nanocomposite of bulk heterojunction and interlayer material), and stacks to manipulate optical field (e.g. MoO_3/Ag/PFN). New triple- and quadruple-junction solar cells are presented. The chapter covers also studies projected to the future upscaling of the technology, and reports where the focus was on reliable characterization methods.

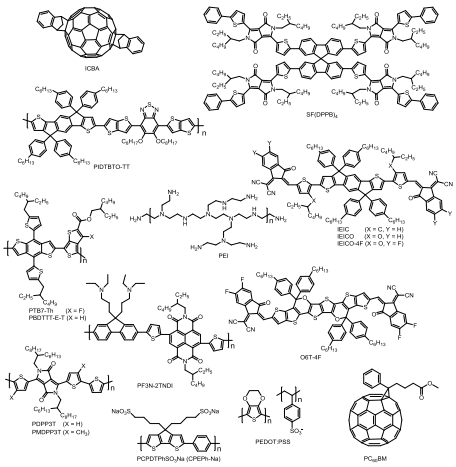

Crucial to the success of manufacturing multi-junction polymer solar cells is the so-called "orthogonality" of the processing solvents used: the solution from which a material is processed must not interfere with the layers deposited already on the substrate. For cells that may contain up to ten different layers that range in thickness from a few tens to few hundreds of nanometers this is far from trivial. **Chapter 3** reports the development of a robust processing technique for the ICL to enable the fabrication of multi-junction solar cells in the so-called n-i-p configuration. In order to do so, a modification of the commercial aqueous dispersion of a hole transporting material (PEDOT:PSS) was developed to enable coating it on hydrophobic surfaces. The key advancement made, was found in diluting the pristine water-based formulation with an organic solvent (1-propanol) at a near azeotropic composition, such that de-wetting is prevented during the formation of the films. For the electron transporting layer zinc oxide nanoparticles were used, dispersed in isoamyl alcohol. The processing of these two charge transport materials on top of each other functioned as very versatile interconnecting layer. With this method six different double and three different triple-junction polymer solar cells were made using a wide range of different photoactive materials, without changing the processing conditions. A very good fabrication

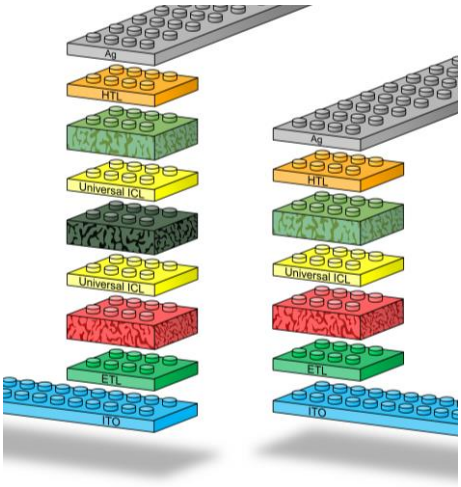

yield was afforded, complemented by efficiencies up to 10%, the latter being limited only by the properties of the materials in the active layers.

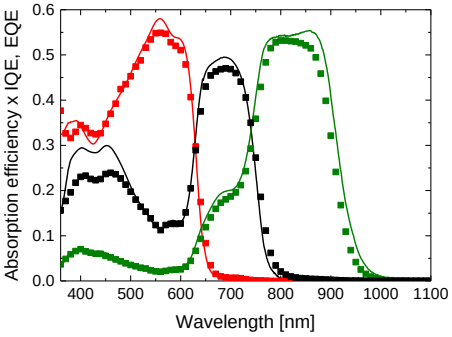

During this series of experiments, it became clear that characterizing the external quantum efficiency (EQE) of triple-junction solar cells is challenging. By adopting different high-power light-emitting diode sources, a characterization protocol was developed for such devices, which involved optical modeling simulations and the use of single-junction cells, representative of the subcells in the triple-junction device. This work is presented in **Chapter 4**. The key feature in this procedure is to optically bias the subcells not to be measured and to correct for the optically induced electric field by using a voltage correction. The latter was determined using the representative single-junction cells. This method was tested on a state-of-the-art triple-junction polymer solar cell with a PCE of 10.0%. Excellent correspondence of the experimental EQE with the optical-electrical modeled EQE was obtained, validating the whole procedure. In principle this approach enables to characterize any complex multi-junction cell, once the performance of the single-junction cells that are used in the stack is known.

The knowledge from the previous Chapters 3 and 4 allowed in the next step to develop and demonstrate the first example ever of a quadruple-junction polymer solar cell comprising four different and complementary absorber active layers, reported in **Chapter 5**. Remarkably, the devices made showed nearly no voltage loss (V_{OC} = 2.45 V) and their EQEs extended up to 1100 nm. Again, the measured performance matched very well with the one expected from the optical-electrical modeling, and the spectral response of each individual subcell was successfully characterized using an extension of the aforementioned protocol. From an analysis of the optical losses, it emerged that the efficiency (7.6% at best) was limited by bimolecular recombination in the photoactive materials, which hinders the use of thicker layers to absorb more light.

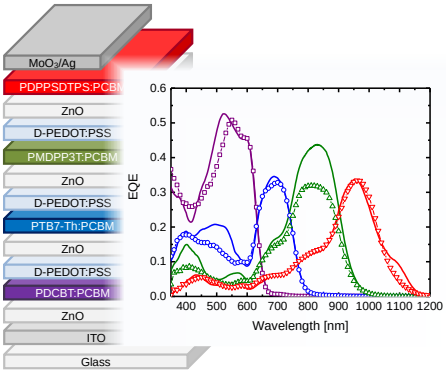

Chapter 6 focuses on exploring new combinations of functional materials for the ICL of tandem solar cells. In particular, the potential of commercially available tin oxide nanoparticle suspensions was investigated. By using tin oxide and PEDOT:PSS, the feasibility of fabricating both p-i-n and n-i-p single-junction solar cells was first demonstrated. A comparable performance was observed for these cells and for a conventional control device. In order to fabricate tandem solar cells in a p-i-n configuration, it was verified that tin oxide is resistant against the deposition of PEDOT:PSS from its acidic aqueous dispersion, which follows in the stack. Also the reverse sequence of depositing tin oxide from butanol on PEDOT:PSS was demonstrated. Subsequently, high efficiency (>10%) tandems in both the p-i-n and the n-i-p configurations were manufactured. The p-i-n tandem in particular proved to have superior characteristics to the traditional stack adopting zinc oxide nanoparticles instead of tin oxide. In fact, the zinc oxide cannot withstand the deposition of acidic PEDOT:PSS, and requires the use of a pH-neutral formulation of PEDOT, which leads occasionally to a lower performance. This drawback is circumvented with tin oxide.

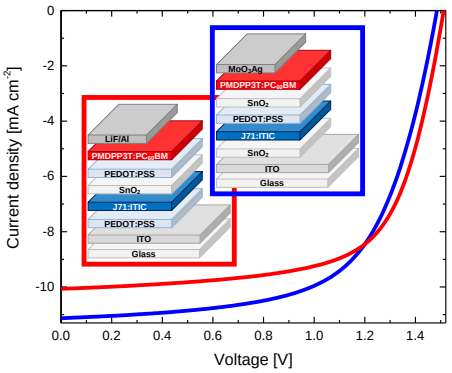

Summarizing, the thesis describes new materials, new processing methods and new characterization methods that have enabled the fabrication of fully functional solution-processed multi-junction solar cell devices of unprecedented complexity and excellent performance.

Biography

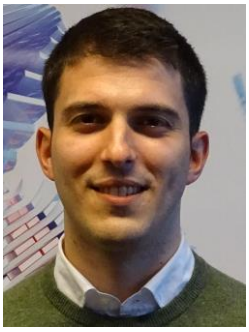

I was born in Frascati (Italy), a small municipality on the outskirts of Rome. During high school education at the Technical Institute E. Fermi in Frascati, I studied Physics and Chemistry of the Environment, which nurtured my interest in science. Thereafter, an undergraduate degree in Materials Science from the University of Rome Tor Vergata allowed me to participate in an interdisciplinary program that was rich in practical laboratory work. As a part of the graduation dissertation, I presented the results of a study on screen-printable conductive pastes for next generation photovoltaic, conducted during an internship at the Center for Hybrid and Organic Solar Energy (CHOSE).

Soon after, I enrolled in the post-graduate program in Materials Science and Technology, also at the University of Rome Tor Vergata. The program laid great emphasis on applied aspects of materials science and covered a broad range of areas such as biochemistry, metallurgy, ceramic materials and superconductors. The Organic Electronics course in particular stimulated my interest and thus a M.Sc. dissertation on polymer solar cells under the guidance of Prof. Thomas Brown followed. In that work, I investigated interlayer materials processed from water and alcohol-based solvents compatible with large-scale manufacturing. Naturally, my enthusiasm for this field increased in that period and led to me applying to a Ph.D. position in Prof. René Janssen's group at Eindhoven University of Technology. After an interview, he offered me an opportunity to work on a project aimed at advancing the design, fabrication and characterization of efficient solution-processed multi-junction polymer solar cells.

List of Publications and Contributions

Publications in scientific journals

The Impact of Device Polarity on the Performance of Polymer-Fullerene Solar Cells
Mengmeng Li, Junyu Li, Dario Di Carlo Rasi, Fallon J. M. Colberts, Junke Wang, Gaël H. L. Heintges, Baojun Lin, Weiwei Li, Wei Ma, Martijn M. Wienk, René A. J. Janssen, *Advanced Energy Materials* **2018**, *8*, 1800550.

A Universal Route to Fabricate n-i-p Multi-Junction Polymer Solar Cells via Solution Processing
Dario Di Carlo Rasi, Koen H. Hendriks, Gaël H. L. Heintges, Giulio Simone, Gerwin H. Gelinck, Veronique S. Gevaerts, Ronn Andriessen, Geert Pirotte, Wouter Maes, Weiwei Li, Martijn M. Wienk, René A. J. Janssen, *Solar RRL* **2018**, *2*, 1800018.

All-Oxide MoO_X/SnO_X Charge Recombination Interconnects for Inverted Organic Tandem Solar Cells
Tim Becker, Sara Trost, Andreas Behrendt, Ivan Shutsko, Andreas Polywka, Patrick Görrn, Philip Reckers, Chittaranjan Das, Thomas Mayer, Dario Di Carlo Rasi, Koen H. Hendriks, Martijn M. Wienk, René A. J. Janssen, Thomas Riedl, *Advanced Energy Materials* **2018**, *8*, 1702533.

New n-Type Solution Processable All Conjugated Polymer Network: Synthesis, Optoelectronic Characterization, and Application in Organic Solar Cells
Hakan Bildirir, Dario Di Carlo Rasi, Martijn M. Wienk, René A. J. Janssen, Apostolos Avgeropoulos, Vasilis G. Gregoriou, Sybille Allard, Ullrich Scherf, Christos L. Chochos, *Macromolecular Rapid Communications* **2018**, *39*, 1700629.

8.0% Efficient All-Polymer Solar Cells with High Photovoltage of 1.1 V and Internal Quantum Efficiency near Unity
Xiaofeng Xu, Zhaojun Li, Wei Zhang, Xiangyi Meng, Xianshao Zou, Dario Di Carlo Rasi, Wei Ma, Arkady Yartsev, Mats R. Andersson, René A. J. Janssen, Ergang Wang, *Advanced Energy Materials* **2018**, *8*, 1700908.

Accurate Characterization of Triple-Junction Polymer Solar Cells
Dario Di Carlo Rasi, Koen H. Hendriks, Martijn M. Wienk, René A. J. Janssen, *Advanced Energy Materials* **2017**, *7*, 1701664.

High-Performance and Stable All-Polymer Solar Cells Using Donor and Acceptor Polymers with Complementary Absorption
Zhaojun Li, Wei Zhang, Xiaofeng Xu, Zewdneh Genene, Dario Di Carlo Rasi, Wendimagegn Mammo, Arkady Yartsev, M. R. Andersson, René A. J. Janssen, Ergang Wang, *Advanced Energy Materials* **2017**, *7*, 1602722.

Quadruple Junction Polymer Solar Cells with Four Complementary Absorber Layers
Dario Di Carlo Rasi, Koen H. Hendriks, Martijn M. Wienk, René A. J. Janssen, *Advanced Materials* **2018**, *30*, 1803836.

Near-Infrared Tandem Organic Photodiodes for Future Application in Artificial Retinal Implants
Giulio Simone, Dario Di Carlo Rasi, Xander de Vries, Gaël H. L. Heintges, Stefan C. J. Meskers, René A. J. Janssen, Gerwin H. Gelinck, *Advanced Materials* **2018**, DOI: 10.1002/adma.201804678.

Solution-Processed Tin Oxide-PEDOT:PSS Interconnecting Layers for Efficient Inverted and Conventional Tandem Polymer Solar Cells
Dario Di Carlo Rasi, Pieter M. J. G. van Thiel, Haijun Bin, Koen H. Hendriks, Gaël H. L. Heintges, Martijn M. Wienk, Tim Becker, Yongfang Li, Thomas Riedl and René A. J. Janssen, *submitted for publication*.

Advances in Solution-Processed Multi-Junction Organic Solar Cells
Dario Di Carlo Rasi and René A. J. Janssen, *submitted for publication*.

Conference contributions

Quadruple Junction Polymer Solar Cells with Four Complementary Absorber Layers
Dario Di Carlo Rasi, Koen H. Hendriks, Martijn M. Wienk, and René A. J. Janssen, *Hybrid and Organic Photovoltaic Conference* **2018**, Benidorm, Spain, **contributed talk**.

A Universal Route to Fabricate n-i-p Multi-Junction Polymer Solar Cells via Solution Processing
Dario Di Carlo Rasi, Koen H. Hendriks, Giulio Simone, Veronique S. Gevaerts, Gerwin H. Gelinck, Ronn Andriessen, Martijn M. Wienk, René A. J. Janssen, *European Materials Research Society Conference* **2017**, Warsaw, Poland, **contributed talk**.

Accurate Characterization of Triple-Junction Polymer Solar Cells
Dario Di Carlo Rasi, Koen H. Hendriks, Martijn M. Wienk, René A. J. Janssen, *Next-Gen III: PV Materials Conference* **2017**, Groningen, The Netherlands, **contributed talk**.

A Universal Route to Fabricate n-i-p Multi-Junction Polymer Solar Cells via Solution Processing
Dario Di Carlo Rasi, Koen H. Hendriks, Giulio Simone, Veronique S. Gevaerts, Gerwin H. Gelinck, Ronn Andriessen, Martijn M. Wienk, René A. J. Janssen, *Next-Gen III: PV Materials Conference* **2017**, Groningen, The Netherlands, **poster presentation**.

Acknowledgements

The work presented in this thesis would not have been possible without the contribution, scientific and otherwise, of some wonderful people.

First and foremost. I am immensely grateful to my supervisor René, for believing in me since the very beginning and for offering me the opportunity to work in one of the best research environments. During these four years I have come to realize and greatly admire the amount of love you put in your work and your way to approach and help people. Your enlightened support and guidance were crucial for the success of this work.

I would also like to convey my sincere appreciation to my co-supervisor Martijn. I enjoyed the many discussions and brainstorming during our meetings, from which I tried to learn how to improve on various, often disparate, aspects of research. Thank you for your belief and for your enthusiasm.

Dear Margot, meeting you was something special! Since the early days at the group, I saw an extraordinary energy in you. You transmitted me a lot of joy, not to mention all the help that I received from you, and not just for work-related matters. Even when it gets too demanding, I appreciate the lengths to which you're willing to go to help those around you. I like this quality a lot. We certainly had a lot of fun together and I hope that there are going to be many such occasions in the future.

Koen, thank you so much for helping me during these years with your amazing synthetic skills, your brilliant ideas and for the useful discussions together. Thanks to all the support from you and Alice, I could get off to a good start and succeed with this thesis.

I want to express my heartfelt gratitude to Jordi Martorell, Jan Anton Koster, Koen Vandewal, Stefan Meskers and Erwin Kessels for participating in the committee of my Ph.D. defence and for their feedback on the dissertation.

Tim and Thomas, it was a great pleasure to spend one month in your group and learn from your experience in metal oxides. I had good time also with the other members of the group, of whom I have good memories. I'm very happy about our collaboration thereafter which led to two very good papers about tin oxide.

Dear Veronique, thanks a lot for your curiosity about my progress, and for sharing the magical zinc oxide and its recipe. It was critical to the success of this thesis. Thanks also to Robin for helping me to replicate exactly the synthesis.

I cannot leave out my dear friend Giulio on this occasion. Caro Giulio, da quando ti conosco abbiamo condiviso svariati momenti insieme, che mi hanno fatto capire quanto tu sia speciale per me. Dalle cose più grandi a quelle più piccole, c'è stata sempre una grande complicità tra di noi. La tua carica di positività è un bene prezioso che tocca chiunque ti sia attorno. Auguro a te, Francesca e alla tua famiglia tutto il bene del mondo e vi ringrazio per la vostra amicizia.

Dear Benjamin, when I saw you in the office for the first time, I immediately recognized a very friendly guy. Spending time with you brought me a lot of fun and enjoyment, and a sense of brotherhood as well. My working days took a different flavor with you around. You made a difference outside work too; I got to know your beautiful friends, with whom we had a good time doing sports, BBQs and more.

Pieter (Leenaers) thank you for friendship. I am glad about the time spent with you and your friends. I was at ease in your company, either watching a movie, cooking, chilling around, or just having a chat. I have many good memories of the time with you and Benji and I hope that the future will bring us more.

Another Pieter of my life is my former student. Thank you for the great work you performed under my supervision. Thanks to you we could submit a beautiful paper on solution-processed tin oxide for tandem solar cells. After your stint at the group, we continued having good relationship and had a lot of fun together, for which I am very grateful.

I want to thank all the M2N group members for helping me and for creating a very nice atmosphere at work. Firstly, thank you Gaël and Miriam; I enjoyed sharing the office with you and we had a good time together. Serkan, you were always available to help me and to have a chat, I really appreciate your kindness. Thank you! Marco and Wijnand, what an amazing duo you form! Thanks a lot for your constant support and for keeping things running efficiently in the lab. Robin, Fallon, Ruurd, Junke, Mike, Hans, Bardo, Bart, Haijun, Anna, Mengmeng, Matt, Dong, Bas, Tom, thank you all for being great colleagues and for sharing good moments with me. I want to thank Kunal, who was always available for proof-reading but also for chatting over a cup of coffee, a movie, a photo exhibition and more. Together we attended the last Dutch course at TU/e taught by Elly, whom I want to thank for nurturing my passion for learning this language, which took me two years, including many weekends. During the Dutch courses I also got to know Adam, Dave and Christian, whom I want to thank on this occasion for their friendship and for the good time together. Thank you Aart, Xander, Niels, Harm and the other colleagues at Spectrum.

I also have a list of (many) Italian friends whom I would like to thank, some already acquainted with since Rome and others whom I met during the Ph.D.

Caro Vito, all'inizio di questo lungo periodo abbiamo cominciato a scoprire l'Olanda insieme. Non avevamo bisogno di chissá quale organizzazione, solo un treno e una destinazione. Abbiamo stretto una buona amiciza e ho avuto il piacere di conoscere delle belle persone a te care durante le mie visite a Otranto e Barcellona. Insieme a Sabrina, Luca, Francesco e Beatrice abbiamo condiviso delle belle esperienze insieme. Grazie a tutti voi!

Grazie a Valerio, Francesco, Simone, Giordano e Annalisa. Ci siamo sparpagliati bene in giro per l'Europa e il mondo ma sono felice che ci sia ancora voglia di stare insieme. Non mi sarei mai e poi mai aspettato di ritrovare Francesco nel mio stesso progetto. Inutile esprimere quanto abbia apprezzato la scoperta!

Grazie ad Alberto, Benedetta, Giulia e gli altri membri del progetto OSNIRO, con cui ho collaborato e condiviso belle esperienze. Caro Alberto, ho trovato in te un buon amico e sono contento che abbiamo potuto passare diversi mesi a contatto, per non parlare delle visite occasionali insieme a Francesco e Benedetta.

Grazie a Gabriele, Emanuele, Andrea, Daniele, Diletta, Tiziana. Sebbene ognuno di noi abbia avanzato nella sua carriera, sono contento che siamo riusciti a restare in contatto durante tutto questo tempo. Ogni volta che tornavo a Roma ho avuto molto piacere nel rivedervi.

Hong, I was waiting to meet someone like you since a long time. Although we had known each other already from quite some time ago via Benji and Adam, it occurred to me just by chance when I saw you one day, close to the thesis submission deadline, parking your bike to go print some articles. I offered my help to print your papers and from then on we got to know each other better. Thank you for being close to me during one of the toughest periods in my Ph.D.

At last but certainly not least, I would like to thank my family. Mamma, papà, grazie di cuore per tutto il sostegno che mi avete dato da sempre. Fare questa esperienza di lavoro (e di vita) molto lontano da voi mi ha aperto la mente e molte possibilitá per il futuro. Tutto questo lo devo soprattutto a voi, che avete sempre assecondato le mie scelte di studi. Vivere lontani non é facile ma vi rigrazio per accettare la mia scelta di restare in Olanda per cercare lavoro. Vi voglio bene. Sara, Simona, Myriam, Luca, grazie anche a voi per il vostro affetto e il supporto. Gigi, Stefania, Chiara, grazie per la vostra amicizia e vicinanza. Sono molto contento che siate riusciti a partecipare alla mia cerimonia di dottorato. Per chiudere, i miei nipotini Giorgio e Giulio, ai quali dedico questo lavoro. Vi amo e vi auguro ogni bene.

Appendix

Appendix 1. Photovoltaic parameters of ITO/ZnO/PDCBT:$PC_{60}BM$/PEDOT:PSS/MoO_3/Ag devices.

Appendix 2. Photovoltaic parameters of ITO/ZnO/PDPPTPT:$PC_{70}BM$/PEDOT:PSS/MoO_3/Ag devices.

Appendix 3. Photovoltaic parameters of ITO/ZnO/PMDPP3T:$PC_{60}BM$/MoO_3/Ag devices.

Appendix 4. Photovoltaic parameters of ITO/PEDOT:PSS/ZnO/PTB7-Th:$PC_{70}BM$/PEDOT:PSS/MoO_3/Ag devices.

Appendix 5. Photovoltaic parameters of ITO/ZnO/PMDPP3T:$PC_{60}BM$/PEDOT:PSS/MoO_3/Ag devices.

Appendix 6. Photovoltaic parameters of ITO/PEDOT:PSS/ZnO/PDPPSDTPS:$PC_{60}BM$/MoO_3/Ag devices.

Appendix 7. Photovoltaic parameters of ITO/PEDOT:PSS/PMDPP3T:$PC_{60}BM$/LiF/Al devices.

Appendix 8. Photovoltaic parameters of ITO/SnO_2/J71:ITIC/PEDOT:PSS/MoO_3/Ag devices.

Appendix 1. Photovoltaic parameters of ITO/ZnO/PDCBT:$PC_{60}BM$/PEDOT:PSS/MoO_3/Ag devices.

Thickness [nm]	V_{OC} [a)] [V]	J_{SC} [a)] [mA cm^{-2}]	FF [a)]	P_{max} [a)] [mW cm^{-2}]	J_{SC}^{EQE} [mW cm^{-2}]	IQE [b)]
90	0.87 ± 0.01	7.14 ± 0.01	0.76 ± 0.01	4.69 ± 0.01	7.28	0.73
115	0.85 ± 0.00	7.85 ± 0.08	0.72 ± 0.00	4.80 ± 0.05	8.11	0.76
133	0.86 ± 0.00	8.61 ± 0.14	0.70 ± 0.01	5.21 ± 0.10	9.10	0.77
190	0.85 ± 0.01	9.93 ± 0.07	0.59 ± 0.01	4.90 ± 0.09	10.07	0.71

[a)] The statistics was calculated over 4 cells for each thickness of the active layer. [b)] IQE was determined as the ratio between the EQE-integrated J_{SC} and the maximum predicted J_{SC} according to the optical modeling.

Appendix 2. Photovoltaic parameters of ITO/ZnO/PDPPTPT:$PC_{70}BM$/PEDOT:PSS/MoO_3/Ag devices.

Thickness [nm]	V_{OC} [a)] [V]	J_{SC} [a)] [mA cm^{-2}]	FF [a)]	P_{max} [a)] [mW cm^{-2}]	J_{SC}^{EQE} [mW cm^{-2}]	IQE [b)]
75	0.77	13.0	0.63	6.26	12.2	0.68
85	0.75	12.6	0.61	5.78	12.3	0.67
100	0.78	12.7	0.60	5.90	12.3	0.67
110	0.76	12.7	0.59	5.65	12.4	0.66
125	0.74	12.2	0.57	5.16	12.1	0.65
145	0.77	13.0	0.56	5.57	12.8	0.64
180	0.74	13.3	0.49	4.77	12.8	0.61

[a)] The best device over 4 cells for each thickness of the active layer was reported. [b)] IQE was determined as the ratio between the EQE-integrated J_{SC} and the maximum predicted J_{SC} according to the optical modeling.

Appendix 3. Photovoltaic parameters of ITO/ZnO/PMDPP3T:$PC_{60}BM$/MoO_3/Ag devices.

Thickness [nm]	V_{OC} [a] [V]	J_{SC} [a] [mA cm^{-2}]	FF [a]	P_{max} [a] [mW cm^{-2}]	J_{SC}^{EQE} [mW cm^{-2}]	IQE [b]
60	0.64 ± 0.01	10.18 ± 0.10	0.63 ± 0.01	4.05 ± 0.05	10.8	0.69
75	0.63 ± 0.01	12.45 ± 0.19	0.61 ± 0.06	4.72 ± 0.56	13.3	0.70
90	0.62 ± 0.00	14.50 ± 0.18	0.63 ± 0.01	5.66 ± 0.17	15.2	0.70
110	0.61 ± 0.00	15.35 ± 0.20	0.61 ± 0.02	5.74 ± 0.22	15.9	0.70
130	0.61 ± 0.00	15.78 ± 0.21	0.58 ± 0.02	5.58 ± 0.25	16.1	0.70
150	0.60 ± 0.00	15.95 ± 0.24	0.56 ± 0.02	5.29 ± 0.11	16.5	0.71
190	0.59 ± 0.01	15.70 ± 0.47	0.43 ± 0.07	3.98 ± 0.85	16.7	0.71

[a] The statistics was calculated over 4 cells for each thickness of the active layer. [b] IQE was determined as the ratio between the EQE-integrated J_{SC} and the maximum predicted J_{SC} according to the optical modeling.

Appendix 4. Photovoltaic parameters of ITO/PEDOT:PSS/ZnO/PTB7-Th:$PC_{70}BM$/ PEDOT:PSS/MoO_3/Ag devices.

Thickness [nm]	V_{OC} [a] [V]	J_{SC} [a] [mA cm^{-2}]	FF [a]	P_{max} [a] [mW cm^{-2}]	J_{SC}^{EQE} [mW cm^{-2}]	IQE [b]
80	0.76 ± 0.00	11.78 ± 0.05	0.64 ± 0.01	5.69 ± 0.06	12.0	0.94
110	0.76 ± 0.00	12.20 ± 0.00	0.62 ± 0.01	5.69 ± 0.05	12.7	0.91
125	0.76 ± 0.00	12.93 ± 0.05	0.59 ± 0.01	5.79 ± 0.06	13.3	0.88
130	0.76 ± 0.00	12.73 ± 0.10	0.56 ± 0.00	5.43 ± 0.08	12.9	0.87
140	0.75 ± 0.01	13.53 ± 0.13	0.54 ± 0.01	5.48 ± 0.09	13.9	0.84
160	0.74 ± 0.00	14.23 ± 0.17	0.48 ± 0.01	5.07 ± 0.14	14.3	0.79
170	0.76 ± 0.00	14.80 ± 0.27	0.49 ± 0.01	5.53 ± 0.12	14.9	0.77

[a] The statistics was calculated over 4 cells for each thickness of the active layer. [b] IQE was determined as the ratio between the EQE-integrated J_{SC} and the maximum predicted J_{SC} according to the optical modeling.

Appendix 5. Photovoltaic parameters of ITO/ZnO/PMDPP3T:$PC_{60}BM$/PEDOT:PSS/MoO_3/Ag devices.

Thickness [nm]	V_{OC} [a)] [V]	J_{SC} [a)] [mA cm^{-2}]	FF [a)]	P_{max} [a)] [mW cm^{-2}]	J_{SC}^{EQE} [mW cm^{-2}]	IQE [b)]
100	0.61 (0.61)	14.8 (14.2)	0.67 (0.67)	6.05 (5.77)	14.4	0.76
120	0.60 (0.60)	14.7 (14.4)	0.66 (0.65)	5.82 (5.59)	14.7	0.76
145	0.60 (0.60)	15.5 (15.2)	0.60 (0.60)	5.58 (5.44)	15.5	0.76
165	0.59 (0.59)	16.1 (15.5)	0.56 (0.55)	5.32 (5.06)	16.1	0.76
175	0.59 (0.59)	17.1 (16.0)	0.55 (0.54)	5.64 (5.13)	16.6	0.76
205 [c)]	0.59 (0.59)	17.4 (17.0)	0.50 (0.50)	5.13 (4.95)	17.3	0.76

[a)] For each thickness of the active layer, values for the best cells are reported, average over 4 cells are given in parentheses. [b)] IQE was determined as the ratio between the EQE-integrated J_{SC} and the maximum predicted J_{SC} according to the optical modeling. [c)] The average was calculated over two devices.

Appendix 6. Photovoltaic parameters of ITO/PEDOT:PSS/ZnO/PDPPSDTPS:$PC_{60}BM$/MoO_3/Ag devices.

Thickness [nm]	V_{OC} [a)] [V]	J_{SC} [a)] [mA cm^{-2}]	FF [a)]	P_{max} [a)] [mW cm^{-2}]	J_{SC}^{EQE} [mW cm^{-2}]	IQE [b)]
60	0.28 (0.27)	7.31 (6.96)	0.52 (0.50)	1.06 (0.94)	7.60	0.48
70	0.26 (0.27)	8.70 (8.56)	0.49 (0.49)	1.11 (1.11)	9.18	0.48
80	0.30 (0.30)	9.99 (9.54)	0.52 (0.52)	1.56 (1.49)	10.19	0.49
120	0.30 (0.30)	12.4 (12.0)	0.48 (0.49)	1.79 (1.75)	12.6	0.51
170	0.32 (0.32)	13.7 (13.0)	0.52 (0.53)	2.28 (2.18)	14.0	0.53

[a)] For each thickness of the active layer, values for the best cells are reported, average over 2 cells are given in parentheses. [b)] IQE was determined as the ratio between the EQE-integrated J_{SC} and the maximum predicted J_{SC} according to the optical modeling.

Appendix 7. Photovoltaic parameters of ITO/PEDOT:PSS/PMDPP3T:$PC_{60}BM$/LiF/Al devices.

Thickness [nm]	V_{OC} [a)] [V]	J_{SC} [a)] [mA cm^{-2}]	FF [a)]	P_{max} [a)] [mW cm^{-2}]	J_{SC}^{EQE} [mW cm^{-2}]	IQE [b)]
60	0.62 (0.62)	11.2 (11.2)	0.70 (0.69)	4.86 (4.77)	11.5	0.76
80	0.62 (0.62)	12.9 (12.8)	0.68 (0.67)	5.44 (5.30)	13.1	0.75
100	0.61 (0.61)	13.9 (13.7)	0.66 (0.66)	5.60 (5.50)	14.2	0.75
125	0.60 (0.60)	14.8 (14.6)	0.64 (0.63)	5.68 (5.51)	14.8	0.74
145	0.60 (0.60)	15.2 (15.0)	0.60 (0.59)	5.47 (5.32)	15.4	0.73
190	0.59 (0.59)	15.5 (15.4)	0.55 (0.54)	5.03 (4.93)	15.6	0.72

[a)] For each thickness of the active layer, values for the best cells are reported, average over 4 cells are given in parentheses. [b)] IQE was determined as the ratio between the EQE-integrated J_{SC} and the maximum predicted J_{SC} according to the optical modeling.

Appendix 8. Photovoltaic parameters of ITO/SnO_2/J71:ITIC/PEDOT:PSS/MoO_3/Ag devices.

Thickness [nm]	V_{OC} [a)] [V]	J_{SC} [a)] [mA cm^{-2}]	FF [a)]	P_{max} [a)] [mW cm^{-2}]	J_{SC}^{EQE} [mW cm^{-2}]	IQE [b)]
55	0.91 (0.91)	15.6 (15.2)	0.65 (0.62)	9.23 (8.52)	15.1	0.95
75	0.92 (0.91)	16.1 (15.8)	0.63 (0.61)	9.33 (8.85)	15.6	0.94
80	0.91 (0.90)	15.7 (15.4)	0.62 (0.61)	8.86 (8.45)	15.3	0.94
100	0.91 (0.91)	15.3 (14.8)	0.61 (0.61)	8.49 (8.17)	14.9	0.93
115	0.92 (0.92)	14.9 (14.7)	0.62 (0.62)	8.50 (8.32)	14.6	0.92

[a)] For each thickness of the active layer, values for the best cells are reported, average over 4 cells are given in parentheses. [b)] IQE was determined as the ratio between the EQE-integrated J_{SC} and the maximum predicted J_{SC} according to the optical modeling.